DESIGN, SIMULATION, AND MEASUREMENT OF NEAR-ZERO-INDEX SHELLS FOR ELECTROMAGNETIC BEAM GENERATION

A THESIS SUBMITTED TO
THE GRADUATE SCHOOL OF NATURAL AND APPLIED SCIENCES
OF
MIDDLE EAST TECHNICAL UNIVERSITY

BY

ÖZGÜR ERİŞ

IN PARTIAL FULFILLMENT OF THE REQUIREMENTS
FOR
THE DEGREE OF MASTER OF SCIENCE
IN
ELECTRICAL AND ELECTRONICS ENGINEERING

SEPTEMBER 2021

Approval of the thesis:

DESIGN, SIMULATION, AND MEASUREMENT OF NEAR-ZERO-INDEX SHELLS FOR ELECTROMAGNETIC BEAM GENERATION

submitted by **ÖZGÜR ERİŞ** in partial fulfillment of the requirements for the degree of **Master of Science in Electrical and Electronics Engineering Department, Middle East Technical University** by,

Prof. Dr. Halil Kalıpçılar
Dean, Graduate School of **Natural and Applied Sciences** _____

Prof. Dr. İlkay Ulusoy
Head of Department, **Electrical and Electronics Engineering** _____

Prof. Dr. Özgür Ergül
Supervisor, **Electrical and Electronics Engineering, METU** _____

Examining Committee Members:

Prof. Dr. Mustafa Kuzuoğlu
Electrical and Electronics Engineering, METU _____

Prof. Dr. Özgür Ergül
Electrical and Electronics Engineering, METU _____

Prof. Dr. Gülbin Dural
Electrical and Electronics Engineering, METU _____

Prof. Dr. Özlem Aydın Çivi
Electrical and Electronics Engineering, METU _____

Assoc. Prof. Dr. Fatih Dikmen
Electronics Engineering, Gebze Technical University _____

Date: 06.09.2021

I hereby declare that all information in this document has been obtained and presented in accordance with academic rules and ethical conduct. I also declare that, as required by these rules and conduct, I have fully cited and referenced all material and results that are not original to this work.

Name, Surname: Özgür Eriş

Signature :

ABSTRACT

DESIGN, SIMULATION, AND MEASUREMENT OF NEAR-ZERO-INDEX SHELLS FOR ELECTROMAGNETIC BEAM GENERATION

Eriş, Özgür
M.S., Department of Electrical and Electronics Engineering
Supervisor: Prof. Dr. Özgür Ergül

September 2021, 189 pages

In this study, design and simulation of three-dimensional (3D) shell structures, which generate directional radiation patterns from isotropic sources, with near-zero-index (NZI) characteristics, as well as their realizations via low-cost 3D printing are presented. Throughout the design process of NZI beam generators, both homogenized structures, in which near-zero relative permittivity and/or permeability values are enforced, and actual models involving periodic arrangements of dielectric rods are examined. The solutions of electromagnetic problems are obtained by using rigorous implementations of novel surface-integral-equation (SIE) formulations in frequency domain. Iterative solutions of matrix equations derived from SIEs are accelerated by different forms of the multilevel fast multipole algorithm (MLFMA) and suitable preconditioners, when necessary. First, reflection and refraction properties of NZI media are extensively examined to obtain efficient structures in the intended frequency regimes. Then, alternative strategies are employed to obtain customized radiation patterns. In this context, various cavities with strong resonance behaviors are designed as source regions of the shells. At the same time, outer surfaces are modified to either enhance or suppress outgoing electromagnetic fields. In addition to comprehensive

simulations and analyses of NZI beam generators, their effective capabilities are verified by measurements on different prototypes fabricated via 3D printing. In order to realize NZI properties efficiently via dielectric rods, various 3D printing materials are extensively investigated by an electromagnetic characterization setup. Measurements of diverse NZI shell structures are presented to demonstrate that NZI properties are successfully achieved by well-designed arrangements of dielectric rods with proper materials. The results demonstrate the feasibility of efficient, effective, low-cost, and reconfigurable NZI shells to generate alternative beam configurations that can be useful in a plethora of microwave applications.

Keywords: Zero-Index Materials, Beam Generators, Metamaterials, Multilevel Fast Multipole Algorithm, Material Characterization, 3D Printing, Microwave Applications.

ÖZ

ELEKTROMANYETİK HÜZME ÜRETİMİ İÇİN SIFIRA YAKIN İNDİSLİ KABUKLARIN TASARIMI, SİMÜLASYONU VE ÖLÇÜMÜ

Eriş, Özgür
Yüksek Lisans, Elektrik ve Elektronik Mühendisliği Bölümü
Tez Yöneticisi: Prof. Dr. Özgür Ergül

Eylül 2021 , 189 sayfa

Bu çalışmada, eşyönlü kaynaklardan yönlü ışınım örüntüleri oluşturan sıfıra yakın indis (SYİ) niteliğine sahip üç boyutlu (3B) kabuk yapılarının tasarım ve benzetimleriyle birlikte, bu yapıların düşük maliyetli 3B baskı ile gerçeklemesi sunulmaktadır. SYİ hüzme üreteçlerinin tasarım süreçlerinde, hem sıfıra yakın bağıl elektriksel geçirgenlik ve/veya manyetik geçirgenlik değerlerinin kullanıldığı homojen modeller, hem de periyodik olarak yerleştirilen diyelektrik çubuklar içeren gerçekçi modeller incelenmiştir. Elektromanyetik problemlerin çözümleri, frekans uzayında etkin yüzey integral denklemi formülasyonlarının titiz uygulamaları vasıtasıyla gerçekleştirilmiştir. Yüzey integral denklemlerinden elde edilen matris denklemlerinin iteratif çözümleri, çok seviyeli hızlı çokkutup yöntemi (ÇSHÇY) ve gerektiğinde önkoşullayıcılarla hızlandırılmıştır. İlk olarak, istenilen frekans aralıklarında etkili yapılar elde etmek için, SYİ ortamlarının yansıma ve kırınım özellikleri kapsamlı olarak incelenmiştir. Sonrasında, isteğe göre uyarlanmış ışınım örüntüleri elde etmek için farklı stratejiler uygulanmıştır. Bu kapsamda, güçlü rezonans davranışlarına sahip çeşitli kovuklar, kabukların kaynak bölgeleri olarak tasarlanmıştır. Aynı zamanda, dış yüzeyler, dışarı çıkan

elektromanyetik dalgaları güçlendirmek veya zayıflatmak için şekillendirilmiştir. SYİ hüzme üreteçlerinin kapsamlı benzetimlerine ve analizlerine ek olarak, bunların etkin kabiliyetleri 3B yazıcılarla üretilen farklı prototiplerin ölçümleriyle doğrulanmıştır. Diyelektrik çubuklarla SYİ özelliklerini verimli bir biçimde elde edilebilmesi için, çeşitli 3B yazıcı malzemeleri bir elektromanyetik karakterizasyon düzeneği ile kapsamlı olarak incelenmiştir. Çok çeşitli SYİ kabuk yapılarının ölçümleriyle, SYİ özelliklerinin iyi tasarlanmış ve uygun malzemeler içeren diyelektrik çubuk dizilimleriyle başarılı bir şekilde elde edildiği gösterilmiştir. Sonuçlar, çok sayıda mikrodalga uygulamasında faydalı olabilecek alternatif hüzme şekillerinin oluşturulabilmesi için, verimli, etkili, düşük maliyetli ve yeniden yapılandırılabilir SYİ kabukların uygulanabilirliğini göstermektedir.

Anahtar Kelimeler: Sıfır-İndisli Malzemeler, Hüzme Üreteçleri, Metamalzemeler, Çok Seviyeli Hızlı Çokkutup Yöntemi, Malzeme Karakterizasyonu, 3B Baskı, Mikrodalga Uygulamaları.

to my family and my Burcu...

aileme ve Burcu’ma...

ACKNOWLEDGMENTS

First and foremost, I would like to express my sincere gratitude to my supervisor Prof. Dr. Özgür Ergül for his valuable support and guidance throughout all stages of this study. Thanks to him, I have learned not only how to conduct scientific research but also how to be a good engineer.

I would like to thank Prof. Dr. Özlem Aydın Çivi for her comments throughout my studies. I accomplished the fabrication and measurement process of this study thanks to her precious suggestions.

I would like to thank Prof. Dr. Sencer Koç for his kind help and suggestions about measurements. I would also like to thank Prof. Dr. Mustafa Kuzuoğlu, Prof. Dr. Gülbin Dural, and Assoc. Prof. Dr. Fatih Dikmen for their valuable comments and participation in the jury.

I would like to thank members of CEMMETU for their insprition and companionship during my studies. Special thanks to Hande İbili, Gökhan Karaova, Şirin Yazar, Göktuğ Işıklar, Uğur Meriç Gür, Sadri Güler, Barışcan Karaosmanoğlu.

I would like to thank the Information and Communication Technologies Authority and Türk Telekom within the framework of 5G and Beyond Joint Graduate Support Programme for their financial and moral support.

I would also like to thank our department technician Mesut Özer and 3D printing company 3dörtgen for their suggestions and help during the fabrication process of this study.

I would like to thank TÜBİTAK for 2210-A scholarship program as the financial support during my Master's study.

Last but not least, I would like to thank my dear wife Burcu Gözükara Eriş and my beloved family for their endless support, love, and encouragement.

TABLE OF CONTENTS

ABSTRACT v

ÖZ vii

ACKNOWLEDGMENTS x

TABLE OF CONTENTS xi

LIST OF TABLES xv

LIST OF FIGURES xvi

LIST OF ABBREVIATIONS xxx

CHAPTERS

1 INTRODUCTION 1

1.1 Metamaterials and Antennas 3

1.2 Contents of the Thesis 7

2 SIMULATIONS OF NEAR-ZERO-INDEX METAMATERIALS 9

2.1 Simulation Environment 9

2.1.1 Surface Integral Equations 11

2.1.2 Discretization and the Method of Moments 17

2.1.3 Surface Formulations 21

2.1.4 Multilevel Fast Multipole Algorithm with Approximate Diagonalization 25

2.1.5 Multilayer Iterative Strategy 27

2.1.6 Incident Fields 29

2.1.7 Far-field and Near-field Calculations 30

2.2 Realization of Near-Zero-Index Structures 31

2.3 Numerical Results 36

2.3.1 Comparison of SIEs for Homogeneous Bodies 36

2.3.2 Simulations of Periodic Structures 39

2.4 Concluding Remarks 49

3 DESIGN AND SIMULATION OF NEAR-ZERO-INDEX SHELLS ACTING AS BEAM GENERATORS 51

3.1 Introduction 51

3.2 Reflection and Transmission at Interfaces Between Vacuum and Near-Zero-Index Media 55

3.2.1 Fresnel Coefficients on a NZI-Vacuum Plane Boundary 56

3.2.2 Reflectance and Transmittance for an NZI Slab 59

3.3 Effective Index Prediction 63

3.4 Improving NZI Shell Structures with Efficient Cavities 70

3.4.1 Homogenized NZI Shells 71

3.4.2 Tapering 82

3.4.3 Realized Structures 85

3.4.4 Beam Generators for Millimeter Waves 89

3.5 Designs of Outer Surfaces 92

3.5.1 NZI Lenses 93

3.5.2 NZI Absorbers 95

3.5.3 Vertical Grids 100

3.6 Designs with More Complicated Radiation Patterns 106

3.7 On the Dielectric Loss Tangents and Permeabilities 113

3.8 Sensitivity Analyses 115

3.8.1 Effects of Surface Corrugations and Unit-Cell Placement Errors 116

3.8.2 Effects of Non-Ideal Source Locations 118

3.8.3 Frequency Response of the Square Cavity 119

3.9 Efficiency Analyses 120

3.9.1 Numerical Calculation of Radiated Power, Directive-Gain, and Efficiency 120

3.9.2 Performances of the NZI Beam Generators 122

3.10 Concluding Remarks 123

4 FABRICATION AND MEASUREMENT OF NEAR-ZERO-INDEX BEAM GENERATORS 125

4.1 On the Measurement of Constitutive Parameters 130

4.2 Material Characterization of 3D Printing Filaments 136

4.2.1 Some Plastic Filaments 136

4.2.2 High-Contrast Dielectric Composite Filaments 138

4.2.3 Effects of the Infill Ratio 142

4.3 Fabrications and Measurements of Cylindrical Rods with Predicted Dimensions 143

4.3.1 Finding the Effective Refractive Index 147

4.4 Measurements of Beam Generators 151

4.4.1 Fine-Tuning Periodicity 151

4.4.2 The Measurement Setup of Beam Generators and the Source Antenna 154

4.4.3 Measurements of Different Cavity Formations 156

4.4.4 Measurements of NZI Lenses and Absorbers 159

4.4.5 Measurements of Bidirectional NZI Shells with Vertical Grids 161

4.5 Concluding Remarks 165

5 CONCLUSIONS 167

REFERENCES 171

APPENDICES

A DERIVATION OF INCIDENT POTENTIALS AND FIELDS 183

B MATRIX FORMS OF JMCFIE AND MF FOR NZI SIMULATIONS 187

LIST OF TABLES

TABLES

Table 2.1 Duality theorem. 12

Table 3.1 Efficiency analysis of the realistic shell in Figure 3.35 when the material of the rods has different loss-tangent values. 123

Table 3.2 Efficiency analysis of the realistic square hole when surface corrugations or unit cell placemet errors are applied. 124

Table 4.1 Some high-contrast dielectric materials with nonmagnetic properties. 126

Table 4.2 Dielectric properties of 3D-printed materials. 129

Table 4.3 Measured relative permittivities of various thermoplastics. 138

Table 4.4 Measured relative permittivity and permeability values of various composite filaments. 144

Table 4.5 List of printing settings used to fabricate copper-filled PLA rods. . . 145

LIST OF FIGURES

FIGURES

Figure 1.1 Antenna specifications with regard to developing communication generations and technologies. 2

Figure 1.2 Constitutive parameters and metamaterials. 3

Figure 2.1 Simulation setup for NZI structures. 10

Figure 2.2 Boundaries between two different regions that can be penetrable, PEC, or PMC. 15

Figure 2.3 Surface models with planar triangulation. 19

Figure 2.4 An RWG function and its spatial distributions. 19

Figure 2.5 The three-layer iterative solution mechanism. 27

Figure 2.6 Stacked layers of different materials. ENZ response can be realized for an incident wave with electric field parallel to the slabs, when appropriate dielectrics are used. 32

Figure 2.7 PEC wire medium. Effective interfaces are a little bit more than the actual size of the periodic structure. When radius and periodicities (a and b) are properly arranged, ENZ property can be achieved. 33

Figure 2.8 All-dielectric PhCs. By proper arrangements, periodic arrays of rectangular prisms, square prisms, and cylinders can effectively have NZI characteristics. 34

Figure 2.9 Convergence histories for different formulations. A homogeneous shell structure with various ϵ_r and μ_r values is considered. 37

Figure 2.10 Near-zone power density distributions in the vicinity of NZI shells excited by a Hertzian dipole when different formulations are used to analyze the problems. Divergent solutions are not shown. 38

Figure 2.11 A metallic structure that demonstrates ENZ behavior.Computational models are on the left-hand side, while the electromagnetic responses are depicted on the right-hand side. 40

Figure 2.12 Far-zone electric field intensity with respect to bistatic angle generated by the structure in Figure 2.11. Omnidirectional radiation is slightly changed to a quaddirectional one by the carefully arranged PEC rods. 40

Figure 2.13 Various shell designs involving dielectric rods to be used as beam generators. Each structure is excited by a Hertzian dipole located at the center of the source region. The relative permittivity is 8.8 for the first and second designs, while it is 9.8 for the last three designs due to different impurity ratios of alumina. 42

Figure 2.14 Convergence histories in numerical solutions of PhCs. Square prisms and cylindrical rods with two different relative permittivity (RP) values are used as unit cells. 43

Figure 2.15 Convergence histories in numerical solutions of PhCs made of square prisms and cylinders. Iterative solutions are accelerated by the three-layer preconditioner considering various AFs for layer-1. 44

Figure 2.16 Convergence histories for the electromagnetic problems involving the shells described in Figure 2.13. The residual errors are plotted with respect to iterations at layer-0. 45

Figure 2.17 Power density distributions for the shells structures involving λ, 2λ, and 3λ rods. Each plot show the values in a $100\lambda \times 100\lambda$ region in the vicinity of the structure. 46

Figure 2.18 Far-zone electric field intensity results obtained for the shell structures involving 2λ rods and a z-directed Hertzian dipole as a source. Colors represent field values considering observation directions. 47

Figure 2.19 Far-zone electric field intensity results obtained for the shell structures involving 3λ rods and a z-directed Hertzian dipole as a source. Colors represent field values considering observation directions. 48

Figure 2.20 Far-zone electric field intensity results obtained for the shell structures involving 3λ rods in the azimuth plane (array plane) with respect to observation angles in degrees. 49

Figure 3.1 The design process of an NZI shell acting as a multi-beam generator. 52

Figure 3.2 NZI shells acting as beam generators in accordance with Snell's law of refraction. 53

Figure 3.3 Electric field, magnetic field, and power density distributions for cubic shells with square cavities. The excitation is a Hertzian dipole located at the centers of the cavity regions. Ordinary and NZI materials are considered. 54

Figure 3.4 Electric field, magnetic field, and power density distributions for cubic shells with square cavities, when different refractive index values are used as shell materials. For the second row, the refractive index is fixed to 5×10^{-3}. 55

Figure 3.5 Reflectance and transmittance calculations for parallel polarization. 56

Figure 3.6 Reflectance and transmittance for plane waves obliquely incident onto boundaries from vacuum to NZI materials. ENZ (3.6a), MNZ (3.6b), and EMNZ (3.6c) cases are considered when the plane wave has parallel polarization. 57

Figure 3.7 Reflectance and transmittance for plane waves obliquely incident onto boundaries from NZI materials to vacuum. ENZ (3.7a), MNZ (3.7b), and EMNZ (3.7c) cases are considered when the plane wave has parallel polarization. 58

Figure 3.8 Oblique incidence into a magneto-dielectric slab. 60

Figure 3.9 Reflectance and transmittance for an incident plane wave directed almost normally onto NZI slabs located in vacuum. EMNZ cases are considered when the plane wave has parallel polarization. 61

Figure 3.10 Reflectance and transmittance for an incident plane wave directed onto an NZI slab in vacuum. ENZ and MNZ cases (with exactly same results) are considered when the plane wave has normal incidence. 62

Figure 3.11 Dielectric rods arranged in 12×12 and 16×16 grids to create triangular prisms. Two CSP illuminations that have different beam widths are used in the simulations. Electric field intensity values are plotted only for the sources (incident fields), without any interaction with the rods. 63

Figure 3.12 Convergence histories in numerical solutions of eight different problems involving triangular prisms made of dielectric rods. Each solution takes less than 10 hours using 16 cores. 64

Figure 3.13 Near-zone field intensity and power density distributions when Source A and Source B are used to illuminate the 12×12 grid of dielectric rods possessing two different relative permittivity values. 65

Figure 3.14 Imaginary part of the electric field intensity for the 12×12 grid when the relative permittivity of the rods is 4.0 (left) and 8.8 (right). Only Source A is considered for the excitation. 66

Figure 3.15 Near-zone field intensity and power density distributions when Source A and Source B are used to illuminate the 16×16 grid of dielectric rods possessing two different relative permittivity values. 67

Figure 3.16 Imaginary part of electric field intensity for the 16×16 grid when the relative permittivity of the rods is 4.0 (left) and 8.8 (right). Only Source A is considered for the excitation. 68

Figure 3.17 Far-zone electric field intensities obtained when Source A is used to illuminate two different grids of dielectric rods possessing two different relative permittivity values. 69

Figure 3.18 Far-zone electric field intensities obtained when Source B is used to illuminate two different grids of dielectric rods possessing two different relative permittivity values. 69

Figure 3.19 Results for homogenized models of cubic shells with square cavities of different sizes. EMNZ (3.7a) , ENZ (3.7b) and MNZ (3.7c) cases are considered. 72

Figure 3.20 Near-zone field intensity and power density distributions when square cavities of different sizes when source regions are considered. These cavities correspond to the source regions of the shell structures. . 73

Figure 3.21 Height sweep for shell structures with a fixed cross section (2λ square cavity) and different NZI properties. Power density distributions are given in a $100\lambda \times 100\lambda$ frame in each case. 73

Figure 3.22 Electric field intensity distributions for homogenized models of cubic shells with circular cavities of different sizes. Cavity regions on $5\lambda \times 5\lambda$ frames and far regions on $100\lambda \times 100\lambda$ frames are investigated for EMNZ, ENZ, and MNZ cases. 74

Figure 3.23 Far-zone electric field intensities obtained when cubic shells with circular cavities having 1.9λ and 2.3λ diameters are investigated for EMNZ, ENZ, and MNZ cases. 75

Figure 3.24 Near-zone field intensity and power density distributions when circular cavities of different sizes are considered. These cavities correspond to the source regions of the shell structures. 76

Figure 3.25 Height sweep for shell structures with a fixed cross section (2.3λ-diameter circular cavity) and different NZI properties. Power density distributions are given in a $100\lambda \times 100\lambda$ frame in each case. 76

Figure 3.26 Near-zone power distributions and far-zone electric field intensity results for homogenized models of cubic shells with elliptical cavities of different sizes. In near-zone plots, $100\lambda \times 100\lambda$ frames are investigated for EMNZ, ENZ, and MNZ cases. 77

Figure 3.27 Near-zone power distributions and far-zone electric field intensity results for homogenized models of triangular prism shells with elliptical cavities of different sizes. In near-zone plots, $100\lambda \times 100\lambda$ frames are investigated for EMNZ, ENZ, and MNZ cases. 78

Figure 3.28 3D and two-dimensional far-zone electric field intensities for triangular prism shells having 4λ major and λ minor axes. EMNZ, ENZ, and MNZ shells are considered. 80

Figure 3.29 Power density distributions for EMNZ, ENZ, and MNZ shells when various cross-sectional geometries are examined. Results for cubic and cylindrical structures involving circular and square holes are given in 3.29a. Results for triangular prisms and a cylindrical structure involving circular, triangular, or square holes are given in 3.29b. 81

Figure 3.30 Power density distributions for EMNZ, ENZ, and MNZ shells when various tapering strategies are applied on the cavity surfaces. Results for linear tapering on square cavity is given in 3.30a. Results for circular and linear tapering on the square and circular cavities are given in 3.30b. 83

Figure 3.31 Realistic shell designs (the square lattice & cylinder design) involving rods with different heights to be used as beam generators. Dielectric cylindrical rods have 8.8 relative permittivity. Increased numbers of unknowns for longer rods lead to numerically challenging problems. 84

Figure 3.32 Iterative convergence histories in solutions of electromagnetic problems involving the structures in Figure 3.31, when the solutions are accelerated by the three-layer preconditioner based on AMLFMA. . 85

Figure 3.33 Far-zone electric field intensity with respect to the bistatic angle on the array plane obtained for the structures in Figure 3.31. 86

Figure 3.34 3D far-zone electric field intensity results of realized square hole having different rod heights. A Hertzian dipole is used as a primary source while its pattern is also given. 86

Figure 3.35 Results for various shell structures made of dielectric rods with different cavity formations. 88

Figure 3.36 Far-zone radiation results for various shells made of dielectric rods (3λ) with different cavity formations. 89

Figure 3.37 Periodic media involving dielectric rods that demonstrate NZI characteristics at mmWaves. 90

Figure 3.38 Imaginary part of electric field intensities, binary images and slopes, and 3D radiation patterns for 12×12 grid when relative permittivity of the rods is 4.0 (top) and 8.8 (bottom). A CSP beam is used in the simulations at 25 GHz. 91

Figure 3.39 Results for realistic NZI shells with different rod heights and square cavities to operate at 25 GHz. 92

Figure 3.40 Power density distributions for EMNZ cubic shells having circular cavities. Cavity ($5\lambda \times 5\lambda$) and far-zone regions ($100\lambda \times 100\lambda$) are considered in the x-y plane, when outer surfaces of the shells are curved. 93

Figure 3.41 Far-zone electric field intensity results when a single lens and four lenses are used for NZI cubic shells having circular cavities. 94

Figure 3.42 Results for various shell structures made of dielectric rods. Two sides of the regular grids (with 2λ and 3λ rods) are modified by extracting rods. 95

Figure 3.43 Parametric sweep for pyramids and inverted pyramids when they are put on one of the outer surfaces of an EMNZ cubic shell involving a circular hole of 2.3λ diameter. 96

Figure 3.44 Power density distributions in the x-y plane when geometries in Figure 3.43 are excited via Hertzian dipoles located at their centers. . . 98

Figure 3.45 Results for EMNZ cubic shells involving circular and square cavities when optimized inverted pyramids are placed onto different sides of the shells. 99

Figure 3.46 Results for ENZ cubic shells ($5\lambda \times 5\lambda \times 5\lambda$) involving elliptical cavities ($4\lambda \& 2\lambda$) when the optimized inverted pyramids are placed onto different sides of the shells. 100

Figure 3.47 Power density results to investigate effective corrugation designs to reach realizable structures with relatively good suppression of radiation in the intended directions. EMNZ, ENZ, and MNZ shells involving square cavities (2λ edge size) are considered. 101

Figure 3.48 Far-zone electric field intensity resuls to investigate effective corrugation designs to reach realizable structures with relatively good suppression of radiation in the intended directions. Only EMNZ shells involving square cavities (2λ edge size) are considered. 102

Figure 3.49 Results for EMNZ cubic shells involving square cavities when VGs are placed onto different shell surfaces. Circular and linear tapering are also implemented. 103

Figure 3.50 Results for various realistic shell structures with modified sides to suppress different beams. 104

Figure 3.51 Results for various realistic shell structures involving dielectric rods of height λ. In each case, the center rod is removed to place a Hertzian dipole. 105

Figure 3.52 Power density distributions for various realistic shell structures involving 3λ rods with VGs. 106

Figure 3.53 Power density distributions for various shell structures involving 3λ rods with VGs. 107

Figure 3.54 Power density distributions for homogenized models of diamond shells with square cavities having 2λ edge lengths. 107

Figure 3.55 Power density distributions for homogenized models of diamond shells with square cavities having 2λ edge lengths and VGs. 109

Figure 3.56 Far-zone radiation patterns for homogenized models of diamond shells with square cavities having 2λ edge lengths and VGs. 109

Figure 3.57 Geometries and numerical results for the realized diamond shells involving 3λ rods. The numbers of unknowns and rods are also given for each structure. 110

Figure 3.58 Iterative convergence histories in numerical solutions of the realized diamond shells involving 3λ rods. 111

Figure 3.59 Results for realized diamond shells with/without VGs. 112

Figure 3.60 Power density distributions for a realistic NZI shell involving a square cavity (see Figure 3.35) when lossy dielectric rods are used. . . . 113

Figure 3.61 3D radiation patterns for a realistic NZI shell involving a square cavity (see Figure 3.35) when lossy dielectric rods are used. 114

Figure 3.62 Results fora realistic NZI shell involving a square cavity when the relative permeability of the rods is not unity. 115

Figure 3.63 Deformed rods with various levels of lateral noise and vertical noise that is adjusted as 10% of the lateral noise. 116

Figure 3.64 Results for an NZI shell geometry involving a square cavity when deformed rods are used. 117

Figure 3.65 Results for an NZI shell geometry involving a square cavity when random positioning errors are introduced. 117

Figure 3.66 Source placement errors represented by five different locations in a $0.5\lambda \times 0.5\lambda$ area. 118

Figure 3.67 Results for an NZI shell geometry involving a square cavity when a Hertzian dipole is randomly located as depicted in Figure 3.66. . 119

Figure 3.68 Frequency response (near-zone power density distributions) of the structure in Figure 3.35. 120

Figure 3.69 Directive gain of a Hertzian dipole (left) and a realistic structure (see Figure 3.35) excited by a Hertzian dipole (right). 122

Figure 4.1 The fabrication and measurement process of an NZI shell acting as a multi-beam generator. 126

Figure 4.2 3D printing process of some composite filaments. 127

Figure 4.3 Various 3D printing filament samples used in this study. Tough-PLA's vendor is Ultimaker. The vendor of the other filaments is colorFabb. 128

Figure 4.4 The measurement structure when a sample having intrinsic impedance Z_s is placed between two sections of waveguides (or transmission lines). 131

Figure 4.5 Electromagnetic characterization setup when a metallic sample holder waveguide with 20 mm thickness is used. 131

Figure 4.6 Complex relative permittivity and permeability measurement results when a metallic sample holder waveguide with 20 mm thickness is used. 133

Figure 4.7 Electromagnetic characterization setup when a 3D-printed sample holder with 5 mm thickness is used. An aluminum tape is used to cover inner walls. 135

Figure 4.8 Complex relative permittivity and permeability measurement results when a 3D-printed sample holder waveguide with 5 mm thickness is used. 136

Figure 4.9 Electromagnetic properties of various thermoplastics. The 3D-printed sample holder with 5 mm thickness is used for measurements. . 137

Figure 4.10 Electromagnetic properties of various composite thermoplastics involving metallic powders. A 3D-printed sample holder with 5 mm thickness is used for measurements. 139

Figure 4.11 3D-printed waveguides with different thicknesses. Samples are fabricated to perfectly fit into the waveguides. 140

Figure 4.12 Electromagnetic properties of various composite thermoplastics with nanoparticles. 3D-printed sample holders with 4, 5, and 6 mm thicknesses are used for measurements. 141

Figure 4.13 Fabrication process for copper-filled PLAs with different infill ratios. 142

Figure 4.14 Electromagnetic properties of copper-filled PLAs with different infill ratios. 143

Figure 4.15 The prediction of radiuses and center-to-center distances of rods to be used to realize NZI behavior. 144

Figure 4.16 Fabrications of copper-filled PLA rods via Ultimaker 2+. 145

Figure 4.17 The preparation of an effective-refractive-index setup based on arrays of dielectric rods that are arranged to create triangular prisms. . . 146

Figure 4.18 Simulated electric field intensities, binary images, and slopes for a triangular prism made of copper-filled PLA rods. A CSP beam illuminates the structure at 10.3 GHz. 147

Figure 4.19 The effective-refractive-index-measurement setup in an anechoic chamber. A horn antenna which operates in the X-band is used to illuminate a structure consisting of cylindrical rods. 148

Figure 4.20 The far-zone radiation pattern of an X-band horn antenna, which is used to illuminate cylindrical rods. On the left, a rectangular plot is given in dB scale. On the right, a polar plot is given in linear scale. . . . 149

Figure 4.21 The far-zone radiation patterns obtained when the horn antenna is used to illuminate the 12×12 grid of dielectric rods arranged as a triangular prism. The rectangular (left) and polar (right) figures use linear scales. The triangular prism is placed in accordance with Setting 1.150

Figure 4.22 The far-zone radiation patterns obtained when the horn antenna is used to illuminate the 12×12 grid of dielectric rods arranged as a triangular prism. The rectangular (left) and polar (right) figures use linear scales. The triangular prism is placed in accordance with Setting 2.150

Figure 4.23 3D far-zone electric field results for realized beam generators with square holes having different periodicities (a). Copper-filled PLA rods with real ϵ_r and μ_r values are used in the simulations. 152

Figure 4.24 Far-zone electric field results for various realized beam generators with respect to the bistatic angle in degrees. Copper-filled PLA rods with real ϵ_r and μ_r values are used in the simulations. 153

Figure 4.25 The measurement setup for the NZI shells in an anechoic chamber. A monopole antenna is used as the primary source at the centers of the shells, while a horn antenna is used to measure the far-zone radiation patterns. 154

Figure 4.26 Photographs of various NZI shells involving copper-filled PLA rods. 155

Figure 4.27 The far-zone radiation pattern of the monopole antenna. On the left-hand side, a rectangular plot is given in a dB scale. On the right-hand side, a polar plot is given in a linear scale. 156

Figure 4.28 Simulation results for NZI shells with copper-filled PLA rods when different cavity formations are investigated. 157

Figure 4.29 Far-zone radiation patterns obtained for the structure with circular hole. On the left-hand side, a rectangular plot is given in a dB scale. On the right-hand side, a polar plot is given in a linear scale. 158

Figure 4.30 Far-zone radiation patterns of obtained for the structure with full grid. On the left-hand side, a rectangular plot is given in a dB scale. On the right-hand side, a polar plot is given in a linear scale. 158

Figure 4.31 Far-zone radiation patterns obtained for the structure with square hole. On the left-hand side, a rectangular plot is given in a dB scale. On the right-hand side, a polar plot is given in a linear scale. 159

Figure 4.32 Simulation results for NZI shells consisting of copper-filled PLA rods when different outer surface designs (VGs and lenses) are employed. 160

Figure 4.33 Far-zone radiation patterns obtained for SH Lens. On the left-hand side, a rectangular plot is given in a dB scale. On the right-hand side, a polar plot is given in a linear scale. 161

Figure 4.34 Far-zone radiation patterns obtained for SH-VG-S1. On the left-hand side, a rectangular plot is given in a dB scale. On the right-hand side, a polar plot is given in a linear scale. 161

Figure 4.35 Far-zone radiation patterns obtained for SH-VG-L1. On the left-hand side, a rectangular plot is given in a dB scale. On the right-hand side, a polar plot is given in a linear scale. 162

Figure 4.36 Far-zone radiation patterns obtained for SH-VG-1. On the left-hand side, a rectangular plot is given in a dB scale. On the right-hand side, a polar plot is given in a linear scale. 162

Figure 4.37 Simulation results for NZI shells when different VGs are investigated. Bidirectional radiations are successfully obtained for NZI shells involving copper-filed PLA rods. 163

Figure 4.38 Far-zone radiation patterns obtained for SH-VG-2A. On the left-hand side, a rectangular plot is given in a dB scale. On the right-hand side, a polar plot is given in a linear scale. 164

Figure 4.39 Far-zone radiation patterns obtained for SH-VG-2S. On the left-hand side, a rectangular plot is given in a dB scale. On the right-hand side, a polar plot is given in a linear scale. 164

Figure 4.40 Far-zone radiation patterns obtained for FG-VG-2A. On the left-hand side, a rectangular plot is given in a dB scale. On the right-hand side, a polar plot is given in a linear scale. 165

Figure 4.41 Far-zone radiation patterns obtained for FG-VG-2S. On the left-hand side, a rectangular plot is given in a dB scale. On the right-hand side, a polar plot is given in a linear scale. 165

Figure A.1 Real part of the electric field intensity in the x-y plane when a Hertzian dipole with $\boldsymbol{I}_d = \hat{\boldsymbol{z}}$ is located (a) at the origin and (b) at a position on the imaginary x axis. 185

LIST OF ABBREVIATIONS

3D	Three dimensional
5G	Fifth generation
ABS	Acrylonitrile butadiene styrene
AD	Approximately diagonalized
AF	Approximation factor
BDP	Block-diagonal preconditioner
CSP	Complex source point
CTF	Combined T formulation
DPS	Double positive materials
EFIE	Electric-field integral equation
EMNZ	ϵ-μ-near-zero
ENZ	ϵ-near-zero
FFF	Fused filament fabrication
FMM	Fast multipole method
GMRES	Generalized minimal residual method
JMCFIE	Electric-magnetic current combined-field integral equation
MCTF	Modified combined T formulation
MF	NZI mixed formulation
MDF	Medium-density fibreboard
MFIE	Magnetic-field integral equation
MLFMA	Multilevel fast multipole algorithm
mmWaves	Millimeter waves
MNMF	Modified N Müller formulation
MNZ	μ-near-zero

MoM	Method of moments
MVM	Matrix-vector multiplication
NMF	N Müller formulation
NRW	Nicholson-Ross-Weir
NT	NZI T formulation
NZI	Near-zero-index
PC	Polycarbonate
PEC	Perfect electric conductor
PhC	Photonic crystal
PLA	Polylactic acid
PMC	Perfect magnetic conductor
PMCHWT	Poggio-Miller-Chang-Harrington-Wu-Tsai
RB	Refracted beam
RF	Radio frequency
RWG	Rao-Wilton-Glisson
SIE	Surface integral equation
SNG	Single-negative materials
SRR	Split-ring resonator
TPU	Thermoplastic polyurethane
TRL	Thru-reflect-line
VG	Vertical grid

CHAPTER 1

INTRODUCTION

Wireless communication is one of the most important technologies in the information age that we live in. It empowers compact and fast communication devices using free space as a propagation medium instead of using bulky and lossy cables. Electromagnetic waves at multifarious frequencies are used to both transmit and receive information thru air, while antennas are used as transducers between electrical circuits and air to transmit and receive waves. Lots of antennas and resonators are designed to satisfy the requirements of each communication generation stemming from advancing technology. As depicted in Figure 1.1, starting from the implementation of the first analog communication systems in 1980s, various communication generations have been developed [1]. With upcoming technologies, such as autonomous driving, virtual reality, artificial reality, wireless surgery, and internet of things, up to 1 Gbps data rate and 1 ms latency are required. Moreover, the sub-6 GHz spectrum, which is commonly used today, remains incapable of satisfying increased demand for data transfers between wireless devices. Thus, the solution is to shift carrier frequencies to relatively empty higher frequencies, such as millimeter wave (mmWave) and microwave regimes. In these frequency ranges, there are large amounts of bandwidth that data rate and latency requirements can be satisfied for huge numbers of devices; however, electromagnetic losses also increase at higher frequencies. Behind a tree or a wall, propagation becomes challenging due to high absorption rates. Thus, fifth-generation (5G) wireless technologies have been introduced to provide efficient and functional solutions at high frequencies [1–4]. Instead of omnidirectional, high-power base stations, directional and low-power base stations, named small cells, are preferred in 5G. Smaller wavelength (higher frequency) enables compact structures with large numbers of resonators and antennas. For instance, an array antenna at 30

GHz and a patch antenna at 3 GHz, which have the same physical size and transmitting power, can provide the same received power despite higher losses at 30 GHz [3]. In order to increase capacity, massive multiple-input multiple-output (MIMO) antennas have been proposed together with a data traffic control system named beamforming. Particularly, phased array antennas are used to provide high-gain beams [5, 6]. Nevertheless, they are bulky, complicated, and lossy. At these frequency regimes, the lack of low-cost components, e.g., phase shifters at power dividing sections of phased arrays, could be disincentive for mass production.

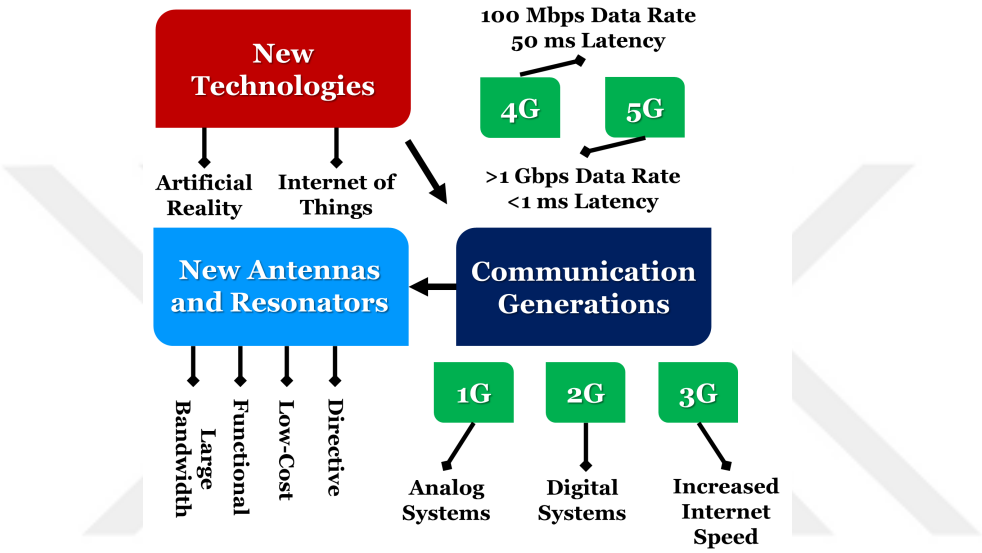

Figure 1.1: Antenna specifications with regard to developing communication generations and technologies.

Horn antennas, reflectors, profiled lenses are some traditional antenna structures at mmWave and microwave regimes, which are well-known in the literature for radar applications. However, they usually occupy large volumes that are not suitable for mobile applications. Considering advantages and disadvantages, antenna types for 5G communication systems are comprehensively studied [7]. When standard antenna design techniques using traditional antennas or phased arrays are insufficient, switched-beam antennas [8, 9] , lenses [10], and leaky wave antennas [11] can be good candidates for highly directive systems. Moreover, in the new generation systems, different kinds of materials (even not found in nature) can be used to enhance antenna qualities. These extraordinary materials can be generated by designing meta-atoms (unit cells), which are examined in the next section.

1.1 Metamaterials and Antennas

Metamaterials are artificial materials that possess unusual electromagnetic properties. Their constitutive parameters can be engineered to provide negative or near-zero relative permittivity (ϵ_r) and/or permeability (μ_r) values, which enable novel antenna and resonator design opportunities that are not available with conventional materials [12, 13]. In the context of metamaterials, initially, Veselago suggested theoretical realization of simultaneously negative permittivity and permeability values [14], in contrast to ordinary materials that typically have positive ϵ_r and μ_r values at mmWave and microwave regimes. On the other side, it was well known for a long time that negative ϵ_r values can be obtained for cold plasmas below their plasma frequencies. For instance, wire arrays can be used as artificial microwave plasmas [15]. However, materials with negative μ_r values were more challenging to obtain, and they were absent in the literature until their realization by arrays of split-ring resonators (SRRs) in 1999 [16]. Accordingly, a combination of wire arrays and SRRs provide simultaneously negative permittivity and permeability values, which was experimentally proved in 2001 [17]. After that, metamaterials have gained quite a lot of interest in the literature [18] owing to diverse design capabilities they provide.

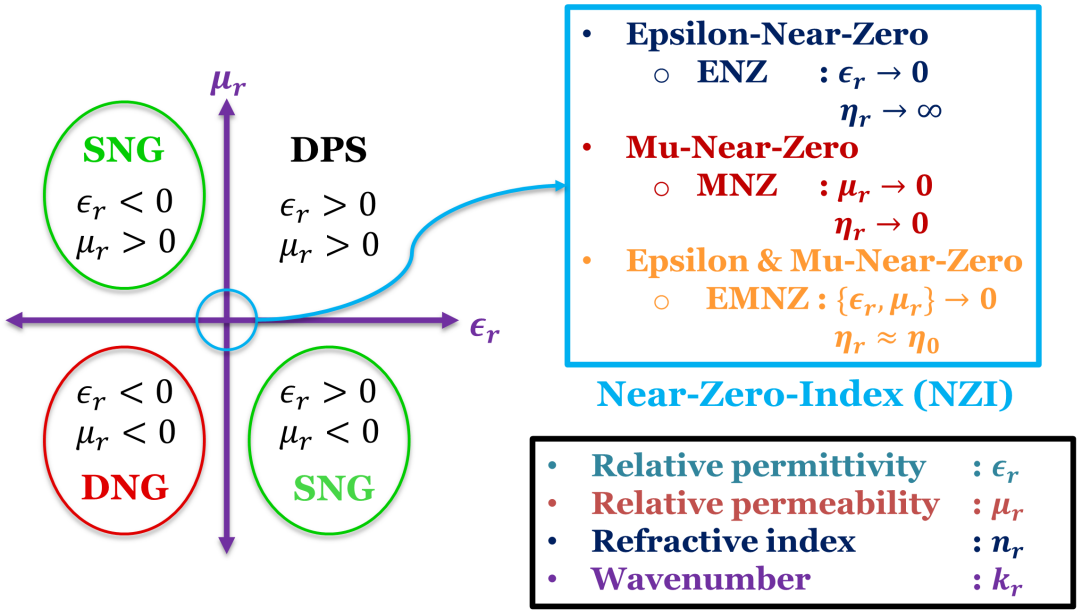

Figure 1.2: Constitutive parameters and metamaterials.

Figure 1.2 illustrates the relationship between different kinds of metamaterials and constitutive parameters. In nature, materials mostly show double positive (DPS) behavior in which both μ_r and ϵ_r are positive. As discussed above, periodic arrays of SRRs and metallic wires are well known negative μ_r and negative ϵ_r structures, respectively. They are considered as single-negative (SNG) materials. Refractive index and wavenumber for a given material can be obtained as

$$n_r = \sqrt{\epsilon_r}\sqrt{\mu_r} \tag{1.1}$$

$$k_r = \omega n_r, \tag{1.2}$$

where ω is the frequency. Since SNG materials have purely imaginary refractive indices, they possess evanescent (decaying) waves within them. On the other hand, a combination of negative μ_r and negative ϵ_r leads to double-negative (DNG) behavior. Interestingly, in a DNG material, propagation of fields is opposite to the flow of power, i.e., the Poynting vector. Substituting negative parameters in (1.1), it can be seen that DNG materials have negative refractive indices.

Near-zero-index (NZI) materials constitute another class of metamaterials exhibiting unusual electromagnetic properties. They can be used in a plethora of applications, such as cloaking [19], tunneling on waveguides [20], wave transformation [21], beam focusing [22], miniaturization in circuits [23], gain enhancement [24], and directive emission [25–29], to name a few. Depending on which parameter is close to zero, NZI materials can be divided into three groups as μ_r-near-zero (MNZ), ϵ_r-near-zero (ENZ), and both ϵ_r and μ_r near-zero (EMNZ). Although refractive indices and wavenumbers go to zero for all cases, electromagnetic responses, such as reflection and transmission, are highly related with which parameters are small. For instance, for ENZ and MNZ objects, the wave impedance goes to infinity and zero, respectively. On the other hand, matched structures can be obtained with EMNZ since the wave impedance can be kept constant and even equal to the vacuum impedance ($\eta_o = \sqrt{\mu_o}/\sqrt{\epsilon_o}$) when both ϵ_r and μ_r are small. In addition, the phase velocity of electromagnetic waves can be expressed as $\upsilon_p = \omega/k_r$; thus, when ϵ_r and/or μ_r have very small values, the phase velocity increases and becomes very large. This is consistent with the fact that the wavelength inside an NZI structure can become very

large, leading to a static-like behavior inside the entire structure. On the other side, as the phase velocity increases and becomes much larger than the speed of light in vacuum, the group velocity ($\upsilon_g = \partial\omega/\partial k_r$), which is related to the speed of power and information transfer, may have moderate values or may decrease to very small values, depending on the NZI characteristics. In general, the group velocity is associated with the frequency dispersion of ϵ_r and μ_r. For instance, for an ENZ object, υ_g can approach to zero, leading to slow-wave structures that can be useful in nonlinear optics [20, 21]. For an EMNZ object, however, the group velocity does not have to be small and it often converges to $\upsilon_g \approx c/2$, where c is the speed of light [20]. Actually, this variety of characteristics facilitates the design of numerous beam-generating NZI structures for different possible applications, as extensively studied in this thesis. Even with similar geometries, different responses can be obtained thanks to the resonating features of ENZ and MNZ materials, as well as matched characteristics of EMNZ materials.

Materials with NZI properties, i.e., EMNZ, ENZ, and MNZ, are realized by diverse methods at optical and microwave frequency regimes in real-life applications. Similar to other metamaterials, NZI structures can be built by arrays of perfect electric conductor (PEC), dielectric or composite layers and rods, which can effectively have refractive index values less than unity [20, 22, 30–32]. Although Dirac-like cone dispersion [22] and effective medium approach [33] provide a low loss way to realize isotropic EMNZ behaviors, anisotropic NZI models can be reached by semi-Dirac cones [34, 35]. Thereby, high-contrast dielectric rod arrays can be used to obtain small refractive index values.

Homogeneous models of actual NZI structures, for which we enforce near-zero ϵ_r and/or μ_r values, can be useful to understand essential information about their electromagnetic responses. However, even when relatively simple structures are considered for homogeneous models, conventional numerical and computational methods suffer from low-frequency and high-contrast breakdowns due to extreme values of ϵ_r and μ_r. On the other side, simulations of actual structures, when they are modeled as finite and three-dimensional (3D) objects, can also be challenging due to subwavelength details, leading to ill-conditioned and large matrix systems. In this study, we developed and used full-wave solvers based on surface integral equations (SIEs)

in frequency domain. Matrix equations are obtained via novel formulations of both homogeneous and realistic models, while they are iteratively solved based on different forms of the multilevel fast multipole algorithm (MLFMA). Iterative solutions are further accelerated by a multi-layer preconditioner for fast solutions of large electromagnetic problems, where necessary.

There are several approaches to combine metamaterials and antennas [36, 37]. For example, to decrease coupling effects of antenna arrays [38] or to enhance new generation antennas, NZI metamaterials can be used above, near, or under them. Even though NZI structures are known to enable diverse design capabilities to enhance new generation antennas, it is not apparent how to effectively design and combine them with radiating components. Accordingly, in this study, we provide novel NZI shell structures, including effective NZI cavities, in order to obtain customized radiation patterns from simple radiating structures. According to Snell's law, while electromagnetic waves leave from an NZI medium, they refract at the boundary, and their propagation direction becomes almost perpendicular to the medium's surface. Hence, an NZI object can reshape radiation patterns depending on its outer surface. However, penetration of electromagnetic waves into an NZI medium can be challenging due to strong reflections stemming from a small refractive index. Even for an EMNZ object, which is matched to vacuum or air in terms of impedance, almost complete reflections occur under oblique incidence. Considering this challenge, we show that, although NZI structures demonstrate highly reflective responses, efficient radiations with directive beams can be achieved by carefully designing cavities around the radiating sources. Different cavity geometries and outer surface profiles of NZI shells are proposed to either suppress or enhance outgoing electromagnetic fields, while resonating features of NZI cavities are employed to generate strong beams [39, 40].

Realized NZI structures involving high-contrast dielectric rod arrays show small refractive index values when the radius of the rods and the center-to-center distances are selected properly [41]. Although the length of the rods seems to be less restricted in comparison to other parameters, its effect on electromagnetic properties of the constructed structure is less known in the literature. Accordingly, we show the importance of rod heights on beam generation responses of NZI shells. We further provide an effective refractive index test setup in order to optimize parameters of realistic

NZI structures when rod materials and operating frequencies are altered [42]. In this context, the developed simulation environment enables us to investigate the effects of inevitable nonidealities; thus, we can rigorously examine the effects of fabrication errors in the simulations.

There are various materials with high relative permittivity values and low loss tangents, such as alumina, silicon, and gallium arsenide. Unfortunately, their usage in fabricating unit cells (such as rods) can be challenging, while their cost can be high, especially when high precision is needed. Considering accessibility and design freedom, we choose additive manufacturing to fabricate high-contrast dielectric rods. Recently, 3D printing have attracted interest of many researches [43–47] owing to rapid fabrication of prototypes. However, commercially available 3D printing materials are not designed for radio frequency (RF) applications. Specifically, their ϵ_r values are low, while their electromagnetic losses are relatively high. Furthermore, their electromagnetic characteristics are sensitive to fabrication processes, e.g., settings of 3D printers. Hence, we use an electromagnetic characterization setup to examine possible materials to fabricate rods of realistic NZI structures. After the material is determined, we fabricate and test the designed NZI beam generators to demonstrate their unique electromagnetic responses that can be used in a plethora of applications.

1.2 Contents of the Thesis

Based on the conducted studies that are briefly discussed above, this thesis consists of four main chapters and two appendices. In Chapter 2, the simulation tools for the actual and homogenized NZI structures are detailed. We show that challenging electromagnetic problems throughout the design steps of NZI beam generators can be handled accurately and efficiently by proper formulations and solution algorithms based on different forms of MLFMA. In addition, modeling and realization of NZI structures are examined via diverse methods from the literature. Next, Chapter 3 is devoted to the step-by-step design process of novel NZI beam generators. NZI shells with superior beam generating characteristics are designed considering their cavity regions and outer surfaces, while the NZI phenomenon is examined in terms of reflection and refraction. Chapter 4 introduces a new method to fabricate NZI structures via additive manufacturing, as well as their measurements. Chapter 5 summarizes the

whole study and emphasizes wider implications as future work. Basic derivations of incident fields for electromagnetic simulations are provided in Appendix A. Finally, examination of some surface formulations for extremely small values of constitutive parameters is presented in Appendix B.

CHAPTER 2

SIMULATIONS OF NEAR-ZERO-INDEX METAMATERIALS

Efficient and accurate simulations of homogeneous NZI models can be challenging due to unconventional constitutive parameters. At the extreme values of relative permittivity and permeability, matrix systems that are constructed to solve electromagnetic problems become highly ill-conditioned (unstable); thus, it becomes almost impossible to reach stable solutions with conventional field solvers in the context of surface formulations for NZI models. Furthermore, additional numerical issues can arise depending on the formulation. For example, some operators can dominate matrix systems, roundoff errors may increase, and operators can be imbalanced.

On the other hand, analyses of realistic NZI structures consisting of periodic arrays of conductors and/or dielectrics are not straightforward since they generally have small (but critical) details with respect to wavelength. Computational representations of these problems involve dense discretizations, leading to ill-conditioned and large matrix systems. We also need to use 3D models without any infinity assumptions in simulations due to practical issues. Therefore, electromagnetic analyses of NZI structures need rigorous and accurate approaches, beyond traditional tools and algorithms.

2.1 Simulation Environment

This chapter provides a sophisticated electromagnetic simulation environment based on in-house implementations of SIEs to eliminate challenges on accurate and efficient designs of novel NZI shells. Similar to other types of metamaterials, NZI structures are typically realized by periodic arrays of dielectrics and/or conductors. However, their homogenized models are also needed and investigated to analyze critical effects of geometrical variations and material characteristics on the operation of the designed

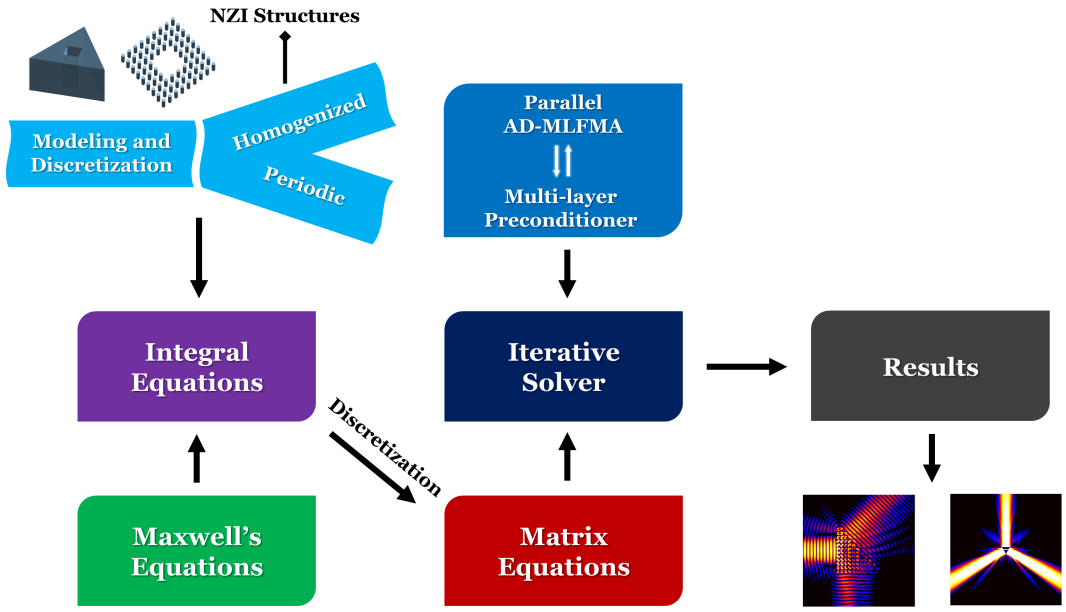

Figure 2.1: Simulation setup for NZI structures.

structures. In this study, we investigate both types of models, i.e., realistic and homogeneous NZI structures. Accordingly, Figure 2.1 presents a general view of the simulation environment based on (1) SIEs, derived from Maxwell's equations, as formulations, (2) AD-MLFMA and multi-layer preconditioner to form the main solution algorithm. We use 3D finite objects discretized with triangles. Various electromagnetic sources can be used to illuminate objects under tests, such as a Hertzian dipole or a complex-source-point (CSP), depending on the application. We use boundary conditions and surface equivalence theorem (Love's theorem [48]) to represent complicated electromagnetic problems involving dielectric and metallic objects in terms of sub-problems that can be solved simultaneously. Rao-Wilton-Glisson (RWG) expansion and weighting functions are employed to construct matrix systems [49]. Once we obtain the discretized forms of equivalent surface currents, near-zone and/or far-zone fields can be obtained by radiation integrals.

Since we use method of moments (MoM) to construct matrix equations, dense matrix equations involving large number of unknowns arise, which can be difficult, if not impossible, to solve directly. Therefore, iterative solution techniques are employed. In these solutions, the required matrix-vector multiplications (MVMs) are performed efficiently via different forms of MLFMA [50]. Convergences of iterative solutions

are further accelerated by a three-layer inner-outer scheme [51]. In the following parts, we examine our simulation environment in more detail.

2.1.1 Surface Integral Equations

Maxwell's equations in time domain can be written as

$$\nabla \times \boldsymbol{E}(\boldsymbol{r},t) = -\frac{\partial \boldsymbol{B}(\boldsymbol{r},t)}{\partial t} - \boldsymbol{M}(\boldsymbol{r},t) \qquad \text{(Faraday's Law)} \tag{2.1}$$

$$\nabla \times \boldsymbol{H}(\boldsymbol{r},t) = \frac{\partial \boldsymbol{D}(\boldsymbol{r},t)}{\partial t} + \boldsymbol{J}(\boldsymbol{r},t) \qquad \text{(Ampere's Law)} \tag{2.2}$$

$$\nabla \cdot \boldsymbol{D}(\boldsymbol{r},t) = \rho_e(\boldsymbol{r},t) \qquad \text{(Gauss's Law)} \tag{2.3}$$

$$\nabla \cdot \boldsymbol{B}(\boldsymbol{r},t) = \rho_m(\boldsymbol{r},t) \qquad \text{(Gauss's Law of Magnetism),} \tag{2.4}$$

where $\boldsymbol{E}$ is the electric field intensity, $\boldsymbol{H}$ is the magnetic field intensity, $\boldsymbol{J}$ and $\boldsymbol{M}$ are the electric and magnetic current densities, ρ_e and ρ_m are the electric and magnetic charge densities. In these equations, $\boldsymbol{r}$ and t represent spatial and temporal dependencies. Although magnetic currents and charges are not physically realizable, (2.1)–(2.4) include equivalent magnetic sources which may originate from the surface equivalence theorem. For a simple medium, field intensities are related to flux densities $\boldsymbol{D}$ and $\boldsymbol{B}$ via constitutive relations as

$$\boldsymbol{D}(\boldsymbol{r},t) = \epsilon \boldsymbol{E}(\boldsymbol{r},t) \tag{2.5}$$

$$\boldsymbol{B}(\boldsymbol{r},t) = \mu \boldsymbol{H}(\boldsymbol{r},t), \tag{2.6}$$

where ϵ and μ represent permittivity and permeability of the homogeneous medium, respectively. In frequency domain with $e^{-i\omega t}$ time convention, Maxwell's equations become

$$\nabla \times \boldsymbol{E}(\boldsymbol{r}) = i\omega\mu \boldsymbol{H}(\boldsymbol{r}) - \boldsymbol{M}(\boldsymbol{r}) \tag{2.7}$$

$$\nabla \times \boldsymbol{H}(\boldsymbol{r}) = -i\omega\epsilon \boldsymbol{E}(\boldsymbol{r}) + \boldsymbol{J}(\boldsymbol{r}) \tag{2.8}$$

$$\nabla \cdot \boldsymbol{E}(\boldsymbol{r}) = \frac{1}{\epsilon}\rho_e(\boldsymbol{r}) \tag{2.9}$$

$$\nabla \cdot \boldsymbol{H}(\boldsymbol{r}) = \frac{1}{\mu}\rho_m(\boldsymbol{r}). \tag{2.10}$$

Currents and charges on the right-hand sides are related according to the continuity equations. They can be derived by evaluating the divergences of (2.7) and (2.8), leading to

$$\nabla \cdot \boldsymbol{J}(\boldsymbol{r}) = i\omega\rho_e(\boldsymbol{r}) \tag{2.11}$$

$$\nabla \cdot \boldsymbol{M}(\boldsymbol{r}) = i\omega\rho_m(\boldsymbol{r}). \tag{2.12}$$

Table 2.1: Duality theorem.

1	$\boldsymbol{E}$	$\boldsymbol{H}$	$\boldsymbol{J}$	$\boldsymbol{M}$	ρ_e	ρ_m	ϵ	μ	η
2	$\boldsymbol{H}$	$-\boldsymbol{E}$	$\boldsymbol{M}$	$-\boldsymbol{J}$	ρ_m	$-\rho_e$	μ	ϵ	$1/\eta$

On the other hand, one can obtain Helmholtz equation for the electric field intensity by taking curl of (2.7), using (2.8), (2.9), and the identity $\nabla \times \nabla \times \boldsymbol{u} = \nabla\nabla \cdot \boldsymbol{u} - \nabla^2\boldsymbol{u}$, which gives

$$\nabla^2\boldsymbol{E}(\boldsymbol{r}) + k^2\boldsymbol{E}(\boldsymbol{r}) = -i\omega\mu\boldsymbol{J}(\boldsymbol{r}) + \frac{1}{\epsilon}\nabla\rho_e(\boldsymbol{r}) + \nabla \times \boldsymbol{M}(\boldsymbol{r}). \tag{2.13}$$

In the above, $k = \omega\sqrt{\epsilon\mu} = 2\pi/\lambda$ is the wavenumber and λ is the wavelength. Helmholtz equation for the magnetic field intensity can be obtained by using the duality theorem given in Table 2.1. The variables in the first row can be exchanged by those in the second row. This way, we obtain

$$\nabla^2\boldsymbol{H}(\boldsymbol{r}) + k^2\boldsymbol{H}(\boldsymbol{r}) = -i\omega\epsilon\boldsymbol{M}(\boldsymbol{r}) + \frac{1}{\mu}\nabla\rho_m(\boldsymbol{r}) - \nabla \times \boldsymbol{J}(\boldsymbol{r}). \tag{2.14}$$

In order to facilitate the solutions of electromagnetic problems, auxiliary vector and scalar potentials can be used to express field intensities as

$$\boldsymbol{E}(\boldsymbol{r}) = i\omega \boldsymbol{A}_m(\boldsymbol{r}) - \nabla \phi_e(\boldsymbol{r}) - \frac{1}{\epsilon} \nabla \times \boldsymbol{A}_e(\boldsymbol{r}) \tag{2.15}$$

$$\boldsymbol{H}(\boldsymbol{r}) = i\omega \boldsymbol{A}_e(\boldsymbol{r}) - \nabla \phi_m(\boldsymbol{r}) + \frac{1}{\mu} \nabla \times \boldsymbol{A}_m(\boldsymbol{r}), \tag{2.16}$$

where A_m, ϕ_m, $\boldsymbol{A}_e$, and ϕ_e are magnetic vector, magnetic scalar, electric vector, and electric scalar potentials, respectively. These potentials are related via Lorenz gauge as

$$\nabla \cdot \boldsymbol{A}_m(\boldsymbol{r}) = i\omega\epsilon\mu\phi_e(\boldsymbol{r}) \tag{2.17}$$

$$\nabla \cdot \boldsymbol{A}_e(\boldsymbol{r}) = i\omega\epsilon\mu\phi_m(\boldsymbol{r}). \tag{2.18}$$

Consequently, we derive Helmholtz equations for potentials, i.e.,

$$\nabla^2 \phi_e(\boldsymbol{r}) + k^2 \phi_e(\boldsymbol{r}) = -\frac{1}{\epsilon} \rho_e(\boldsymbol{r}) \tag{2.19}$$

$$\nabla^2 \phi_m(\boldsymbol{r}) + k^2 \phi_m(\boldsymbol{r}) = -\frac{1}{\mu} \rho_m(\boldsymbol{r}) \tag{2.20}$$

$$\nabla^2 \boldsymbol{A}_e(\boldsymbol{r}) + k^2 \boldsymbol{A}_e(\boldsymbol{r}) = -\epsilon \boldsymbol{M}(\boldsymbol{r}) \tag{2.21}$$

$$\nabla^2 \boldsymbol{A}_m(\boldsymbol{r}) + k^2 \boldsymbol{A}_m(\boldsymbol{r}) = -\mu \boldsymbol{J}(\boldsymbol{r}). \tag{2.22}$$

Fundamental solutions of (2.19)–(2.22) can be expressed by homogeneous-space Green's function as

$$g(\boldsymbol{r}, \boldsymbol{r}') = \frac{\exp(ik|\boldsymbol{r} - \boldsymbol{r}'|)}{4\pi|\boldsymbol{r} - \boldsymbol{r}'|}, \tag{2.23}$$

where $\boldsymbol{r}$ and $\boldsymbol{r}'$ represent observation and source points, respectively. For arbitrary source distributions, solutions of (2.19)–(2.22) can be obtained by using (2.23) as a kernel, i.e.,

$$\phi_e(\boldsymbol{r}) = \frac{1}{\epsilon} \int d\boldsymbol{r}' g(\boldsymbol{r}, \boldsymbol{r}') \rho_e(\boldsymbol{r}') \tag{2.24}$$

$$\phi_m(\boldsymbol{r}) = \frac{1}{\mu} \int d\boldsymbol{r}' g(\boldsymbol{r}, \boldsymbol{r}') \rho_m(\boldsymbol{r}') \tag{2.25}$$

$$\boldsymbol{A}_e(\boldsymbol{r}) = \epsilon \int d\boldsymbol{r}' g(\boldsymbol{r}, \boldsymbol{r}') \boldsymbol{M}(\boldsymbol{r}') \tag{2.26}$$

$$\boldsymbol{A}_m(\boldsymbol{r}) = \mu \int d\boldsymbol{r}' g(\boldsymbol{r}, \boldsymbol{r}') \boldsymbol{J}(\boldsymbol{r}'). \tag{2.27}$$

Substituting (2.24)–(2.27) into (2.15) and (2.16), field intensities due to arbitrary source distributions can be obtained as

$$\begin{aligned} \boldsymbol{E}(\boldsymbol{r}) = ik\eta \int d\boldsymbol{r}' \left[\boldsymbol{J}(\boldsymbol{r}') + \frac{1}{k^2} \nabla' \cdot \boldsymbol{J}(\boldsymbol{r}') \nabla \right] g(\boldsymbol{r}, \boldsymbol{r}') \\ - \int d\boldsymbol{r}' \nabla g(\boldsymbol{r}, \boldsymbol{r}') \times \boldsymbol{M}(\boldsymbol{r}') \end{aligned} \tag{2.28}$$

$$\begin{aligned} \boldsymbol{H}(\boldsymbol{r}) = ik\eta^{-1} \int d\boldsymbol{r}' \left[\boldsymbol{M}(\boldsymbol{r}') + \frac{1}{k^2} \nabla' \cdot \boldsymbol{M}(\boldsymbol{r}') \nabla \right] g(\boldsymbol{r}, \boldsymbol{r}') \\ + \int d\boldsymbol{r}' \nabla g(\boldsymbol{r}, \boldsymbol{r}') \times \boldsymbol{J}(\boldsymbol{r}'), \end{aligned} \tag{2.29}$$

where $\eta = \sqrt{\mu/\epsilon}$ is the intrinsic impedance of the medium under interest. To simplify expressions, integro-differential operators $\boldsymbol{\mathcal{T}}$ and $\boldsymbol{\mathcal{K}}$ can be defined as

$$\boldsymbol{\mathcal{T}}\{\boldsymbol{X}\}(\boldsymbol{r}) = ik \int d\boldsymbol{r}' \left[\boldsymbol{X}(\boldsymbol{r}') + \frac{1}{k^2} \nabla' \cdot \boldsymbol{X}(\boldsymbol{r}') \nabla \right] g(\boldsymbol{r}, \boldsymbol{r}') \tag{2.30}$$

$$\boldsymbol{\mathcal{K}}\{\boldsymbol{X}\}(\boldsymbol{r}) = \int d\boldsymbol{r}' \boldsymbol{X}(\boldsymbol{r}') \times \nabla' g(\boldsymbol{r}, \boldsymbol{r}'). \tag{2.31}$$

This way, electromagnetic fields in terms of electric and magnetic currents can be written as

$$\boldsymbol{E}(\boldsymbol{r}) = \eta \boldsymbol{\mathcal{T}}\{\boldsymbol{J}\}(\boldsymbol{r}) - \boldsymbol{\mathcal{K}}\{\boldsymbol{M}\}(\boldsymbol{r}) \tag{2.32}$$

$$\boldsymbol{H}(\boldsymbol{r}) = \eta^{-1} \boldsymbol{\mathcal{T}}\{\boldsymbol{M}\}(\boldsymbol{r}) + \boldsymbol{\mathcal{K}}\{\boldsymbol{J}\}(\boldsymbol{r}). \tag{2.33}$$

At this step, to solve electromagnetic problems involving penetrable objects with magnetic and/or dielectric characteristics and conducting objects, the surface equivalence theorem is used to generate sub-problems by ensuring boundary conditions on the equivalent surfaces. These surfaces can be chosen same as actual interfaces of

objects and/or media. Figure 2.2 depicts three different boundaries with surface normal vectors. We note that non-penetrable objects are categorized into two: PECs and perfect magnetic conductors (PMCs). They satisfy different boundary conditions:

- The tangential component of the electric field intensity, i.e. $\boldsymbol{M}$, vanishes on a PEC surface.
- The tangential component of the magnetic field intensity, i.e. $\boldsymbol{J}$, vanishes on a PMC surface.

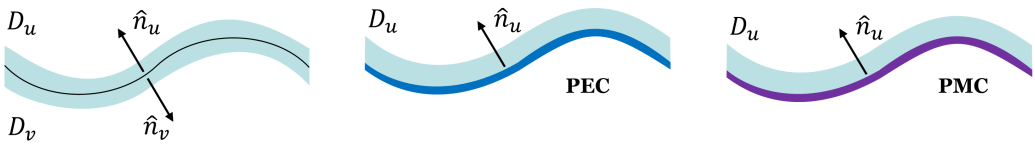

Figure 2.2: Boundaries between two different regions that can be penetrable, PEC, or PMC.

Consider a homogeneous region D_u with constitutive parameters ϵ_u and μ_u, bounded by a surface S_u, as given in Figure 2.2. By sampling the tangential fields on the surface S_u, i.e., $\boldsymbol{r} \in S_u$, and satisfying continuity of them by equivalent surface currents, basic integral equations can be derived. Accordingly, the boundary condition for the electric field intensity can be written as

$$-\boldsymbol{M}(\boldsymbol{r}) = \hat{\boldsymbol{n}}_u \times \boldsymbol{E}_u(\boldsymbol{r}) = \hat{\boldsymbol{n}}_u \times \boldsymbol{E}_u^{\text{inc}}(\boldsymbol{r}) + \hat{\boldsymbol{n}}_u \times \boldsymbol{E}_u^{\text{sec}}(\boldsymbol{r}), \tag{2.34}$$

where $\hat{\boldsymbol{n}}_u$ is the normal unit vector, while $\boldsymbol{E}_u$, $\boldsymbol{E}_u^{\text{inc}}$, and $\boldsymbol{E}_u^{\text{sec}}$ are total, incident, and secondary (scattered) electric field intensities, respectively. Then, basic integral equations can be obtained by applying integro-differential operators. In these applications, operator $\mathcal{K}$ is commonly used as a combination of its principal-value and limit parts. In this way, we convert equations with singularities into those with weak singularities that are integrable [52]. In domain D_u, we have

$$\boldsymbol{\mathcal{T}}_u\{\boldsymbol{X}\}(\boldsymbol{r}) = ik\int_{S_u} d\boldsymbol{r}'\left[\boldsymbol{X}(\boldsymbol{r}') + \frac{1}{k^2}\nabla'\cdot\boldsymbol{X}(\boldsymbol{r}')\nabla\right] g_u(\boldsymbol{r},\boldsymbol{r}') \tag{2.35}$$

$$\boldsymbol{\mathcal{K}}_u\{\boldsymbol{X}\}(\boldsymbol{r}) = \boldsymbol{\mathcal{K}}_u^{\text{PV}}\{\boldsymbol{X}\}(\boldsymbol{r}) - \frac{4\pi-\Omega_u}{4\pi}\hat{\boldsymbol{n}}_u\times\boldsymbol{\mathcal{I}}\{\boldsymbol{X}\}(\boldsymbol{r}) \tag{2.36}$$

$$\boldsymbol{\mathcal{K}}_u^{\text{PV}}\{\boldsymbol{X}\}(\boldsymbol{r}) = \int_{PV,S_u} d\boldsymbol{r}'\boldsymbol{X}(\boldsymbol{r}')\times\nabla' g_u(\boldsymbol{r},\boldsymbol{r}'), \tag{2.37}$$

where $\boldsymbol{\mathcal{I}}$ represents the identity operator and PV indicates the principal value of the integral. In the above, $0 \leqslant \Omega_u \leqslant 4\pi$ is the solid angle that is nonzero when the observation point is on a surface. For the electric field intensity, substituting operators into (2.34) by using (2.32), we have

$$\begin{aligned}-\boldsymbol{M}_u(\boldsymbol{r}) &= \hat{\boldsymbol{n}}_u\times\boldsymbol{E}_u^{\text{inc}}(\boldsymbol{r}) + \eta_u\hat{\boldsymbol{n}}_u\times\boldsymbol{\mathcal{T}}_u\{\boldsymbol{J}_u\}(\boldsymbol{r}) - \hat{\boldsymbol{n}}_u\times\boldsymbol{\mathcal{K}}_u\{\boldsymbol{M}_u\}(\boldsymbol{r})\\ &= \hat{\boldsymbol{n}}_u\times\boldsymbol{E}_u^{\text{inc}}(\boldsymbol{r}) + \eta_u\hat{\boldsymbol{n}}_u\times\boldsymbol{\mathcal{T}}_u\{\boldsymbol{J}_u\}(\boldsymbol{r}) - \hat{\boldsymbol{n}}_u\times\boldsymbol{\mathcal{K}}_u^{\text{PV}}\{\boldsymbol{M}_u\}(\boldsymbol{r})\\ &\quad - \boldsymbol{\mathcal{I}}\{\boldsymbol{M}_u\}(\boldsymbol{r})\frac{4\pi-\Omega_u}{4\pi}.\end{aligned} \tag{2.38}$$

After simplifying the terms in (2.38), we obtain the normal electric-field integral equation (N-EFIE), while further multiplying N-EFIE with $-\hat{\boldsymbol{n}}_u$ leads to the tangential electric-field integral equation (T-EFIE). N-EFIE and T-EFIE can be written as

$$\begin{aligned}-\hat{\boldsymbol{n}}_u\times\boldsymbol{E}_u^{\text{inc}}(\boldsymbol{r}) &= \eta_u\hat{\boldsymbol{n}}_u\times\boldsymbol{\mathcal{T}}_u\{\boldsymbol{J}_u\}(\boldsymbol{r})\\ &\quad - \hat{\boldsymbol{n}}_u\times\boldsymbol{\mathcal{K}}_u^{\text{PV}}\{\boldsymbol{M}_u\}(\boldsymbol{r}) + \frac{\Omega_u}{4\pi}\boldsymbol{\mathcal{I}}\{\boldsymbol{M}_u\}(\boldsymbol{r})\end{aligned} \tag{2.39}$$

$$\begin{aligned}\hat{\boldsymbol{n}}_u\times\hat{\boldsymbol{n}}_u\times\boldsymbol{E}_u^{\text{inc}}(\boldsymbol{r}) &= -\eta_u\hat{\boldsymbol{n}}_u\times\hat{\boldsymbol{n}}_u\times\boldsymbol{\mathcal{T}}_u\{\boldsymbol{J}_u\}(\boldsymbol{r})\\ &\quad + \hat{\boldsymbol{n}}_u\times\hat{\boldsymbol{n}}_u\times\boldsymbol{\mathcal{K}}_u^{\text{PV}}\{\boldsymbol{M}_u\}(\boldsymbol{r}) - \frac{\Omega_u}{4\pi}\hat{\boldsymbol{n}}_u\times\boldsymbol{\mathcal{I}}\{\boldsymbol{M}_u\}(\boldsymbol{r}).\end{aligned} \tag{2.40}$$

Considering the duality theorem given in Table 2.1, the normal magnetic-field integral equation (N-MFIE), the tangential magnetic-field integral equation (T-MFIE), and boundary conditions involved in MFIE can be found by rearranging (2.39), (2.40), and (2.34), respectively. Specifically, the boundary condition for MFIE can be written as

$$\boldsymbol{J}(\boldsymbol{r}) = \hat{\boldsymbol{n}}_u \times \boldsymbol{H}_u(\boldsymbol{r}) = \hat{\boldsymbol{n}}_u \times \boldsymbol{H}_u^{\text{inc}}(\boldsymbol{r}) + \hat{\boldsymbol{n}}_u \times \boldsymbol{H}_u^{\text{sec}}(\boldsymbol{r}). \tag{2.41}$$

Then, N-MFIE (2.42) and T-MFIE (2.43) can be written as

$$\begin{aligned} -\hat{\boldsymbol{n}}_u \times \boldsymbol{H}_u^{\text{inc}}(\boldsymbol{r}) &= \eta_u^{-1} \hat{\boldsymbol{n}}_u \times \boldsymbol{\mathcal{T}}_u\{\boldsymbol{M}_u\}(\boldsymbol{r}) \\ &\quad + \hat{\boldsymbol{n}}_u \times \boldsymbol{\mathcal{K}}_u^{\text{PV}}\{\boldsymbol{J}_u\}(\boldsymbol{r}) - \frac{\Omega_u}{4\pi}\boldsymbol{\mathcal{I}}\{\boldsymbol{J}_u\}(\boldsymbol{r}) \end{aligned} \tag{2.42}$$

$$\begin{aligned} \hat{\boldsymbol{n}}_u \times \hat{\boldsymbol{n}}_u \times \boldsymbol{H}_u^{\text{inc}}(\boldsymbol{r}) &= -\eta_u^{-1} \hat{\boldsymbol{n}}_u \times \hat{\boldsymbol{n}}_u \times \boldsymbol{\mathcal{T}}_u\{\boldsymbol{M}_u\}(\boldsymbol{r}) \\ &\quad - \hat{\boldsymbol{n}}_u \times \hat{\boldsymbol{n}}_u \times \boldsymbol{\mathcal{K}}_u^{\text{PV}}\{\boldsymbol{J}_u\}(\boldsymbol{r}) + \frac{\Omega_u}{4\pi}\hat{\boldsymbol{n}}_u \times \boldsymbol{\mathcal{I}}\{\boldsymbol{J}_u\}(\boldsymbol{r}). \end{aligned} \tag{2.43}$$

Thanks to diverse combinations of T-EFIE, N-EFIE, T-MFIE, and N-MFIE, various surface formulations can be obtained.

2.1.2 Discretization and the Method of Moments

As far as electromagnetic simulations are concerned, we need to convert continuous equations into discretized matrix equations that can be solved numerically. Integral equations in the previous section can be solved by means of the well-known MoM approach [53]. Firstly, we define

$$\boldsymbol{\mathcal{L}}\{\boldsymbol{f}\}(\boldsymbol{r}) = \boldsymbol{w}(\boldsymbol{r}), \tag{2.44}$$

where $\boldsymbol{\mathcal{L}}$ is a linear operator such as integro-differential operators $\boldsymbol{\mathcal{T}}$, $\boldsymbol{\mathcal{K}}$, and $\boldsymbol{\mathcal{I}}$, $\boldsymbol{w}(\boldsymbol{r})$ is the known source referring to incident fields, and $\boldsymbol{f}(\boldsymbol{r})$ is the unknown function to be determined. In the context of this work, the unknown function corresponds to equivalent surface currents. It can be expressed in terms of a set of known basis functions as

$$\boldsymbol{f}(\boldsymbol{r}) \approx \sum_{n=1}^{N} \boldsymbol{a}[n]\boldsymbol{b}_n(\boldsymbol{r}), \tag{2.45}$$

where $\boldsymbol{a}[n]$ is the expansion coefficient vector of the n^{th} basis function. Then, we define a residual (or an error) function to be minimized as

$$\boldsymbol{R}(\boldsymbol{r}) = \boldsymbol{\mathcal{L}}\{\boldsymbol{f}\}(\boldsymbol{r}) - \boldsymbol{w}(\boldsymbol{r}) \approx \sum_{n=1}^{N} \boldsymbol{a}[n]\boldsymbol{\mathcal{L}}\{\boldsymbol{b}_n\}(\boldsymbol{r}) - \boldsymbol{w}(\boldsymbol{r}). \tag{2.46}$$

The locations of the operator and summation can be changed thanks to linearity. To minimize the residual in an average sense, we define an inner product as

$$\langle \boldsymbol{a}(\boldsymbol{r}), \boldsymbol{b}(\boldsymbol{r}) \rangle = \int d\boldsymbol{r}\boldsymbol{a}(\boldsymbol{r}) \cdot \boldsymbol{b}(\boldsymbol{r}). \tag{2.47}$$

In order to have sufficient numbers of equations to solve unknowns, the inner product of the residual can be evaluated with a set of weighting (testing) functions $\boldsymbol{t}_m$ for $m = 1, ..., N$ and the result can be equated to zero ($\langle \boldsymbol{R}(\boldsymbol{r}), \boldsymbol{t}_m(\boldsymbol{r}) \rangle = 0$). Then we obtain N equations and N unknowns as

$$\int d\boldsymbol{r}\boldsymbol{t}_m(\boldsymbol{r}) \cdot \sum_{n=1}^{N} \boldsymbol{a}[n]\boldsymbol{\mathcal{L}}\{\boldsymbol{b}_n\}(\boldsymbol{r}) = \int d\boldsymbol{r}\boldsymbol{t}_m(\boldsymbol{r}) \cdot \boldsymbol{w}(\boldsymbol{r}). \tag{2.48}$$

To form a linear system, interchanging summation and integral leads to

$$\sum_{n=1}^{N} \boldsymbol{a}[n] \underbrace{\int d\boldsymbol{r}\boldsymbol{t}_m(\boldsymbol{r}) \cdot \boldsymbol{\mathcal{L}}\{\boldsymbol{b}_n\}(\boldsymbol{r})}_{\bar{\boldsymbol{Z}}[m,n]} = \underbrace{\int d\boldsymbol{r}\boldsymbol{t}_m(\boldsymbol{r}) \cdot \boldsymbol{w}(\boldsymbol{r})}_{\boldsymbol{v}[m]}, \tag{2.49}$$

where $\boldsymbol{v}[m]$ is the excitation vector and $\bar{\boldsymbol{Z}}[m,n]$ is the impedance matrix including electromagnetic interactions between discretization elements. A widely-used discretization method of 3D objects is to use small planar triangles on which RWG functions are defined [49]. Their dimensions should be sufficiently small in terms of wavelength to avoid possible discretization errors. On the other hand, smaller discretization elements mean larger matrix equations which can cause memory and time bottlenecks in their solutions.

Figure 2.3 illustrates two different discretized models using triangles. On these models, the RWG functions are defined on pairs of triangles. The spatial distribution of an RWG function located on the model in Figure 2.3b is depicted in Figure 2.4. An RWG function can be written as

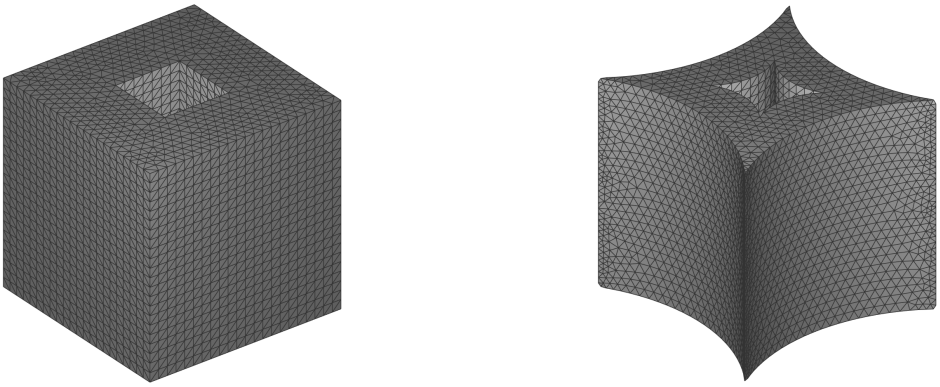

(a) A shell model. (b) A shell model with modified surfaces.

Figure 2.3: Surface models with planar triangulation.

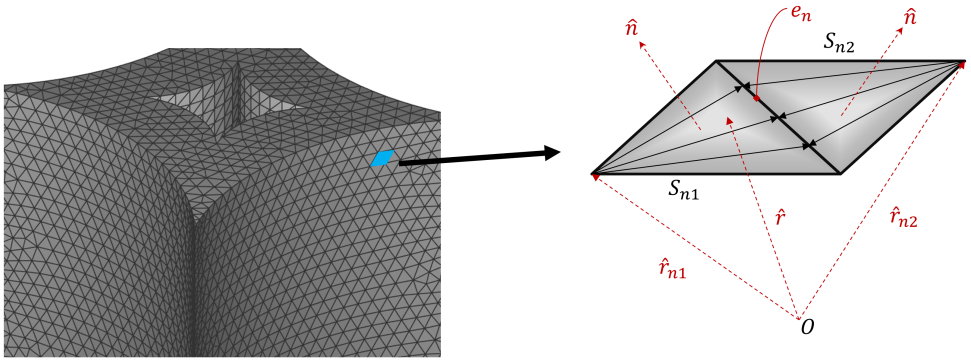

Figure 2.4: An RWG function and its spatial distributions.

$$\boldsymbol{b}_n(\boldsymbol{r}) = \begin{cases} \dfrac{l_n}{2A_{n1}}(\boldsymbol{r} - \boldsymbol{r}_{n1}), & \boldsymbol{r} \in S_{n1} \\ \dfrac{l_n}{2A_{n2}}(\boldsymbol{r}_{n2} - \boldsymbol{r}), & \boldsymbol{r} \in S_{n2} \\ 0, & \boldsymbol{r} \notin S_n, \end{cases} \tag{2.50}$$

where l_n represents the length of the intersection edge (e_n), while A_{n1} and A_{n2} are the areas of the first (S_{n1}) and the second (S_{n2}) triangles, respectively. One of the most substantial features of the RWG functions is that they are divergence conforming.

Specifically, their divergence is finite everywhere, i.e.,

$$\nabla \cdot \boldsymbol{b}_n(\boldsymbol{r}) = \begin{cases} \dfrac{l_n}{A_{n1}}, & \boldsymbol{r} \in S_{n1} \\ -\dfrac{l_n}{A_{n2}}, & \boldsymbol{r} \in S_{n2} \\ 0, & \boldsymbol{r} \notin S_n. \end{cases} \tag{2.51}$$

Using a Galerkin scheme, i.e., when both basis and test functions are chosen as the same set of the RWG functions, discretized operators can be written as

$$\begin{aligned} \bar{\boldsymbol{T}}_u^T[m,n] &= ik_u \int_{S_m} d\boldsymbol{r} \boldsymbol{t}_m(\boldsymbol{r}) \cdot \int_{S_n} d\boldsymbol{r}' g_u(\boldsymbol{r},\boldsymbol{r}') \boldsymbol{b}_n(\boldsymbol{r}') \\ &\quad + \frac{i}{k_u} \int_{S_m} d\boldsymbol{r} \boldsymbol{t}_m(\boldsymbol{r}) \cdot \int_{S_n} d\boldsymbol{r}' \nabla g_u(\boldsymbol{r},\boldsymbol{r}') \nabla' \cdot \boldsymbol{b}_n(\boldsymbol{r}') \qquad (2.52) \\ \bar{\boldsymbol{T}}_u^N[m,n] &= ik_u \int_{S_m} d\boldsymbol{r} \boldsymbol{t}_m(\boldsymbol{r}) \cdot \hat{\boldsymbol{n}} \times \int_{S_n} d\boldsymbol{r}' g_u(\boldsymbol{r},\boldsymbol{r}') \boldsymbol{b}_n(\boldsymbol{r}') \\ &\quad + \frac{i}{k_u} \int_{S_m} d\boldsymbol{r} \boldsymbol{t}_m(\boldsymbol{r}) \cdot \hat{\boldsymbol{n}} \times \int_{S_n} d\boldsymbol{r}' \nabla g_u(\boldsymbol{r},\boldsymbol{r}') \nabla' \cdot \boldsymbol{b}_n(\boldsymbol{r}') \qquad (2.53) \\ \bar{\boldsymbol{K}}_{PV,u}^T[m,n] &= \int_{S_m} d\boldsymbol{r} \boldsymbol{t}_m(\boldsymbol{r}) \cdot \int_{PV,S_n} d\boldsymbol{r}' \boldsymbol{b}_n(\boldsymbol{r}') \times \nabla' g_u(\boldsymbol{r},\boldsymbol{r}') \qquad (2.54) \\ \bar{\boldsymbol{K}}_{PV,u}^N[m,n] &= \int_{S_m} d\boldsymbol{r} \boldsymbol{t}_m(\boldsymbol{r}) \cdot \hat{\boldsymbol{n}} \times \int_{PV,S_n} d\boldsymbol{r}' \boldsymbol{b}_n(\boldsymbol{r}') \times \nabla' g_u(\boldsymbol{r},\boldsymbol{r}') \qquad (2.55) \\ \bar{\boldsymbol{I}}^T[m,n] &= \int_{S_m} d\boldsymbol{r} \boldsymbol{t}_m(\boldsymbol{r}) \cdot \boldsymbol{b}_n(\boldsymbol{r}) \qquad (2.56) \\ \bar{\boldsymbol{I}}^N[m,n] &= \int_{S_m} d\boldsymbol{r} \boldsymbol{t}_m(\boldsymbol{r}) \cdot \hat{\boldsymbol{n}} \times \boldsymbol{b}_n(\boldsymbol{r}) \qquad (2.57) \end{aligned}$$

and excitation vectors can be obtained as

$$\begin{aligned} \boldsymbol{v}_E^T[m] &= \int d\boldsymbol{r} \boldsymbol{t}_m(\boldsymbol{r}) \cdot \boldsymbol{E}^{\text{inc}}(\boldsymbol{r}) \qquad (2.58) \\ \boldsymbol{v}_E^N[m] &= \int d\boldsymbol{r} \boldsymbol{t}_m(\boldsymbol{r}) \cdot \hat{\boldsymbol{n}} \times \boldsymbol{E}^{\text{inc}}(\boldsymbol{r}) \qquad (2.59) \\ \boldsymbol{v}_H^T[m] &= \int d\boldsymbol{r} \boldsymbol{t}_m(\boldsymbol{r}) \cdot \boldsymbol{H}^{\text{inc}}(\boldsymbol{r}) \qquad (2.60) \\ \boldsymbol{v}_H^N[m] &= \int d\boldsymbol{r} \boldsymbol{t}_m(\boldsymbol{r}) \cdot \hat{\boldsymbol{n}} \times \boldsymbol{H}^{\text{inc}}(\boldsymbol{r}). \qquad (2.61) \end{aligned}$$

2.1.3 Surface Formulations

Electromagnetic problems involving a homogeneous object in a simple medium can be separated into two media as D_o and D_i with different constitutive parameters. Using equivalence principle, integral equations can be considered as two sets, corresponding to the outer and inner media. Specifically, we obtain inner and outer integral equations by substituting discretized operators (2.52)–(2.57) into (2.39),(2.40),(2.42), and (2.43). In these practices, $\hat{\boldsymbol{n}}$ can be fixed as the normal vector outward the object. In our applications, excitations are located outside the objects such that incidents fields are nonzero for the integral equations derived for the outer medium (D_0). Solid angles Ω_o and Ω_i are set to 2π, considering that observation (testing) points are located only inside the triangles.

In general, combinations of tangentially and rotationally tested inner and outer equations can be written as

$$\left[\begin{array}{c} a\text{T-EFIE-O} + b\text{T-EFIE-I} \\ c\text{T-MFIE-O} + d\text{T-MFIE-I} \end{array}\right] + \left[\begin{array}{c} e\text{N-MFIE-O} - f\text{N-MFIE-I} \\ -g\text{N-EFIE-O} + h\text{N-EFIE-I} \end{array}\right]. \tag{2.62}$$

Then, tangential formulations are derived by setting coefficients as $e = f = g = h = 0$ and others as nonzero. On the other hand, normal formulations are derived by setting coefficients as $a = c = d = e = 0$, while others as nonzero. Using both tangential and normal integral equations in 2.62 leads to mixed formulations. In the most general form, the constructed matrix system can be written as

$$\left[\begin{array}{cc} \bar{\boldsymbol{Z}}_{11} & \bar{\boldsymbol{Z}}_{12} \\ \bar{\boldsymbol{Z}}_{21} & \bar{\boldsymbol{Z}}_{22} \end{array}\right] \cdot \left[\begin{array}{c} \boldsymbol{a}_J \\ \boldsymbol{a}_M \end{array}\right] = \left[\begin{array}{c} \boldsymbol{v}_1 \\ \boldsymbol{v}_2 \end{array}\right], \tag{2.63}$$

where matrix elements can be calculated as

$$\bar{\boldsymbol{Z}}_{11} = a\eta_o \bar{\boldsymbol{T}}_o^T + b\eta_i \bar{\boldsymbol{T}}_i^T + e\bar{\boldsymbol{K}}_o^N - f\bar{\boldsymbol{K}}_i^N - (e+f)\bar{\boldsymbol{I}}^T/2 \tag{2.64}$$

$$\bar{\boldsymbol{Z}}_{12} = -a\bar{\boldsymbol{K}}_o^T - b\bar{\boldsymbol{K}}_i^T - (a-b)\bar{\boldsymbol{I}}^N/2 + e\eta_o^{-1}\bar{\boldsymbol{T}}_o^N - f\eta_i^{-1}\bar{\boldsymbol{T}}_i^N \tag{2.65}$$

$$\bar{\boldsymbol{Z}}_{21} = c\bar{\boldsymbol{K}}_o^T + d\bar{\boldsymbol{K}}_i^T + (c-d)\bar{\boldsymbol{I}}^N/2 - g\eta_o \bar{\boldsymbol{T}}_o^N + h\eta_i \bar{\boldsymbol{T}}_i^N \tag{2.66}$$

$$\bar{\boldsymbol{Z}}_{22} = c\eta_o^{-1}\bar{\boldsymbol{T}}_o^T + d\eta_i^{-1}\bar{\boldsymbol{T}}_i^T + g\bar{\boldsymbol{K}}_o^N - h\bar{\boldsymbol{K}}_i^N - (g+h)\bar{\boldsymbol{I}}^T/2. \tag{2.67}$$

In the above η_i and η_o are characteristic impedance of the related media. Right-hand-side (RHS) elements are also given as

$$\boldsymbol{v}_1 = -a\boldsymbol{v}_E^T - e\boldsymbol{v}_H^N \tag{2.68}$$

$$\boldsymbol{v}_2 = -c\boldsymbol{v}_H^T + g\boldsymbol{v}_E^N. \tag{2.69}$$

Diverse formulations depending on the coefficients given above can be obtained in tangential, normal, and mixed forms. Mixed and normal formulations generally have diagonally dominant matrix systems leading to relatively small condition numbers [50]. We often prefer mixed formulations as they (1) are free of internal (numerical) resonances and (2) provide well-conditioned matrix systems. For example, for perfectly conducting objects, the combined-field integral equation is commonly used [54, 55]. In general, however, effectiveness of a mixed formulation, independent of its resonance-free and/or well-conditioned characteristics, strongly depends on combination parameters (signs, imaginary factors, coefficients, etc.), as well as other factors such as the types of basis and testing functions [56,57]. Different formulations based on the selection of coefficients $\{a, b, c, d, e, f, g, h\}$ can be exemplified as follows.

- N Müller formulation (NMF) [58]:
  $a = 0, b = 0, c = 0, d = 0, e = \mu_o, f = \mu_i, g = \epsilon_o, h = \epsilon_i$
- Modified N Müller formulation (MNMF) [59]:
  $a = 0, b = 0, c = 0, d = 0, e = \mu_o/(\mu_o + \mu_i), f = \mu_z/(\mu_o + \mu_i),$
  $g = \epsilon_o/(\epsilon_o + \epsilon_i), h = \epsilon_i/(\epsilon_o + \epsilon_i)$

- Electric-magnetic current combined-field integral equation (JMCFIE) [57]:
  $a = \eta_o^{-1}, b = \eta_i^{-1}, c = \eta_o, d = \eta_i, e = 1, f = 1, g = 1, h = 1$

- Poggio-Miller-Chang-Harrington-Wu-Tsai (PMCHWT) [60–62]:
  $a = 1, b = 1, c = 1, d = 1, e = 0, f = 0, g = 0, h = 0$

- Combined T formulation (CTF) [63]:
  $a = \eta_o^{-1}, b = \eta_i^{-1}, c = \eta_o, d = \eta_i, e = 0, f = 0, g = 0, h = 0$

- Modified combined T formulation (MCTF) [64]:
  $a = 1, b = 1, c = \eta_o\eta_i, d = \eta_o\eta_i, e = 0, f = 0, g = 0, h = 0$

- NZI Tangential Formulation (NT) [65–67]:
  $a = \eta_o^{-1}, b = \epsilon_i\epsilon_o^{-1}\eta_o^{-1}, c = \eta_o, d = \mu_i\mu_o^{-1}\eta_o, e = 0, f = 0, g = 0, h = 0$

- NZI Mixed Formulation (MF) [65–67]:
  $a = \eta_o^{-1}, b = \epsilon_i\epsilon_o^{-1}\eta_o^{-1}, c = \eta_o, d = \mu_i\mu_o^{-1}\eta_o, e = 1, f = \mu_i\mu_o^{-1},$
  $g = 1, h = \epsilon_i\epsilon_o^{-1}$

Although tangential formulations generally lead to ill-conditioned matrix systems, they provide relatively accurate results. On the other hand, mixed and normal formulations have well-tested identity operators, leading to well-conditioned matrix equations with dominant diagonal blocks, while numerical errors stemming from identity operators may deteriorate the accuracy of solutions [50]. Depending on the electromagnetic parameters of a given problem, e.g., permittivity, permeability, and operating frequency, some formulations can be more preferable than others. For instance, PMCHWT and CTF lead to highly accurate solutions at the cost of poor iterative convergences due to ill-conditioned matrix equations. NMF provides very effective iterative solutions of low-frequency problems; but, at high frequencies and for high permittivity values, it becomes inaccurate. By MNMF, better-conditioned matrices can be obtained in comparison to NMF, while inaccuracy issues often persist. JMCFIE is preferred for many electromagnetic problems since it provides reliable and accurate analysis of most dielectric objects. On the other hand, for objects with large negative permittivity values, such as plasmonic structures, MCTF is proposed and extensively used [64].

Simulations of homogeneous metamaterial models need rigorous and accurate treatment due to extraordinary constitutive parameters leading to unbalanced matrix terms. For example, while investigating homogeneous models of negative-index or low-index structures, the popular JMCFIE suffers from inaccuracy and instability issues [65, 66, 68]. The scalar potential part (of the inner T operator) becomes very large and dominates matrix equations for simulations of NZI objects. While investigating ENZ and MNZ structures, one of the diagonal blocks becomes enormously large. Although NMF was introduced as a stable formulation for NZI structures [69], it fails at extreme values of medium parameters [70].

NM and NT are novel formulations that have been introduced to provide accurate and efficient solutions of NZI structures considering the limit cases, i.e., $\epsilon_i \to 0$ and $\mu_i \to 0$ [65–67]. NT is a part of MF with only tangential operators. Although it provides stable solutions in most cases, it fails when either ϵ_i or μ_i goes to zero. However, for all NZI cases (EMNZ, ENZ, and MNZ), operators are well-balanced for MF, which also maintains well-tested identity operators in diagonal blocks. Matrix and RHS elements of JMCFIE and MF for different NZI cases are detailed in Appendix B.

There are also some novel formulations derived from potential integral equations rather than field integral equations [71, 72]. They provide low-frequency stability often together with broadband operation, which can be very useful for PEC-based metamaterials. Some NZI structures are realized by using PEC pillars with quite small dimensions in terms of wavelength, leading to challenging low-frequency problems [30]. Potential formulations can be good candidates for performing accurate and efficient solutions of such structures, preventing time and memory bottlenecks in field formulations, especially as the number of unknowns grows.

In this study, JMCFIE and MF are employed for the design and simulation of actual (realized) and homogenized NZI structures, respectively. However, while investigating NZI models, we need to use not only these suitable formulations but also low-frequency-stable solution algorithms.

2.1.4 Multilevel Fast Multipole Algorithm with Approximate Diagonalization

In the context of MoM, iterative algorithms can be used to obtain solutions of dense matrix equations in the form of $\boldsymbol{v} = \bar{\boldsymbol{Z}} \cdot \boldsymbol{a}$ with N number of unknowns. Then, MVMs are needed through solution steps, i.e., iterations. When direct computations of MVMs are performed during iterative solutions, the complexity for time per iteration and memory is $\mathcal{O}(N^2)$. Consequently, iterative solutions of large objects with large numbers of unknowns become impossible even for today's cutting-edge computer hardware due to time and memory bottlenecks of MoM. To overcome this problem, the fast multipole method (FMM) [73, 74] was proposed to reduce computational complexity per MVM from $\mathcal{O}(N^2)$ to $\mathcal{O}(N^{3/2})$. Moreover, FMM was further improved by recursive multi-level clustering scheme of MLFMA [75, 76], which reduces the complexity of MVMs to $\mathcal{O}(N \log N)$. In this study, matrix equations of actual and homogenized versions of NZI shells are efficiently solved by different versions of MLFMA.

While constructing the impedance matrix in (2.49), interactions are calculated between discretized elements (basis and testing) via surface integrals. For a large-scale electromagnetic problem, there are many basis (radiating) and testing (receiving) elements far from each other. Instead of direct calculations of all interactions, the impedance matrix is separated into two groups in MLFMA: 1) near-zone and 2) far-zone interactions as $\bar{\boldsymbol{Z}} = \bar{\boldsymbol{Z}}^{NZ} + \bar{\boldsymbol{Z}}^{FZ}$. The interactions are directly calculated and stored in memory for $\bar{\boldsymbol{Z}}^{NZ}$, whereas $\bar{\boldsymbol{Z}}^{FZ}$ elements are calculated on-the-fly. To determine such rules for interactions, the computational domain, where the object is placed, is constructed as a cube completely enclosing the object. Then, a tree structure is formed by recursively dividing the domain into sub-cubes at different levels. A one-box buffer scheme is used to decide whether the interaction between a pair of elements belongs to the far-zone matrix or not [50]. As the core of MLFMA, Gegenbauer's addition theorem and plane-wave expansion method are used to enable factorization and diagonalization, respectively, of the homogeneous-space Green's function. The factorization is employed by representing Green's function as summations of spherical Henkel and Bessel functions of the first kind. The diagonalization is related to the conversion of spherical waves into plane waves, leading to angular

integration and a diagonal translation operator.

There are three main stages of MLFMA; aggregation, translation, and disaggregation. In the aggregation stage, starting with basis functions at the lowest level boxes, radiated fields are computed and shifted to higher level box centers until the highest level box. Next, during the translation, radiated fields are translated into incoming fields. Finally, in the disaggregation stage, starting with the highest level box, incoming fields are shifted to lower box centers until the lowest level boxes consisting of testing functions. After receiving incoming fields by testing functions, an MVM cycle is completed to be used in the iterative solution of the electromagnetic problem.

Although MLFMA is very suitable for large-scale problems, the conventional plane wave expansion of the homogeneous-space Green's function becomes invalid for short-distance interactions. Hence, the diagonalization becomes the most critical factor of the low-frequency stability of MLFMA [50]. In the context of NZI problems, when the wavelength inside an object becomes large due to small permittivity and/or permeability values, the inner medium corresponds to a low-frequency problem, even for moderate size objects at mmWave and optical frequencies. Hence, their solutions become challenging and need rigorous treatments. The low-frequency breakdown of MLFMA is well-known in the literature, and there are several approaches to overcome this problem [77]. For instance, in a mixed form MLFMA, a multipole expansion can be used for short-distance interactions, while the plane wave expansion can still be employed for long-distance interactions. [78]. Hybridization methods are used to further improve this technique [79]. A non-directional plane wave algorithm [80] and approximately diagonalized MLFMA (AD-MLFMA) [81] are among other techniques proposed to provide low-frequency stability. In this study, while simulating homogeneous objects with low refractive indices, AD-MLFMA is employed for stable solutions. On the other hand, arrays of dielectric pillars to realize NZI structures are simulated by standard MLFMA.

AD-MLFMA employs well-engineered scaling constants on spherical Bessel functions at low frequencies to maintain stability. It is based on the approximate form of the Green's function [82] as

$$g(\boldsymbol{r},\boldsymbol{r}') \approx \frac{ik}{(4\pi)^2}\int d^2\hat{\boldsymbol{k}}\exp(i\boldsymbol{k}\cdot\boldsymbol{v}/s)G(\boldsymbol{k},\boldsymbol{w}) \tag{2.70}$$

$$\nabla' g(\boldsymbol{r},\boldsymbol{r}') \approx \frac{k^2}{(4\pi)^2 s}\int d^2\hat{\boldsymbol{k}}\exp(i\boldsymbol{k}\cdot\boldsymbol{v}/s)G(\boldsymbol{k},\boldsymbol{w})\hat{\boldsymbol{k}} \tag{2.71}$$

$$G(\boldsymbol{k},\boldsymbol{w}) \approx \sum_{t=0}^{\tau} i^t(2t+1)s^t h_t^{(1)}(kw)P_t(\hat{\boldsymbol{k}}\cdot\hat{\boldsymbol{w}}), \tag{2.72}$$

where $h_t^{(1)}$ is the spherical Hankel function of the first kind, P_t represents Legendre polynomial, τ is the truncation number, and s is the scale factor. We also note that standard MLFMA can be obtained without programming efforts by setting $s = 1$.

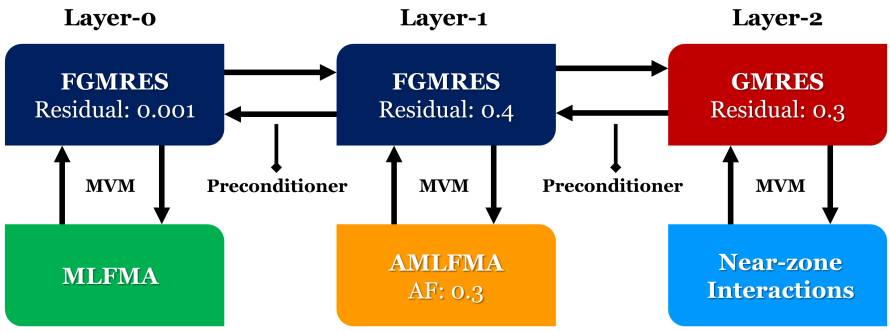

Figure 2.5: The three-layer iterative solution mechanism.

2.1.5 Multilayer Iterative Strategy

Novel second-kind surface formulations are employed throughout the design of NZI shells as discussed in Section 2.1.3. While simulating actual models with ordinary constitutive parameters, JMCFIE is used. On the other hand, for homogeneous NZI models, the recently developed MF is used. Although proper formulations are employed for given problem types, simulations can still be challenging. For example, in actual models, even tough triangles (discretization elements) are generally selected nearly $\lambda/10$, smaller discretizations are often needed to accurately model pillars since they are thin cylindrical structures. Consequently, due to dense discretizations with respect to wavelength, both numbers of unknowns grow and low-frequency (dense-discretization) instabilities arise. Accordingly, iterative simulations in this work are carried out by applying a robust preconditioning technique based on a three-layer inner-outer scheme consisting of exact and approximate forms of MLFMA [51, 83].

MLFMA provides controllable accuracy in MVMs during iterative solutions. For example, truncation number in (2.72) can be decided considering two digits accuracy based on the excess bandwidth formula and the one-box-buffer-scheme. Then, less accurate forms of MLFMA (approximate MLFMA [AMLFMA]) can be constructed by approximating the operations in MLFMA [84]. Since near-zone interactions are critical, such approximations are merely applied on far-zone interactions ($\bar{\boldsymbol{Z}}^{FZ}$). As a relatively straightforward but effective method, an approximation factor (AF) can be used to scale the number of harmonics in translation operators and plane-wave sampling [76]. For instance, AF $= 1.0$ corresponds to standard MLFMA, while AF $= 0.0$ indicates completely discarding far-zone interactions and maintaining only near-zone interactions. It should be noted that this approach is different from AD-MLFMA discussed in the previous section, where low-frequency-stability was achieved at the cost of a nonparametric approximation.

On-the-fly adjustable accuracy control provided by MLFMA facilitates the construction of the three-layer solution mechanism. In this strategy, iterative solutions at a lower layer are used as a preconditioner for a higher layer. From the top layer to the bottom layer, the accuracy and residual errors are systematically reduced. Figure 2.5 depicts a general diagram of three-layer solutions, where commonly used values for critical parameters are also indicated. It can be summarized as follows.

- Layer-0 is the main solver at the top layer. Iterative solutions are obtained by a flexible generalized minimal residual method (FGMRES) via full MLFMA (AF $= 1.0$). Layer-0 solutions are preconditioned by inner layer-1. It should be noted that while computing iterations at a higher layer, preconditioner solutions of all lower layers are needed.

- Layer-1 provides iterative solutions with FGMRES, and MVMs are accelerated by AMLFMA with AF $= 0.3$. The residual error is determined as 0.4. This inner solution is further preconditioned by layer-2.

- Layer-2 solutions are computed by generalized minimal residual method (GMRES) considering only near-zone interactions (AMLFMA with AF $= 0.0$). The residual error is chosen as 0.3. A block-diagonal preconditioner (BDP) can also be applied at this layer to further accelerate iterative solutions.

Since the target residual is selected as 0.001 and full MLFMA is employed at layer-0, accuracy of a main solution is not affected by preconditioning (in fact, improved as mentioned below). The number of iterations of the main solver, hence the overall solution time, is decreased considerably by the three-layer mechanism. Parameters of the mechanism (AFs, residuals, etc.) generally depend on the problem type. Thus, they are heuristically decided by initial tests. Moreover, the three-layer inner-outer scheme does not only reduce the number of iterations of the main layer but also decreases the deviation between true and computed residuals that typically occurs due to rounding errors in long iterative solutions.

2.1.6 Incident Fields

When a Hertzian dipole is used for excitation, incoming fields in (2.58)–(2.61) are given as

$$\boldsymbol{E}^{\text{inc}}(\boldsymbol{r}) = i\omega\mu \frac{\exp(ik|\boldsymbol{r}-\boldsymbol{r}_d|)}{4\pi|\boldsymbol{r}-\boldsymbol{r}_d|} \left[\boldsymbol{I}_d \left(1 + \frac{i}{k|\boldsymbol{r}-\boldsymbol{r}_d|} - \frac{1}{k^2|\boldsymbol{r}-\boldsymbol{r}_d|^2} \right) - (\boldsymbol{r}-\boldsymbol{r}_d) \frac{\boldsymbol{I}_d \cdot (\boldsymbol{r}-\boldsymbol{r}_d)}{|\boldsymbol{r}-\boldsymbol{r}_d|^2} \left(1 + \frac{3i}{k|\boldsymbol{r}-\boldsymbol{r}_d|} - \frac{3}{k^2|\boldsymbol{r}-\boldsymbol{r}_d|^2} \right) \right] \tag{2.73}$$

$$\boldsymbol{H}^{\text{inc}}(\boldsymbol{r}) = \boldsymbol{I}_d \times (\boldsymbol{r}-\boldsymbol{r}_d) \frac{\exp(ik|\boldsymbol{r}-\boldsymbol{r}_d|)}{4\pi|\boldsymbol{r}-\boldsymbol{r}_d|^2} \left(\frac{1}{|\boldsymbol{r}-\boldsymbol{r}_d|} - ik \right), \tag{2.74}$$

where $\boldsymbol{r}$ and $\boldsymbol{r}_d$ are observation and source points. In the above, $\boldsymbol{I}_d$ is the dipole moment and $|\boldsymbol{I}_d| = LI_0$ (which is set to unity in simulations) to represent a radiating element with short length (L) and uniform current (I_0). Moreover, a Hertzian dipole can be easily manipulated by using complex coordinates as the dipole's location to generate electromagnetic (CSP) beam [85]. For this purpose, the distance between the source and observation locations in (2.73) and (2.74) can be written as

$$|\boldsymbol{r}-\boldsymbol{r}_d| = \sqrt{(\boldsymbol{r}-\boldsymbol{r}_d)\cdot(\boldsymbol{r}-\boldsymbol{r}_d)^*}, \tag{2.75}$$

where $\boldsymbol{r}_d = \boldsymbol{r}_{d,R} + i\boldsymbol{r}_{d,I}$. The real part of the source location corresponds to the beam's position, similar to the Hertzian dipole's location, while the imaginary part

is related to the beam width. Together with source patterns, derivation of incident potentials and fields for CSP beams and Hertzian dipoles are given in Appendix A.

2.1.7 Far-field and Near-field Calculations

When a dielectric object is placed in a host medium, the total electric and magnetic fields in the vicinity of the object can be found as

$$\begin{aligned}\boldsymbol{E}(\boldsymbol{r}) &= \boldsymbol{E}^{\text{inc}}(\boldsymbol{r}) + ik_u\eta_u \int d\boldsymbol{r}' \boldsymbol{J}(\boldsymbol{r}') g_u(\boldsymbol{r},\boldsymbol{r}') + i\frac{\eta_u}{k_u} \int d\boldsymbol{r}' \nabla' \cdot \boldsymbol{J}(\boldsymbol{r}') \nabla g_u(\boldsymbol{r},\boldsymbol{r}') \\ &\quad - \int d\boldsymbol{r}' \nabla g_u(\boldsymbol{r},\boldsymbol{r}') \times \boldsymbol{M}(\boldsymbol{r}') \qquad (2.76) \\ \boldsymbol{H}(\boldsymbol{r}) &= \boldsymbol{H}^{\text{inc}}(\boldsymbol{r}) + i\frac{k_u}{\eta_u} \int d\boldsymbol{r}' \boldsymbol{M}(\boldsymbol{r}') g_u(\boldsymbol{r},\boldsymbol{r}') + \frac{i}{k_u\eta_u} \int d\boldsymbol{r}' \nabla' \cdot \boldsymbol{M}(\boldsymbol{r}') \nabla g_u(\boldsymbol{r},\boldsymbol{r}') \\ &\quad + \int d\boldsymbol{r}' \nabla g_u(\boldsymbol{r},\boldsymbol{r}') \times \boldsymbol{J}(\boldsymbol{r}'), \qquad (2.77)\end{aligned}$$

where fields can be computed for $u = \{i, o\}$, corresponding to inner and outer medium. In our applications, sources are placed in the host medium, leading to $\boldsymbol{E}^{\text{inc}}(\boldsymbol{r}) = 0$ and $\boldsymbol{H}^{\text{inc}}(\boldsymbol{r}) = 0$ for the inner medium. According to the surface equivalence theorem, inner fields should be identically zero for the outer problem, and vice versa. Hence, accuracy of formulations and solution algorithms can be examined by the presence of fields in cross cases.

As discussed before, unknown surface coefficients $\boldsymbol{J}(\boldsymbol{r}')$ and $\boldsymbol{M}(\boldsymbol{r}')$ are solutions of a given electromagnetic problem, which can be approximated as (2.45). Once we obtain expansion coefficients, electromagnetic fields can be computed at the intended locations. Far-zone fields can be found by using well-known far-zone approximations to (2.76), (2.77). In addition, whenever required, the complex power density can be calculated as

$$\boldsymbol{S}(\boldsymbol{r}) = \frac{1}{2}\boldsymbol{E}(\boldsymbol{r}) \times \boldsymbol{H}^*(\boldsymbol{r}), \qquad (2.78)$$

where * is conjugate operation.

2.2 Realization of Near-Zero-Index Structures

In the previous sections, it has been argued that accurate and efficient simulations of NZI geometries can be possible with novel formulations such as MF and JMC-FIE supported by proper solution algorithms. On the other side, in order to obtain NZI beam generating structures, they should be realizable at the intended frequency regimes, such as mmWaves and microwaves in this study.

There are several approaches to the realization of different NZI properties, i.e., ENZ, MNZ, or EMNZ. ENZ behavior can be realized by some homogeneous materials at their plasma frequencies [20]. For instance, potassium at THz frequencies, silicon carbide (SiC) at mid-infrared frequencies, some doped semiconductors (transparent conducting oxides [TCOs] and aluminum-doped zinc oxide [AZO]) at THz frequencies and topological insulators at ultraviolet frequencies show nonmagnetic ENZ characteristics. However, their performances are highly limited by losses. In this direction, metamaterials can be good candidates to mimic low loss NZI structures. Considering effective medium theory [33], arrays of metallic, dielectric, and composite rods, layers, and pillars can be used to induce effective permittivity and/or effective permeability. For instance, stacked layers of dielectrics can demonstrate ENZ behavior [31]. When two dielectrics are used as in Figure 2.6, effective permittivity of the overall system can be written as [20]

$$\epsilon_{eff} = \frac{t_1\epsilon_1 + t_2\epsilon_2}{t_1 + t_2}, \tag{2.79}$$

where t_1 and t_2 are the thicknesses of the slabs. Then, via two materials with $\epsilon_1 > 0$, $\epsilon_2 < 0$, and by choosing proper thicknesses, an ENZ property can be acquired. Another choice is to use artificial dielectrics, such as waveguides at their near cut-off frequencies [20] and PEC wire media [30]. Effective propagation constant and impedance of TE_{10} mode inside a parallel plate waveguide of height h can be written as

$$k_{eff} = k_o \sqrt{1 - \frac{\lambda}{2h}^2} \tag{2.80}$$

$$Z_{eff} = \frac{\eta_o}{\sqrt{1 - \frac{\lambda}{2h}^2}}. \tag{2.81}$$

Therefore, a waveguide at near-cutoff frequency ($h = \lambda/2$) can be treated as an ENZ structure.

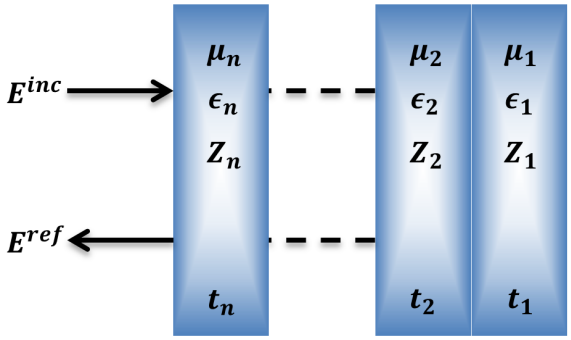

Figure 2.6: Stacked layers of different materials. ENZ response can be realized for an incident wave with electric field parallel to the slabs, when appropriate dielectrics are used.

PEC wire media can be used to obtain small effective refractive index values. In particular, an ENZ medium with nearly $n_{eff} = 0.5$ can be realized [30] by metallic cylindrical rods, as illustrated in Figure 2.7. By examining transmission line equivalent models and properly arranging spacing and radii of the rods, a wire medium can demonstrate small effective refractive indices. For artificial dielectrics, NZI responses (independent of frequency) can be obtained, as long as spacings between unit cells can be made relatively small considering the operating frequency. Such a feature may be desirable for many applications; however, metallic losses and relatively high effective refractive index values (much lower values are preferred) can restrain the usage of such structures.

All-dielectric photonic crystals (PhCs) are other alternatives in order to achieve low-loss NZI behaviors [22, 86, 87]. Conical, i.e., Dirac-like, dispersion can be obtained with PhCs, which can be mapped to an effective zero refractive index with isotropic

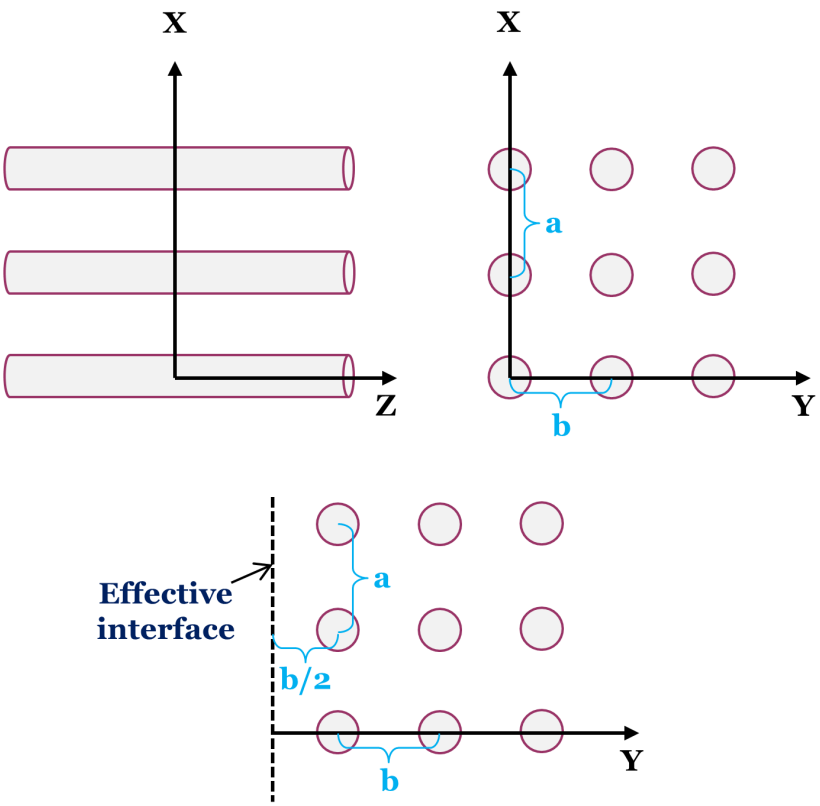

Figure 2.7: PEC wire medium. Effective interfaces are a little bit more than the actual size of the periodic structure. When radius and periodicities (a and b) are properly arranged, ENZ property can be achieved.

EMNZ property. By appropriate arrangements of dielectric rods, Dirac-like cone dispersion occurs at the Brillouin zone center of PhCs. At a Dirac-like point corresponding to a particular frequency ω_0, PhCs have a linear and conical dispersion at $\boldsymbol{k} = 0$, considering their band diagrams. This is the way how a periodic structure can be mapped to an effective medium with simultaneously near-zero ϵ_r and μ_r. In other words, since high-contrast dielectric rods support electric and magnetic dipole responses due to Mie resonances, an effective EMNZ medium can be obtained by proper selections of material properties and dimensions. The particular aim is to cross the antiresonances of electric and magnetic dipoles at zero simultaneously.

Considering other approaches, Dirac-like cone dispersion provides a low loss way to realize isotropic and impedance-matched EMNZ behavior since the usage of metallic parts is avoided. Effective media with ENZ and MNZ properties can also be realized

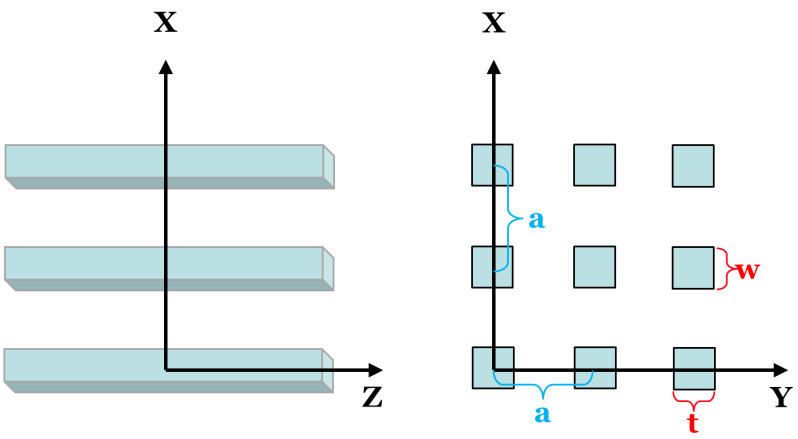

(a) All-dielectric rectangular rods and their dimensions.

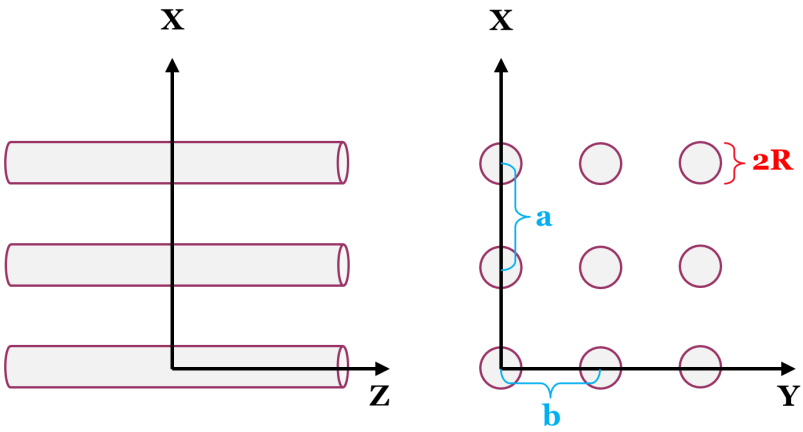

(b) All-dielectric cylindrical rods and their dimensions.

Figure 2.8: All-dielectric PhCs. By proper arrangements, periodic arrays of rectangular prisms, square prisms, and cylinders can effectively have NZI characteristics.

based on PhCs with Dirac-like cone dispersion [32]. Although incident waves are limited such that the electric field is polarized parallel to the longitudinal direction of the rods, it is possible to remove such restrictions by using additional sets of wires at directions perpendicular to the original ones [88]. There are diverse application areas of such structures. Specifically, other than the microwave regime, they can be used at optical frequencies [89], as well as in acoustics [90]. As illustrated in Figure 2.8, other than cylindrical rods, square prisms can be used to obtain a periodic medium with effective NZI characteristics. Furthermore, unit cells can be arranged in square or rectangular lattices as different alternatives. Since unit cells have rotational

symmetry in the transverse plane (x-y plane), the effective index is the same for all directions in this plane. Note that, considering the configuration in Figure 2.8, electric field should be polarized in the z direction.

While isotropic artificial EMNZ behavior can be obtained by PhCs having Dirac-like cone dispersion, anisotropic NZI structures can be realized by semi-Dirac dispersion [34, 35]. For example, elliptical cylindrical rods in a square lattice [34], rectangular prisms in a square lattice, or cylindrical rods in a rectangular lattice [35] can be used to realize anisotropic NZI behaviors due to the absence of rotational symmetry. A PhC with semi-Dirac cone dispersion acts as an EMNZ medium along one axis and as an ENZ medium along the perpendicular axis.

Considering the configurations given in Figures 2.7 and 2.8, several PhC structures that demonstrate NZI characteristics can be exemplified as follows.

- Wire media (isotropic ENZ) [30]:
  $a = 4$ cm, $b = 4$ cm, $R = 0.25$ cm, $\lambda = 10$ cm, PEC
- Square lattice & cylinder (isotropic EMNZ) [22]:
  $a = b = 0.584\lambda, R = 0.220a, \epsilon_r = 8.8$
- Triangular lattice & cylinder (isotropic EMNZ) [22]:
  $a = b = 0.584\lambda, R = 0.203a, \epsilon_r = 8.8$
- Square lattice & square prism (isotropic EMNZ) [89]:
  $a = 0.422\lambda, w = t = 0.433a, \epsilon_r = 13.7, \epsilon_{r,coating} = 2.25$
- Square lattice & square prism (isotropic EMNZ) [35]:
  $a = 0.557\lambda, w = t = 0.336a, \epsilon_r = 9.8$
- Square lattice & rectangular prism (anisotropic EMNZ) [35]:
  $a = 0.553\lambda, w = 0.465a, t = 0.360a, \epsilon_r = 9.8$
- Rectangular lattice & cylinder (anisotropic EMNZ) [35]:
  $a = 0.494\lambda, b = 1.262a, R = 0.259a, \epsilon_r = 9.8$

It should be noted that, except for the fourth one for which a coating is used around rods, outer media are considered as vacuum. For the fourth case, unit cells are ob-

tained by Si ($\epsilon_r = 13.7$) rods separated by SiO_2 ($\epsilon_r = 2.25$) and coated by polymethyl methacrylate ($\epsilon_r = 2.23$). For the first one, metallic rods are used, while the other realizations include alumina (Al_2O_3) rods having different purity values (permittivities). For all structures, materials are assumed to be nonmagnetic, i.e., μ_r equals to unity.

2.3 Numerical Results

In this part, we compare formulations and solution algorithms for some of the NZI shell structures that are used to generate directive beams. Considering Snell's law of refraction, when electromagnetic waves enter an NZI medium, they leave perpendicularly to its surface, i.e., NZI-vacuum interface. Thus, when the outer surfaces of an object are planar, highly directive beams can be obtained, which leads to a plethora of applications, as listed before. Shell geometries can be modeled as homogeneous structures, on which NZI properties with small permittivity and permeability values are enforced. On the other hand, their actual models as periodic structures can be employed to demonstrate beam generation in more realistic ways.

2.3.1 Comparison of SIEs for Homogeneous Bodies

In order to compare the surface formulations that are discussed in Section 2.1.3, a homogeneous shell structure is considered. Its outer edge, inner edge, and height are 5.0λ, 2.1λ, and 2.0λ, respectively. The geometry is discretized with $57,360$ unknowns. The operating frequency is 10.3 GHz ($\lambda \approx 29$ mm). The primary source is modeled as a z-oriented Hertzian dipole at the center of the shell. Figure 2.9 presents iteration history when GMRES is used without restart and preconditioner. AD-MLFMA with five levels is used to accelerate iterative solutions of different formulations. Once expansion coefficients are obtained, electric and magnetic fields and power density distributions can be calculated. In the far-zone, electric field can be approximated as $\boldsymbol{E}^{far}(\theta,\phi) = \lim_{r\to\infty}\{r\boldsymbol{E}(\boldsymbol{r})\}$, where $\boldsymbol{r}$ is the position vector.

As the electromagnetic parameters of the shell, different ϵ_r and μ_r values are used to represent various NZI properties. In particular, we consider $\{\epsilon_r, \mu_r\} = \{1\times10^{-5}, 1\times$

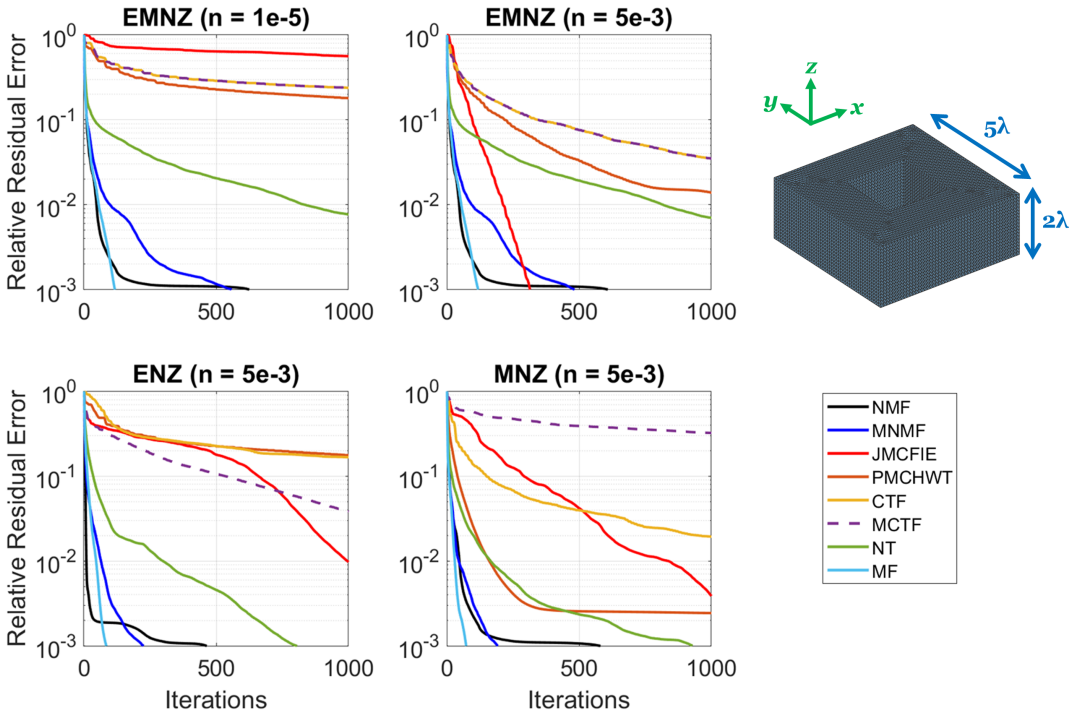

Figure 2.9: Convergence histories for different formulations. A homogeneous shell structure with various ϵ_r and μ_r values is considered.

$10^{-5}\}$ case, in addition to $\{\epsilon_r, \mu_r\} = \{5 \times 10^{-3}, 5 \times 10^{-3}\}$, $\{\epsilon_r, \mu_r\} = \{1, 2.5 \times 10^{-5}\}$, and $\{\epsilon_r, \mu_r\} = \{2.5 \times 10^{-5}, 1\}$ cases where the refractive index values are fixed to 5×10^{-3} for EMNZ, MNZ, and ENZ conditions. Among eight formulations, only NMF, MNMF, and the novel MF converge within 1000 GMRES iterations for all problems when the target residual is set to 10^{-3}. JMCFIE provides convergence only for the EMNZ case with $n = 5 \times 10^{-3}$. Obviously, the best performances with the fastest converge rates are provided by MF for all NZI cases.

Figure 2.10 depicts power density results obtained with MF, NMF, and MNMF in the x-y plane at $z = 0$. Only outer problems are considered according to the surface equivalence theorem. The surfaces of the shell are represented by green square lines, and inside the shell (in the region between the smaller and larger squares), power density values should be vanishingly small according to the equivalence principle. However, for all NZI cases, only MF provides sufficiently small power density values that are represented by black for the given color range. The other convergent formulations suffer from inaccuracy issues even they reach the preset residual error value within

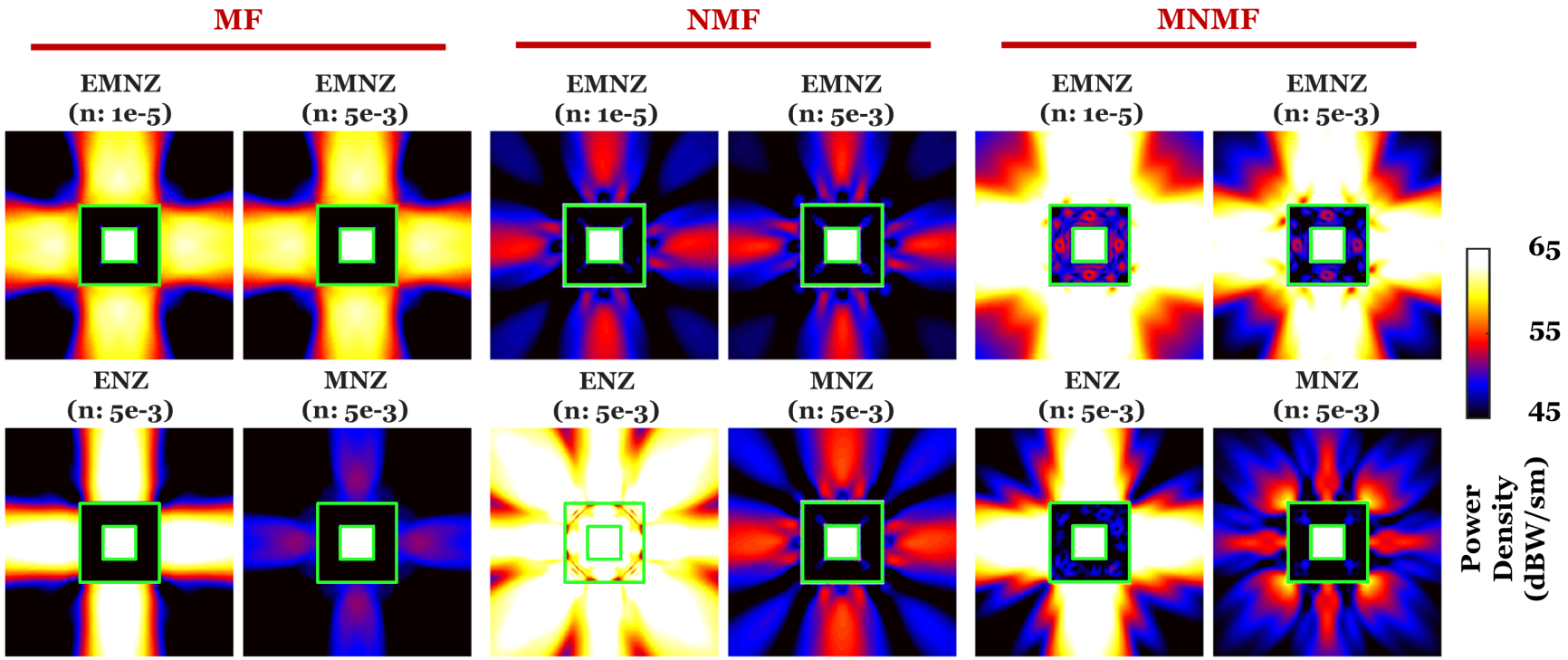

Figure 2.10: Near-zone power density distributions in the vicinity of NZI shells excited by a Hertzian dipole when different formulations are used to analyze the problems. Divergent solutions are not shown.

a thousand GMRES iterations. Specifically, there are undesired power levels in the inner media, which shows the inaccuracy of these formulations and their solutions. Moreover, for NMF and MNMF, there are unsymmetrical power density distributions that are not expected for a symmetric structure with simple medium characteristics. If we investigate the reliable power density results obtained with MF, it can be seen that strong beams emerge from the flat surfaces of the shells, as predicted via Snell's law. On the other side, different refractive indices and NZI properties lead to different beam characteristics. This diversity allows alternative design opportunities, which are examined in the following chapter.

Consequently, conventional full-wave solvers suffer from accuracy, stability, and efficiency issues when they are used for the analyses of homogeneous NZI objects. Among alternatives, the developed MF is the most suitable choice to simulate NZI structures with extreme constitutive parameters.

2.3.2 Simulations of Periodic Structures

Next, we consider wire media that consist of PEC cylindrical rods to demonstrate ENZ behavior. Such metallic problems can be formulated by CFIE with a combination parameter $\alpha = 0.5$. Iterative solutions are accelerated by the three-layer preconditioner based on AMLFMA.

Figure 2.11 presents discretized models and near-field results of a wire array involving a 9×9 grid, where three different mesh sizes are used. Triangulations with $\lambda/10$, $\lambda/20$, and $\lambda/33$ edge sizes lead to $23,328$, $44,064$, and $110,808$ unknowns, respectively. The heights of the rods are fixed as $\lambda$when the operating frequency is 3 GHz. 3D and top views of the overall structure and unit cells can be seen on the left-hand side of Figure 2.11. We note that 3×3 rods are removed from the center to generate a source (cavity) region. A z-oriented Hertzian dipole is used at the center to excite the structure. Even $\lambda/33$ mesh size is not enough to adequately represent the circular cross sections of the rods; however, the electromagnetic response of the structure does not change significantly with varying mesh sizes. Near-field plots are located on the right-hand side of Figure 2.11, where the columns correspond to different mesh sizes. As can be seen in these distributions, as well as in the far-field results illustrated in

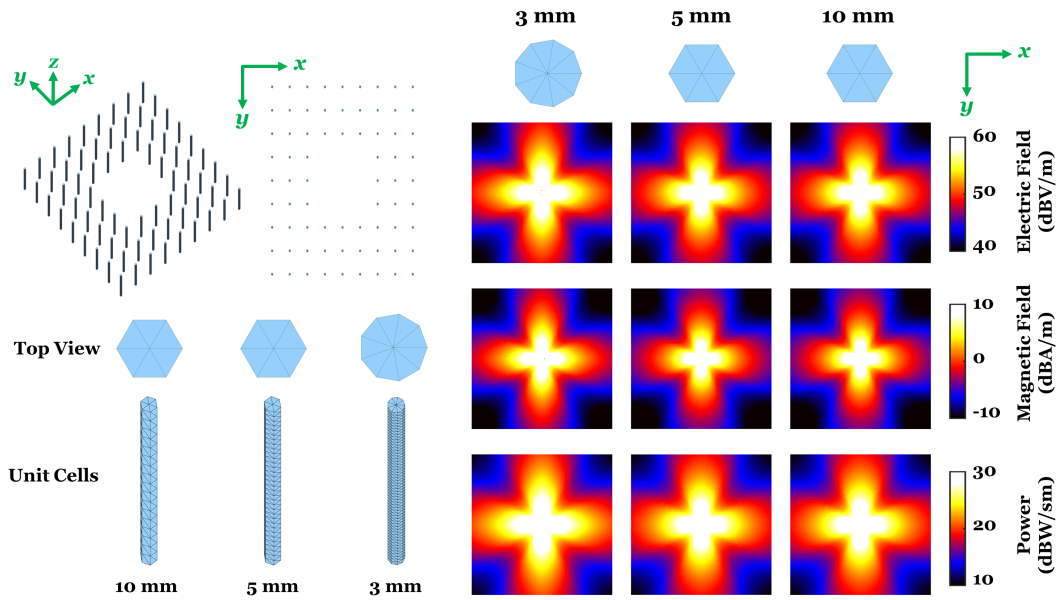

Figure 2.11: A metallic structure that demonstrates ENZ behavior.Computational models are on the left-hand side, while the electromagnetic responses are depicted on the right-hand side.

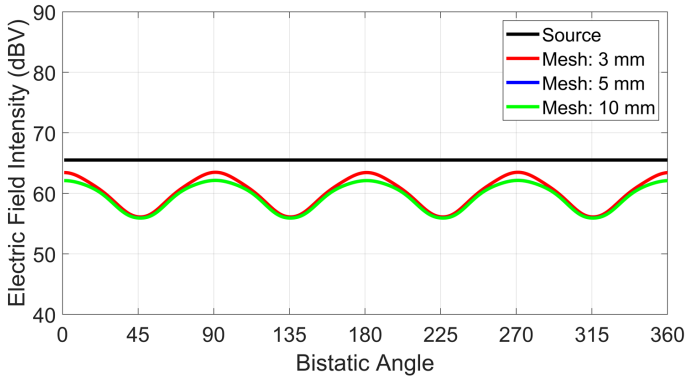

Figure 2.12: Far-zone electric field intensity with respect to bistatic angle generated by the structure in Figure 2.11. Omnidirectional radiation is slightly changed to a quaddirectional one by the carefully arranged PEC rods.

Figure 2.12, relatively weak four beams emerge from the outer surfaces of the shell structure. In order to enhance outgoing beams, much smaller effective refractive index values are needed, while this does not seem to be possible with wire media.

Another approach, which is extensively followed in this thesis, to realize NZI behav-

ior is using dielectric rods. In a set of examples below, we consider 9×9 grids of dielectric rods. For each structure, in order to generate a source region, 3×3 of the rods are removed from the center so that the remaining part becomes completely separated from the source. In general, with the described strategy, all designed shells are rotatable, isolated, and replaceable structures, while also being reconfigurable due to independent characteristics of the rods (their unconnected placements). In the literature, theoretical two-dimensional analyses of PhCs involving dielectric rods behaving as effective NZI structures are provided together with experimental results mostly in waveguides. However, 3D models are needed to investigate the actual responses of the designed structures and identify deviations in their characteristics from those of ideal infinitely long cases. To compare some strategies to realize NZI behaviors, we first consider five different arrangements of dielectric rods, as depicted in Figure 2.13. Each structure is excited by a z-oriented Hertzian dipole located at the center of the cavity region. The first two designs consist of cylindrical alumina rods that have 8.8 relative permittivities. While the first design has a square lattice leading to rotational symmetry, the second design has a triangular lattice leading to a mirror symmetry. The radii of their rods are 3.75 mm and 3.45 mm, respectively, while the center-to-center distances are fixed to 17 mm. The operating frequency is 10.3 GHz ($\lambda \approx 29$ mm). The last three designs consist of square prisms, rectangular prisms, and cylindrical rods, respectively. Even though they are made of alumina too, the relative permittivity in these three cases is 9.8 since alumina with a different purity is used as rod materials. Consequently, the center frequency (Dirac-like or semi-Dirac points) that we expect to see NZI behavior is 12.1 GHz ($\lambda \approx 25$ mm) for these designs. We note that since ordinary material properties are used in the PhC simulations, JMCFIE is used to formulate such electromagnetic problems, without needing any alternative formulation.

Among all-dielectric realizations, the first numerical comparison includes the first design in Figure 2.13 and a similar periodic structure involving square prisms. Edges of square unit cells are selected same as diameters of cylindrical unit cells. As the permittivity, $\epsilon_r = 8.8$ and $\epsilon_r = 2.0$ are used to test solution algorithms, without considering the required material properties to realize NZI behavior. The height of the rods is 2λ ($\lambda \approx 29$ mm). Discretizations with $\lambda/10$ mesh size lead to $111,456$ un-

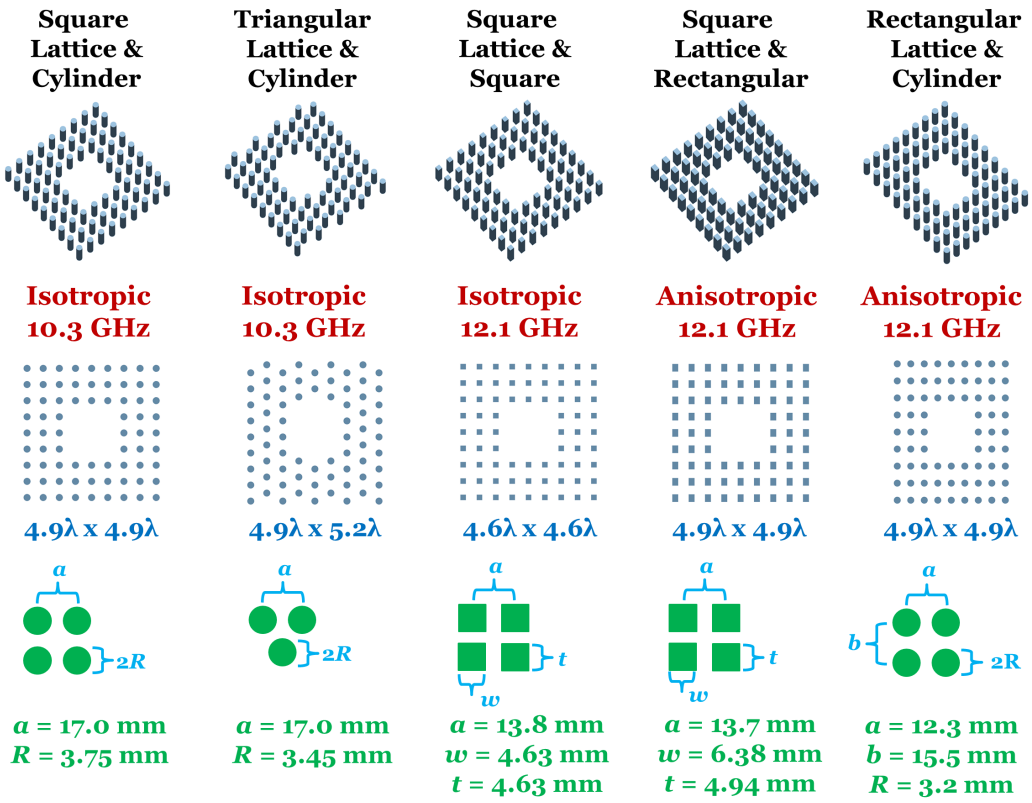

Figure 2.13: Various shell designs involving dielectric rods to be used as beam generators. Each structure is excited by a Hertzian dipole located at the center of the source region. The relative permittivity is 8.8 for the first and second designs, while it is 9.8 for the last three designs due to different impurity ratios of alumina.

knowns for the square prism array and $212,544$ unknowns for the cylinder array. Figure 2.14 depicts convergence histories for four different structures when electromagnetic problems are solved without preconditioner or with BDP. We have the following observations: (1) Higher ϵ_r values lead to high-contrast problems, which increases iteration numbers. (2) It is more straightforward to discretize a square prism rod than a cylinder rod via nearly equilateral triangles. Thus when the geometry is selected as a cylinder, the number of unknowns is increased, leading to dramatic increases in the iteration counts and solution times. (3) BDP, which is easy to implement within MLFMA, reduces iteration counts by nearly 15%. (4) In order to investigate more complicated and larger arrays, the number of iterations that directly affects solution times should be further decreased.

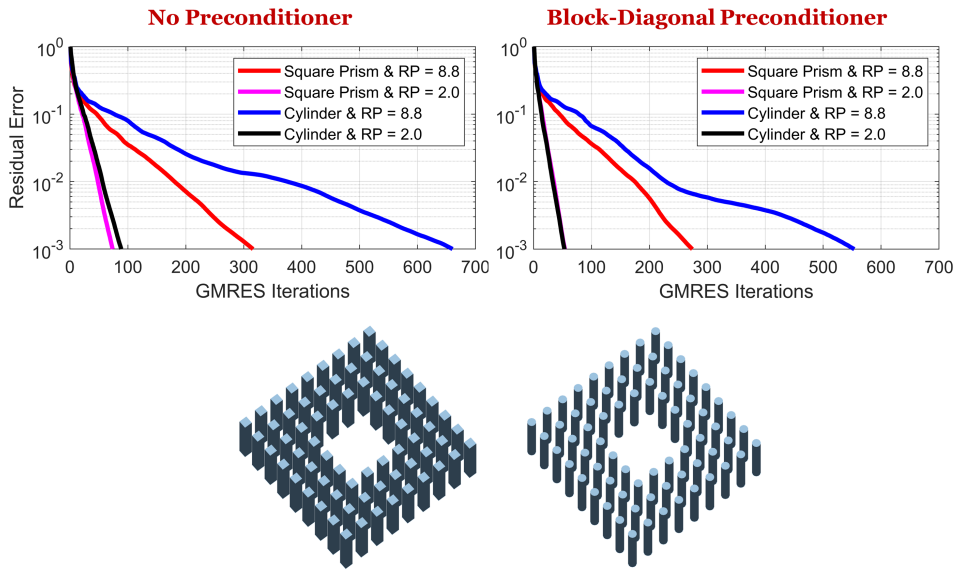

Figure 2.14: Convergence histories in numerical solutions of PhCs. Square prisms and cylindrical rods with two different relative permittivity (RP) values are used as unit cells.

Another set of numerical examples, in which we examine convergence characteristics of electromagnetic simulations of structures consisting of square prisms and cylindrical rods, is presented in Figure 2.15. In this set, iterative solutions are accelerated by three-layer preconditioning based on AMLFMA. In the figure, iterations at layer-0 (main-layer) are presented. Simulation parameters are used as given in Section 2.1.5 apart from AF of layer-1. Specifically, for this layer, AF $\in [0, 1]$ is swept for solutions of the two geometries with two different material properties. It is remarkable that the convergence of JMCFIE is significantly improved by the three-layer preconditioner in comparison to both no preconditioner and BDP cases. We note that by increasing AF of layer-1, the inner layer solutions, which are needed to carry out iterations at the main layer, need larger numbers of iterations (not seen in these graphs). In fact, very large AF values lead to longer overall solution times. Based on numerical results, AF is heuristically optimized as 0.3. This value is used for all simulations of realistic NZI models when three-layer preconditioning is employed.

As the last set of numerical examples, Figure 2.16 illustrates solution histories for 15 different electromagnetic problems involving five realistic NZI shells given in Figure

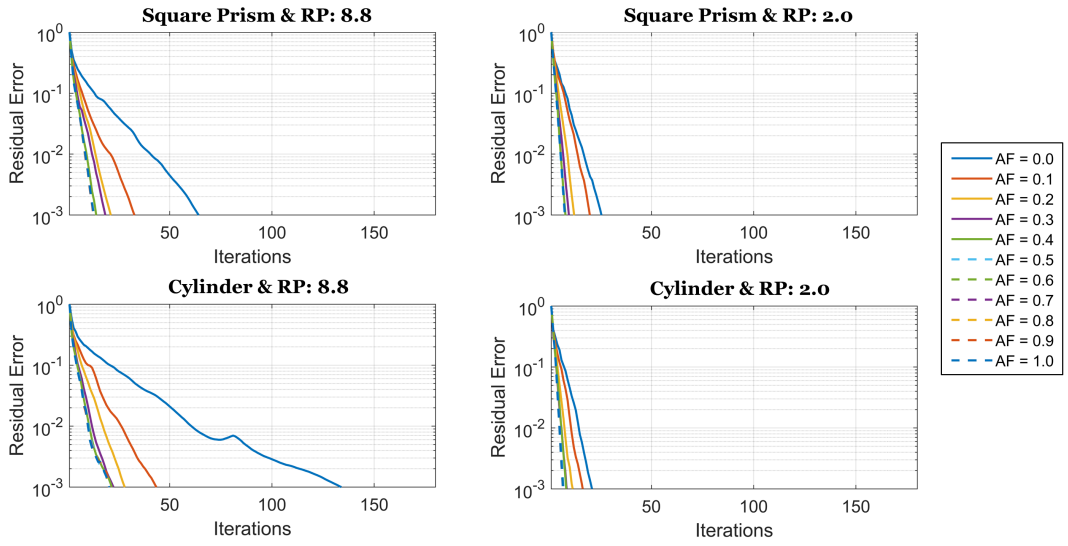

Figure 2.15: Convergence histories in numerical solutions of PhCs made of square prisms and cylinders. Iterative solutions are accelerated by the three-layer preconditioner considering various AFs for layer-1.

2.13. The target residual is set to 10^{-3}, while the three-layer mechanism is employed with the optimized parameters. The height of the rods varies from λ to 3λ, leading to numbers of unknowns in a wide range from $38,016$ to $327,456$. Since it is easier to accurately discretize a square prism than a cylinder, the third design (square prisms in a square lattice) with λ rods has the smallest number of unknowns, while the fifth design (cylindrical rods in a rectangular lattice) with 3λ rods has the largest one. For simulations of structures with λ rods, the required numbers of iterations are less than 20, except the fifth design. When the rods become longer, the problem size and the required number of iterations naturally increase. However, solutions are efficiently obtained via the three-layer preconditioner even for the shells with 3λ rods, four of which require only 22–33 iterations. The most challenging case, which is the fifth design involving 3λ rods, needs only 50 iterations.

Figure 2.17 depicts the power density distributions in the vicinity of the 15 different structures, where we observe how these designs act as NZI beam generators when they are excited simply by a Hertzian dipole. Power density values are sampled in a $100\lambda \times 100\lambda$ region in the array planes. We recall that the operating frequencies for the first two and the last three designs are 10.3 GHz and 12.1 GHz, respectively,

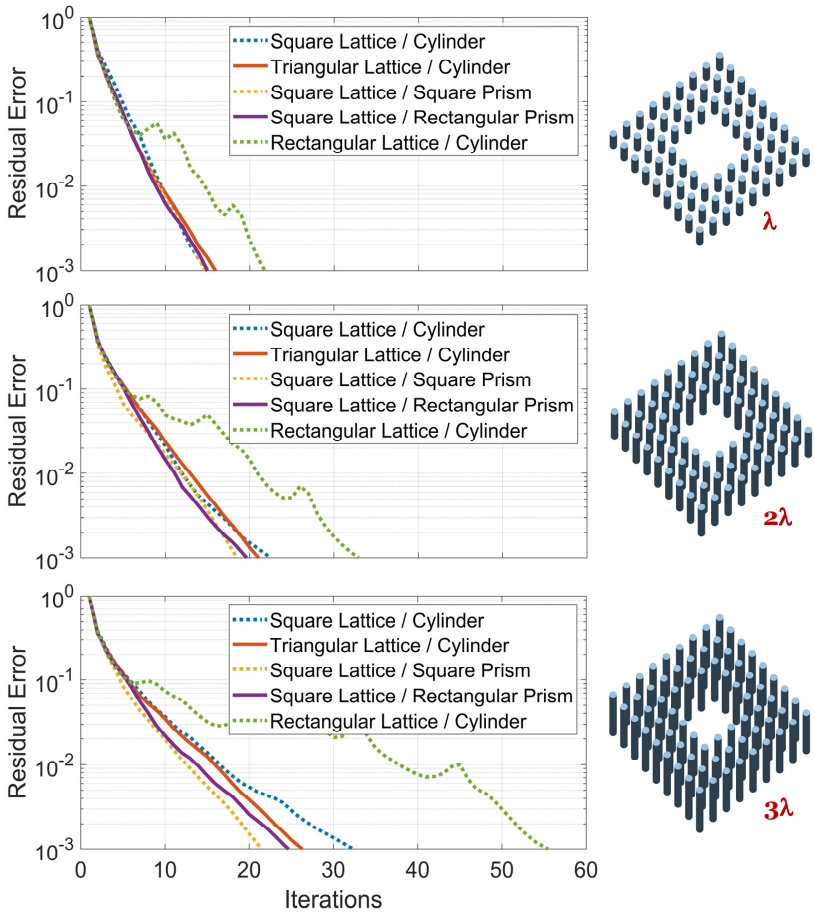

Figure 2.16: Convergence histories for the electromagnetic problems involving the shells described in Figure 2.13. The residual errors are plotted with respect to iterations at layer-0.

which correspond to Dirac-like or semi-Dirac points of PhCs. In the plots, 20 dB dynamic ranges are used to visualize power density distributions. We have the following observations.

- The first design leads to four strong beams that emerge from the flat surfaces of the represented shell, as expected due to its NZI characteristics, in addition to some minor side lobes in diagonal directions.
- With many significant side lobes, two main beams are created in the horizontal directions by the second structure when λ rods are used. Two of the four sides of this design do not represent planar surfaces; thus, these surfaces do not produce proper beams. When the rods are enlarged to 2λ and 3λ, a relatively weak

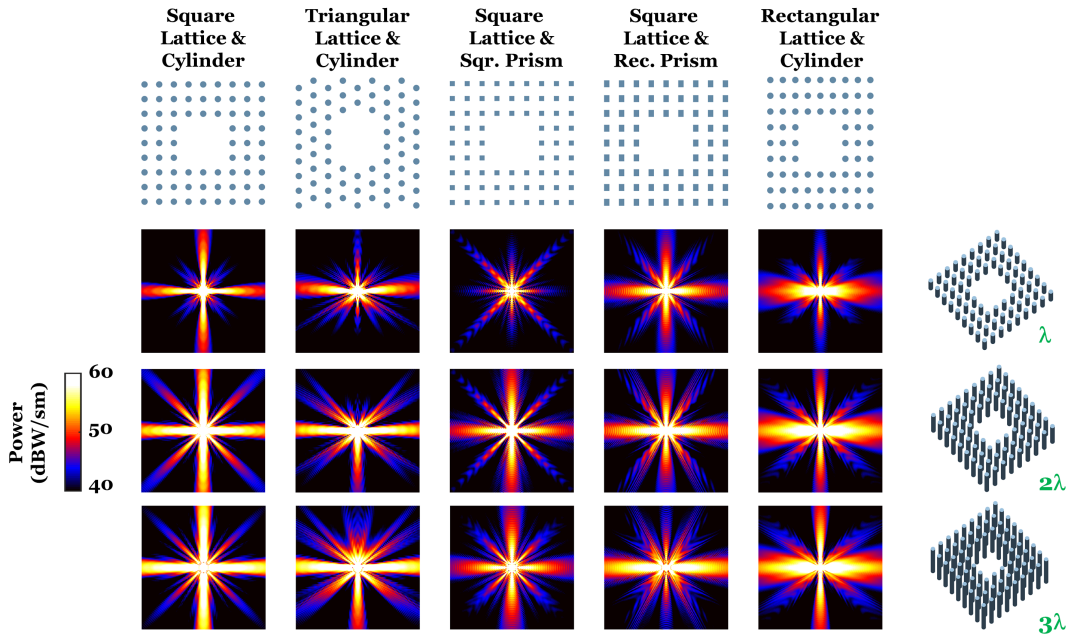

Figure 2.17: Power density distributions for the shells structures involving λ, 2λ, and 3λ rods. Each plot show the values in a $100\lambda \times 100\lambda$ region in the vicinity of the structure.

beam emerges in the vertical direction. In fact, as shown in the next chapter, such corrugations on two sides, which naturally occur for a triangular lattice, can be used to suppress undesired beams, depending on the application.

- When the third structure is used as a shell, we observe effects of unit cells, i.e., rod shapes and periodicity. This structure produces relatively weak beams. In particular, it cannot produce any major beams for λ rods. Although not shown in this thesis, further investigations on this design reveal that fine-tuned cross-sectional dimensions as 5.36×5.36 mm and periodicity as 14.1 mm lead to four clear beams, as a further verification on the sensitivity of NZI characteristics to unit cell dimensions.

- In the case of the fourth structure, four main beams, as well as four side lobes between them, are clearly visible for λ rods. One can observe that the pair of beams in the horizontal directions are slightly different from the other pair in the vertical directions due to the anisotropic characteristics of the structure.

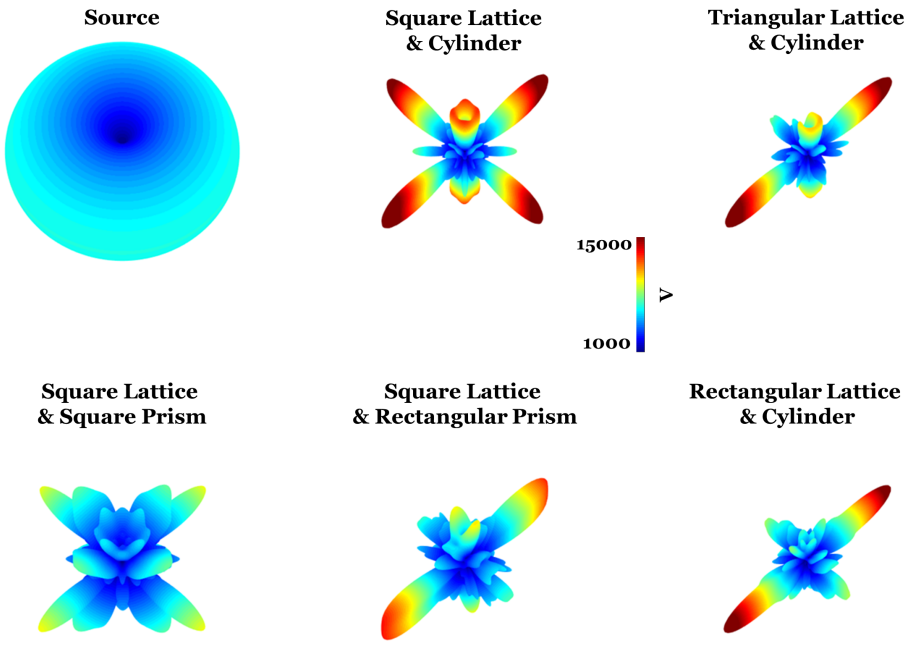

Figure 2.18: Far-zone electric field intensity results obtained for the shell structures involving 2λ rods and a z-directed Hertzian dipole as a source. Colors represent field values considering observation directions.

When the heights of the rods increased, the bidirectional pattern appears more clearly.

- Being the second structure with anisotropic properties, the fifth design leads to two sharp but minor beams in the vertical directions, while the beams in the horizontal directions are dispersed and accompanied by side lobes.

- Even though some main characteristics are maintained, we observe interesting changes in the behaviors of the designs when the rods are enlarged to 2λ and 3λ. In general, all radiations strengthened in comparison to those provided by the structures with λ rods since less power can escape from the top and bottom openings of the cavity regions, leading to increased field and density values in the array planes. For instance, considering the first design, the side lobes are combined into single beams in the diagonal directions, while the main beams still dominate the overall radiation. On the other hand, with 2λ rods, the third design generates stronger beams in the horizontal and vertical directions, in comparison to its performance with λ rods.

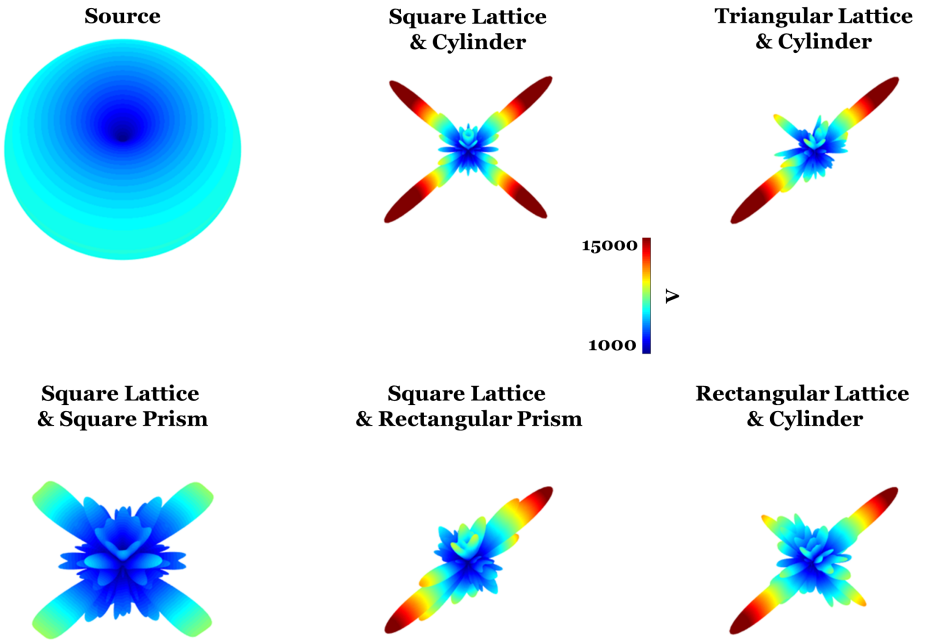

Figure 2.19: Far-zone electric field intensity results obtained for the shell structures involving 3λ rods and a z-directed Hertzian dipole as a source. Colors represent field values considering observation directions.

Since all these plots in Figure 2.17 provide information only on the two-dimensional radiation characteristics, we further consider 3D plots in Figures 2.18 and 2.19. In these complementary results, the electric field intensity values in the far zone are plotted, considering all observation directions to reveal the overall radiation characteristics of the designs. The color range is designated to represent values from 1000 V to 15000 V. We observe that in addition to main and side lobes in the array planes (shown in Figure 2.17), there are many other lobes in various directions. Considering the first design, upward and downward radiations (as the source region is not closed from above or below) that contain nulls at the poles are remarkable. Similar radiations exist for the other structures, while the main lobes are visible in all cases. The fourth and fifth designs have quite bidirectional patterns, thanks to the anisotropic natures of these structures. Finally, the relatively poor performance of the third design persists when the rods have 3λ heights.

For more quantitative comparisons, Figure 2.20 presents the far-zone electric field intensity with respect to observation angle in the array plane for each design involving

3λ rods. Considering operating frequencies given as 10.3 GHz and 12.1 GHz, the first two and the last three designs are illustrated on the left-hand side and the right-hand side, respectively. The electric field intensity values due to sources without shells are also included for comparisons. In these results, we observe that, while the third design mainly suppresses radiation to generate four beams, the others can provide intensity values well above the corresponding Hertzian dipole. The fourth design seems to be better than the fifth design, considering side-lobe levels. For the second design, it is remarkable that the radiation is effectively suppressed at $90°$, while radiation at $270°$ is still significant, so that this design may even be categorized as a tridirectional beam generator.

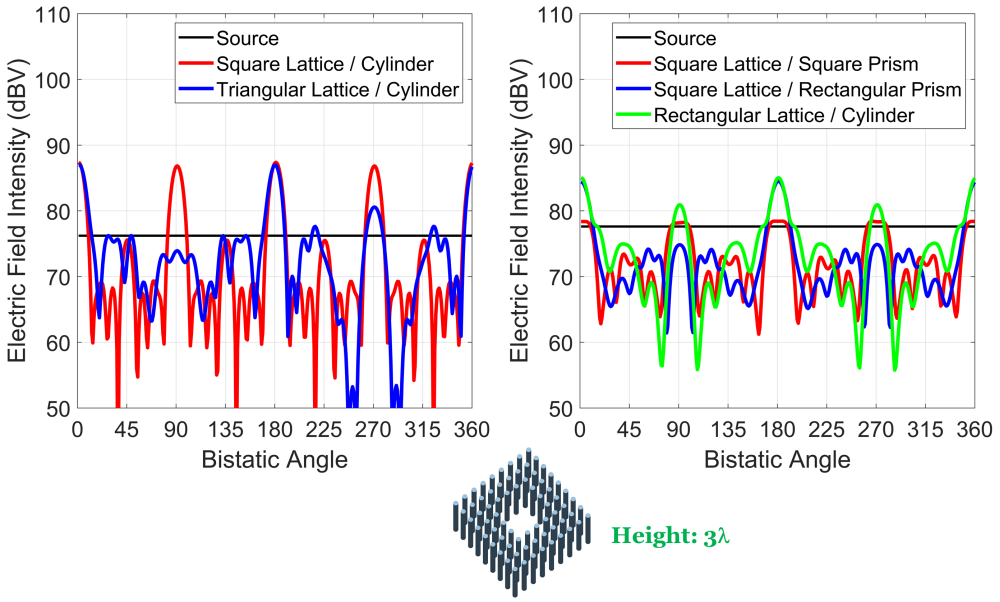

Figure 2.20: Far-zone electric field intensity results obtained for the shell structures involving 3λ rods in the azimuth plane (array plane) with respect to observation angles in degrees.

2.4 Concluding Remarks

In this section, a powerful simulation tool to conduct efficient, accurate, and stable electromagnetic analyses of NZI structures is presented. In the context of SIEs, JMCFIE and MF are used to formulate realistic and homogeneous NZI models, respectively. For homogeneous models that we enforce small ϵ_r and/or μ_r values in

simulations, low-frequency and high-contrast problems are handled with MF and AD-MLFMA. Specifically, as shown in the numerical results, MF stands out as the most reliable formulation while investigating homogeneous NZI structures having different NZI properties, i.e., EMNZ, ENZ, and MNZ. On the other side, the three-layer inner-outer scheme based on AMLFMA is used to accelerate iterative solutions of periodic arrays of high-contrast dielectric rods that mimic NZI behavior, while these structures can efficiently and accurately be formulated with the conventional JMCFIE.

Small refractive indices can be realized at intended frequencies to design NZI shells acting as efficient beam generators. Accordingly, a summary of the literature on the realization of NZI behaviors is also provided in this chapter. As exemplified via various numerical results, beam generation properties of 3D structures depend not only on cross sections and arrangements of the unit cells (rods) but also on their heights, indicating the need for full-wave computational tools to support design procedures.

CHAPTER 3

DESIGN AND SIMULATION OF NEAR-ZERO-INDEX SHELLS ACTING AS BEAM GENERATORS

In the following part of this thesis, we describe in greater detail how efficient NZI beam generator structures can be designed. First, the importance of small ϵ_r and μ_r values are examined to design beam generators, particularly considering that mismatches between free space and NZI structures can deteriorate the performances of the designed shells even for EMNZ cases. Thus, NZI cavities at the center of the shells are improved for optimal radiation properties. Second, homogenized versions are considered, in addition to actual structures, to facilitate design and analyses of alternative configurations. Third, we show that enhancement or suppression of outgoing beams can be achieved by proper modifications on the outer surfaces of the shells. Finally, thanks to the full-wave 3D electromagnetic solver, detailed sensitivity analyses of the designed shells are investigated regarding practical issues.

3.1 Introduction

In this chapter, simulations of NZI structures are performed by proper formulations and solutions algorithms developed for homogenized and periodic NZI models, as discussed in Chapter 2. Near-zone and far-zone interactions are computed with 1% maximum error; meanwhile, the target residual is set to 0.001 for iterative convergences.

Figure 3.1 presents an overview of design steps to reach multi-beam generating shells with NZI properties. After determining the maximum number of beams in target radiation patterns, the initial NZI shell model is suggested in homogeneous form according to Snell's law. Their dimensions are approximately decided considering

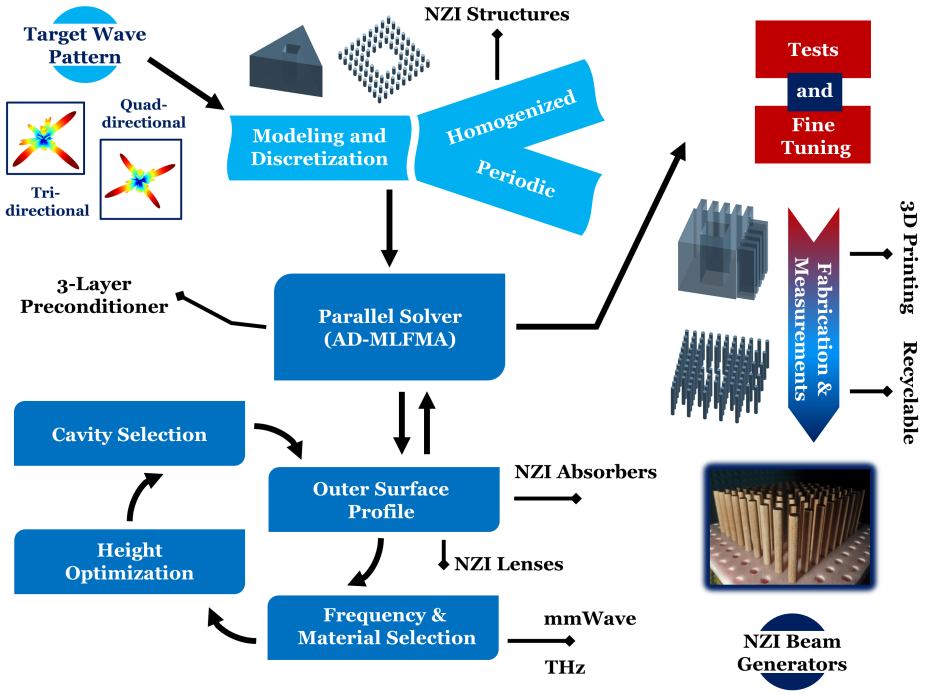

Figure 3.1: The design process of an NZI shell acting as a multi-beam generator.

effective boundaries of realistic NZI models (e.g., 9×9 rods) discussed in Section 2.2. A source region at the center is considered as an empty space so that the NZI structure is completely detached from its main source. This way, rotatable, isolated, and replaceable shell structures are obtained. Various optimization trials and parametric sweeps are employed on cavities, outer surfaces, and height values of the shells, followed by tests and fine-tuning on rod arrangements. Consequently, efficient NZI beam generators are obtained. In addition, following the fabrication of selected periodic structures, simulation and measurement results are compared to demonstrate the effectiveness of the designed structures as NZI beam generators, as detailed in the next chapter.

In Figure 3.2, various homogeneous NZI shells and their realistic models are illustrated. According to Snell's law, when electromagnetic waves leave from an NZI medium, their propagation direction is nearly parallel to the surface normal, as shown in the figure. Therefore, when the outer surfaces of an object are planar, highly directive beams can be obtained. We note that beam widths are related to the outer edge lengths of the designed shell. In particular, wide beams can be obtained with larger

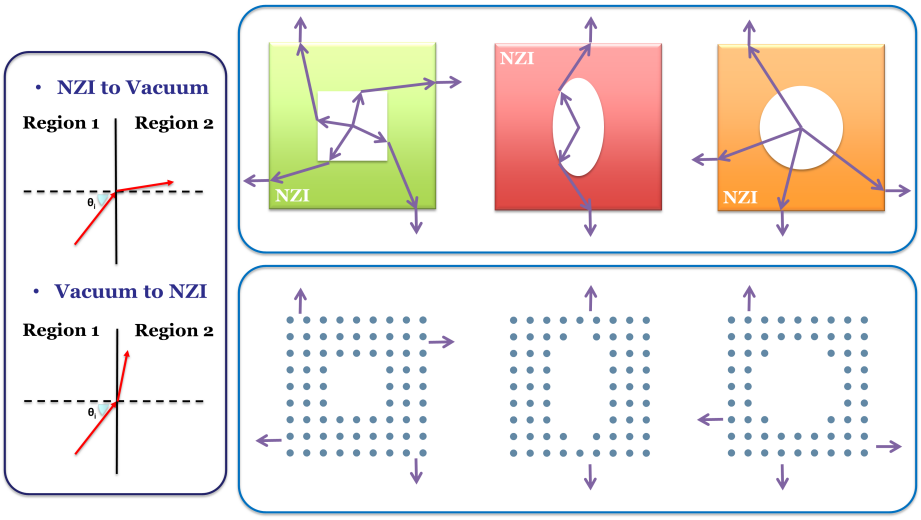

Figure 3.2: NZI shells acting as beam generators in accordance with Snell's law of refraction.

effective surface areas. For square and circular cavities, beams are created in four perpendicular directions; however, outgoing beam strengths can be different depending on the dimensions and shape of the shell. For the ellipse in Figure 3.2, considering ray optics, bidirectional radiation patterns can be observed due to the horizontal/vertical asymmetry of the cavity. The realistic models, which are also shown in Figure 3.2, can be improved by increasing the number of elements to achieve higher resolutions when mimicking homogeneous cavities, although compactness, beam widths, and extra material usage are all critical trade-offs.

As a comparison of ordinary and NZI structures under the same excitation, homogeneous cubic shells with 1.5λ outer and 0.5λ inner edges, where λ is the wavelength in vacuum, are considered in Figure 3.3. For the discretization, $\lambda/15$ triangles are used, leading to matrix equations involving $21,432$ unknowns. The shells and Hertzian dipoles at their centers are oriented in the z direction and located in vacuum. Figure 3.3 depicts field intensity and power density distributions in the cross-sectional planes for an ordinary dielectric case (ϵ_r of the shell is 4.0, while μ_r is the unity) and an NZI case (both ϵ_r and μ_r values are equal to 0.05, leading to an EMNZ material). We observe quite different electromagnetic characteristics when ordinary and NZI materials are used. The electromagnetic fields created by the dipole can easily penetrate into the structure and are reshaped by it when NZI material is used, since it matches the

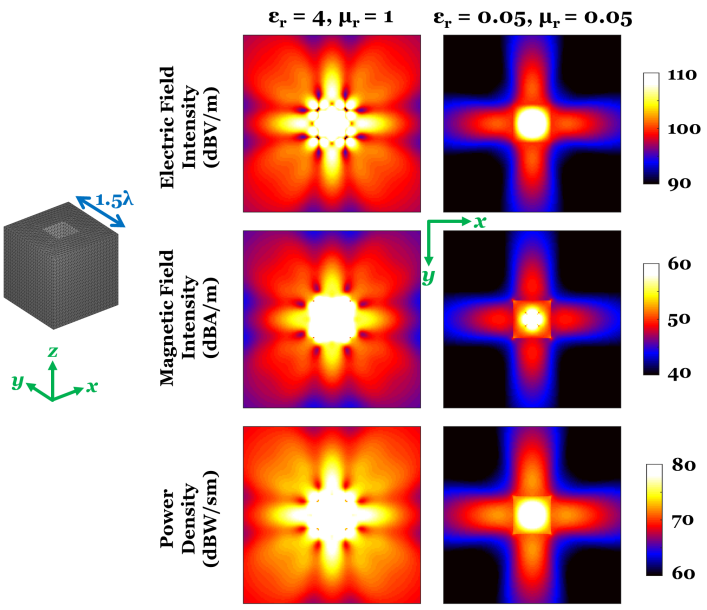

Figure 3.3: Electric field, magnetic field, and power density distributions for cubic shells with square cavities. The excitation is a Hertzian dipole located at the centers of the cavity regions. Ordinary and NZI materials are considered.

vacuum in terms of the intrinsic impedance value. Then, the NZI shell creates beams in four perpendicular directions, as opposed to the less functional pattern created by the shell with ordinary material properties.

Figure 3.4 illustrates simulation results for the geometry in Figure 3.3 when different ϵ_r and μ_r values are used. In the first row, together with EMNZ, we examine different NZI properties such as ENZ and MNZ cases, where either ϵ_r or μ_r is 2.5×10^{-4}, while the other is unity. On the other hand, the refractive index of the material is fixed to 5×10^{-3} in the second row for all NZI types. For both ENZ and MNZ cases, the vacuum region inside a shell turns into a resonator, whose efficiency depends on the dimensions of the region with respect to wavelength, as well as the material properties of the structure. Comparing power density distributions, we observe that electromagnetic characteristics do not change significantly for the MNZ and EMNZ cases. On the other hand, for the ENZ, increased mismatch between the structure and vacuum leads to weaker beams when ϵ_r is reduced to 2.5×10^{-5}. The radiation outside the shell is relatively weak in both ENZ and MNZ cases in comparison to the EMNZ case, even though beam characteristics are still observable.

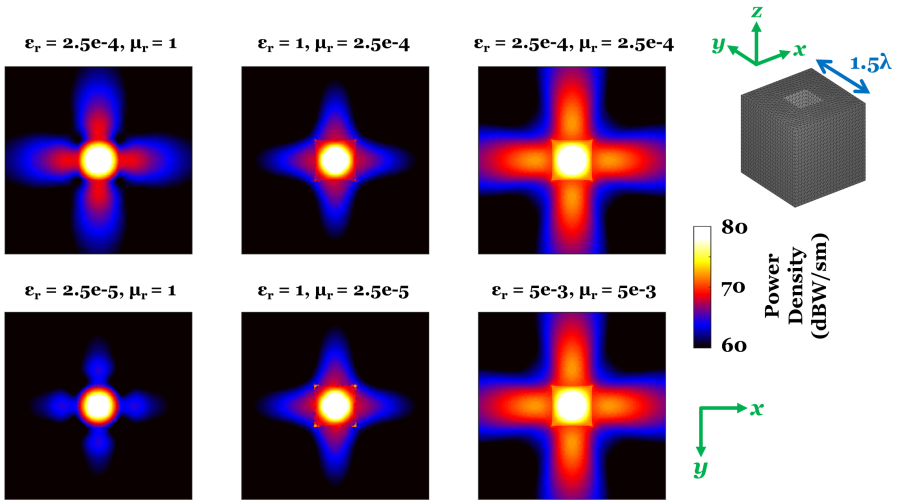

Figure 3.4: Electric field, magnetic field, and power density distributions for cubic shells with square cavities, when different refractive index values are used as shell materials. For the second row, the refractive index is fixed to 5×10^{-3}.

As presented in this thesis in more detail, electromagnetic behaviors of NZI shells, e.g., characteristics obtained via different cavity structures, differ significantly with geometric properties. Some of these characteristics, e.g., modification of phase patterns via cylindrical shells with ENZ and MNZ properties, could be predicted [25,91] without computational analyses. Alternatively, such predictions could be based on less complex tools, e.g., by solving 2D boundary value problems in cylindrical coordinates. Nevertheless, for the three-dimensional structures, whose fabrication is aimed in this thesis, electromagnetic characteristics of different geometries are difficult to formulate via basic rules. Even minor modifications on a cavity lead to dramatic changes on the response of an overall structure. Consequently, full-wave solvers employed in this study become inevitable tools to perform parametric analyses and reveal exotic behaviors of alternative structures before their realizations.

3.2 Reflection and Transmission at Interfaces Between Vacuum and Near-Zero-Index Media

Next, we focus on the reflection phenomenon at an interface between vacuum and an NZI medium with different material properties in order to understand how electromagnetic waves can effectively penetrate into an NZI medium. We consider two

specific scenarios: (1) an infinite planar boundary and (2) an infinite planar slab. It is well-known that since the intrinsic impedance can be tuned to the vacuum impedance, a matched EMNZ medium does not have any reflection under normal incidence, although ENZ and MNZ materials lead to high reflections at vacuum-NZI and NZI-vacuum interfaces. However, even for an EMNZ case, incident waves can largely be reflected under oblique illumination due to very small refractive indices.

3.2.1 Fresnel Coefficients on a NZI-Vacuum Plane Boundary

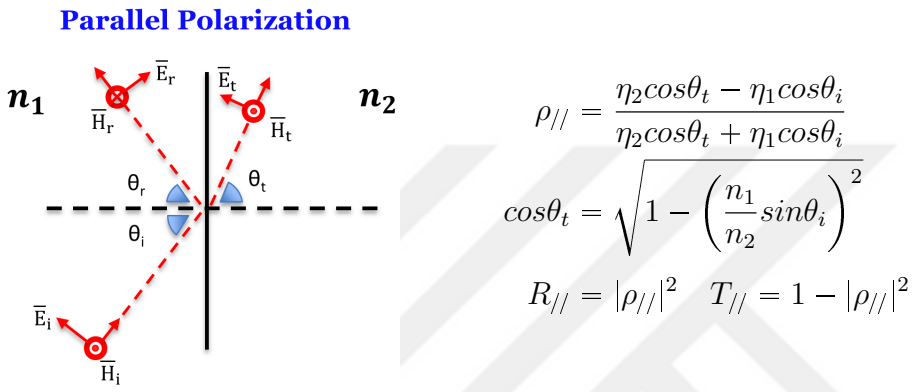

$$\rho_{//} = \frac{\eta_2 cos\theta_t - \eta_1 cos\theta_i}{\eta_2 cos\theta_t + \eta_1 cos\theta_i}$$

$$cos\theta_t = \sqrt{1 - \left(\frac{n_1}{n_2} sin\theta_i\right)^2}$$

$$R_{//} = |\rho_{//}|^2 \quad T_{//} = 1 - |\rho_{//}|^2$$

Figure 3.5: Reflectance and transmittance calculations for parallel polarization.

Firstly, we examine reflections at NZI-vacuum and vacuum-NZI planar boundaries. Considering the geometries in Figure 3.2, there are two interfaces as (1) source region (vacuum) to NZI and (2) NZI to vacuum, for a shell structure, while any boundary between two regions lies along the z direction. Although waves emerging from the main source (Hertzian dipole) illuminates the vacuum-to-NZI interface with arbitrary angles and polarizations (depending on locations on the interface), we focus on a simplified scenario with parallel polarization, as the results represent the general characteristics of the waves on such interfaces. We define the fraction of the incident power reflected from the interface as reflectance (R), and the fraction transmitted to the second medium as transmittance (T). Under an obliquely incident plane wave that has a parallel polarization, Fresnel coefficients can be calculated, as illustrated in Figure 3.5.

In Figure 3.6, reflectance and transmittance values are plotted for the first interface, i.e., when the first medium is the source region (vacuum) and the second one is NZI

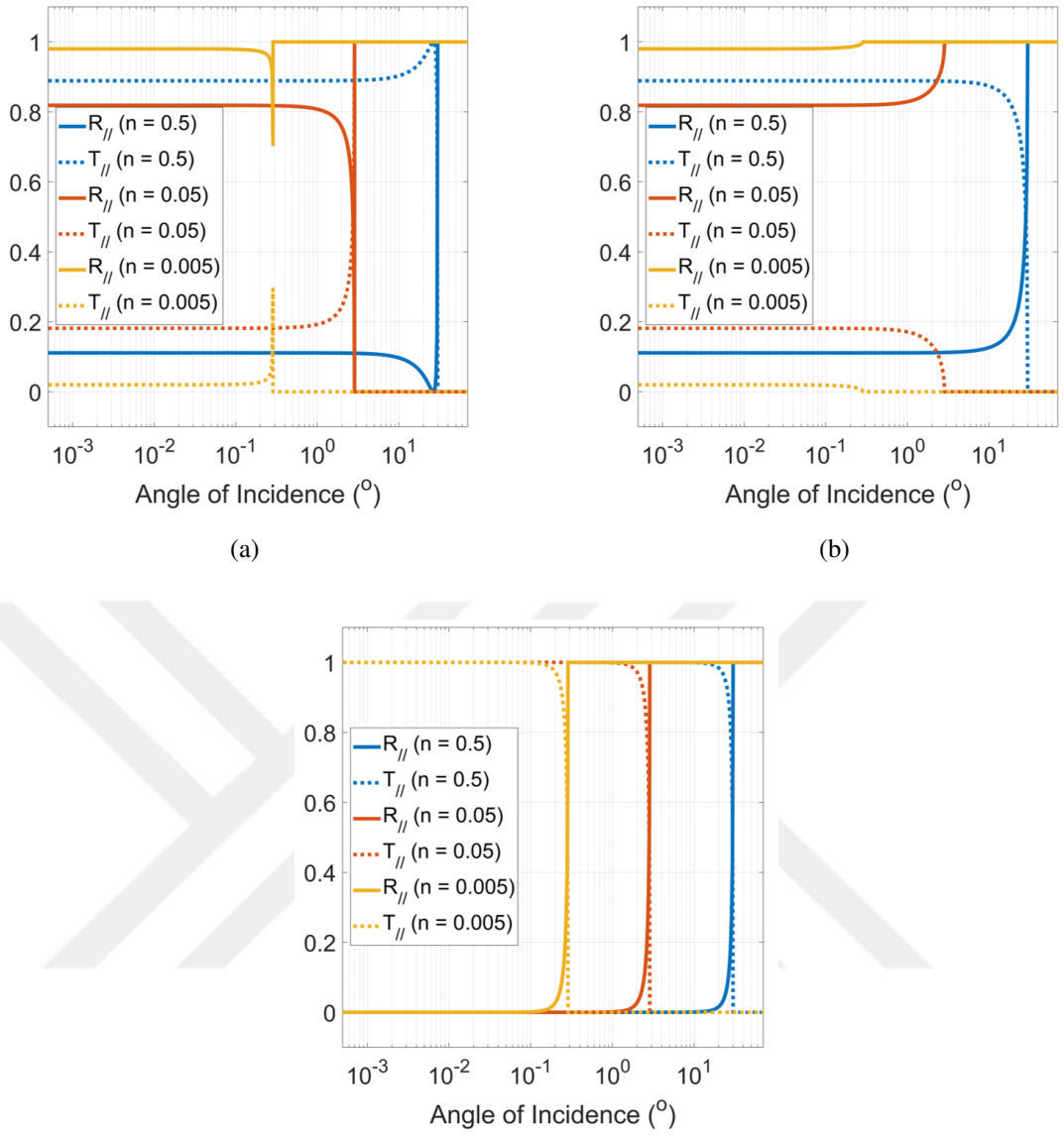

Figure 3.6: Reflectance and transmittance for plane waves obliquely incident onto boundaries from vacuum to NZI materials. ENZ (3.6a), MNZ (3.6b), and EMNZ (3.6c) cases are considered when the plane wave has parallel polarization.

medium. Different NZI properties are investigated, by assuming different refractive index values as $n \in [0.005, 0.05, 0.5]$ for the second medium. In each case, almost 100% reflectance value is observed after a critical angle. When vacuum has a much higher refractive index than the NZI medium, critical angle values become very small.

For vacuum-ENZ and vacuum-MNZ cases, transmission is relatively low due to mis-

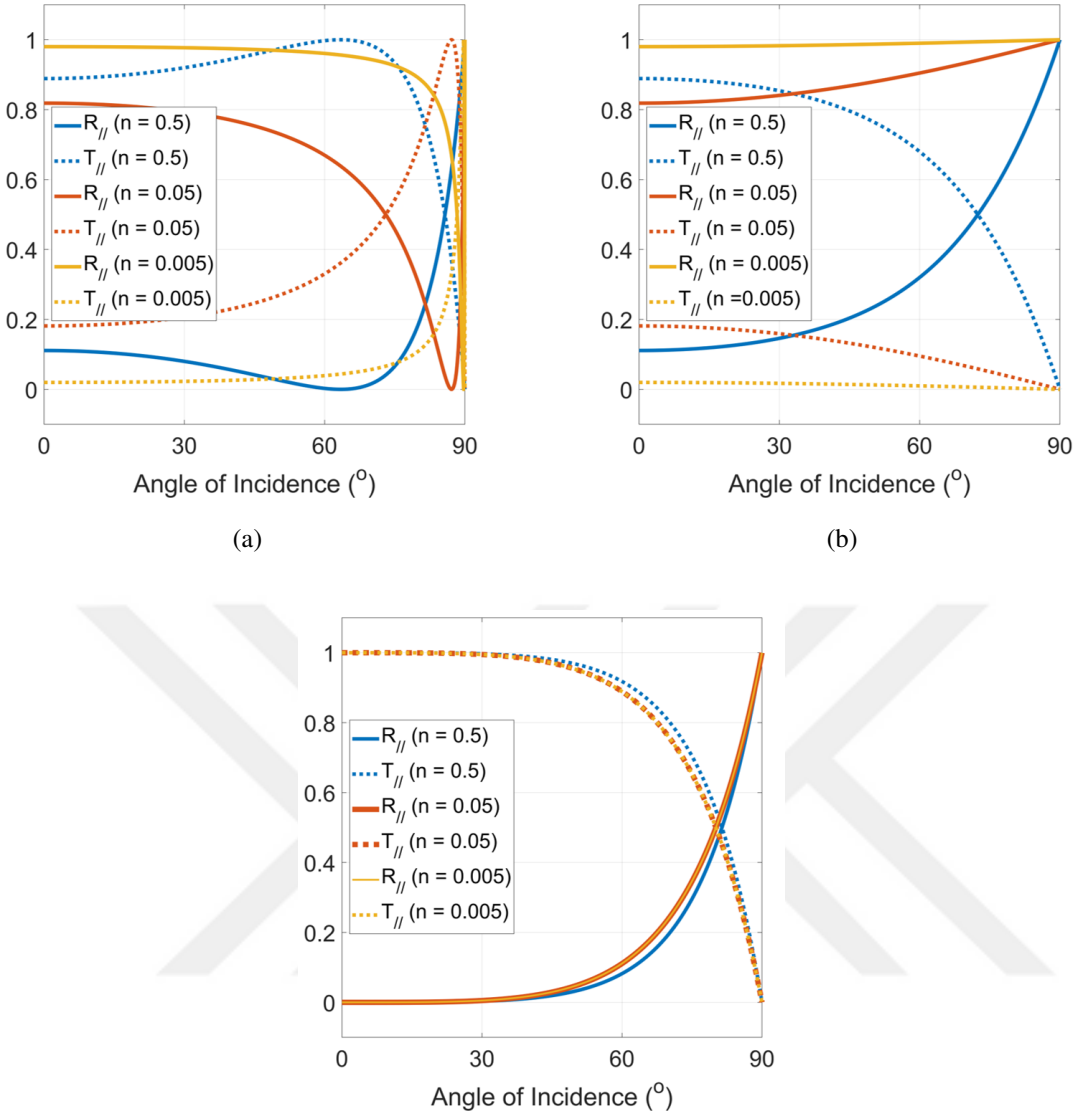

Figure 3.7: Reflectance and transmittance for plane waves obliquely incident onto boundaries from NZI materials to vacuum. ENZ (3.7a), MNZ (3.7b), and EMNZ (3.7c) cases are considered when the plane wave has parallel polarization.

match between the media, even before the critical angles. In addition, extraordinary responses for the ENZ cases can be seen in Figure 3.6a, where full (or nearly full due to discretization of the frequency) transmissions can be observed at the corresponding Brewster angles. The reason for why we observe the Brewster angle only for ENZ cases is related to the polarization. Specifically, for parallel polarization, the Brewster angle is not defined for magnetic materials; thus, we cannot observe it for MNZ cases.

In fact, if the polarization was perpendicular, Figures 3.6a and 3.6b would directly be interchanged. On the other hand, for a vacuum-EMNZ interface, full transmission occurs before the critical angle, but the transmittance value dramatically decreases, only after a few degrees for a small refractive index, even if the intrinsic impedance of the medium is perfectly matched to the vacuum impedance (nearly 377Ω). Thus, in order to design an NZI structure regardless of the NZI property, reflections are important issues that need to be analyzed and resolved for efficient operations. For instance, to overcome the high reflection problem for an EMNZ medium, transparent metasurfaces are proposed to enable efficient coupling between vacuum and NZI materials [26].

Fresnel power reflection and transmission coefficients for plane waves from NZI media to vacuum are plotted in Figure 3.7, again with respect to the angle of incidence but in a wider range. These cases represent interfaces between the outer surfaces of NZI shells and the host media (vacuum) where the shells are placed. We observe that Brewster angles exist for the ENZ cases, similar to those in Figure 3.6, while these angles approach 90° with decreasing refractive index values. We also observe that ENZ cases, in general, involve better transmission values in comparison to MNZ cases. Since the critical angle phenomenon is not observed when a medium involving incident waves has a lower refractive index, we generally observe that reflectance values are considerably decreased for all NZI cases, in comparison to vacuum-NZI cases depicted in Figure 3.6. If the material has EMNZ characteristics, a complete transmission occurs even when refractive index values approach very small values. Considering the results in Figure 3.6, we reach the conclusion that, as long as electromagnetic waves penetrate into an NZI medium, they can leave it relatively easier. Thus, effective cavities should be designed as suitable source regions of the designed shells to obtain strong beam characteristics for these structures.

3.2.2 Reflectance and Transmittance for an NZI Slab

To further investigate transmission characteristics of an NZI object, we consider a single-slab problem. It is assumed to have different NZI properties, i.e., EMNZ, ENZ, or MNZ, while separating two semi-infinite media (both vacuum) with two interfaces. These slab scenarios actually represent actual shell problems better than

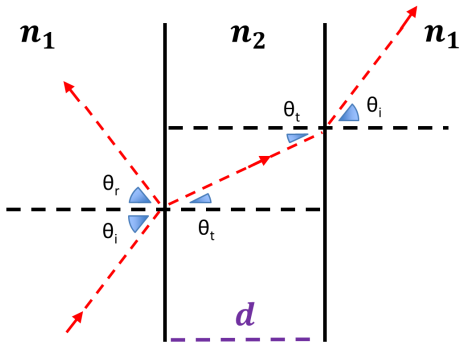

Figure 3.8: Oblique incidence into a magneto-dielectric slab.

single-interface scenarios. For a given thickness d, the reflection coefficient Γ can be calculated via matching and propagation matrices that provide solutions to multiple-interface problems [92]. The normal-incidence solution can also be extended to oblique incidence cases by substituting $e^{\pm ikz} \rightarrow e^{\pm ikzcos\theta}$, which leads to

$$\Gamma = \frac{\rho(1 - e^{i4\pi n_2 d_\lambda cos\theta_t})}{1 - \rho^2 e^{i4\pi n_2 d_\lambda cos\theta_t}} \tag{3.1}$$

$$R = |\Gamma|^2 \quad T = 1 - |\Gamma|^2 \tag{3.2}$$

$$cos\theta_t = \sqrt{1 - \left(\frac{n_1}{n_2} sin\theta_i\right)^2}, \tag{3.3}$$

where n_2 is the refractive index of the slab, $d_\lambda = d/\lambda$ is the normalized thickness of the slab, and ρ is the Fresnel reflection coefficient for a plane boundary that can be calculated for perpendicular and parallel polarizations. Another method to calculate the transmission coefficient of an NZI slab is provided in [25]. However, it only considers the ENZ case with parallel polarization, assuming unity μ_r. Thus, for thorough and consistent analyses, we consider (3.1)–(3.3) for all NZI properties.

Figure 3.9 depicts reflectance and transmittance values of an EMNZ slab with respect to slab thickness when almost normal incidence cases are considered, i.e., when $\theta_i \in [1^\circ, 2^\circ, 3^\circ]$ are selected as incident angles. Parallel polarization is assumed, similar to the earlier analyses of single-interface problems. Since the EMNZ medium $(\epsilon_r = \mu_r = 5 \times 10^{-3})$ is designed to be matched to vacuum in terms of impedance,

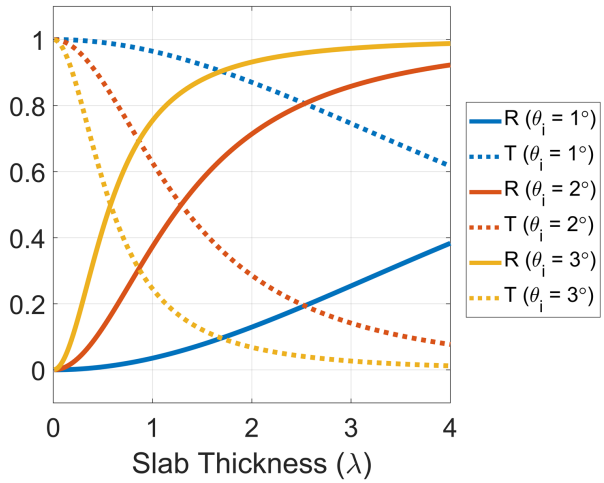

Figure 3.9: Reflectance and transmittance for an incident plane wave directed almost normally onto NZI slabs located in vacuum. EMNZ cases are considered when the plane wave has parallel polarization.

we expect zero reflection for normal incidence regardless of polarization. However, when the angle of the incident wave is slightly changed, there is a dramatic increase in reflection, which can further be enhanced by the increasing thickness of the slab.

Another set of trials involving normal incidence is illustrated in Figure 3.10, where ENZ and MNZ properties are examined since full transmission occurs for EMNZ. Refractive index values are assumed to be $n \in [0.005, 0.05, 0.5]$. In this case, we observe that, even though there is a very high mismatch between an NZI slab and vacuum when the thickness of the slab is small, the transmission value can be relatively high. Resonance-like behaviors are also are observed when the refractive index of the slab is 0.5. Specifically, for integer values of the slab thickness, full transmission is obtained. On the other hand, transmission characteristics have smooth convergences for small refractive index values.

Resonating behaviors of ENZ and MNZ slabs can be linked to the conventional PEC and PMC resonators. When the first transition is examined (vacuum-to-NZI), considering the normal incidence, Fresnel reflection coefficients for ENZ and MNZ properties are given as follows

- ENZ $[\epsilon_2 \approx 0, \mu_2 = 1]$ & $\eta_1 = \eta_0$
  $\rho \rightarrow \dfrac{\infty - \eta_1}{\infty + \eta_1} = 1 \longrightarrow$ PMC-like boundary

- MNZ $[\epsilon_2 = 1, \mu_2 \approx 0]$ & $\eta_1 = \eta_0$
  $\rho \rightarrow \dfrac{0 - \eta_1}{0 + \eta_1} = -1 \longrightarrow$ PEC-like boundary

On the other side, when the second transition is examined (NZI-to-vacuum), reflection coefficients for ENZ and MNZ properties can be found as follows

- ENZ $[\epsilon_1 \approx 0, \mu_1 = 1]$ & $\eta_2 = \eta_0$
  $\rho \rightarrow \dfrac{\eta_2 - \infty}{\eta_2 + \infty} = -1 \longrightarrow$ PEC-like boundary

- MNZ $[\epsilon_1 = 1, \mu_1 \approx 0]$ & $\eta_2 = \eta_0$
  $\rho \rightarrow \dfrac{\eta_2 - 0}{\eta_2 + 0} = 1 \longrightarrow$ PMC-like boundary

We observe that PEC-like and PMC-like states are interchanged for (1) different NZI properties and (2) opposite transitions.

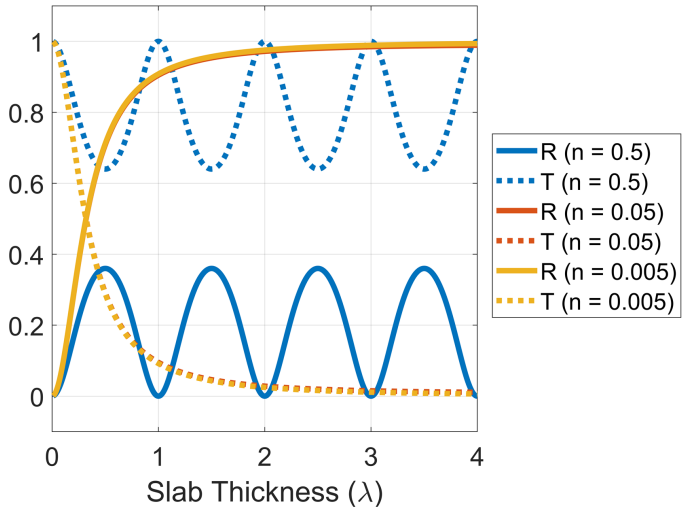

Figure 3.10: Reflectance and transmittance for an incident plane wave directed onto an NZI slab in vacuum. ENZ and MNZ cases (with exactly same results) are considered when the plane wave has normal incidence.

In summary, this section has attempted to provide reflection and transmission characteristics of NZI media located in free space by using two different models. Even

though NZI structures show highly reflective behaviors, as long as effective cavities are designed at the source regions of NZI shells, strong beam characteristics can be obtained since electromagnetic waves can leave from an NZI medium relatively easily and be reshaped by it. In the next section that follows, an effective index prediction method will be presented so that material and dimension arrangements of the realized NZI shell structures can be easily configured.

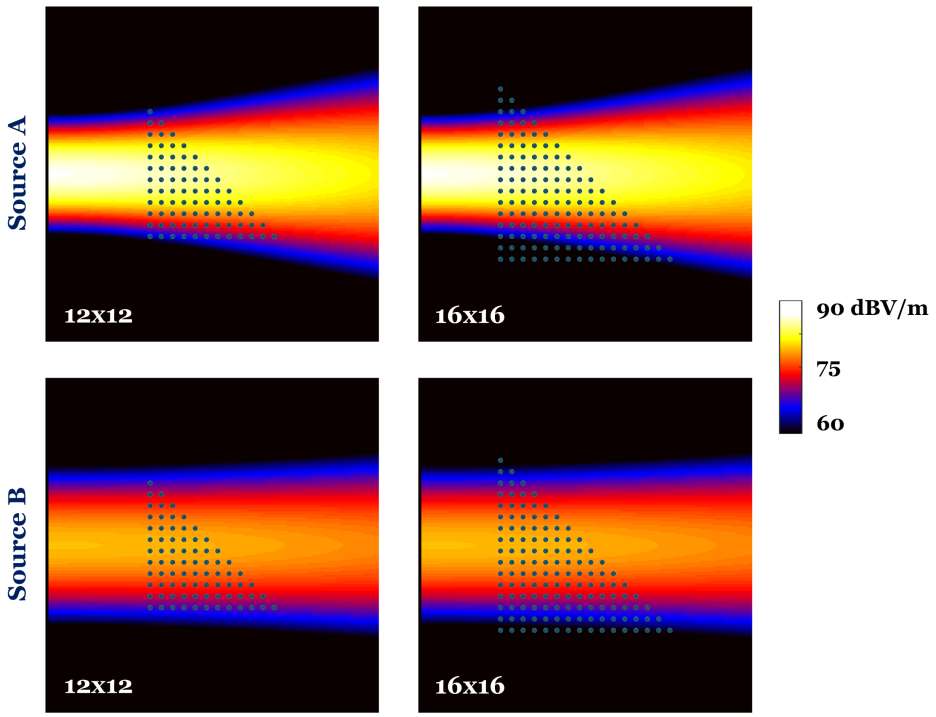

Figure 3.11: Dielectric rods arranged in 12×12 and 16×16 grids to create triangular prisms. Two CSP illuminations that have different beam widths are used in the simulations. Electric field intensity values are plotted only for the sources (incident fields), without any interaction with the rods.

3.3 Effective Index Prediction

Small refractive indices can be reached by relatively simple arrangements of unit cells as long as geometric and material properties are selected carefully, as shown in Section 2.2. In order to investigate effects of rod dimensions and material properties on effective refractive indices of the periodic structures, we develop a test setup based on arrays of dielectric rods that are arranged to create triangular prisms located in

vacuum, which is illustrated in Figure 3.11. Specifically, near-zone electric field intensity distributions are used to extract effective refractive index values, as discussed below. For this purpose, edge detection and Hough line transform are applied to field images. In particular, 78 and 136 identical rods are used in 12×12 and 16×16 grids, respectively, such that the overall structures can be used for the refraction of incoming waves depending on the effective medium parameters induced by the rods.

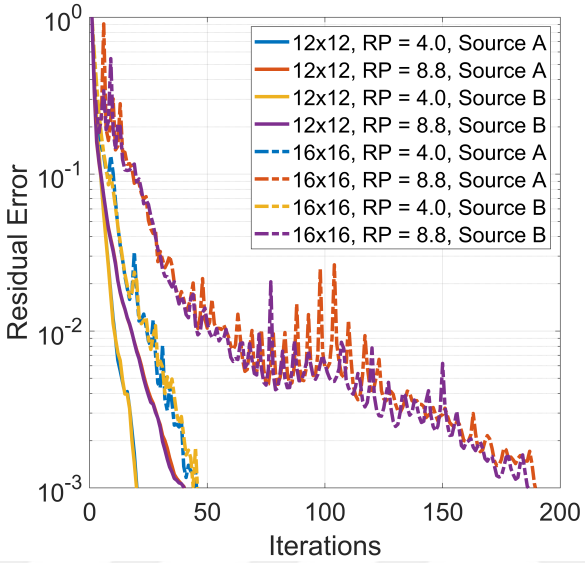

Figure 3.12: Convergence histories in numerical solutions of eight different problems involving triangular prisms made of dielectric rods. Each solution takes less than 10 hours using 16 cores.

Arrangements of cylindrical rods in a square lattice, as depicted in Figure 2.13, are used to achieve effective NZI characteristics, i.e., EMNZ behavior. Considering realistic simulations, the rods must have finite lengths, while the selection seems to be less restricted in comparison to other parameters. To suppress end effects that may deteriorate the performances of the prisms, we choose sufficiently long rods, i.e., 8.74 cm that corresponds to 3λ, where λ is the wavelength in vacuum. With the given dimensions, 12×12 and 16×16 grids cover 19.45 cm $\times$ 19.45 cm ($\approx 6.7\lambda \times 6.7\lambda$) and 26.25 cm $\times$ 26.25 cm ($\approx 9\lambda \times 9\lambda$) areas, respectively.

The grids are located in the x-y plane, while the beams are positioned symmetrically in the y (vertical) and z (along rods) axes. Two different CSP beams are used, namely Source A and Source B, as also depicted in Figure 3.11 together with the prisms.

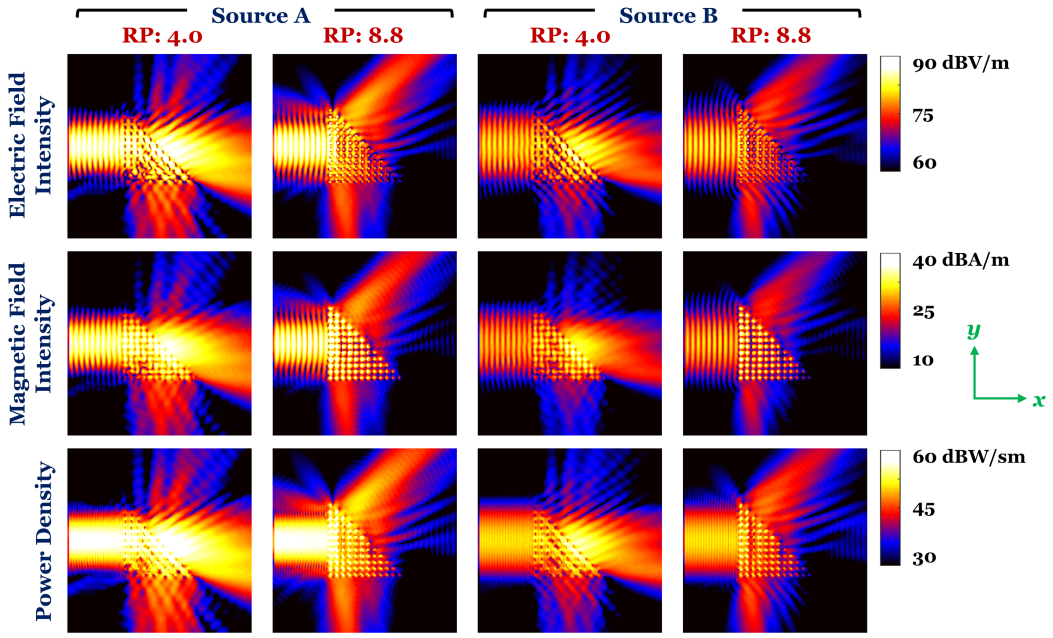

Figure 3.13: Near-zone field intensity and power density distributions when Source A and Source B are used to illuminate the 12×12 grid of dielectric rods possessing two different relative permittivity values.

CSP beams propagate in the x direction and illuminate prisms from the left-hand side. The complex positions of the associated Hertzian dipoles, whose imaginary location determines the beam width and expansion rate, are different. Source A has a smaller beam width in comparison to Source B when they emerge, while it expands faster as propagation occurs. Thus, these sources interact differently with the prisms.

Figure 3.12 presents iterative convergence histories. Considering two grids (12×12 and 16×16), two ϵ_r values (8.8 and 4.0), and two sources (Source A and Source B), a total of eight different simulations are performed. For each solution, the residual error of the main solver (layer-0) is plotted with respect to FGMRES iterations. Problems become more challenging when the number of rods is increased or higher ϵ_r values are used. On the other hand, source types do not significantly affect iterative convergences.

Figure 3.13 depicts near-zone electric field intensity, magnetic field intensity, and power density distributions obtained for the smaller prism structure (12×12 grid).

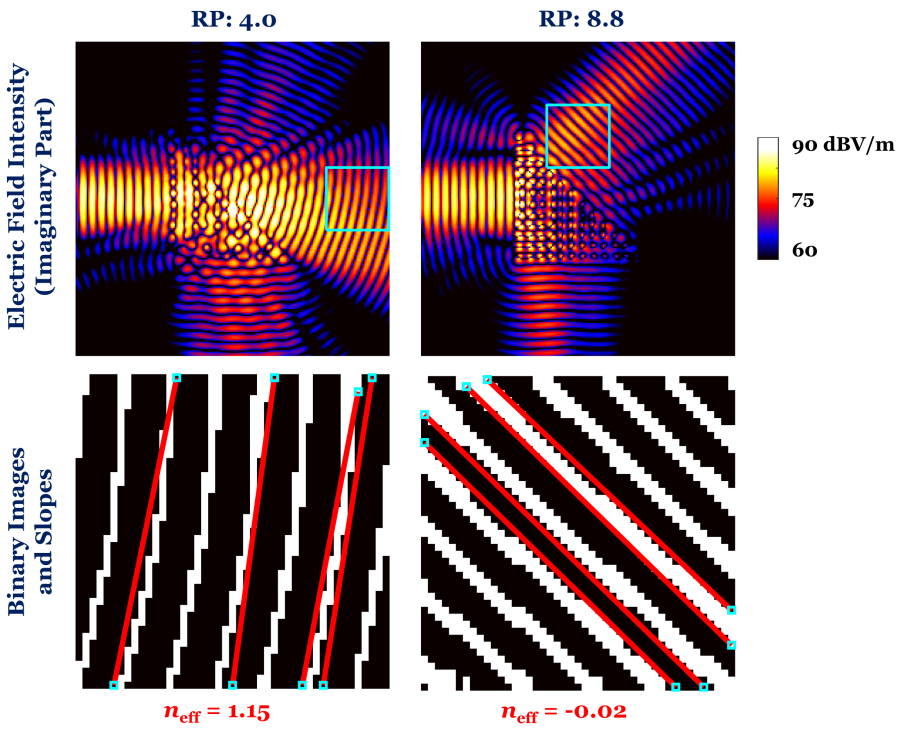

Figure 3.14: Imaginary part of the electric field intensity for the 12×12 grid when the relative permittivity of the rods is 4.0 (left) and 8.8 (right). Only Source A is considered for the excitation.

Although there are different responses with respect to different sources, ϵ_r of the rods determines the main features. When it is 8.8, the NZI behavior of the prism can be observed. After the beam enters the prism, it leaves in two main directions, both of which are perpendicular to the hypothetical (oblique and bottom) surfaces. The oscillatory patterns on the left-hand side of the prism indicate that there are also reflected waves, which may be caused by direct (from the left surface) and secondary (from the internal surfaces) reflections. On the other hand, when ϵ_r is 4.0, we observe quite an ordinary behavior. In addition to scattered waves towards many directions, the main beam occurs in a downward direction, i.e., as expected when a wave passes from a high-index region to a low-index region.

In Figure 3.14, we focus on oscillation patterns of the waves considering the imaginary part of the electric field intensity. In each case, a frame shown as a cyan square is automatically placed to a region at the right-hand side of the effective hypotenuse of the prism, based on the conformity of consecutive peaks with the wavelength. Next,

the values inside the frame are converted into a binary image. This allows us to employ Hough line transform for line fitting. As can be seen in Figure 3.14, red lines are automatically created for each image. Finally, the mean of slope values of the generated lines provides reliable information on the direction of the wave. Since we arranged rods as an isosceles right-angled triangle on the cross-sectional plane, the effective refractive index can be found as

$$n_{\text{eff}} = \frac{\sin\left(45^\circ - \alpha\right)}{\sin\left(45^\circ\right)}, \tag{3.4}$$

where α is the mean value of the generated lines' normals with respect to the horizontal axis. Using this procedure, we compute the effective refractive indices as -0.02 and 1.15, respectively, when ϵ_r of the rods is 8.8 and 4.0. Consequently, in addition to the interpretation of the visual data, we quantitatively verify the NZI behavior of the structure when ϵ_r is 8.8.

Figures 3.15 and 3.16 present the results for the larger prism structure using 16×16

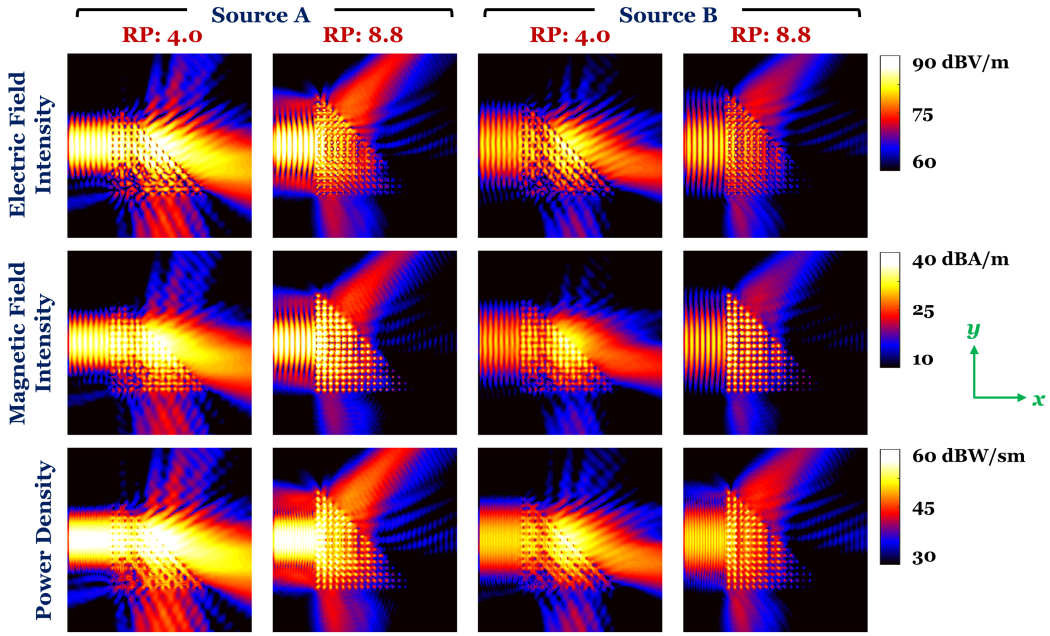

Figure 3.15: Near-zone field intensity and power density distributions when Source A and Source B are used to illuminate the 16×16 grid of dielectric rods possessing two different relative permittivity values.

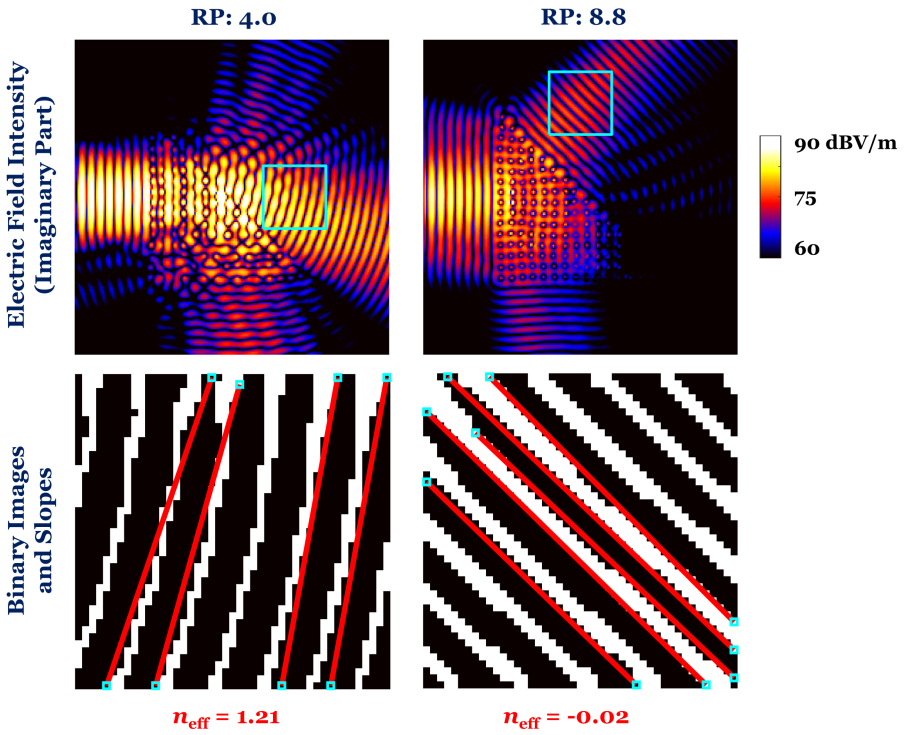

Figure 3.16: Imaginary part of electric field intensity for the 16×16 grid when the relative permittivity of the rods is 4.0 (left) and 8.8 (right). Only Source A is considered for the excitation.

grid. In Figure 3.15, there can be seen many visible differences due to the increased number of rods considering Figure 3.13; however, the main characteristics are preserved. The imaginary part of the electric field intensity, binary images, and Hough lines are illustrated in Figure 3.16. Considering the slopes, the effective refractive indices are computed as -0.02 and 1.21, respectively, when ϵ_r of the rods is 8.8 and 4.0.

We finally investigate the far-zone radiation patterns, as depicted in Figures 3.17 and 3.18, when the prisms are excited via Source A and Source B, respectively. Considering the results for Source A, we observe four major beams for both smaller and larger prism structures, whether ϵ_r of the rods is 4.0 or 8.8. When ϵ_r is 4.0, the main lobe occurs in accordance with ordinary refraction, while three other beams are created due to reflections. On the other side, when ϵ_r is 8.8, a large beam is generated perpendicular to the oblique surface of the prism as a result of its NZI behavior. We also

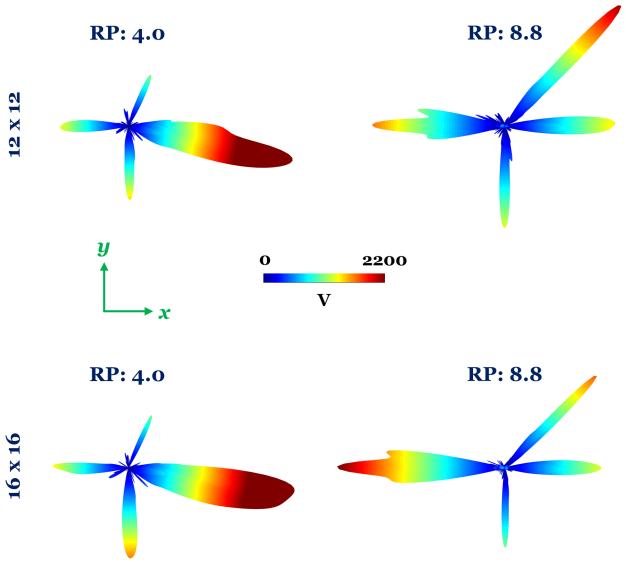

Figure 3.17: Far-zone electric field intensities obtained when Source A is used to illuminate two different grids of dielectric rods possessing two different relative permittivity values.

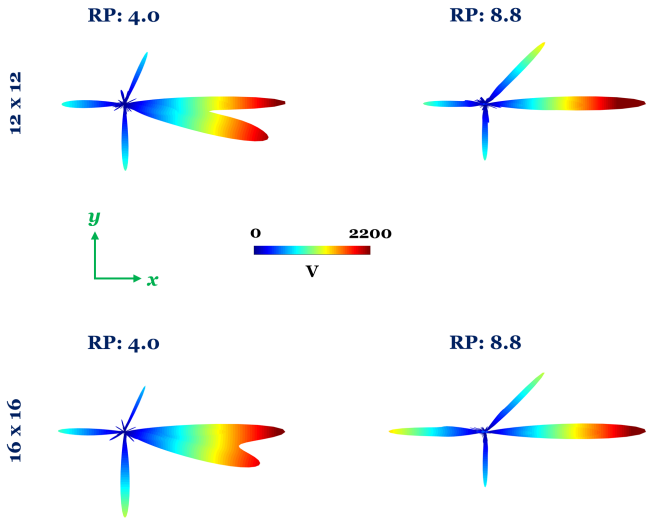

Figure 3.18: Far-zone electric field intensities obtained when Source B is used to illuminate two different grids of dielectric rods possessing two different relative permittivity values.

note that these patterns of NZI prisms involve forward-directed beams due to portions of incoming waves that do not interact with the prisms, as well as larger back-directed beams. NZI prisms are expected to demonstrate EMNZ behavior, while the effective intrinsic impedance of them is not considered in these simulations. Hence, investigation of reflected waves may provide further information on possible differences between the effective permittivity and effective permeability, which causes mismatches with vacuum. Considering the results obtained for Source B, we observe that the forward-directed beams are visible also for the ordinary cases, while they are even stronger for the NZI structures. Using larger prisms would possibly reduce these beams; but, the results still demonstrate the NZI characteristics of the prisms with rods having 8.8 relative permittivity, in contrast to the ordinary characteristics when ϵ_r is 4.0.

3.4 Improving NZI Shell Structures with Efficient Cavities

NZI structures typically suffer from high reflections due to mismatches between vacuum and the NZI media. Even for a matched EMNZ structure, full reflections can be observed under oblique incidence, as discussed. On the other hand, as long as electromagnetic waves penetrate into an NZI medium, they emerge outside relatively easily, and strong beams can be obtained owing to NZI characteristics. Therefore, considering the shell geometries in Figure 3.2, effective cavities should be designed as efficient source regions to generate strong beams. We note that, in this context, the terms cavity, source, and hole regions are used interchangeably to define the innermost regions of the shells where we put isotropic sources.

In order to design effective cavities, firstly, we consider homogenized models, where $5\lambda \times 5\lambda \times 5\lambda$ cubic shells with different cavities are investigated (λ is the wavelength in the host medium). In particular, square, circular, triangular, and elliptical cavities with various dimensions are examined. Initial geometries and sizes are chosen according to effective boundaries of the realized NZI models (9×9 grids, 3×3 of them are removed from the center). Besides, refractive indices of the shells are fixed to 5×10^{-3}, which corresponds to $(\epsilon_r, \mu_r) = (2.5 \times 10^{-5}, 1)$ for ENZ, $(\epsilon_r, \mu_r) = (1, 2.5 \times 10^{-5})$ for MNZ, and $(\epsilon_r, \mu_r) = (5 \times 10^{-3}, 5 \times 10^{-3})$ for EMNZ. MF is used to formulate all such electromagnetic problems with homogeneous bodies.

3.4.1 Homogenized NZI Shells

In Figure 3.19, cubic shells involving square cavities of different sizes are investigated when a Hertzian dipole (oriented in the z direction) is used at the center of the shells as the primary source. Power density distributions are given in $100\lambda \times 100\lambda$ frames in the x-y plane, as well as the values of the far-zone electric field intensity with respect to the observation angle in degrees in the same plane. Different NZI properties are considered as EMNZ, ENZ, and MNZ. We observe that cavity dimensions are extremely crucial to achieve high-quality beams. For EMNZ cases (Figure 3.7a), cavities with 1.9λ and 2λ edge sizes provide intended beam qualities; however, beam generation ability diminishes dramatically for 2.1λ edge size. We also note that 2λ edge size provides stronger beams even though the cavity with 1.9λ edge sizes leads to lower side lobes. In ENZ cases (Figure 3.7b), the best response is achieved for the cavity with 2.1λ edge size in terms of both side-lobe levels and beam strengths. Nevertheless, wider beams are obtained, which leads to lower directivity values in comparison to the EMNZ cases. On the other side, the shells with the same dimensions but MNZ properties (Figure 3.7c) provide relatively low-quality beams since the orientation of the primary source is not suitable for MNZ shells (e.g., considering the existence of the Brewster angle). We also note that, if the primary source was changed into a magnetic current (a Hertzian dipole is an electric current), the results for the ENZ and MNZ cases would be interchanged. In other words, MNZ shells would have better performances in terms of beam generation when magnetic-type sources, such as loop antennas, are used.

To further investigate the operating principles of the shells, we focus on source regions in Figure 3.20. Electric field intensity, magnetic field intensity, and power density distributions are given in this figure, while the dynamic ranges of the colors are readjusted to distinguish the values in the source regions. For each NZI property, 2λ and 2.1λ square cavities are examined. We observe that (i) brighter (stronger) intensity and density values are obtained when the best beam qualities are observed, regardless of the NZI property, (ii) resonating characteristics of the cavities are crucial to generate strong beams, and (iii) resonance conditions are not trivial to be derived without computational simulations.

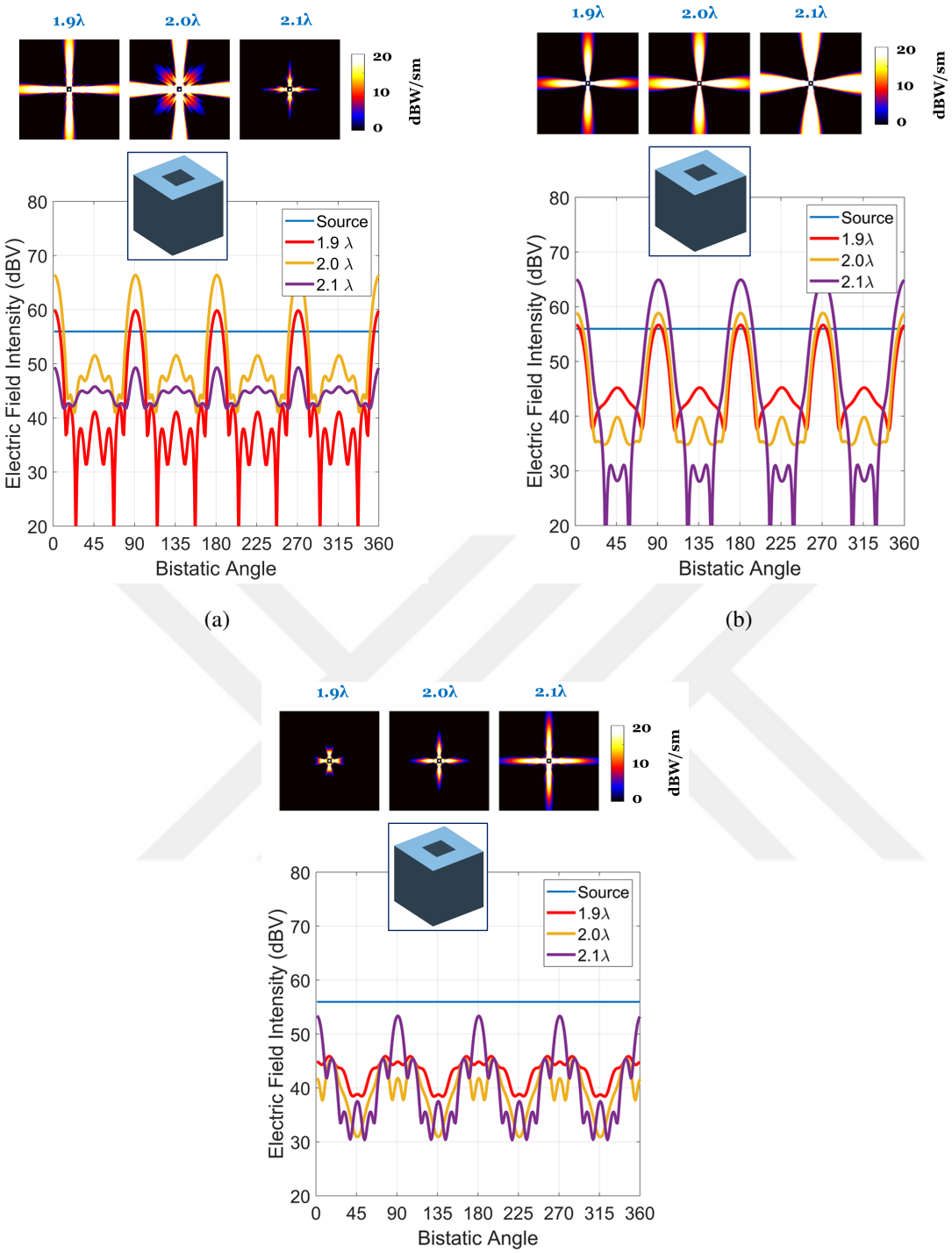

Figure 3.19: Results for homogenized models of cubic shells with square cavities of different sizes. EMNZ (3.7a) , ENZ (3.7b) and MNZ (3.7c) cases are considered.

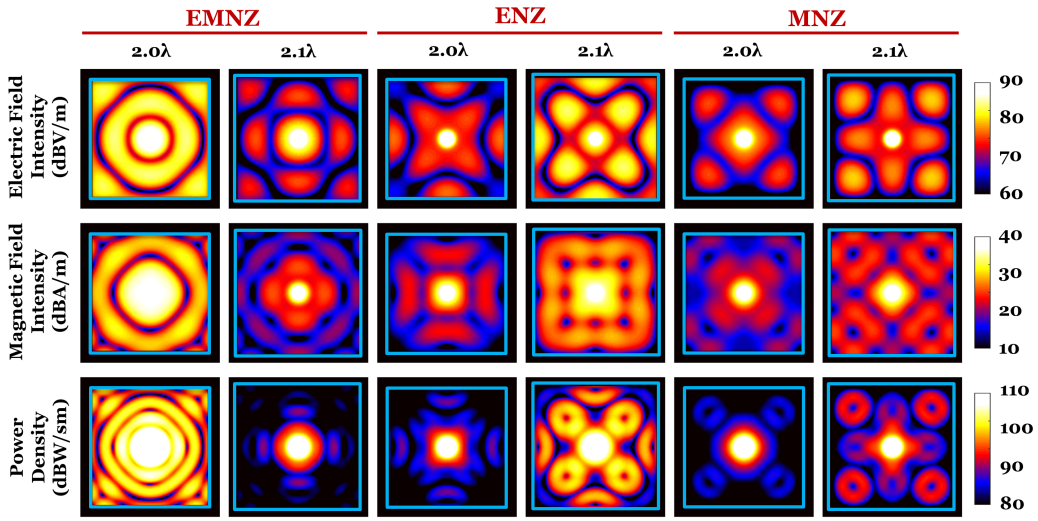

Figure 3.20: Near-zone field intensity and power density distributions when square cavities of different sizes when source regions are considered. These cavities correspond to the source regions of the shell structures.

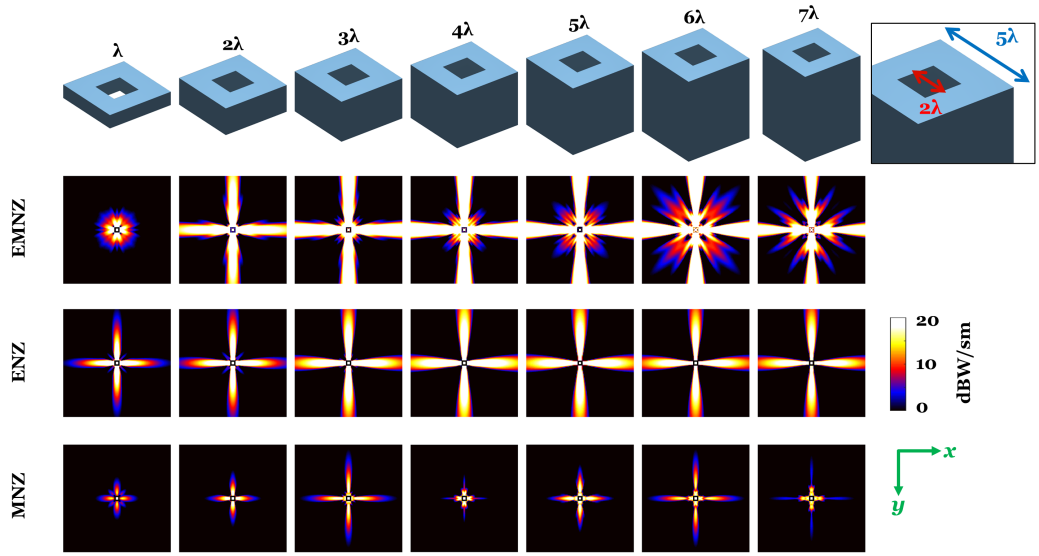

Figure 3.21: Height sweep for shell structures with a fixed cross section (2λ square cavity) and different NZI properties. Power density distributions are given in a $100\lambda \times 100\lambda$ frame in each case.

Figure 3.21 presents the results for homogenized shells with 2λ square cavities and different NZI properties. In these comparisons, the cross section is fixed to $5\lambda \times 5\lambda$, whereas the height changes from λ to 7λ. We observe that neither very short nor very

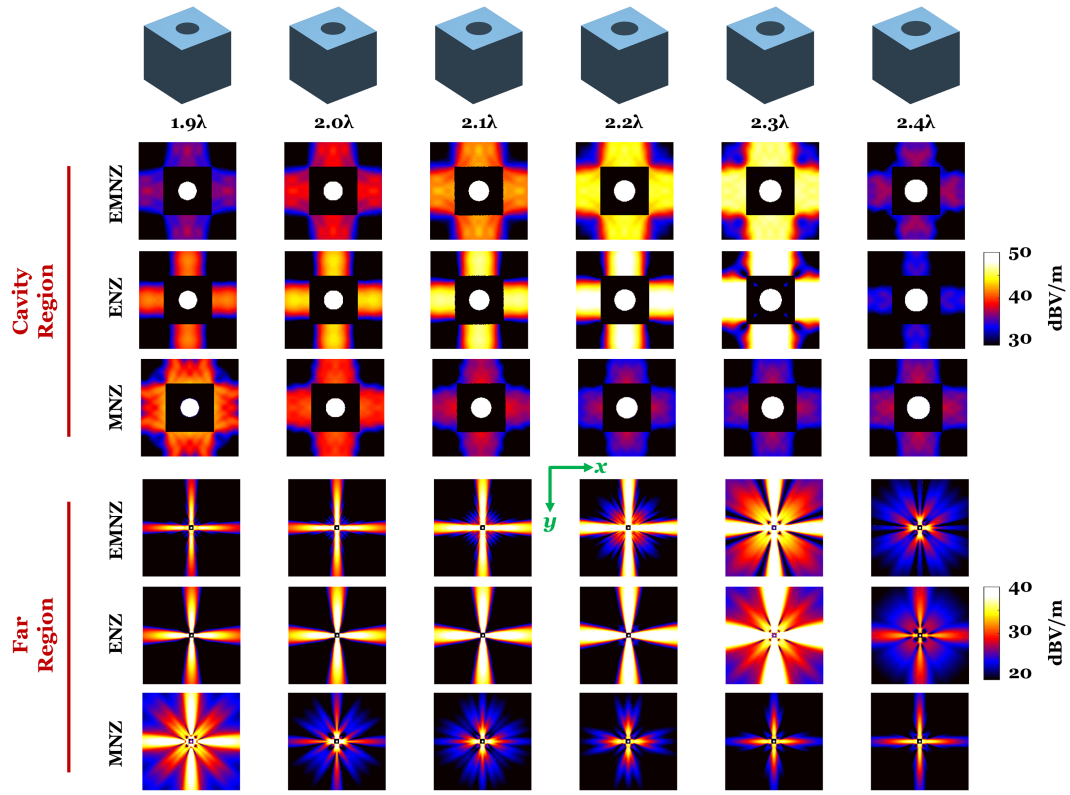

Figure 3.22: Electric field intensity distributions for homogenized models of cubic shells with circular cavities of different sizes. Cavity regions on $5\lambda \times 5\lambda$ frames and far regions on $100\lambda \times 100\lambda$ frames are investigated for EMNZ, ENZ, and MNZ cases.

long shells provide the desired radiation characteristics (e.g., four precise beams). For EMNZ cases, after 2λ height, beams can clearly be observed, whereas side lobes become significant as the height is increased. For ENZ cases, even λ height is enough to observe four clear beams. Although there are not remarkable side lobes, beam strengths decrease (leading to slightly darker colors) after 5λ height. On the other side, for MNZ cases, there is a periodic response, i.e., beam strengths increase at 3λ and 6λ, while it generally has the worst response among NZI cases.

Next, we consider cubic shells with circular cavities of different diameters from 1.9λ to 2.4λ. Figure 3.22 presents near-zone electric field intensity distributions when EMNZ, ENZ, and MNZ cases are considered with the same refractive indices (5×10^{-3}). In order to simulate such structures, matrices involving $112,014$ to $249,960$ unknowns are iteratively solved via AD-MLFMA. Once again, after we

reach solutions by achieving preset residual values, near-zone fields are computed in $5\lambda \times 5\lambda$ (cavity region) and $100\lambda \times 100\lambda$ (far region) frames. Considering the results in both frames, the cubic shell with 2.3λ-diameter cavity has the best quality beams for EMNZ and ENZ cases, while 1.9λ diameter provides the best response among MNZ cases. Similar to the square cavity, the size of the cavity is critical to observe four clear beams when using circular cavities. Figure 3.23 further depicts far-zone electric field intensities in the x-y plane to demonstrate the quality of the beams for the MNZ shell involving a circular cavity with 1.9λ diameter, as well as for the ENZ and EMNZ shells involving circular cavities with 2.3λ diameters.

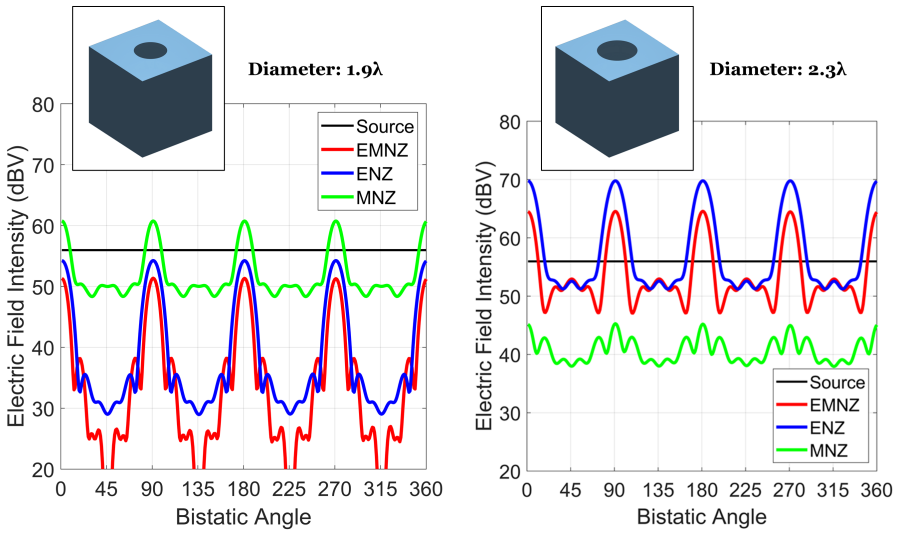

Figure 3.23: Far-zone electric field intensities obtained when cubic shells with circular cavities having 1.9λ and 2.3λ diameters are investigated for EMNZ, ENZ, and MNZ cases.

In Figure 3.24, source regions of the structures with circular cavities are examined considering the best cases, i.e., 1.9λ diameter for MNZ, and 2.3λ diameter for ENZ and EMNZ. Electric field intensity, magnetic field intensity, and power density distributions are given in the figure. Our observations are generally same as those for square cavities, whereas, for circular cavities, strong resonances can also be seen for MNZ shells, e.g., for 1.9λ diameter. Considering 2.3λ diameter, the ENZ shells have the strongest resonances, which is consistent with the fact that they provide four clear beams. We note that, compared to the square cavities, the resonance patterns differentiate into circular ones, as expected.

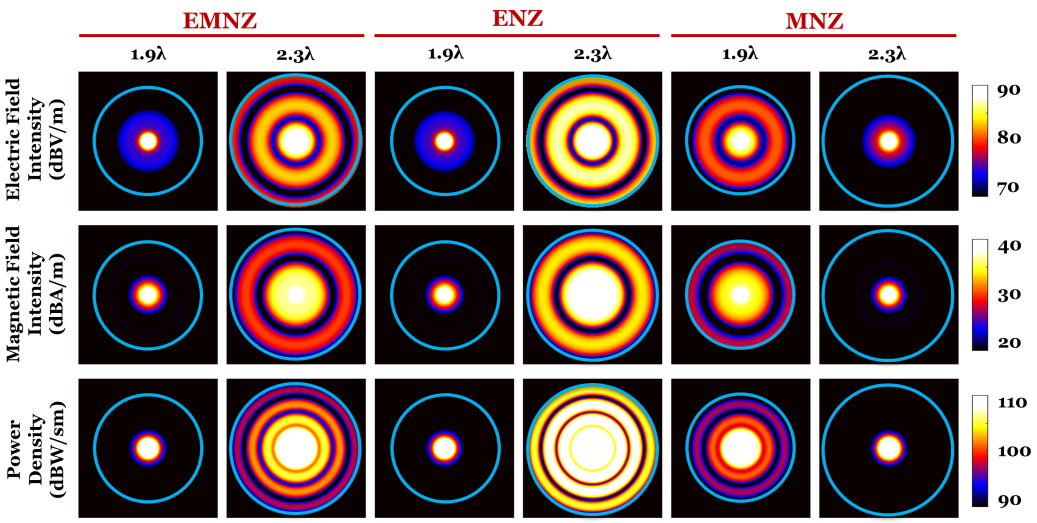

Figure 3.24: Near-zone field intensity and power density distributions when circular cavities of different sizes are considered. These cavities correspond to the source regions of the shell structures.

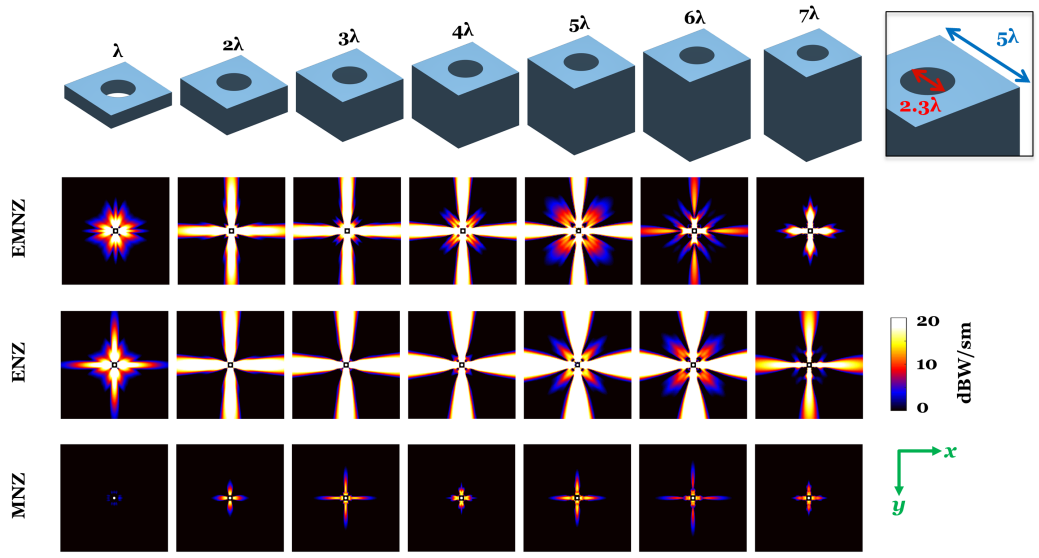

Figure 3.25: Height sweep for shell structures with a fixed cross section (2.3λ-diameter circular cavity) and different NZI properties. Power density distributions are given in a $100\lambda \times 100\lambda$ frame in each case.

Effect of the height on the beam-generation characteristics of the structures with circular cavities having 2.3λ diameters are examined in Figure 3.25. Power density distributions in $100\lambda \times 100\lambda$ frames (x-y plane) are given for different NZI proper-

ties. Height values are swept from λ to 7λ, while the cubic shells possess a fixed $5\lambda \times 5\lambda$ cross section. We have the following observations: (1) Only for ENZ cases, beams can emerge from outer surfaces of the cubic shell with λ height. (2) Above 5λ and 6λ heights, beam qualities significantly drop for the EMNZ and ENZ cases, respectively. (3) Side lobes are more significant for circular cavities in comparison to square cavities (particularly for ENZ). (4) MNZ shells cannot provide high-quality beams, while the diameters of the cavities can be changed to obtain a better beam generation, as shown in the previous results. (5) Height values are quite critical to obtain beams with desirable qualities.

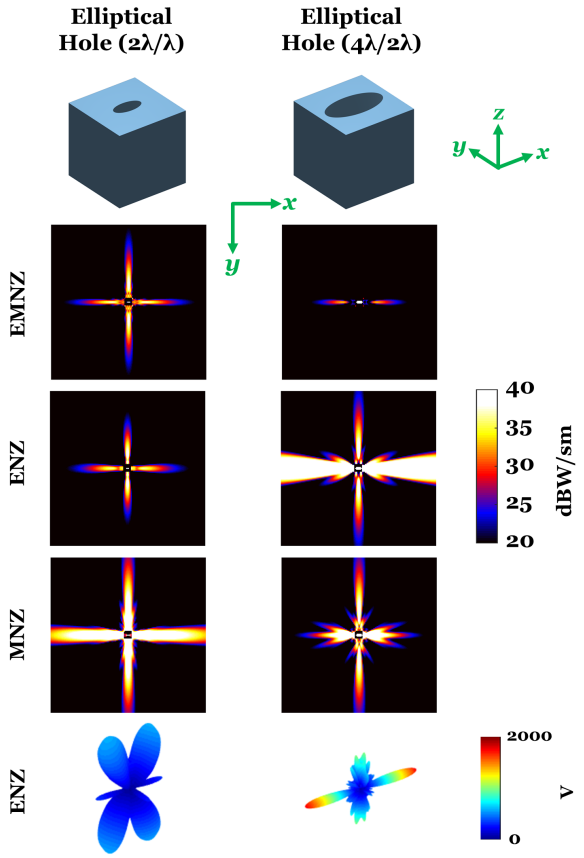

Figure 3.26: Near-zone power distributions and far-zone electric field intensity results for homogenized models of cubic shells with elliptical cavities of different sizes. In near-zone plots, $100\lambda \times 100\lambda$ frames are investigated for EMNZ, ENZ, and MNZ cases.

When a cavity is elliptical, considering Snell's law, NZI shell structures can provide bidirectional radiation due to the asymmetry. Accordingly, in Figure 3.26, we

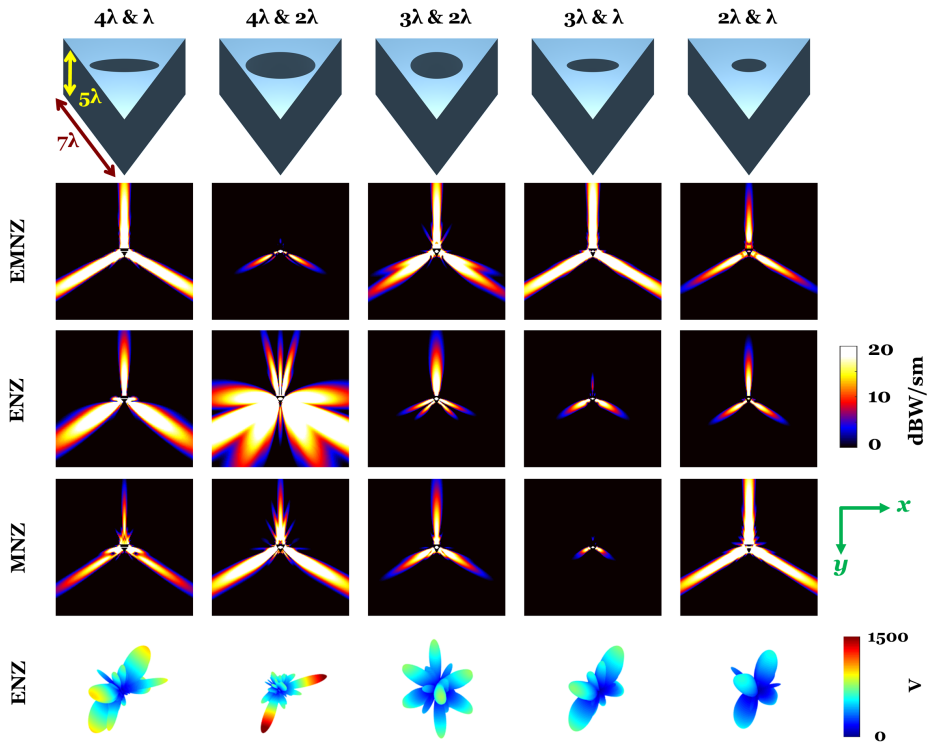

Figure 3.27: Near-zone power distributions and far-zone electric field intensity results for homogenized models of triangular prism shells with elliptical cavities of different sizes. In near-zone plots, $100\lambda \times 100\lambda$ frames are investigated for EMNZ, ENZ, and MNZ cases.

demonstrate NZI cubic shells involving elliptical holes with different major/minor axes values. Power density distributions are provided in the x-y plane for EMNZ, ENZ, and MNZ cases, as usual. We observe that the electromagnetic characteristics are heavily dependent on both dimensions and NZI specifications for elliptical holes. In particular, the ENZ cubic shell with 4λ major and 2λ minor axes values, leads to the best bidirectional pattern with maximum radiations in opposite directions. At the bottom of the figure, 3D far-zone electric field intensity results are given to further investigate ENZ shells. The plots show that the desired radiation pattern is successfully achieved with the $4\lambda\&2\lambda$ elliptical cavity. Undesired radiations towards top and bottom directions due to the highly reflective nature of the NZI structures are also visible in these plots, while suppressions of these radiations are not considered (hence, they are irrelevant) in these examples.

As shown in Figure 3.27, other than cubic shells whose overall cross sections are square, different polygons, such as triangular prisms, can be used to achieve alternative beam configurations. In these particular examples, similar to cubic shells, elliptical cavities are used to create source regions. Considering equilateral triangles with 7λ edges in the x-y plane, center of each ellipse is placed at the center of gravity of the corresponding triangle. The height of the shells is fixed as 5λ. A parametric investigation on the values of the major and minor axes of the ellipses is conducted. While the cubic shells considered so far create beams in four perpendicular directions, triangular prisms provide three beams considering their outer surfaces. Based on the selection of major/minor axes of the elliptical holes, tridirectional and nearly bidirectional beams separated by 120° are clearly obtained. Hence, regardless of the overall cross section of a shell, such as square or triangular, high-quality beams can be reached via proper cavities, as proved by $4\lambda\&2\lambda$ elliptical extraction for both cubes and triangular prisms with ENZ properties. Moreover, Figure 3.28 depicts computational experiments when $4\lambda\&\lambda$ elliptical extractions are performed on EMNZ, ENZ, and MNZ triangular prisms. The results demonstrate that elliptical holes can efficiently be used on EMNZ shells to obtain nearly bidirectional responses. Highly directive beams can be obtained, in addition to suppressions as high as 40 dB at the edges of the shell. The third beam at 270° angle has a 3 dB lower peak value than the other two beams. In addition, there is a little shift at angular locations of the main beams, which should be at 150° and 30° angles, since the elliptical hole does not lie perpendicular to the outer surfaces of the triangular prism. In general, 3D far-field results in Figure 3.27 and Figure 3.28 show that, depending on the NZI characteristics and dimensions, quite large fields are directed towards intended directions, while this is not guaranteed. Although we obtain the intended beam characteristics in the x-y plane (two-dimensional results) for all NZI properties, the material selection becomes critical to reach clear beams with low side-lobe levels.

Finally, Figure 3.29 presents the effects of different holes (cavities) and structures (outer geometries) on the beam generation feature. Eight shells with three NZI properties are investigated, which leads to a total of 24 simulations. The optimized dimensions are set for square and circular holes as obtained in Figures 3.19 and 3.22, respectively, when the EMNZ property is considered. Specifically, edge sizes of the

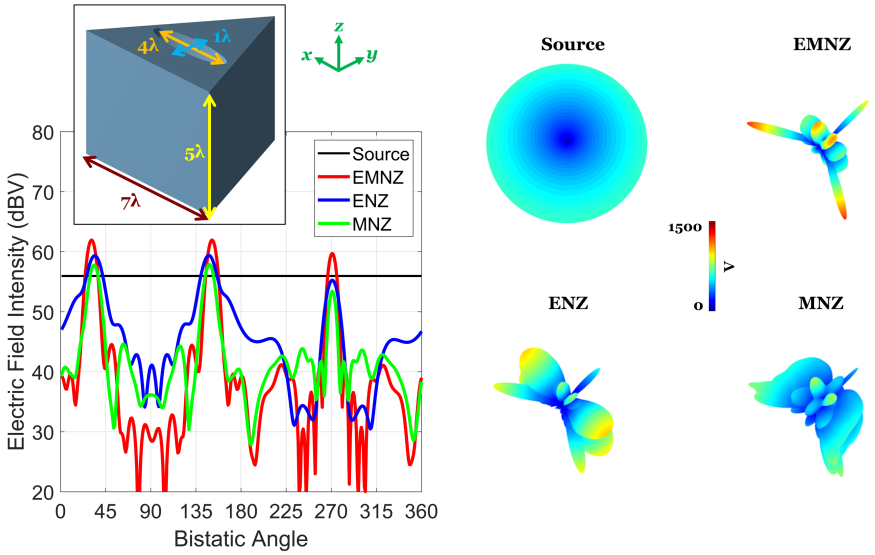

Figure 3.28: 3D and two-dimensional far-zone electric field intensities for triangular prism shells having 4λ major and λ minor axes. EMNZ, ENZ, and MNZ shells are considered.

square holes are 2λ, while the diameters of the circular holes are 2.3λ. Cylindrical and square outer surfaces have 5λ diameters and edge lengths, respectively. Triangular prisms in Figure 3.29b have 10λ edge lengths, while triangular hole (cavity) edge lengths are 3λ. All cavities are placed at the center of gravity of the prisms considering cross-sectional geometries, while the center of gravity of triangular holes and prisms overlap. The number of unknowns to simulate the corresponding electromagnetic problems are between $91,258$ (geometry 2) and $171,378$ (geometry 5). Considering Figure 3.29, we have the following observations.

- In the cases of geometries 2, 4, and 8, since they do not have planar surfaces, these structures do not produce any proper beam. Nevertheless, the isotropic radiation is symmetrically enhanced, particularly for geometry 2. Specifically, the power density in the x-y plane is increased by around 4 dB and 8 dB for EMNZ and ENZ cases, respectively. Although cylindrical shapes of the outer surfaces seem to be the most important factor, we also observe that non-circular cavities limit the equal distributions of electromagnetic wave towards all directions in the x-y plane.

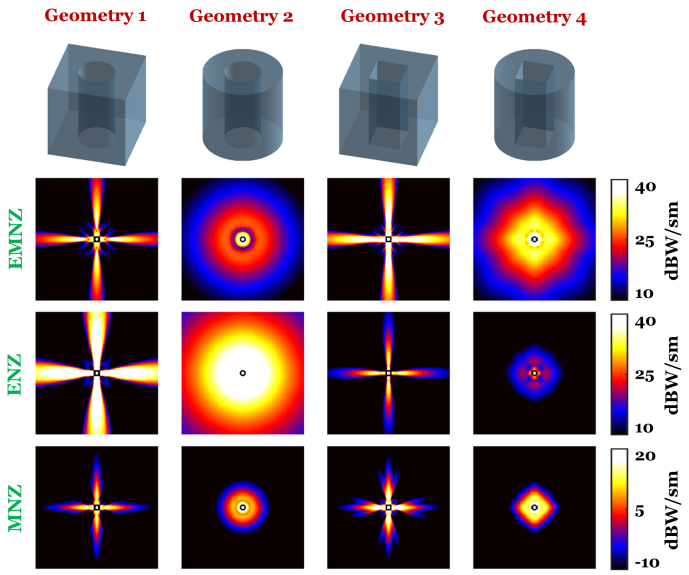

(a)

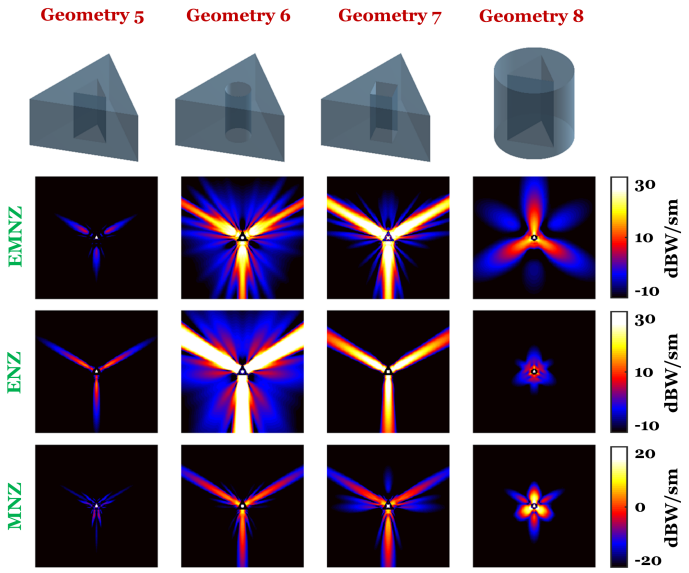

(b)

Figure 3.29: Power density distributions for EMNZ, ENZ, and MNZ shells when various cross-sectional geometries are examined. Results for cubic and cylindrical structures involving circular and square holes are given in 3.29a. Results for triangular prisms and a cylindrical structure involving circular, triangular, or square holes are given in 3.29b.

- Geometries 1 and 3 provide four strong beams that emerge from the flat surfaces of the shells.

- When a triangular prism is used as an NZI shell, such as in geometries 5, 6, and 7, we observe the importance of the proper cavity selection. For instance, one could expect that when outer surfaces and cavities match in terms of the geometry, beam qualities might increase; however, quite weak beams are obtained for such a case of geometry 5. In fact, electromagnetic fields escape easily from a triangular cavity, which leads to relatively weak resonances. An important factor to obtain an efficient beam generation is achieving strong resonances in the source region, which can be possible via circular and square cavities, as shown in the previous results. By using them in the triangular prisms, tridirectional radiation patterns are successfully realized via geometries 6 and 7.

- Once again, we observe relatively poor performances of the MNZ shells as cavities and the primary sources are not suitable for this type of a material, whereas some main characteristics are still observed in their results.

3.4.2 Tapering

When a Hertzian dipole is placed at the center of a homogeneous NZI cubic shell, i.e., inside its source region, electromagnetic waves propagate with a spherical wavefront to the shell's inner surface. Thus, normal and oblique incidences occur at the first (vacuum-to-NZI) transition. For example, the angle of incidence can be from 0° (normal incidence) to $\pm 65^\circ$ considering dimension of the circular cavity with 2.3λ diameter and 5λ height. As shown in Section 3.2.2, due to the existence of critical angles in vacuum-to-NZI transitions for all NZI properties, for larger than a few degrees, full reflection occurs. In this context, higher cavities support many reflections and multiple reflections, while we need shells with sufficient heights to obtain sufficient radiation and generate clear beams. Accordingly, we propose tapering on the surfaces of cavity regions in order to decrease both side lobes and undesired upward/downward radiations while preserving the outer surface heights of the designed shells.

Figure 3.30 shows power density distributions of homogeneous NZI cubic shells

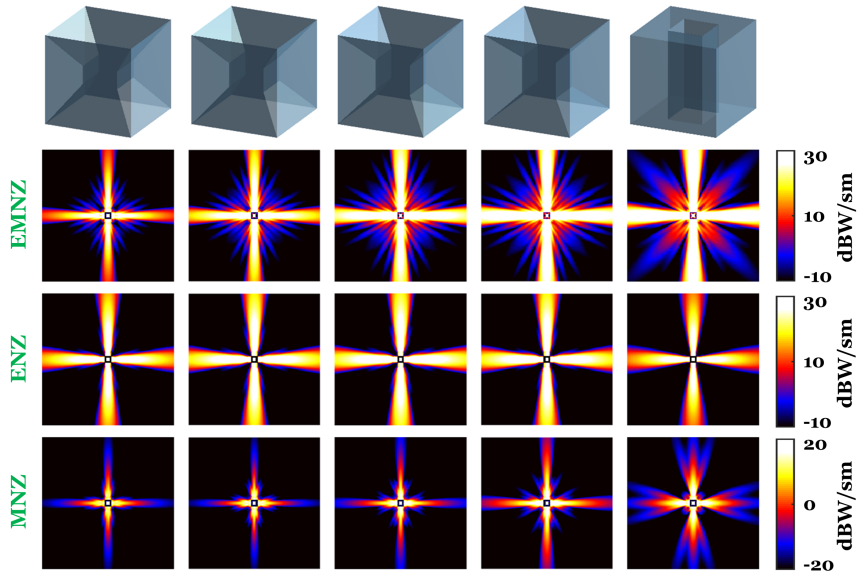

(a)

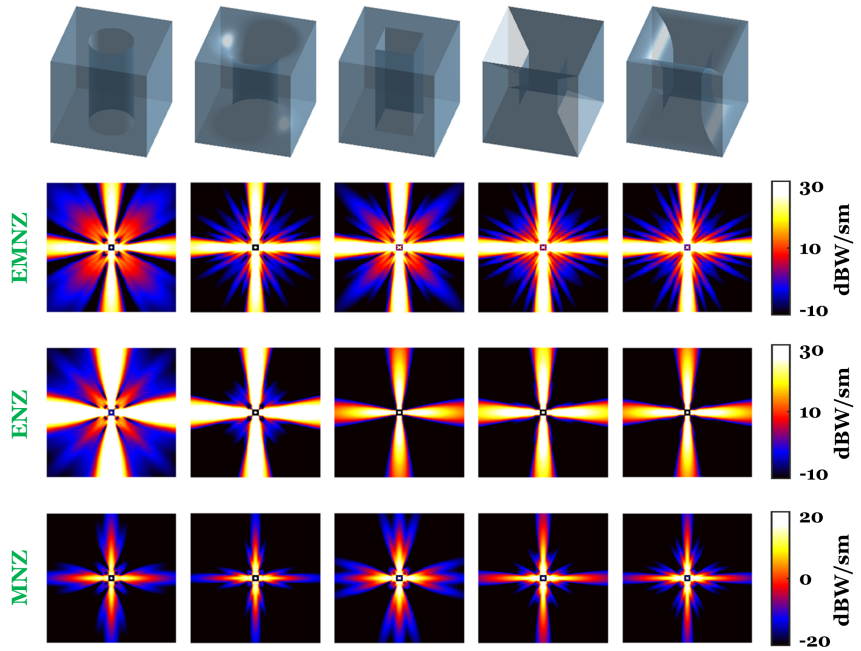

(b)

Figure 3.30: Power density distributions for EMNZ, ENZ, and MNZ shells when various tapering strategies are applied on the cavity surfaces. Results for linear tapering on square cavity is given in 3.30a. Results for circular and linear tapering on the square and circular cavities are given in 3.30b.

when their inner surfaces are tapered differently. As optimized before, the square hole with 2λ edge sizes (the fifth column in Figure 3.30a and the third column in Figure 3.30b) and the circular hole with 2.3λ diameter (the first column in Figure 3.30a) are used as the reference cavity designs. Then, various tapering strategies are applied to them, such as linear and curved (circular). In Figure 3.30a, tapering is decreased from left to right, while the results for the reference square cavity are shown at the rightmost column. In each case, a chamfer is applied onto the top and bottom regions of the shell. We observe that, when tapering is applied, (1) side lobes decrease and (2) brighter (stronger) main beams are obtained for all NZI cases. Even for the MNZ material, the separated beams are united as main beams that are normal to the outer surfaces. The design in the fourth column (it is also given in the same column in Figure 3.30b) provides the most strong beams while it leads to lower side lobes than the reference design. As depicted in Figure 3.30b, circular tapering can be used on both square and circular holes to further increase beam qualities. It is remarkable that when a circular taper is applied to the circular cavity (the second column), the persistent side lobes emerging from the edges of the cubic shell are considerably decreased for both EMNZ and ENZ cases. A circular taper can also be used for the square cavity to decrease side lobes, as given in the fifth column of Figure 3.30b.

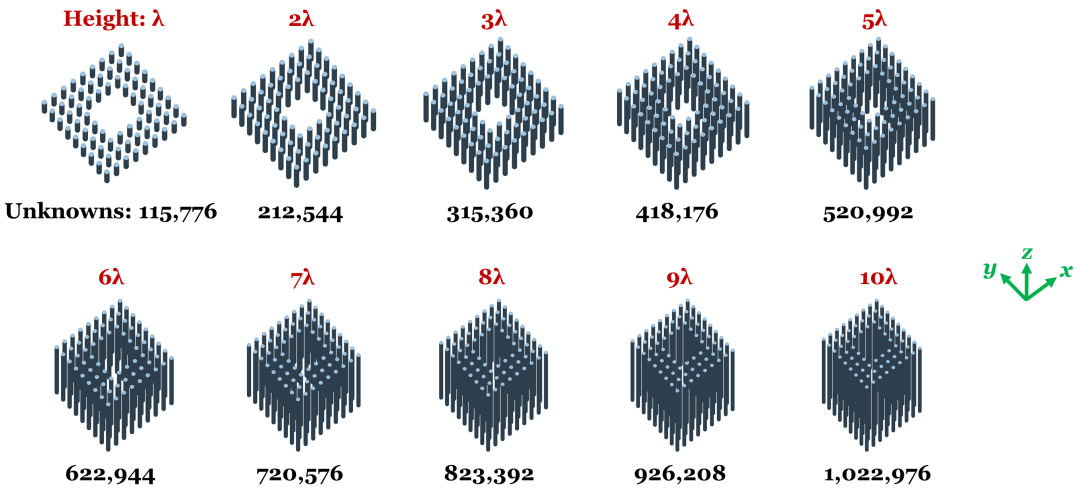

Figure 3.31: Realistic shell designs (the square lattice & cylinder design) involving rods with different heights to be used as beam generators. Dielectric cylindrical rods have 8.8 relative permittivity. Increased numbers of unknowns for longer rods lead to numerically challenging problems.

3.4.3 Realized Structures

Next, we consider realistic NZI structures involving periodic arrangements of dielectric (alumina) rods. The relative permittivity, radius, and center-to-center distance of cylindrical rods are set with respect to the square lattice & cylinder design in Figure 2.13, which shows effective EMNZ characteristics. In simulations of realistic NZI structures, we need finite height values, while they should be long enough to prevent undesirable end effects. In order to investigate the effect of rod heights on the electromagnetic responses of periodic media, λ to 10λ rods are used to construct 9×9 grids as shown in Figure 3.31. In the grids, 3×3 rods are removed from the center to create an effective square cavity with strong resonances. Numbers of unknowns can reach nearly a million for the longest rods; thus, these challenging problems are solved by using a three-layer preconditioner while JMCFIE is used as the formulation. FGMRES iteration histories of the main solver (layer-0) are given in Figure 3.32 for different rod heights. Efficient solutions are obtained even for 10λ rods, which require only 49 main iterations. The most challenging case interestingly seems to be the structure involving 8λ rods that requires 61 iterations. The maximum solution time (obtained for 9λ rods) is 5.1 hours using 16 cores.

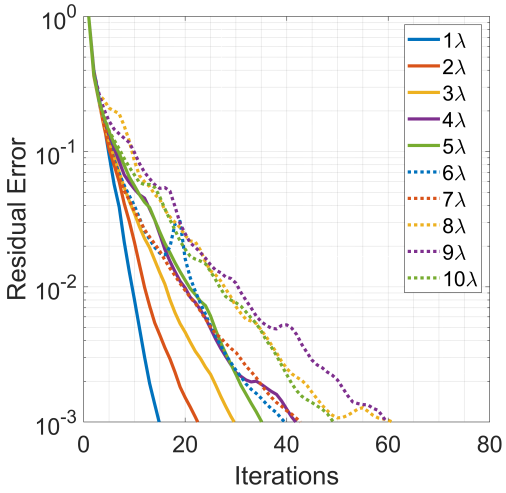

Figure 3.32: Iterative convergence histories in solutions of electromagnetic problems involving the structures in Figure 3.31, when the solutions are accelerated by the three-layer preconditioner based on AMLFMA.

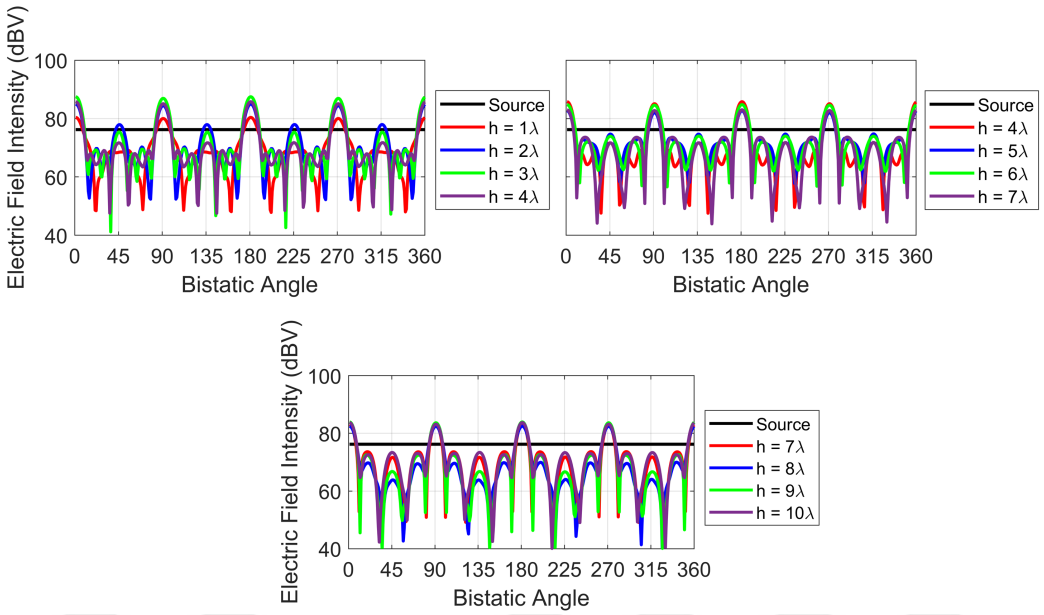

Figure 3.33: Far-zone electric field intensity with respect to the bistatic angle on the array plane obtained for the structures in Figure 3.31.

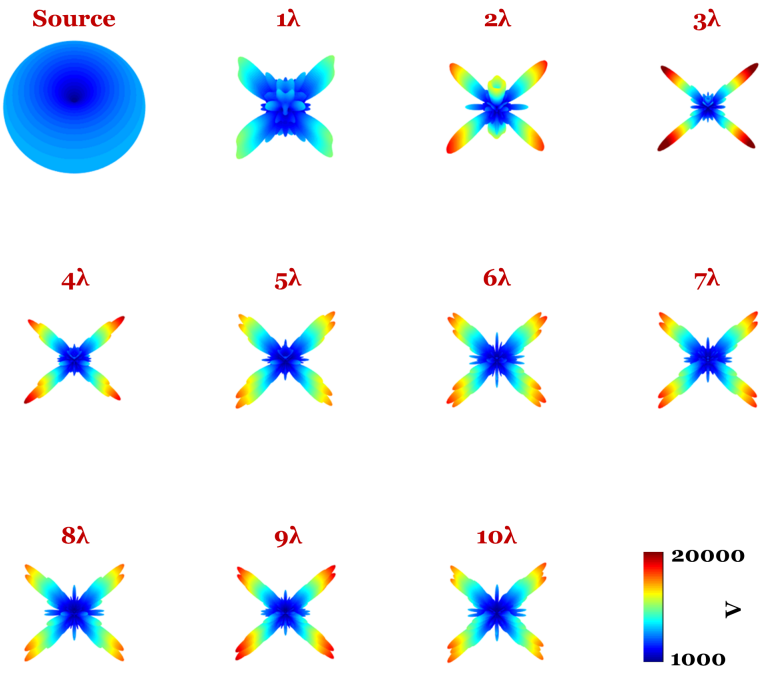

Figure 3.34: 3D far-zone electric field intensity results of realized square hole having different rod heights. A Hertzian dipole is used as a primary source while its pattern is also given.

Figure 3.33 presents the far-zone electric field intensity results for the structures in Figure 3.31 when they are excited by z-oriented Hertzian dipoles at their centers. The electric field intensity is plotted with respect to the bistatic angle on the array plane. We observe that even λ rods are enough to provide four beams, while relatively strong beams are achieved when the rods become longer than 2λ. At the same time, significant side lobes are present, particularly for 2λ rods. The maximum peak value of the electric field intensity is obtained by using 3λ rods among all rod heights. It seems that two-dimensional radiation characteristics do not differ too much with the change of rod heights. Considering all observation angles, we further examine 3D radiation plots in Figure 3.34, where the color range is designated to represent values from 1000 V to 20000 V. In addition to those in array planes, we observe many side lobes in various directions. There are also some upward and downward radiations that become vanishingly small as the rods become longer. On the top of these unwanted radiations, nulls at the poles can also be observed. Although main lobes are visible for all cases, it is remarkable that these main lobes are divided into multiple parts when the rods become longer than 3λ. We note that these observations cannot be made without considering 3D patterns (e.g., with the two-dimensional plots in Figure 3.33). The best beam-generating response belongs to 3λ rods; thus, increasing height values beyond this value seems to be both unnecessary and undesired.

In Figure 3.35, we investigate 9×9 grids, where three different cavities (circular, elliptical, and square) are formed by removing some of the rods at the center. Considering near-zone power density distributions obtained for different rod heights, we observe successful generations of four beams for the circular and square cavities. We also observe that the intensity of the side lobes depends on both cavity type and height of the rods. For example, the structure with circular cavity leads to stronger side lobes than the one with square cavity. On the other side, the elliptical cavity seems to suffer from the *finite resolution* provided by the 9×9 grid. When the rod heights are increased, the predicted beam response of elliptical cavity with $\pm y$ radiation emerges. However, there are significant side lobes that deteriorate its radiation performance even with 3λ rods, which indicate that the realistically achieved cavity operates quite differently than the one with an ideal elliptical shape. A possible solution could be increasing the number of rods to obtain a better resolution to represent the elliptical

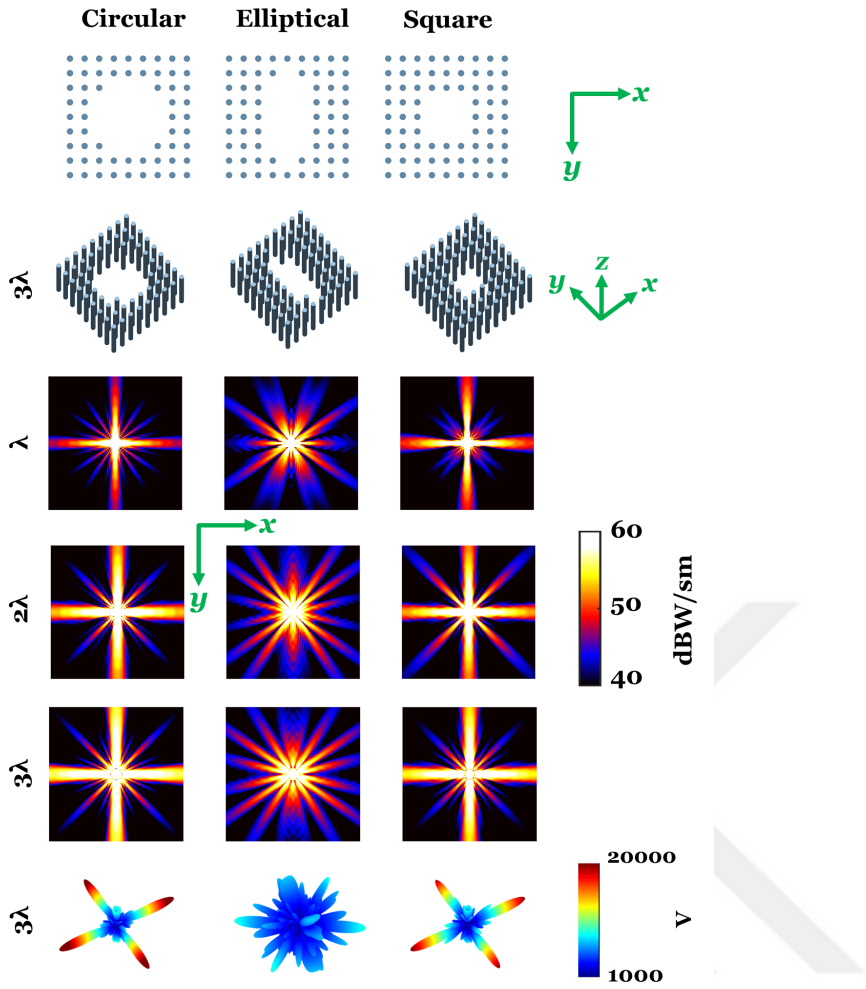

Figure 3.35: Results for various shell structures made of dielectric rods with different cavity formations.

cavity; however, keeping the number of rods in a realized shell structure small is one of the top design priorities in this study.

Figure 3.36 further depicts the far-zone electric field intensity in the array plane when the height of rods is 3λ. Omnidirectional source pattern provides a horizontal line, as expected. On the other side, in the beam directions, circular and square cavities provide approximately 15 dB higher values in comparison to the source pattern. These values demonstrate the quality of the beams, which can be obtained via relatively simple and compact shell structures that act as effective beam generators thanks to the NZI characteristics of the periodic designs.

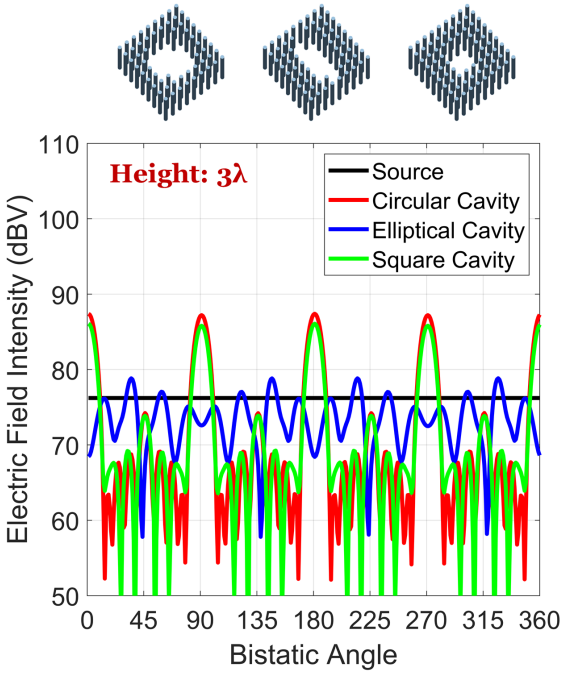

Figure 3.36: Far-zone radiation results for various shells made of dielectric rods (3λ) with different cavity formations.

3.4.4 Beam Generators for Millimeter Waves

As shown in Section 2.2, high-contrast dielectric rod arrays can show NZI characteristics, while their NZI behavior depends not only on geometrical properties but also on the operating frequency. If we assume that ϵ_r of rods does not alter much throughout a relatively wide band, which is a quite good assumption for alumina, new designs can be made at various frequencies, considering Figure 2.13. After deciding the center frequency (Dirac-like or semi-Dirac points), the radius of the rods and the center-to-center distance between them can be adjusted with respect to the frequency. Accordingly, Figure 3.37 illustrates different arrangements of dielectric rods at mmWaves. In this figure, the dimensions of the rods are given in terms of wavelength, while the operating frequency is chosen as 25 GHz ($\lambda = 12$ mm). Then, the dimensions of the full dielectric PhCs considered below are also given with respect to this wavelength. While the first four designs are directly related to those in Figure 2.13, the last two realizations to generate effective ENZ and MNZ media are based on [32]. Since the operating frequency is shifted to a higher value, more

compact beam generating structures can be obtained as their metric dimensions are reduced. We consider cylinders, square prisms, and rectangular prisms as unit cells, while the rods are made of three different materials. In the simulations, we only consider the first design in Figure 3.37 to show the scalability of a designed NZI structure to operate at different frequencies.

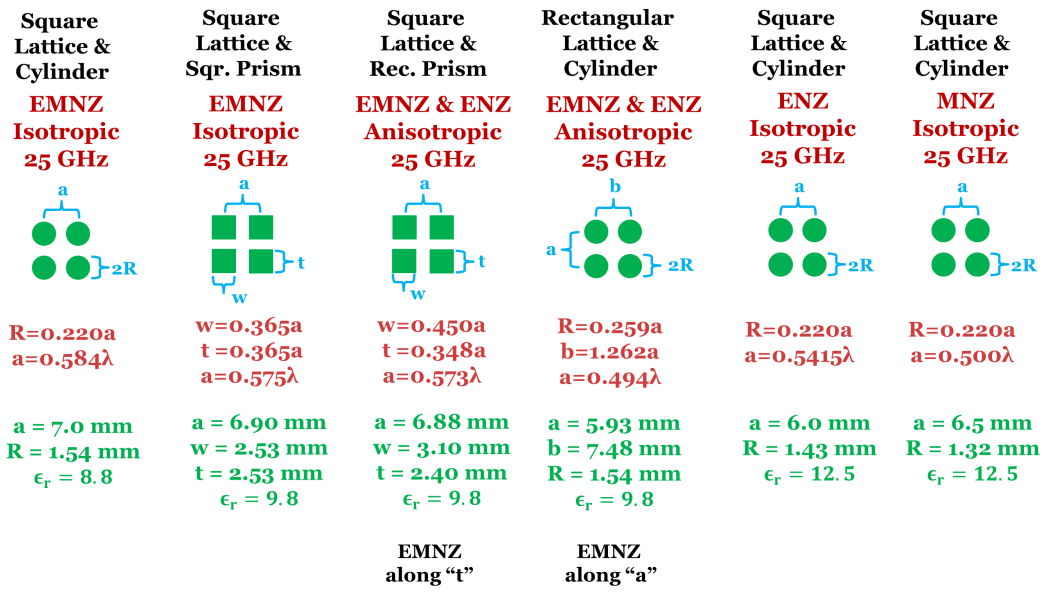

Figure 3.37: Periodic media involving dielectric rods that demonstrate NZI characteristics at mmWaves.

First, we examine a 12×12 grid of cylindrical rods arranged to create a triangular prism (78 rods) that is expected to operate as an EMNZ structure (with correct permittivity values for the rods) at 25 GHz. In the design, 3λ rods are used. Following the procedure described in Section 3.3, we predict the effective refractive index of the prism when the rods have different permittivity values. Figure 3.38 presents oscillatory patterns of the near-zone waves (imaginary parts of the electric field intensity distributions), as well as the corresponding 3D radiation patterns. Based on the Hough line transform, we compute the effective refractive index as -0.03 and 1.18, when ϵ_r of the rods is 8.8 and 4.0, respectively. These results can be seen as a quantitative verification of the NZI characteristics of cylindrical rods with 8.8 relative permittivity at 25 GHz. Considering the 3D far-zone radiation patterns on the right-hand side of Figure 3.38, we observe that the main lobe occurs in accordance

with ordinary refraction (downward from the oblique surface of the triangular prism) when ϵ_r is 4.0. On the other hand, when ϵ_r is 8.8, a beam is generated perpendicular to the oblique surface of the prism due to the EMNZ behavior. The large reflected beam in this case does not indicate that the EMNZ characteristics (small permittivity and permeability values) are unsatisfied; it shows that the effective medium does not match with vacuum in terms of impedance.

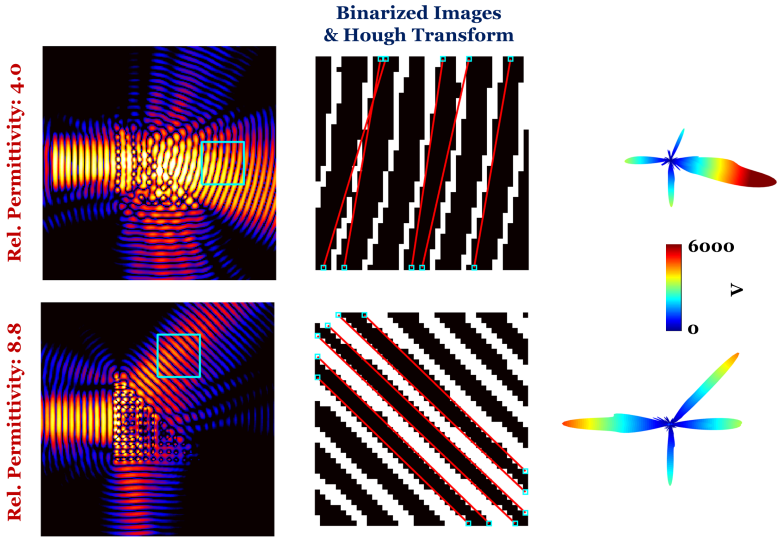

Figure 3.38: Imaginary part of electric field intensities, binary images and slopes, and 3D radiation patterns for 12×12 grid when relative permittivity of the rods is 4.0 (top) and 8.8 (bottom). A CSP beam is used in the simulations at 25 GHz.

Figure 3.39 depicts 9×9 grids of cylinders, 3×3 of which are removed at the center to create an effective NZI beam generator at 25 GHz. Three different rod heights are considered, while a Hertzian dipole is placed at the center of the represented shells. Power density distributions and far-zone radiation patterns are given for these structures. We observe a similar performance compared to the results in Figure 3.35. In other words, we observe successful generations of four beams even for λ rods, while the best result belongs to 3λ rods. Consequently, we conclude that NZI structures can be realized at diverse frequencies, such as for mmWaves. Thanks to the developed refractive index check mechanism (see Section 3.3), the parameters of the grids can further be optimized to reach the best radiation response. In the following sections, we return back NZI structures designed for 10.3 GHz, considering practical issues such as the availability of fabrication and experimental tools.

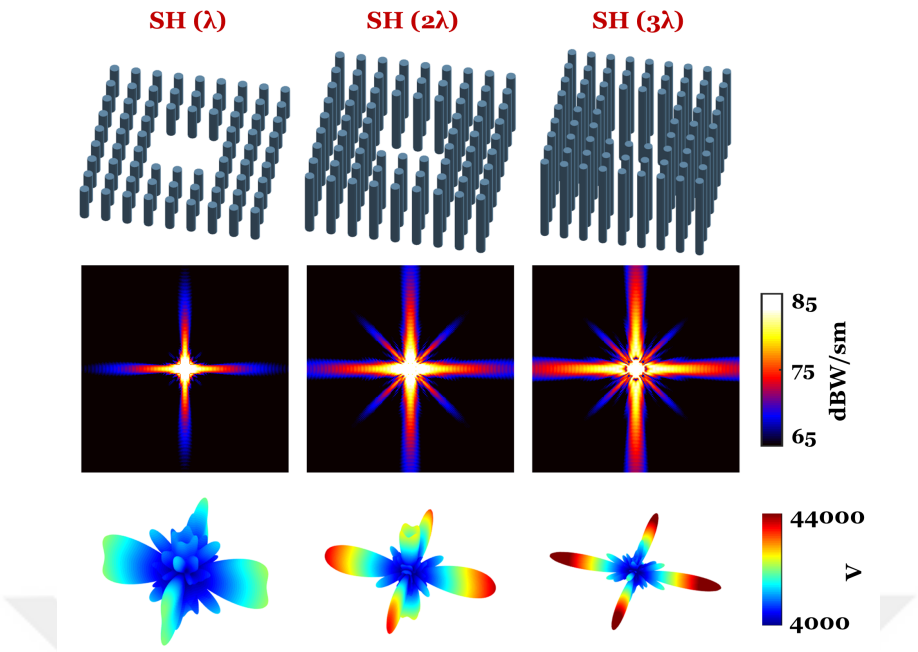

Figure 3.39: Results for realistic NZI shells with different rod heights and square cavities to operate at 25 GHz.

3.5 Designs of Outer Surfaces

Following the design of source regions, we focus on geometric properties of outer surfaces of NZI shells. Both homogenized and actual models involving periodic arrangements of unit cells are investigated via accurate solvers. Various strategies to enhance or suppress selected beams to form alternative beam configurations are discussed to demonstrate the extensive capabilities of NZI shells for diverse applications. All simulation parameters, e.g., formulations and solution algorithms, stay the same other than the applied geometric modifications. As the primary source, a Hertzian dipole is located at the center of each NZI shell, unless stated otherwise. Since the realized structures demonstrate effective EMNZ characteristics, we mainly investigate EMNZ cases for homogeneous designs. On the other side, ENZ shells are also studied for the generalization of the study.

3.5.1 NZI Lenses

In order to enhance the radiation of outgoing waves, relatively simple modifications are applied to the outer surfaces of NZI shells. For instance, we obtain increased radiation in the direction of the surface when it is curved (like a lens), as shown in Figure 3.40. In these simulations, $5\lambda \times 5\lambda \times 5\lambda$ cubic shells with 2.1λ-diameter circular cavities are considered. For numerical simulations, the structures are discretized with $235,344$–$255,126$ unknowns when $\lambda/15$ elements are used. From the left-hand side to the right-hand side of Figure 3.40, the same type of curvature is applied on different surfaces of the original cubic shell. Power density distributions are given in the cavity region ($5\lambda \times 5\lambda$) and in the far-zone region ($100\lambda \times 100\lambda$) in the top and bottom plots, respectively. Both relative permittivity and relative permeability of the material are set to 5×10^{-3} (EMNZ characteristics). We observe enhanced beams in the directions of the modified surfaces, which can be explained by the increased effective apertures of the corresponding surfaces. Radiations from the other surfaces without curvatures are not significantly affected by the applied changes. However, the geometry of the curvature should be adjusted carefully since it also increases the beamwidth in addition to the increased radiation. In fact, due to the focusing properties of the lenses, surface curvatures may even split the beam.

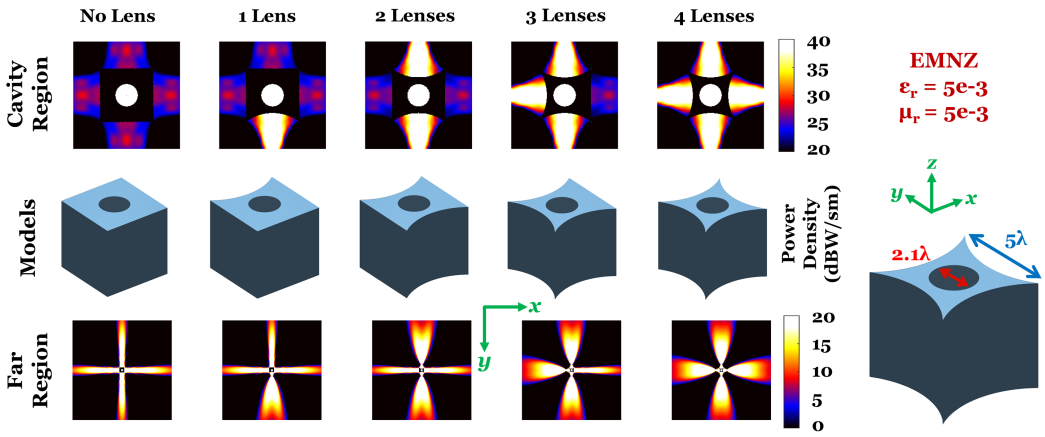

Figure 3.40: Power density distributions for EMNZ cubic shells having circular cavities. Cavity ($5\lambda \times 5\lambda$) and far-zone regions ($100\lambda \times 100\lambda$) are considered in the x-y plane, when outer surfaces of the shells are curved.

Figure 3.41 depicts two-dimensional far-zone electric field intensity patterns to further demonstrate radiation characteristics of NZI shells involving lenses. On the left-hand side, a single lens is applied onto NZI shells with various NZI characteristics (EMNZ, ENZ, and MNZ), whereas, on the right-hand side, all lateral outer surfaces of the shells are curved. We observe increased radiation for the EMNZ and ENZ cases when a single lens is used, while the beam is not split for the ENZ case. EMNZ and ENZ shells with four lenses can be used to obtain higher coverage towards intended directions (angles), providing more than 20 dB suppression for other locations. Since we focus on the realization of EMNZ properties in general, the designs are mainly obtained and examined for EMNZ cases. Therefore, MNZ shells show relatively weak performances since the designs are not suitable for MNZ materials (e.g., in this set, 1.9λ diameter can provide better performances for MNZ shells).

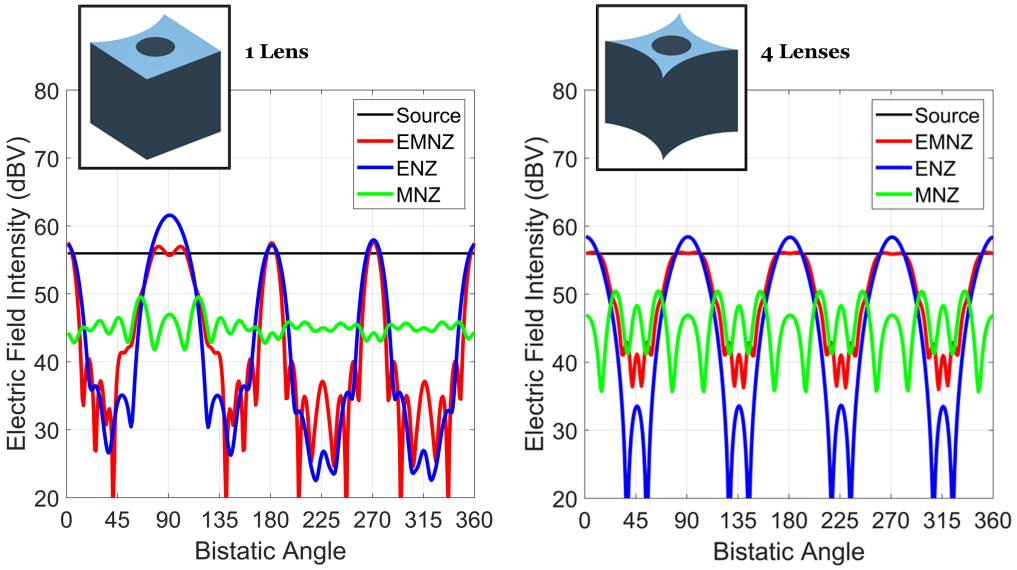

Figure 3.41: Far-zone electric field intensity results when a single lens and four lenses are used for NZI cubic shells having circular cavities.

Modifications like curving in cylindrical forms are favorable since they are applicable in actual structures involving dielectric rods. Accordingly, Figure 3.42 presents the results of computational experiments when two sides of 9×9 grids with square cavities are modified. These modifications, which involve the removal of rods, correspond to curvatures (as in Figure 3.40) on the outer surfaces of the shells. Although the resulting practical structures do not possess ideal curvatures, we observe that the

corresponding beams can effectively be enhanced, leading to bidirectional radiation characteristics with two (wider) main beams. This is particularly visible in the tri-dimensional patterns depicted for the structure with 2λ rods.

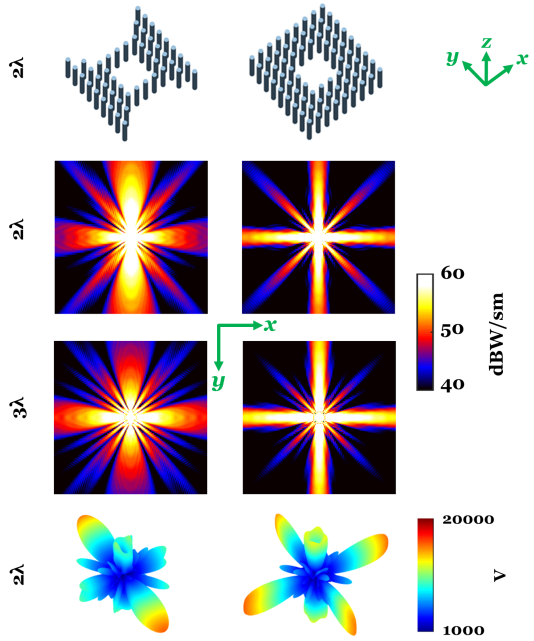

Figure 3.42: Results for various shell structures made of dielectric rods. Two sides of the regular grids (with 2λ and 3λ rods) are modified by extracting rods.

3.5.2 NZI Absorbers

Electromagnetic absorbers are commonly studied in the literature in the context of diverse applications. For instance, in antenna measurement setups, anechoic chambers are widely used, where pyramidal absorbers are placed to reduce interference and reflections. In a very different application area, inverted pyramids are used in solar cells to improve their absorption capabilities. For example, in a detailed study, such structures are developed to efficiently absorb incoming optical waves [93]. In this study, considering their useful properties, similar types of absorbers are used to engineer radiation characteristics of NZI shells, i.e., by suppressing outgoing waves in certain directions.

In Figure 2.17, we observe that corrugations on the outer surfaces of realistic NZI shells (that naturally occur when a triangular lattice is used) can suppress outgoing

beams (as opposed to the enhancement with lenses) in comparison to the radiations from the "flat" surfaces of the same structures. The generated beams can further be suppressed when the outer surfaces of the shells are properly designed. Accordingly, stemming from these observations, we design and investigate both homogenized and realistic NZI absorbers. This way, compact and efficient beam-generating shell structures with customized radiation patterns are designed, without using any additional components or reflectors such as conducting plates.

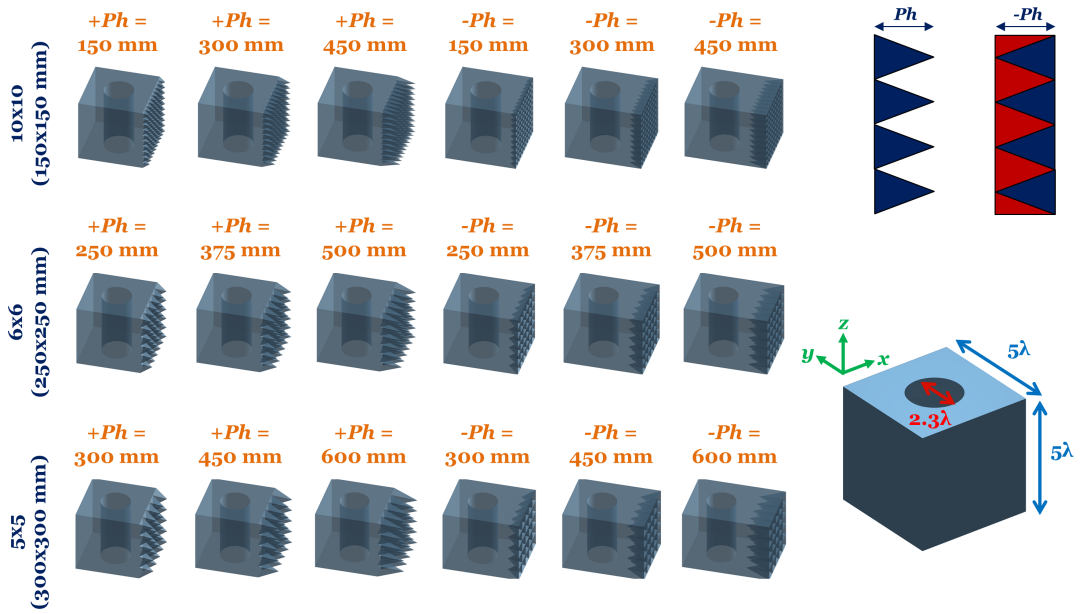

Figure 3.43: Parametric sweep for pyramids and inverted pyramids when they are put on one of the outer surfaces of an EMNZ cubic shell involving a circular hole of 2.3λ diameter.

Figure 3.43 illustrates various NZI shells having pyramidal textures. In particular, two types are examined: (1) ordinary pyramids and (2) inverted pyramids. Specifically, 10×10, 6×6, and 5×5 pyramidal textures are placed on a side surface of a $5\lambda \times 5\lambda \times 5\lambda$ EMNZ cubic shell with a circular cavity having 2.3λ diameter. The pyramids have various sizes with 150 mm $\times$ 150 mm, 250 mm $\times$ 250 mm, and 300 mm $\times$ 300 mm base dimensions (λ is 300 mm). In the first three columns of Figure 3.43, there are ordinary pyramids while their heights (pyramid height [Ph]) vary in a range from 150 mm to 450 mm. In the last three columns, inverted pyramids are placed on the same side surface while the same height values are used. Simulation results of

all these geometries are depicted in Figure 3.44, where power density distributions are investigated when a Hertzian dipole is placed symmetrically at the center of the circular cavities. Considering these results, we reach the following conclusions: (1) Pyramids destroy the phase coherence. Then, the beam on the associated side is suppressed, while the suppression rate highly depends on the parameters of the pyramidal textures. (2) The inverted pyramids lead to better results in terms of beam suppression than the ordinary pyramids. (3) Higher height leads to better suppression values for the inverted pyramids, whereas an opposite behavior is observed for the ordinary pyramids. A possible explanation is related to the tapering direction. For the ordinary pyramids, from NZI to vacuum transition, there is a linear decrease in the overall NZI volume towards the free space, which may facilitate the coupling of electromagnetic waves. Thus, relatively weak suppression is obtained with these structures, while higher Ph provides stronger beams. On the contrary, when using inverted pyramids, the overall NZI volume decreases towards the outer surface of the shell; thus, we may reach a stronger suppression, which is enhanced with the increased height. (4) The best response belongs to 10×10 inverted pyramids (150×150 mm base dimensions) having 450 mm height, which is located on the top right of Figure 3.44.

As the next step, we combine the optimized cavities and NZI absorbers in diverse ways in order to obtain different multi-directional beam generators. As shown in Figure 3.44, when we place inverted pyramids on a side surface of a shell, nearly 15 dB suppression is achieved (in the best case) with respect to the other main beams. Then, other side surfaces of an NZI shell can also be covered with well-designed pyramidal textures to obtain alternative beam configurations. Accordingly, Figure 3.45 presents results of $5\lambda \times 5\lambda \times 5\lambda$ EMNZ cubic shells with 10×10 inverted pyramids possessing 150 mm $\times$ 150 mm base dimensions and 450 mm heights. Power density distributions are given in the x-y plane ($100\lambda \times 100\lambda$ regions) below the simulated structures. We consider two different cavities as square (2λ edge sizes) and circular (2.3λ diameter). From the left-hand side to the right-hand side, the designed inverted pyramids are placed onto one or two side surfaces of the shells. The obtained radiation characteristics can be described as follows.

- In the first two columns of Figure 3.45, we observe the effects of the pyramidal textures on the shells with different cavity types. In each case, one of the beams

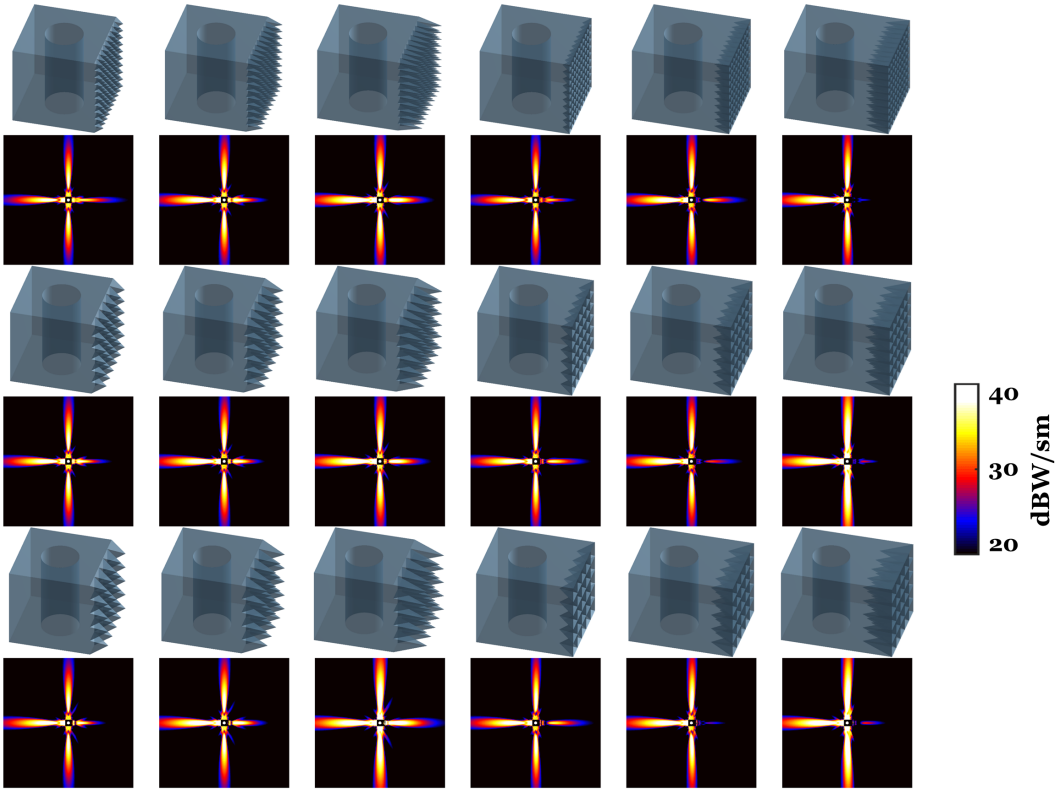

Figure 3.44: Power density distributions in the x-y plane when geometries in Figure 3.43 are excited via Hertzian dipoles located at their centers.

is significantly suppressed such that the overall response of the shell becomes tridirectional when the inverted pyramids are used.

- As shown in the third column of Figure 3.45, regardless of the cavity type, the structure operates as a double-beam generator with a 90° angle between the beams. The square cavity generates stronger beams; thus, there are still weak radiations on the side surfaces covered by inverted pyramids.

- In the last column of Figure 3.45, bidirectional radiations with two antisymmetric beams are obtained when the inverted pyramids are placed onto opposite side surfaces of the cubic shells. In these cases, beam strengths seem to be decreased in comparison to the other beam generators.

Up to now, pyramidal textures on homogeneous EMNZ shells have been discussed. On the other hand, well-designed homogeneous ENZ shells, such as those in Figure

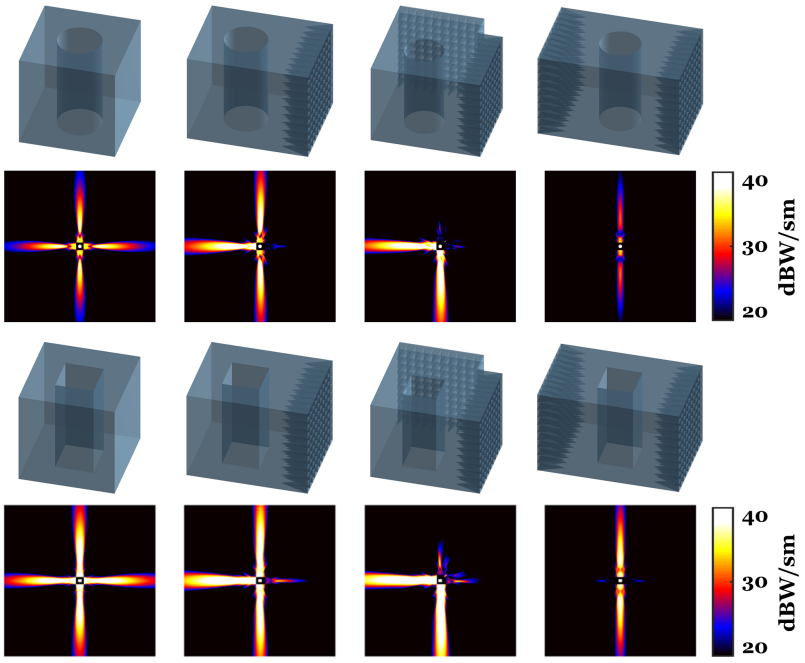

Figure 3.45: Results for EMNZ cubic shells involving circular and square cavities when optimized inverted pyramids are placed onto different sides of the shells.

3.26, can also be used with optimized inverted pyramids in order to provide unidirectional beams. Since such shells with elliptical cavities already show bidirectional radiation characteristics, single-beam structures can be obtained by adding pyramidal textures on one of the surfaces to suppress one of the beams. Accordingly, Figure 3.46 presents simulations of ENZ cubic shells with elliptical extractions ($4\lambda\&2\lambda$). We consider two different types of excitations. In the first case, a Hertzian dipole is located at the center (the second and third rows in Figure 3.46), as usual. In the second case (the fourth and fifth rows in Figure 3.46), it is located at one of the focal points of the ellipse. Power density distributions and 3D electric field intensity results are considered to investigate the designs extensively. We observe that, by adding the pyramidal texture, the bidirectional radiation is successfully converted into a unidirectional one when the source is located at the center. On the other hand, when the source is at the focal point, a relatively weak unidirectional operation can be reached even without inverted pyramids. Then, a better response can be obtained with the pyramids. Note that, in Figure 3.46, we also include two trials, where NZI absorbers (pyramids) are further added onto one of the perpendicular side surfaces to see if some

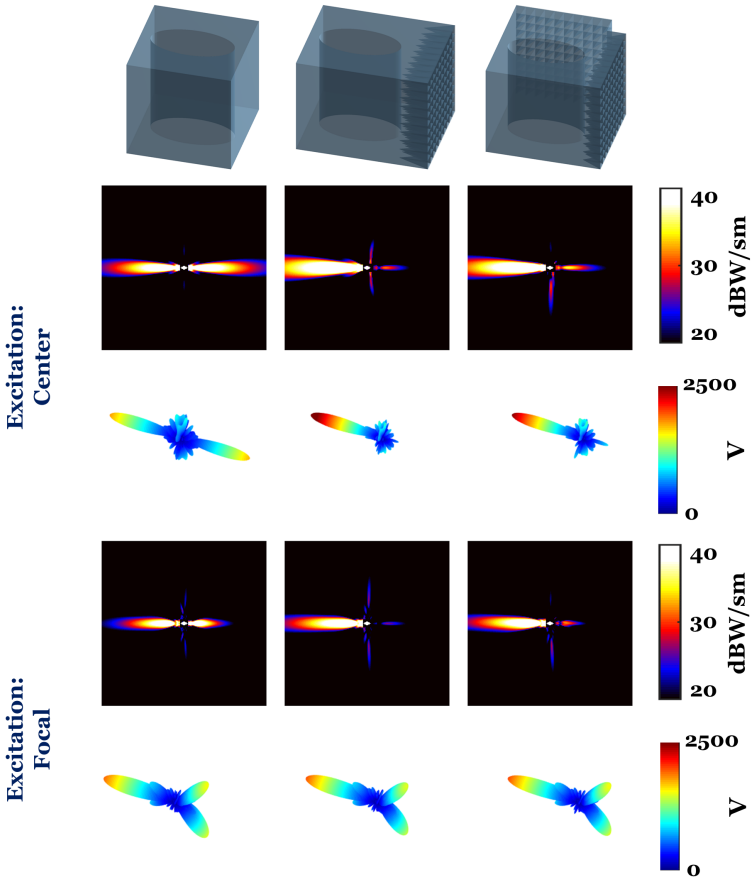

Figure 3.46: Results for ENZ cubic shells ($5\lambda \times 5\lambda \times 5\lambda$) involving elliptical cavities ($4\lambda\&2\lambda$) when the optimized inverted pyramids are placed onto different sides of the shells.

remaining unintended radiations can further be suppressed. However, this type of an application appears to be useless since it decreases the suppression on the surface that is originally covered by the inverted pyramids. To sum up, the best unidirectional radiation pattern is obtained by using the ENZ cubic shell involving an elliptical cavity and inverted pyramids added on one of its surfaces, while the excitation (Hertzian dipole) is located at the center.

3.5.3 Vertical Grids

In homogeneous NZI models, inverted pyramids can be used to mimic conventional absorbers. However, considering practical issues, such as realization and fabrication of NZI shell structures, pyramidal textures can be difficult to implement, while there

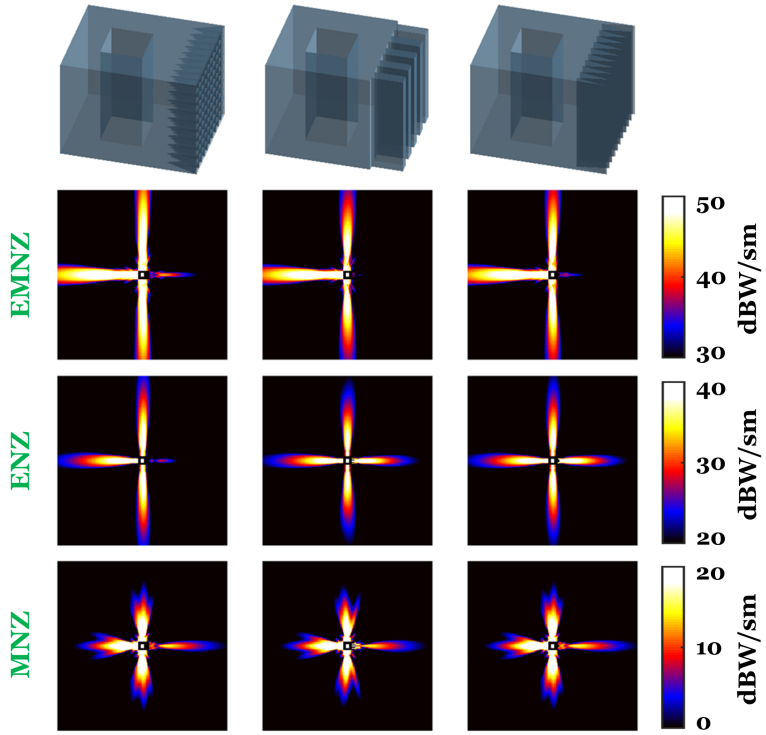

Figure 3.47: Power density results to investigate effective corrugation designs to reach realizable structures with relatively good suppression of radiation in the intended directions. EMNZ, ENZ, and MNZ shells involving square cavities (2λ edge size) are considered.

can be better options to provide corrugations on side surfaces of NZI shells. For instance, removal and movement of rods can provide corrugations on shell surfaces considering realistic models. Before their realistic tests, however, removal of rods can be tested in equivalent homogeneous models. In Figure 3.47, we compare three different possible corrugations when inverted pyramids, relatively less complicated vertical grids (VGs), and triangular prisms are placed on a side surface of the NZI shell involving a square cavity (2λ edge size). EMNZ, ENZ, and MNZ cases are considered, while dimensions of the corrugations are adjusted based on the optimized parameters in Figure 3.44, i.e., heights and base dimensions are 450 mm and 150 mm, respectively. In the first row, EMNZ shells are compared considering the generated power density distributions. We observe that all three corrugations show quite sufficient suppressions, leading to the desired tridirectional radiation patterns. Although beam qualities for the shells with triangular prisms and VGs are slightly lower than

the shell with inverted pyramids (especially in vertical directions from the point of view for the plots), the best result belongs to VGs in terms of suppression. On the other hand, for ENZ characteristics, only inverted pyramids seem effective, while none of the designs is successful for the MNZ material. Figure 3.48 depicts 3D and two-dimensional far-zone electric field intensity results for different corrugations on EMNZ shell surfaces. Nearly 15 dB suppression can be reached with VGs. However, we observe unintended upward/downward radiations in the 3D results, which can be decreased by tapering.

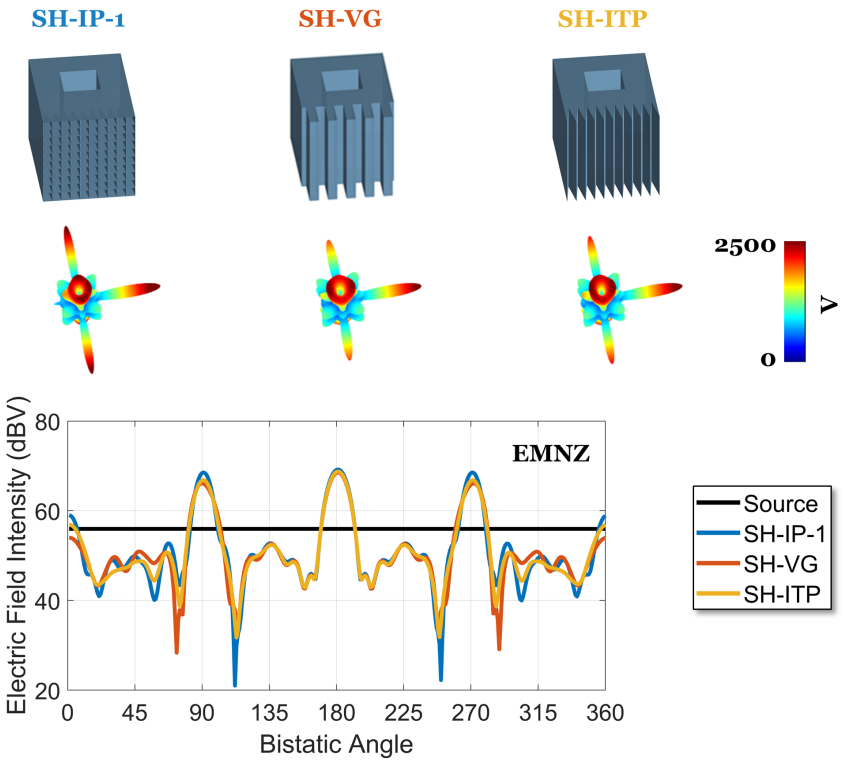

Figure 3.48: Far-zone electric field intensity resuls to investigate effective corrugation designs to reach realizable structures with relatively good suppression of radiation in the intended directions. Only EMNZ shells involving square cavities (2λ edge size) are considered.

Similar to pyramidal textures that can be used to design multi-direction beam generators, such as depicted in Figure 3.45, VGs provide efficient suppression rates that enable engineering beam configurations. Also, they are more practical to be realized in actual designs. As practiced for other corrugation types, more than one shell

surface can be covered with VGs to generate alternative radiation patterns, as shown in Figure 3.49. In these simulations, the structures are discretized with $164,526$–$215,058$ unknowns when $\lambda/10$ mesh sizes are used. Similar to the earlier results, ϵ_r and μ_r values are selected equally to obtain EMNZ characteristics with 5×10^{-3} refractive index. Power density distributions are given in the cavity ($5\lambda \times 5\lambda$) and far-zone ($100\lambda \times 100\lambda$) regions, where color ranges are carefully selected (different from other plots of this section) to observe all radiation characteristics, including side lobes. Tridirectional beams are observed to be generated by the first design (SH-VG). With the design in the second column, a bidirectional beam generator is obtained with a 90° between the beams. However, for both this design and the one in the first column, many side lobes can be seen in diagonal directions. Accordingly, linear (third and fourth columns) and circular (fifth and sixth columns) tapering are applied onto the source regions. We observe that, without notable effects on the main beams, side-lobe levels can significantly be decreased thanks to implemented tapers.

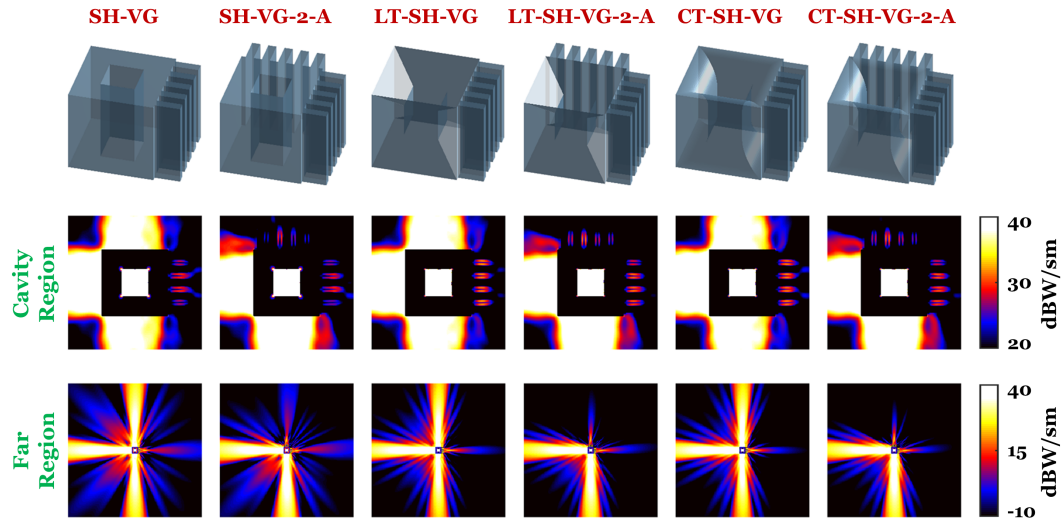

Figure 3.49: Results for EMNZ cubic shells involving square cavities when VGs are placed onto different shell surfaces. Circular and linear tapering are also implemented.

Next, we consider realistic corrugations as NZI absorbers. Figure 3.50 depicts several examples involving 9×9 grids of 3λ rods. Both square and circular cavities are examined, whereas corrugations are realized by the removal of selected rods. For a complete analysis, they are applied on one, two, and three sides of the structures. We

observe that, when a single side is modified, the corresponding beam is effectively suppressed, leaving three main beams in addition to some side lobes. Corrugations on the second and third surfaces further lead to radiations with two and single main beams, respectively, while side lobes become significant.

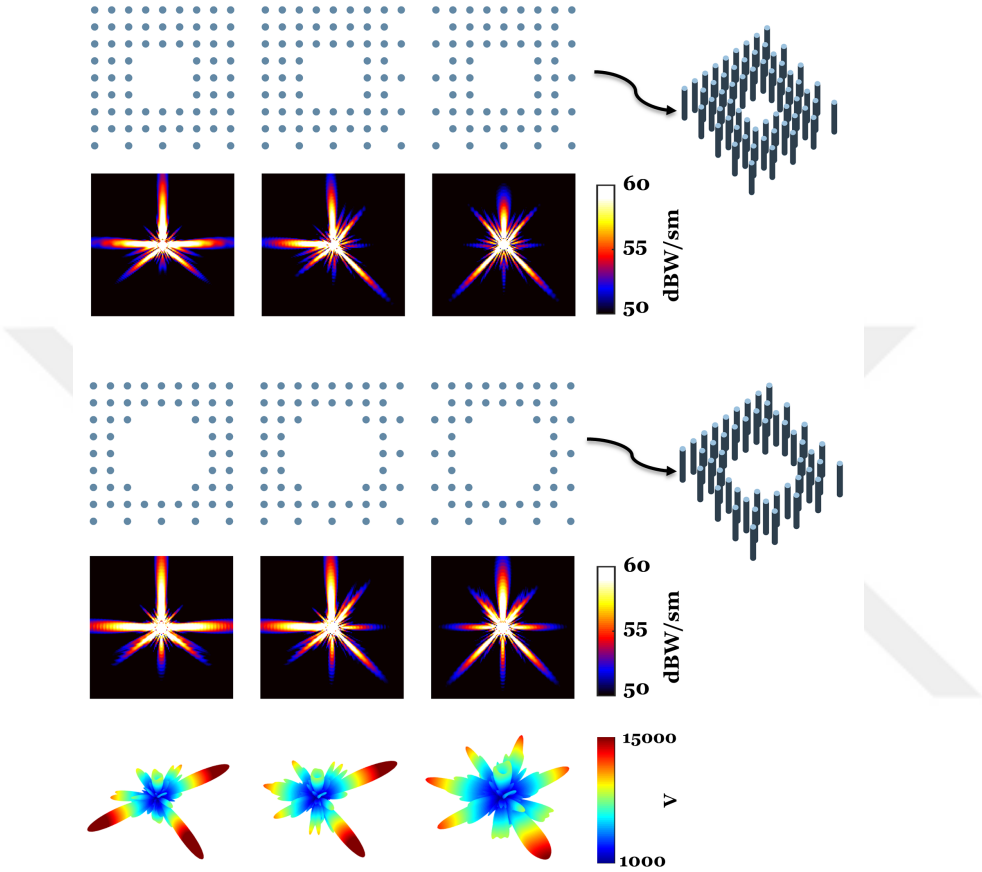

Figure 3.50: Results for various realistic shell structures with modified sides to suppress different beams.

Figure 3.51 presents the possibility of more compact (flat) shells involving 9×9 grids of λ rods. Alternative configurations and the corresponding near-zone power density distributions and far-zone radiation patterns are depicted to demonstrate the diversity of radiation characteristics that can be obtained via relatively simple structures. Quad-directional, tridirectional, and bidirectional radiation patterns are obtained, as can be seen in the first four columns, while the unidirectional pattern in the fifth column is problematic due to significant side lobes.

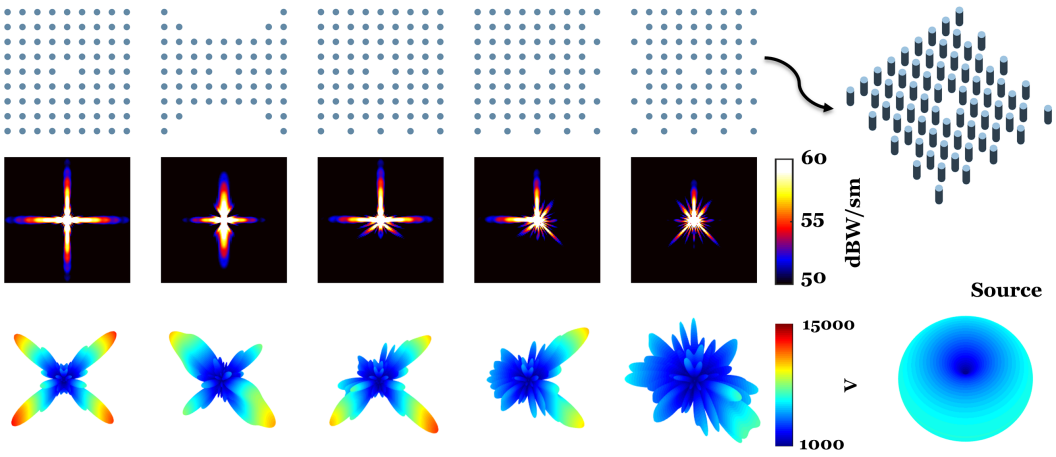

Figure 3.51: Results for various realistic shell structures involving dielectric rods of height λ. In each case, the center rod is removed to place a Hertzian dipole.

Numerical simulations show that, in order to reach more efficient NZI absorbers with lower side-lobe levels, we need alternative strategies for the realization of VGs. Accordingly, Figure 3.52 presents a comparison of different realistic corrugation designs, based on the reference square hole (SH) design given in Figure 3.35 and the SH design with a single modified face (SH-SMF) given in Figure 3.50. The last three columns of Figure 3.52 depict applications of alternative VGs on a single side. In the design shown in the third column, two lines of VGs are placed on the side of the structure. On the other hand, in the fourth column, a full line of rods is added before a single line of VGs (VG-L-1). The design in the last column consists of a single line of VGs (VG-S-1) on the same side of the shell. Considering power density distributions and 3D radiation results, we conclude that the best performance is provided by the fifth design that involves less number of rods (hence less material usage) together with sufficient suppression rates. In addition, the other designs, such as SH-VG-1, can be preferred for different materials and operating frequencies.

Next, we apply VGs to different sides of realistic shells, as exemplified in Figure 3.53. We investigate four NZI shells, of which one, two, or three sides, are modified by VG-S-type designs (additional rods). The numbers of unknowns varies from $343,728$ to $388,368$. Power density distributions and far-zone radiation patterns are depicted in Figure 3.53. When one of the sides is modified, tridirectional beams are observed, as shown in the first column. When corrugations are places on two adja-

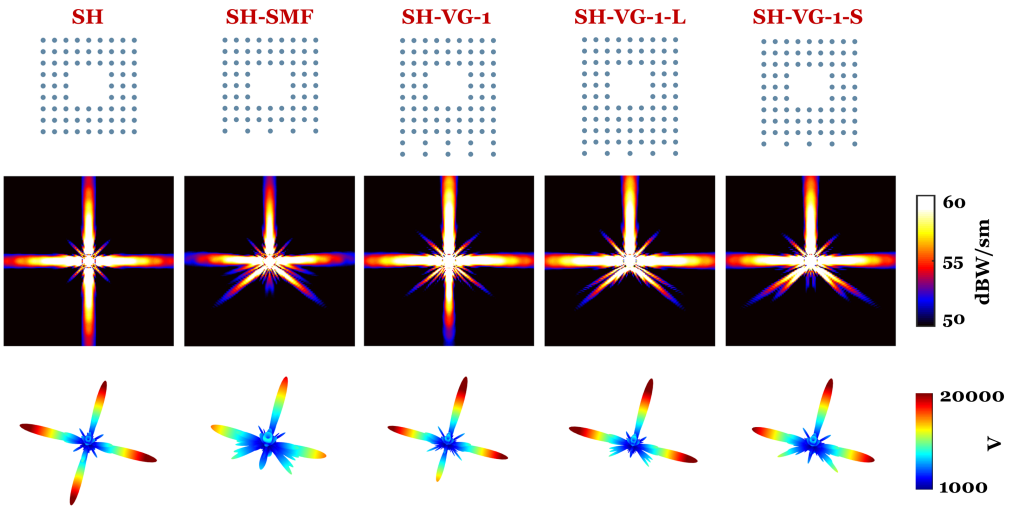

Figure 3.52: Power density distributions for various realistic shell structures involving 3λ rods with VGs.

cent sides, we obtain two perpendicular beams, as depicted in the second column. Although quite high suppression rates are obtained, there are remarkable side lobes, particularly in the diagonal directions of the represented shells. These side lobes become more significant when the two opposite sides of the shell are modified, as shown in third column. Bidirectional radiation with two clear beams is observed; however, the generated side lobes can be prohibitive for some applications. The last structure includes modifications on three of four sides. Unidirectional radiation with a single clear beam, along with some significant side lobes, is reached via this design. All designs in Figure 3.53 have better radiation performances in comparison to the results in Figure 3.50 (when corrugations are obtained by removal of the selected rods), especially in terms of side-lobe levels.

3.6 Designs with More Complicated Radiation Patterns

NZI shells provide us diverse design opportunities in the context of multi-beam generation. As an engineering problem, in order to reach an arbitrary beam pattern, compact and efficient NZI shells can be designed throughout several steps. First, we decide the outer geometry of the homogeneous shell as a polygon considering the required number of beams. On the other side, to enhance omnidirectional radiation rather than directive patterns, circular outer geometries can be used together with cir-

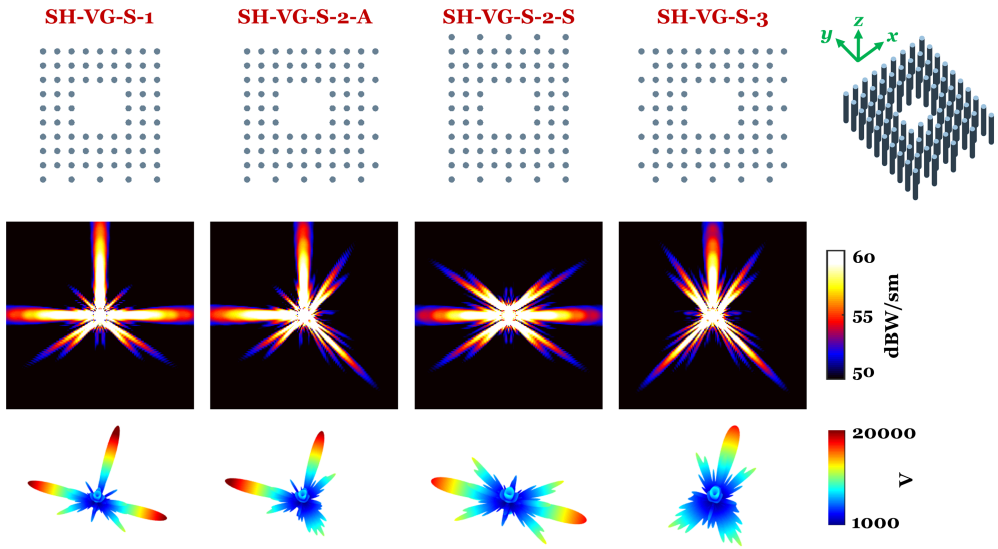

Figure 3.53: Power density distributions for various shell structures involving 3λ rods with VGs.

cular holes (cavities). Next, we use well-designed cavities, such as square or circular holes, that show strong resonances with optimized dimensions. Then, depending on the desired pattern, some of the beams can be suppressed or enhanced using NZI absorbers and lenses, respectively. Finally, the designed NZI shells are realized by periodically arranging high-contrast dielectric rods. It is remarkable that the realized structures are also fully reconfigurable. In other words, alternative radiation characteristics can be obtained by instantly removing and/or adding rods.

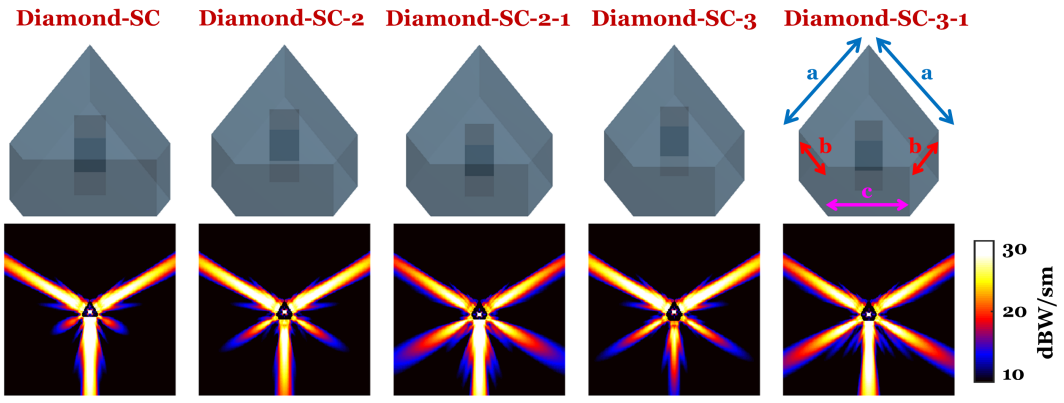

Figure 3.54: Power density distributions for homogenized models of diamond shells with square cavities having 2λ edge lengths.

Cubic shells can be used to obtain quaddirectional beams, as discussed in the previous sections. On the other side, more complicated beam patterns can be generated by NZI shells with alternative geometries both in homogenized and realized forms. For instance, we consider diamond-like (pentagonal) shells in Figure 3.54 in order to obtain radiation patterns with five main beams. Similar to cubic shells, cavities are constructed by extracting square prisms from the shells. Considering cross sections, the dimensions of the pentagons are different. On the right-hand side of Figure 3.54, main parameters of the pentagons are given. Using this convention, the shells have the following dimensions.

- Diamond-SC:
  $a = 10\lambda, b \approx 1.67\lambda, c \approx 8.33\lambda$
- Diamond-SC-2:
  $a = 10\lambda, b \approx 3.33\lambda, c \approx 6.67\lambda$
- Diamond-SC-3:
  $a = 10\lambda, b \approx 4.17\lambda, c \approx 5.83\lambda$

We emphasize that the outer shape and dimensions of Diamond-SC-2-1 and Diamond-SC-3-1 are the same as those of Diamond-SC-2 and Diamond-SC-3, respectively. Only the placement of the cavities is different for these alternative designs, as described in Figure 3.54. The height of each shell is 5λ, while the square cavities have 2λ edge sizes. The numbers of unknowns vary from $192,348$ to $221,022$, while a Hertzian dipole is used as the primary source in each case. Considering power density distributions in Figure 3.54, we have the following observations.

- For the first structure, the surfaces with the shortest edges of the pentagon cannot provide strong beams. Therefore a tridirectional pattern is obtained instead of a quintdirectional one. The surface at the bottom that is the nearest one to the cavity has a stronger (brighter) beam than the other ones. We conclude that both cavity location and edge sizes are crucial in terms of the quality of the beams.
- In the case of the second and third structures, effects of increased edge lengths and cavity locations are observed. When the edge lengths shown by the red

lines in Figure 3.54 are increased, the corresponding surfaces lead to better beams. Similarly, the quality of the beams increases when the cavity is brought closer to the corresponding edges.

- The edges corresponding to the red lines in Figure 3.54 are further lengthened in the fourth design to increase the quality of some weak beams. Then, by bringing the cavity closer to the bottom surfaces, a five-beam radiation pattern is achieved, as depicted in Figure 3.54.

Figure 3.55: Power density distributions for homogenized models of diamond shells with square cavities having 2λ edge lengths and VGs.

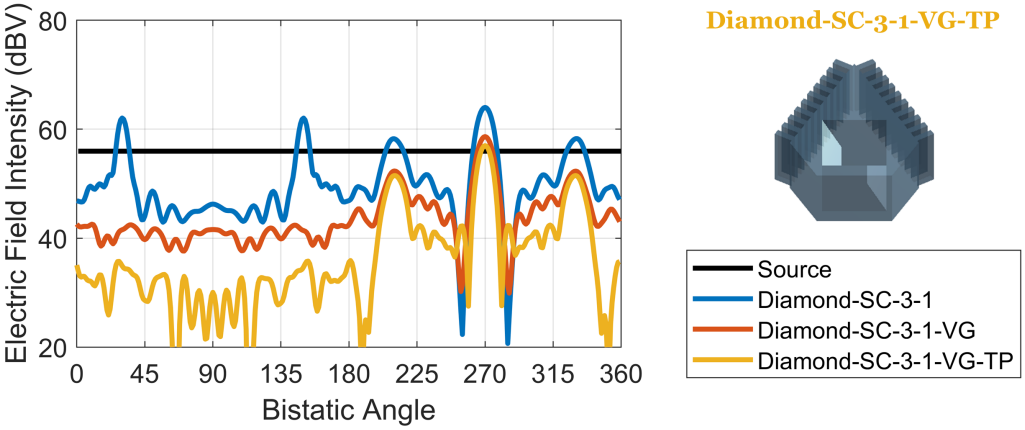

Figure 3.56: Far-zone radiation patterns for homogenized models of diamond shells with square cavities having 2λ edge lengths and VGs.

In order to inhibit electromagnetic waves that emerge from some of the surfaces, well-designed VGs are employed as shown in Figure 3.55. Specifically, two of five side surfaces of the diamond shell are covered via VGs, as shown in the second column of Figure 3.55. We observe high-quality suppression of radiation from the intended surfaces. However, VGs also decrease the beam strengths (darker beams) in terms of power density values. Next, we further apply tapers to square cavities, leading to dramatic results, as shown in Figure 3.56. Specifically, when supported by tapers, nearly 20 dB suppression is achieved via VGs. It is remarkable that tapering decreases side lobes significantly without any visible change in the main-lobe levels. Further improvements can be made in these designs considering different applications. For instance, one can obtain a wider beam at 270° by employing NZI lenses to Diamond-SC-3-1-VG-TP. As a result, one wider and two directive beams can be obtained by such a design.

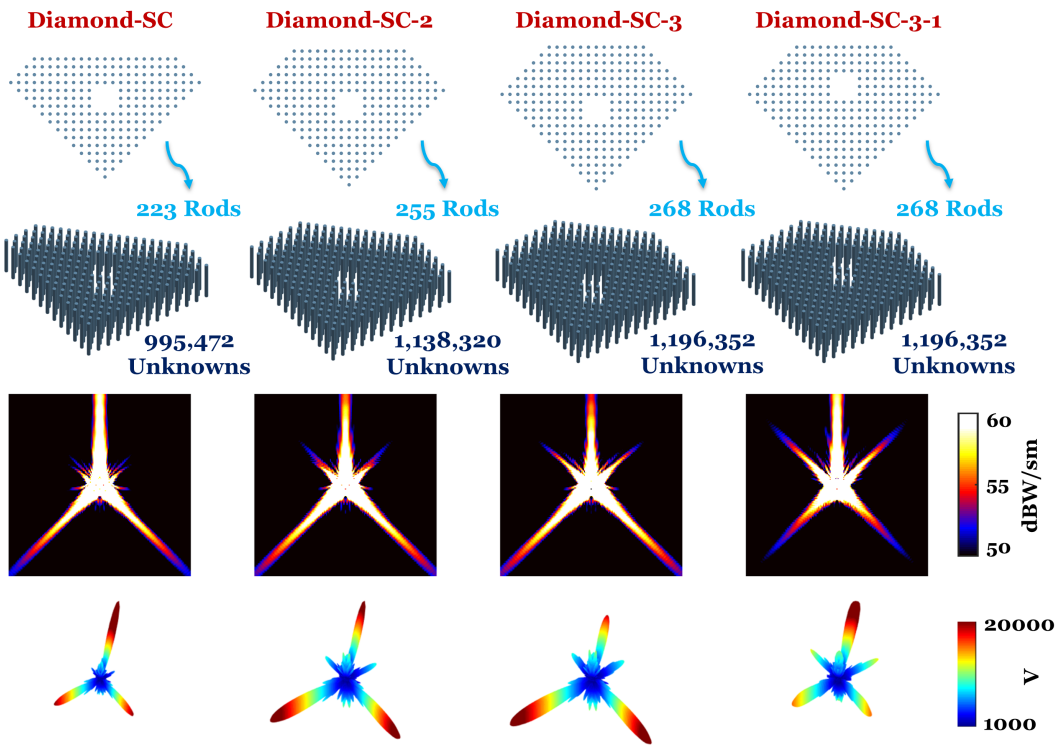

Figure 3.57: Geometries and numerical results for the realized diamond shells involving 3λ rods. The numbers of unknowns and rods are also given for each structure.

Next, we consider realized diamond shells involving periodic arrangements of alumina rods. Radius, center-to-center distances, and materials are chosen considering

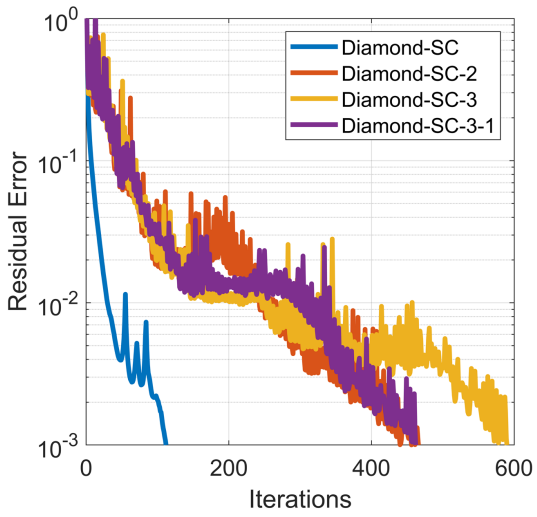

Figure 3.58: Iterative convergence histories in numerical solutions of the realized diamond shells involving 3λ rods.

the optimized designs in Section 3.4.3. Figure 3.57 illustrates geometries of four different diamond shells involving 3λ rods and the results of their simulations. Each design involves a square cavity (obtained by removing 3×3 rods) where a Hertzian dipole is placed as the source, as usual. For accurate representations of the homogeneous shells, large numbers of rods are used, leading to electromagnetic problems with more than one million unknowns (also listed in Figure 3.57). Thanks to the developed efficient solver involving a three-layer preconditioner based on AMLFMA, such large-scale simulations become feasible; the most challenging solutions take less than two days using 16 cores. Figure 3.58 depicts iterative solution histories (FGMRES iterations of the main layer) when JMCFIE is used as the formulation. The resulting power density distributions are provided in the third row of Figure 3.57. Similar to the results obtained for the homogenized diamond shells, smaller edges cannot provide strong beams when the realized models are used. In addition, cavity locations are crucial to obtain strong and clear beams. We note that, in Figure 3.57, from the left-hand side to the right-hand side, the realized diamonds are optimized step-by-step to obtain a quintdirectional beam pattern. For the first design, a tridirectional pattern is obtained instead of a quintdirectional one. Therefore, similar to the homogenized versions, the edges corresponding to weak beams are lengthened in the second and third designs. Finally, when the cavity location is shifted to reach

the final structure, the weaker beams are strengthened as desired, leading to the final high-quality radiation pattern.

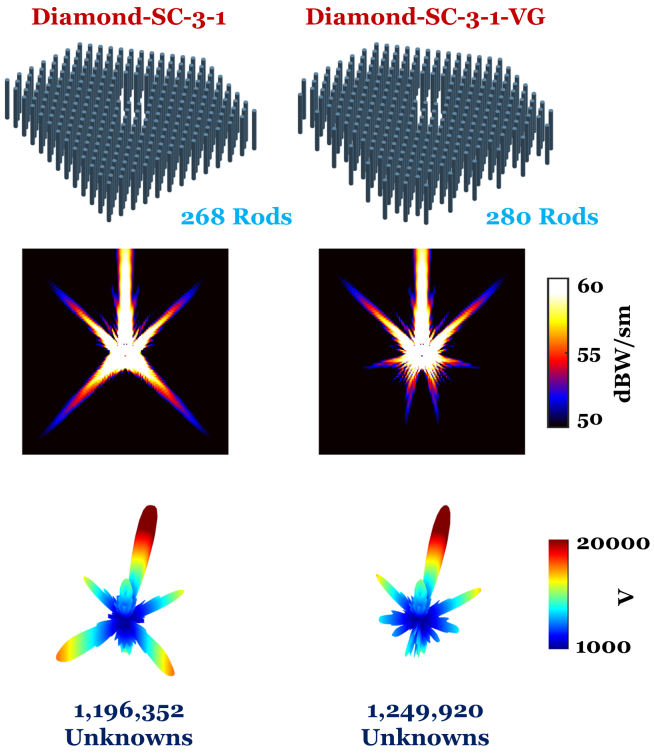

Figure 3.59: Results for realized diamond shells with/without VGs.

In order to suppress some of the beams, well-designed realistic VGs are placed on two sides of Diamond-SC-3-1, as shown in Figure 3.59. A total of 280 rods having 3λ heights are used to form the resulting Diamond-SC-3-1-VG design, which is discretized with $1,249,920$ unknowns. Near-zone power density distributions in the x-y plane (array plane) and 3D far-zone electric intensities are given below the simulated structures in Figure 3.59. Main beams are clearly visible in the consistent near-zone and far-zone results. On the other hand, unintended side lobes, such as upward and downward radiations, are observed in 3D results. When VGs are placed onto two of five sides of the realized diamond shell, nearly 10 dB suppression is obtained for the corresponding beams that emerge from these sides. As opposed to the observations for the homogenized models (where main beam levels are reduced), the three other beams are enhanced by nearly 1 dB when VGs are applied to the two surfaces. Although homogenized models can provide essential information on the main characteristics of NZI structures, these types of differences are commonly observed between

the homogenized and realized models, which indicates the necessity of simulations with both modeling strategies.

3.7 On the Dielectric Loss Tangents and Permeabilities

Up to now, dielectric rods used in realistic NZI shells are assumed to be lossless, which means that relative permittivity is purely real in the simulations. However, in real-life applications, dielectric losses may significantly deteriorate the overall performances of the designs. In particular, loss tangents must be considered in simulations when the frequency gets larger and they become non-negligible. Accordingly, we investigate the effect of the loss tangent on the performance of a realistic NZI shell involving a square cavity in Figure 3.60. The design of the shell can be seen in Figure 3.35, while dielectric losses are included for the first time in these numerical results.

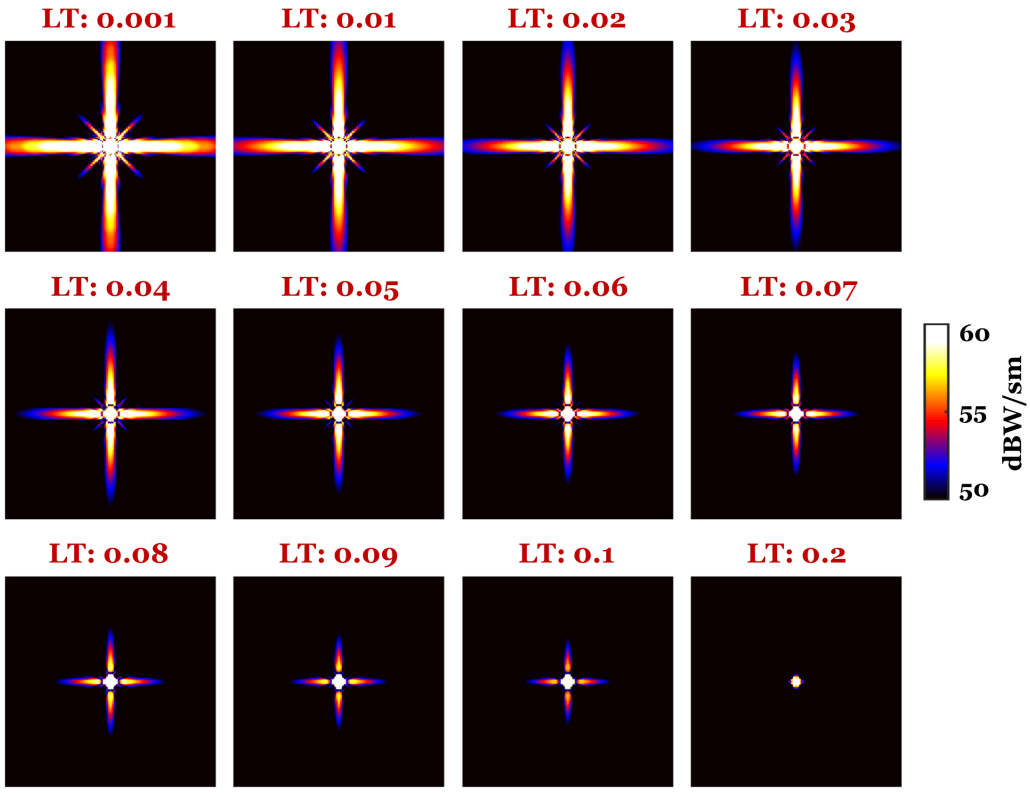

Figure 3.60: Power density distributions for a realistic NZI shell involving a square cavity (see Figure 3.35) when lossy dielectric rods are used.

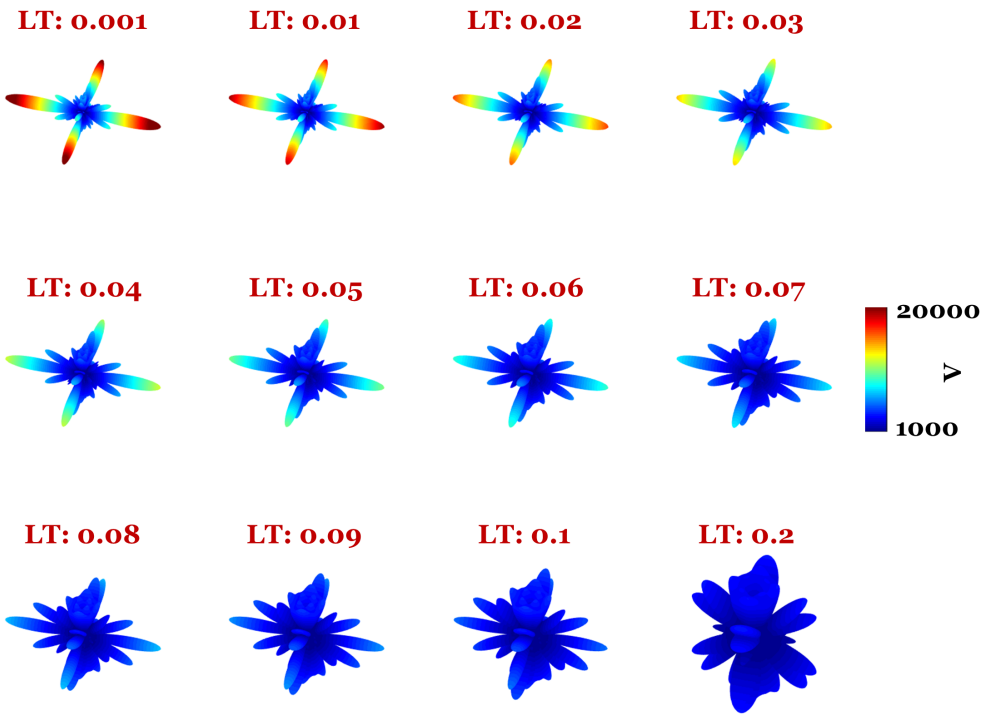

Figure 3.61: 3D radiation patterns for a realistic NZI shell involving a square cavity (see Figure 3.35) when lossy dielectric rods are used.

The relationship between the complex permittivity and loss tangent can be written as

$$\epsilon_r = \epsilon_{Rr} + i\epsilon_{Ir} \tag{3.5}$$

$$\tan\delta = \frac{\epsilon_{Ir}}{\epsilon_{Rr}}, \tag{3.6}$$

where ϵ_{Rr} and ϵ_{Ir} correspond to real and imaginary parts of the complex relative permittivity and $\tan\delta$ represents the loss tangent. In the simulations presented in Figure 3.60 and Figure 3.61, the loss tangent is used in a range $[0.001, 0.2]$. Considering power density results, we observe that, although the quaddirectional pattern is preserved, radiations become weaker with higher loss values. On the other hand, when we consider 3D electric field intensity results in Figure 3.61, we observe that there are significant side lobes that deteriorate the radiation performance (without any recognizable quaddirectional pattern in the overall radiation) when the loss increases. Thus, material properties, including losses, are extremely critical parameters to be considered while designing NZI shells.

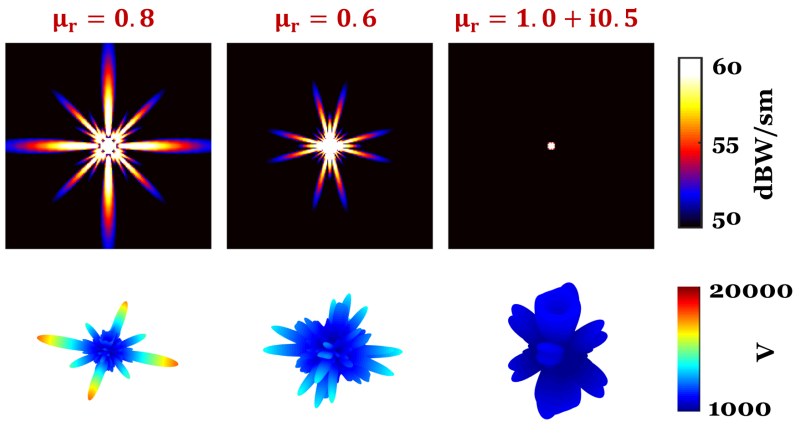

Figure 3.62: Results fora realistic NZI shell involving a square cavity when the relative permeability of the rods is not unity.

Next, we investigate possible effects of relative permeability values other than unity. Similar to ϵ_r, the complex relative permeability can be written as

$$\mu_r = \mu_{Rr} + i\mu_{Ir}, \tag{3.7}$$

where μ_{Rr} and μ_{Ir} correspond to real and imaginary parts. In the literature, while designing PhCs that demonstrate NZI properties, μ_r is assumed to be unity. However, effects of μ_r values other than unity (as well as magnetic losses) should also be considered, depending on the material used. Figure 3.62 illustrates near-zone and far-zone results for a realistic NZI geometry involving 9×9 rods and a square cavity. When μ_r of the rods decreases, or magnetic losses are added, the radiation characteristics of the NZI shells significantly deteriorate. Consequently, in practical applications, precise values of both ϵ_r and μ_r that correctly represent the material must be used.

3.8 Sensitivity Analyses

In this thesis, the designs are analyzed as 3D structures using full-wave computational methods based on SIEs and different forms of MLFMA. This simulation environment allows us to investigate inevitable fabrication errors; thus, we can predict the effects of nonidealities and possible solutions to them before the fabrication process. The

following sections present such sensitivity analyses on a realistic NZI shell involving a square cavity.

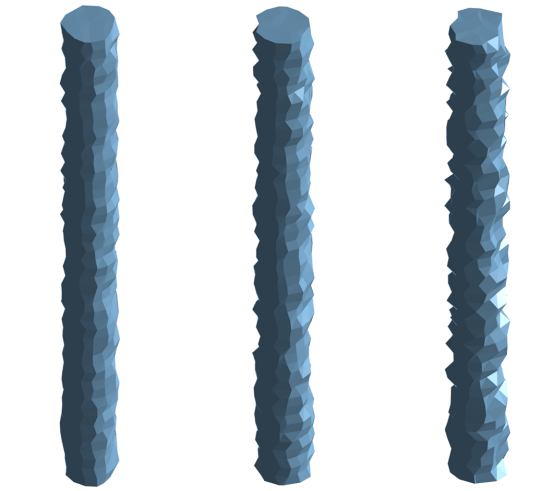

Figure 3.63: Deformed rods with various levels of lateral noise and vertical noise that is adjusted as 10% of the lateral noise.

3.8.1 Effects of Surface Corrugations and Unit-Cell Placement Errors

We consider computational analyses of deformed or disordered rods, considering the realistic structure with 3λ rods and a square cavity depicted in Figure 3.35. In these analyses, our aim is to obtain realistic data to support experimental analyses of NZI shells. Figure 3.63 illustrates deformed rods having a base radius of 3.75 mm ($\approx 0.13\lambda$) with [$-\lambda/M$, λ/M] shifts in the lateral directions, where M is set as 80, 60, and 40, corresponding to maximum 0.36 mm, 0.49 mm, and 0.73 mm shifts, respectively. We also apply random shifts in the vertical direction by 10% (in order to preserve the rod geometry) of the lateral noise. In Figure 3.64, we investigate the effects of surface corrugations by using the deformed rods as unit cells of the realistic geometry. Next, we focus on how random positioning errors can affect the characteristics of the realistic structure with non-deformed rods, as shown in Figure 3.65. To model random errors in positioning, we introduce a parameter Δa such that each rod is randomly shifted within [$-\Delta a$, Δa] area. In Figure 3.65, from the left-hand side to the right-hand side, Δa is set as 0.02, 0.04, and 0.06, respectively. Considering the results, we have the following conclusions.

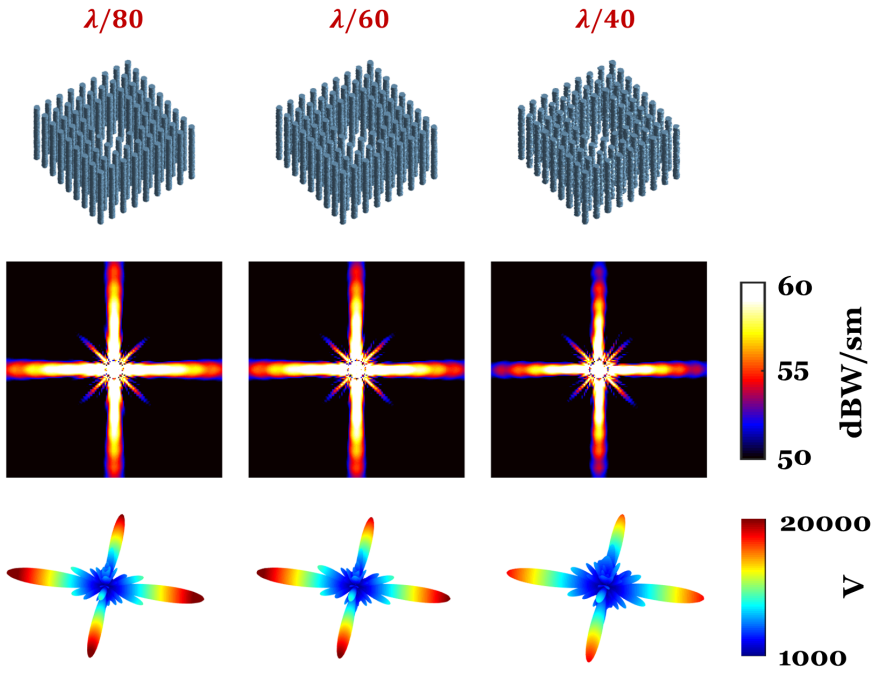

Figure 3.64: Results for an NZI shell geometry involving a square cavity when deformed rods are used.

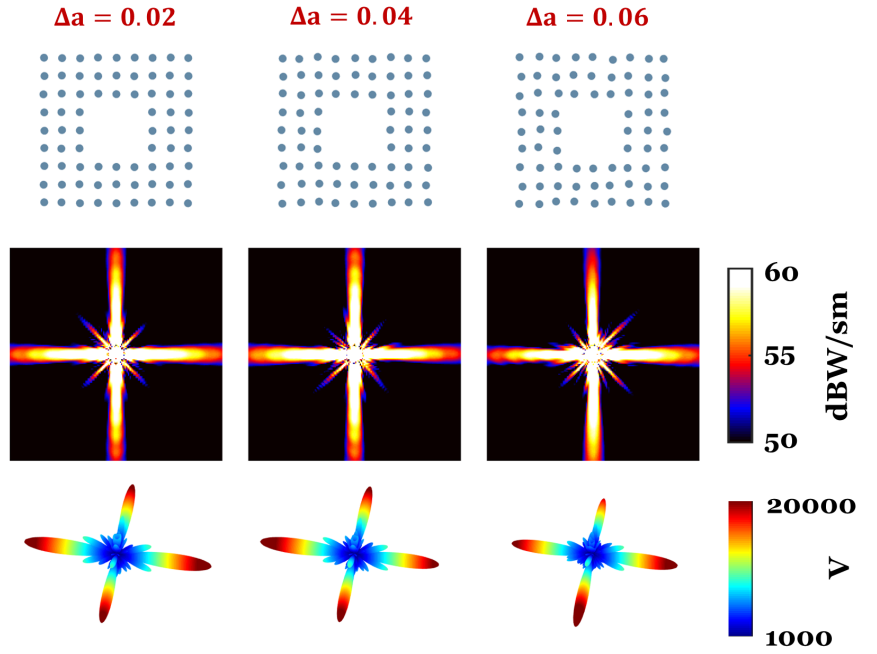

Figure 3.65: Results for an NZI shell geometry involving a square cavity when random positioning errors are introduced.

- When surface corrugations are applied onto the rods, as shown in Figure 3.64, we observe that the main beams become weaker in terms of the power density. In addition, asymmetric radiations are visible due to the corrugated rods. However, it is remarkable that even for the highly deformed rods in the third column, the quaddirectional pattern is perfectly preserved.

- The influence of randomly misplaced rods is depicted in Figure 3.65. We observe that the beam characteristics change when the rods become more disordered, leading to unequally distributed electromagnetic power towards the four directions. Nevertheless, the quaddirectional pattern is successfully maintained even for the most disordered case.

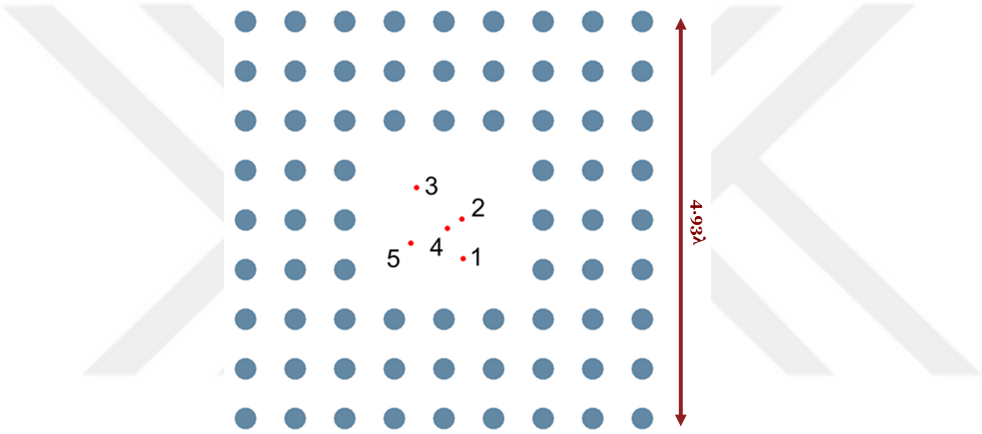

Figure 3.66: Source placement errors represented by five different locations in a $0.5\lambda \times 0.5\lambda$ area.

3.8.2 Effects of Non-Ideal Source Locations

Next, we examine the effect of the non-ideal source location, i.e., when the Hertzian dipole is misplaced, as depicted in Figure 3.66. If the center of the square hole is assumed as the reference point $(0, 0)$, five different locations are randomly chosen in a $0.5\lambda \times 0.5\lambda$ area. In fact, these locations represent placement errors that are too high to be made in real-life applications, but our aim here is to see the limits of source misplacement. Figure 3.67 illustrates near-zone power density results for the realistic structure with a square hole when five different source locations are investigated. When the source location approaches the center of the cavity (see locations 2 and 4),

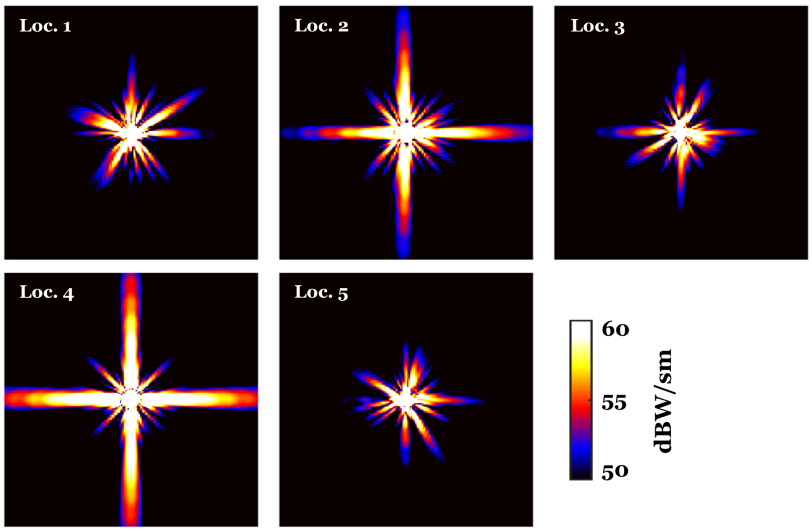

Figure 3.67: Results for an NZI shell geometry involving a square cavity when a Hertzian dipole is randomly located as depicted in Figure 3.66.

the quaddirectional radiation characteristics are observed, even though the pattern becomes asymmetric. Specifically, the beams in the direction of the source shift become stronger. On the other side, the structure becomes useless when the source is placed at locations 1, 3, and 5. These results indicate the importance of the cavity region, particularly its strong excitation via internal mechanisms (e.g., resonances), to obtain an efficient beam generator.

3.8.3 Frequency Response of the Square Cavity

We also check the frequency response of the designed structure, which is now exemplified by a realistic structure with 3λ rods and a square cavity (see Figure 3.35). Figure 3.68 illustrates near-zone power density distributions when a Hertzian dipole is placed at the center of the structure. The operating frequency is altered from 9.9 GHz to 10.7 GHz with 0.1 GHz steps. It is remarkable that the quaddirectional characteristics are preserved in the whole range of the frequency. In fact, at some frequencies other than the design frequency, the structure operates better with stronger main beams and lower side lobes.

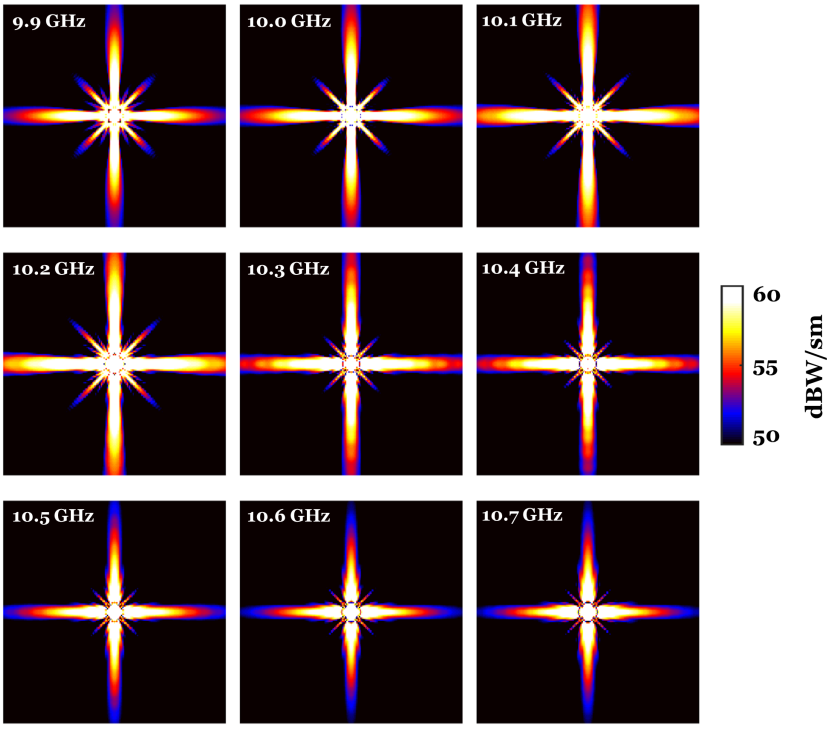

Figure 3.68: Frequency response (near-zone power density distributions) of the structure in Figure 3.35.

3.9 Efficiency Analyses

The designed structures are also investigated in terms of efficiency, considering general parameters of antennas, such as radiated power, directive-gain, and directivity.

3.9.1 Numerical Calculation of Radiated Power, Directive-Gain, and Efficiency

Farzone electric field intensity radiated from an antenna can be written as

$$\boldsymbol{E}(\boldsymbol{r}) = \frac{e^{ikr}}{r}\left(\hat{\boldsymbol{\theta}}E_\theta(\theta,\phi) + \hat{\boldsymbol{\phi}}E_\phi(\theta,\phi)\right) \tag{3.8}$$

$$F(\theta,\phi) = |E_\theta(\theta,\phi)|^2 + |E_\phi(\theta,\phi)|^2, \tag{3.9}$$

where E_θ and E_ϕ are far-zone electric field components, $1/r$ is the decay factor, and e^{ikr} is the phase factor, while $\boldsymbol{r} = \hat{\boldsymbol{r}}r + \hat{\boldsymbol{\theta}}\theta + \hat{\boldsymbol{\phi}}\phi$ is the position vector. Using series approximation of integrals, the radiated power can be found numerically as

$$P_{\text{rad}} = \frac{1}{2\eta}\int_0^{2\pi}\int_0^{\pi}\frac{F(\theta,\phi)}{r^2}r^2\sin\theta d\theta d\phi = \frac{1}{2\eta}\int_0^{2\pi}\int_0^{\pi}F(\theta,\phi)\sin\theta d\theta d\phi \tag{3.10}$$

$$P_{\text{rad}} = \frac{1}{2\eta}\left(\frac{\pi}{N}\right)\left(\frac{2\pi}{M}\right)\sum_{m=1}^{M}\left[\sum_{n=1}^{N}F(\theta_n,\phi_m)\sin\theta_n\right]. \tag{3.11}$$

Then, the directive gain of the antenna can be obtained by

$$D = \frac{4\pi F(\theta,\phi)}{\left(\frac{\pi}{N}\right)\left(\frac{2\pi}{M}\right)\sum_{m=1}^{M}\left[\sum_{n=1}^{N}F(\theta_n,\phi_m)\sin\theta_n\right]}, \tag{3.12}$$

while directivity can be expressed as the maximum value of the directive gain. For multi-beam antennas, the directive gain can be found for different beams by using (3.12). In addition, power radiated by an infinitesimal dipole can be found analytically as [94]

$$P_{\text{Hertz}} = \eta\left(\frac{\pi}{3}\right)^2\left|\frac{I_0 L}{\lambda}\right|^2, \tag{3.13}$$

where I_0 and L correspond to the current (constant) and the length of the antenna, while $|I_0 L| = 1$ is used in our simulations for both Hertzian-dipole and CSP beam excitations. A significant parameter to assess the designed NZI structures is efficiency. In this thesis, the efficiency is defined as the ratio of the total radiated power by an NZI structure (when it is excited by a Hertzian dipole) to the radiated power of the Hertzian dipole in free space. Derivations of field values for a Hertzian dipole (and a CSP beam) without any approximation are presented in Section 2.1.6. On the other hand, (3.13) can directly be used to calculate the radiated power by a Hertzian dipole. Radiated power of an overall system, which includes both the Hertzian dipole and the NZI structure, can be calculated by using (3.11). Then, the efficiency can be found as

$$e_{\text{system}} = \frac{P_{\text{rad}}}{P_{\text{Hertz}}}. \tag{3.14}$$

3.9.2 Performances of the NZI Beam Generators

Some of the designed NZI beam generators are considered and studied in terms of directivity and efficiency (with respect to the primary source).

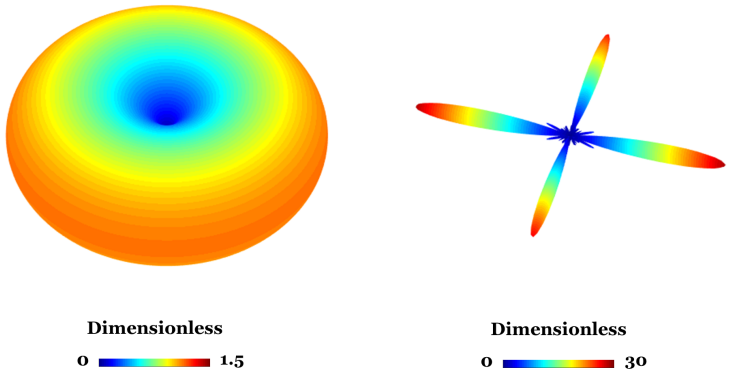

Figure 3.69: Directive gain of a Hertzian dipole (left) and a realistic structure (see Figure 3.35) excited by a Hertzian dipole (right).

First, by using (3.13), a Hertzian dipole's radiated power at 10.3 GHz can be computed as $P_{\text{Hertz}} = 4.65 \times 10^5$ W. Then, its directivity can be found as $D_{max} = 1.500$ in a linear scale. On the other side, we can numerically calculate the radiated power and directivity of the Hertzian dipole at 10.3 GHz by using (3.11) and (3.12). We compute the 3D electric field intensity at 181×361 samples (on a sphere) in the far zone. Then, the radiated power and directivity are obtained approximately as $P_{\text{Hertz}} = 4.63 \times 10^5$ W and $D_{max} = 1.508$, respectively. Consistency with the analytical values indicate that the expressions in (3.11) and (3.12) can successfully be used to compute the radiated field and directivity for NZI structures. Figure 3.69 depicts 3D directive-gain plots for the Hertzian dipole and the realistic shell with a square hole in Figure 3.35, when they are calculated by using (3.12).

Table 3.2 demonstrates the effect of the loss tangent on the efficiency and directivity, considering the realistic shell with 3λ rods and a square hole in Figure 3.35. The ratio of the radiated power by the overall system and the Hertzian dipole is used to compute the efficiency via (3.14). When a lossless material is used for the rods, the efficiency is 69.7%, while a very high directivity can be obtained as 14.63 dBi. We note that all four beams of the square cavity have the same directive-gain value. On the other side,

Table 3.1: Efficiency analysis of the realistic shell in Figure 3.35 when the material of the rods has different loss-tangent values.

Loss Tangent	$P_{\text{rad}}(W)$	e_{system}	$e_{\text{system}}(\%)$	$D_{\text{max}}(dBi)$
0	3.225×10^5	0.697	69.7	14.6
0.001	3.109×10^5	0.672	67.2	14.6
0.01	2.381×10^5	0.515	51.5	14.3
0.04	1.279×10^5	0.276	27.6	12.7
0.08	0.802×10^5	0.173	17.3	9.95
0.1	0.697×10^5	0.151	15.1	8.37
0.2	0.535×10^5	0.116	11.6	5.93

we observe that radiated powers become smaller with higher loss values, as expected. For very high loss values, both the efficiency and directivity can be considered to be at unacceptable levels.

Table 3.2 presents the efficiency and directivity results when surface corrugations or placement errors are introduced for the same shell structure with a square hole. It is remarkable that placement errors do not negatively influence efficiency and directivity. However, when surface corrugations are increased, both the efficiency and directivity decrease, while they remain at quite high levels even for large deformations.

3.10 Concluding Remarks

We present computational design and analyses of novel NZI shell structures. In the devised design procedure, we initially decide the number of sides of the shell geometry considering the number of desired beams. Then, well-designed NZI cavities with strong resonance characteristics are obtained, when isotropic sources are placed in them. Both homogeneous and realistic NZI structures are considered in the design steps. An effective index analysis setup is developed based on Hough line transform, where reflection characteristics of NZI prisms are investigated to estimate refractive index for given rod arrangements, and, this way, to reach efficient NZI designs. We

Table 3.2: Efficiency analysis of the realistic square hole when surface corrugations or unit cell placemet errors are applied.

Structure	$P_{\text{rad}}(W)$	e_{system}	$e_{\text{system}}(\%)$	$D_{\text{max}}(dBi)$
Placement Error, $\Delta a = 0.02$	3.198×10^5	0.691	69.1	14.46
Placement Error, $\Delta a = 0.04$	3.253×10^5	0.703	70.3	14.65
Placement Error, $\Delta a = 0.06$	3.340×10^5	0.722	72.2	14.97
Surface Error ($\lambda/80$)	3.040×10^5	0.657	65.7	14.42
Surface Error ($\lambda/60$)	2.848×10^5	0.615	61.5	14.33
Surface Error ($\lambda/40$)	2.395×10^5	0.518	51.8	13.41

also show the scalability of the designs in terms of frequency.

Various VGs and inverted pyramids are designed to suppress outgoing fields, whereas cylindrical lenses are used to enhance beams and widen their beamwidths. The obtained results clearly demonstrate that modifications on outer surfaces of both homogeneous and actual shell models can suppress or enhance intended beams; thus, compact NZI shells with diverse radiation patterns can be obtained for a plethora of applications. As examples of more complicated beam patterns, we examine diamond-like NZI shells both in homogenized and realized forms.

We show that the designed beam generators can be sensitive to source location errors, while they are more resistant to surface corrugations and rod placement errors. Consequently, efficient, effective, and error-tolerant beam generators are obtained by using NZI structures. In the next chapter, we consider the fabrication and measurement of some selected structures, as the verification of these designs in real life.

CHAPTER 4

FABRICATION AND MEASUREMENT OF NEAR-ZERO-INDEX BEAM GENERATORS

NZI shells enable the design of compact and efficient beam generating structures that can be used in a plethora of applications, such as small cells in new-generation communication systems. While homogenized models facilitate design and analyses of various configurations, actual models are realized structures in real life. Consequently, both homogenized and actual models have been considered so far to design effective structures with strong resonance characteristics and beam-generating capabilities. On the other hand, in order to fabricate NZI shells, suitable materials with high relative permittivity values are needed, whereas they must also have low losses to obtain sufficiently high efficiency. In this chapter, we finally focus on the fabrication and measurement of NZI beam generators, considering and studying various alternatives as the fabrication material.

Figure 4.1 depicts a detailed version of the fabrication and measurement steps given in Figure 3.1. Firstly, considering the operating frequency, initial dimensions and material properties of the rods are decided. However, it is not straightforward to find proper materials with high relative permittivity values or to fabricate them with desired sizes. Therefore, in order to identify materials with intended properties, such as high relative permittivity and low loss tangent values, a material characterization setup is prepared based on the Nicholson-Ross-Weir (NRW) method [95–97]. In particular, we measure the reflection and transmission coefficients of promising samples by placing them into waveguides and using a vector network analyzer. Then, constitutive parameters are found by using these coefficients.

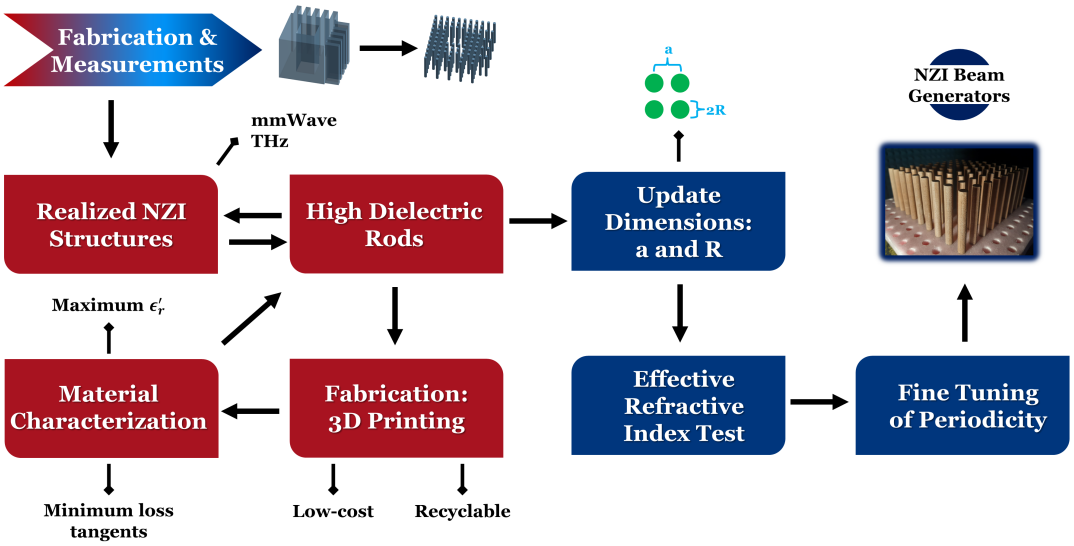

Figure 4.1: The fabrication and measurement process of an NZI shell acting as a multi-beam generator.

Table 4.1: Some high-contrast dielectric materials with nonmagnetic properties.

Material	Frequency (GHz)	ϵ_{Rr}	ϵ_{Ir}	$\tan\delta$
Alumina (99.5%)	10	9.5–10	0.0028–0.003	0.0003
Silicon	10	11.9	0.0476	0.004
Gallium Arsenide	10	13.0	0.078	0.006
Glazed Ceramic	10	7.2	0.0576	0.008

Table 4.1 presents major properties of some high-contrast dielectrics [98]. As shown in the previous sections, throughout the design steps of various NZI shells, alumina with different purity values is considered. Alumina can provide high permittivities with low-loss tangent values; however, its fabrication is relatively difficult, and particularly expensive when high tolerance values are required. Considering the ease of fabrication, accessibility, and design freedom, we prefer 3D printers. Then, high-contrast dielectric materials compatible with 3D printing are needed to fabricate cylindrical rods. We note that defective or low-quality products can be recycled as feedstocks (namely, 3D printing filaments) of 3D printers. Hence, both low-cost and recyclable structures can be obtained via 3D printing. After the material selection, the

radius of rods and center-to-center distances between them are carefully calculated for the optimal performance. Using the developed effective refractive index test setup in the simulation environment, we check whether or not the realized NZI structures are expected to demonstrate low refractive index characteristics. After fine-tuning center-to-center distances, we end up with NZI beam generator.

Additive manufacturing have attracted the interest of many researchers in the area of electromagnetics as they may provide rapid fabrication of some RF devices and antennas [43–47]. However, commercially available 3D printing materials are generally not designed for microwave engineering. Therefore, they mostly have relatively low permittivity values and high loss tangents. In addition, an accurate electromagnetic characterization of 3D-printed materials is needed to find and insert their constitutive parameters into design steps of antennas and resonators.

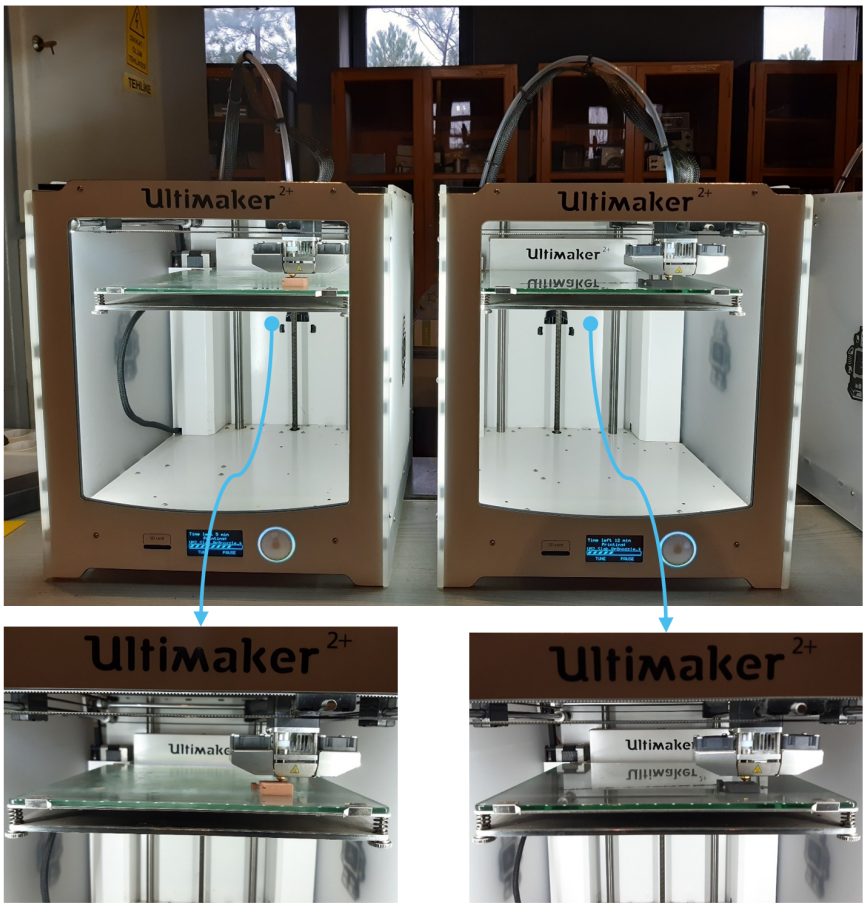

Figure 4.2: 3D printing process of some composite filaments.

Fused filament fabrication (FFF), which is used in this study, is one of the most common 3D printing methods due to its simplicity and low cost. In this method, a thermoplastic polymer is used in the shape of a filament. Then, a heated nozzle is employed to produce melted plastics that form the printed object layer-by-layer. Figure 4.2 depicts the fabrication environment involving two 3D printers. At the bottom of the figure, zoomed images show some objects that are being built on the heated plates (beds). We use Ultimaker 2+ 3D printers having FFF technology, as they are compatible with different filament types and nozzle sizes.

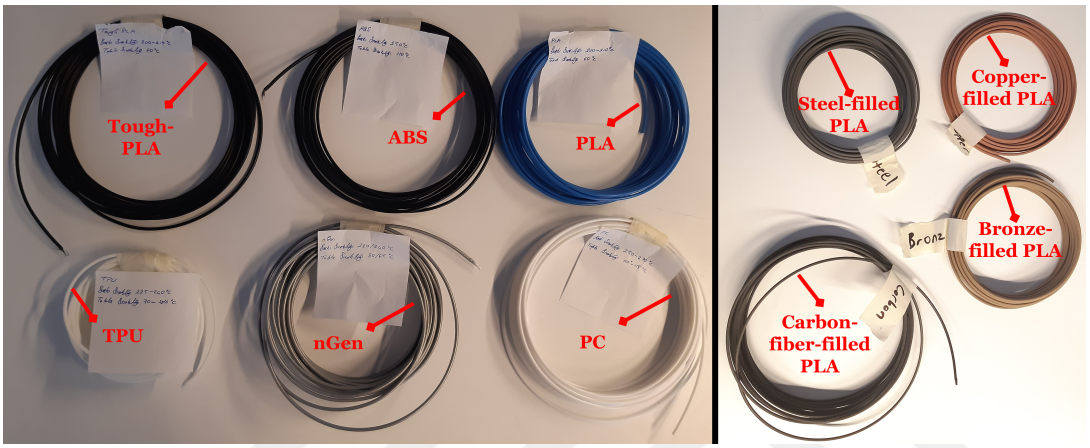

Figure 4.3: Various 3D printing filament samples used in this study. Tough-PLA's vendor is Ultimaker. The vendor of the other filaments is colorFabb.

Figure 4.3 presents ten different 3D printing filaments that were considered to be potential materials to build NZI structures. They are generally thermoplastic-based materials. For instance, polylactic acid (PLA), which is a biodegradable thermoplastic, is a polymer involving lactic acid molecules. Acrylonitrile butadiene styrene (ABS) is an amorphous thermoplastic, which has a high strength suitable for industrial applications. Polycarbonate (PC) is a highly durable and heat-resistant material. Thermoplastic polyurethane (TPU) is an elastic filament that can be bent or compressed. nGen (made of amphora AM3300) has good flow properties suitable for printer nozzles, even at low temperatures. On the other hand, composite filaments consist of various additives, such as ceramics, carbon, bronze, copper, aluminum, and stainless steel. In particular, these additives are used together with thermoplastics (PLA and ABS) to obtain special qualities for different application areas. For instance, the addition of conductive carbon particulates to PLA leads to conductive

PLA. Similarly, iron powders can be added to PLA to obtain magnetic PLA. On the other side, carbon fiber PLA composite can provide high resistance to melting. The mix of some metal powders (bronze, copper, and stainless steel) and either PLA or ABS are mostly used to obtain shiny outlooks, like in statues. We note that all these 3D printing filaments are low-cost and commercially available. Although there is a wide range of such commercially available composite materials for additive manufacturing, their applications are limited in the area of electromagnetics. There are also a few special filaments that can be used particularly in RF applications. For example, in order to obtain high dielectric constants with low loss values, some ceramics, such as $\mathrm{BaTiO_3}$ micro-particles, can be used in ABS, leading to $\epsilon_r = 11$ in the GHz range [46, 99].

Table 4.2: Dielectric properties of 3D-printed materials.

Material		**Frequency**	ϵ_{Rr}	ϵ_{Ir}	$\tan\delta$
PLA	[43]	300 MHz	2.95	0.041	0.014
	[44]	200 MHz	2.72	0.022	0.008
	[45]	2.5 GHz	2.90	0.061	0.021
	[47]	9–10 GHz	3.47	0.253	0.073
PC [44]		200 MHz	3.64	0.015	0.004
ABS	[43]	300 MHz	3.11	0.044	0.014
	[44]	200 MHz	3.50	0.018	0.005
	[45]	2.5 GHz	2.60	0.047	0.018
Conductive PLA [47]		9–10 GHz	6.81	3.357	0.493
Magnetic PLA [47]		9–10 GHz	3.65	0.683	0.187
Steel-filled PLA [45]		2.5 GHz	6.30	0.214	0.034
Copper-filled PLA [44]		200 MHz	8.42	0.059	0.007
Ceramic-filled ABS [46]		10 GHz	9.64	0.029	0.003

Table 4.2 lists complex relative permittivity values for various 3D printing filaments. Resonators and cavities are used to measure the relative permittivity, especially at lower frequencies, while transmission lines and waveguides are used for the mea-

surements in the GHz regime. We note that all these measurements assume unity relative permeability (nonmagnetic assumption), which may not be correct for some materials. Considering Table 4.2, thermoplastics seem to have lower ϵ_{Rr} values. Specifically, the maximum available ϵ_{Rr} values are 3.47, 3.64, and 3.50 for PLA, PC, and ABS, respectively. The discrepancy in the measured results can be related to different fabrication (printing) settings. Specifically, 3D printed objects typically have pores with different sizes and 100% homogeneous structures cannot be obtained, while the sizes, numbers, and distributions of pores directly affect constitutive parameters. Also, the vendors of the filaments are different, such as Proto-pasta, Fillamentum, eSUN, and Preperm, while different measurement techniques are used in the studies in Table 4.2. Although conductive PLA at the ninth row of Table 4.2 has a relatively high dielectric constant, its loss tangent is also high that reduces its suitability to realize efficient shells. On the other hand, composite filaments at the last three rows (marked by light cyan) can provide the desired relative permittivity values, which are critical to obtain realistic NZI shells.

4.1 On the Measurement of Constitutive Parameters

3D printing has plenty of advantages, such as being low-cost and providing diverse design options; however, electromagnetic parameters of 3D printing filaments are not "stable" in the context of RF applications. Due to the diversity of printing options and conditions in the fabrication environment, such as the temperature, fabricated samples may not have consistent ϵ_r and μ_r values even if they are made of the same material. Thus, before designing realistic NZI shells, electromagnetic parameters of the high-contrast dielectric printing filaments that can potentially be used must be studied carefully, considering printing options and other parameters. Accordingly, to measure electromagnetic properties, we use NRW method based on the transmission line technique. The method was initially proposed by Nicholson and Ross [100], and then adapted to network analyzers by Weir [95, 96]. Via a network analyzer and a computer software, complex ϵ_r and μ_r values can be obtained from the measured scattering parameters (S-parameters).

In the measurements of electromagnetic parameters, we consider a waveguide structure, as shown in Figure 4.4. The sample to be measured is placed in a sample

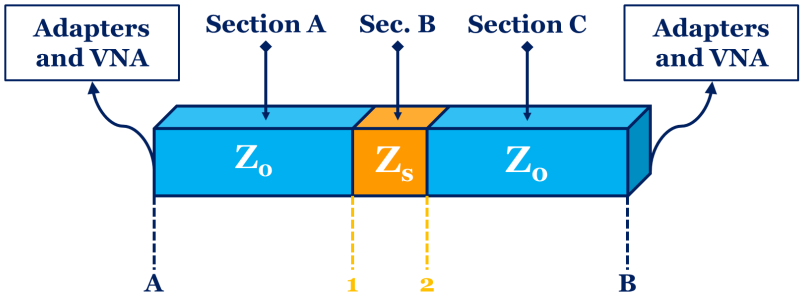

Figure 4.4: The measurement structure when a sample having intrinsic impedance Z_s is placed between two sections of waveguides (or transmission lines).

holder waveguide section (Sec. B), while two additional sections A and C are also used to prevent higher-order evanescent waves due to coaxial-to-waveguide transitions (adapters). The reflection coefficient (S_{11}) at the air-to-sample interface and the transmission coefficient (S_{21}) thru the sample should be found in reference planes 1 and 2. Therefore, measurement planes should be shifted from coaxial cable ends of the network analyzer to sample holder surfaces 1 and 2 via a thru-reflect-line (TRL) calibration.

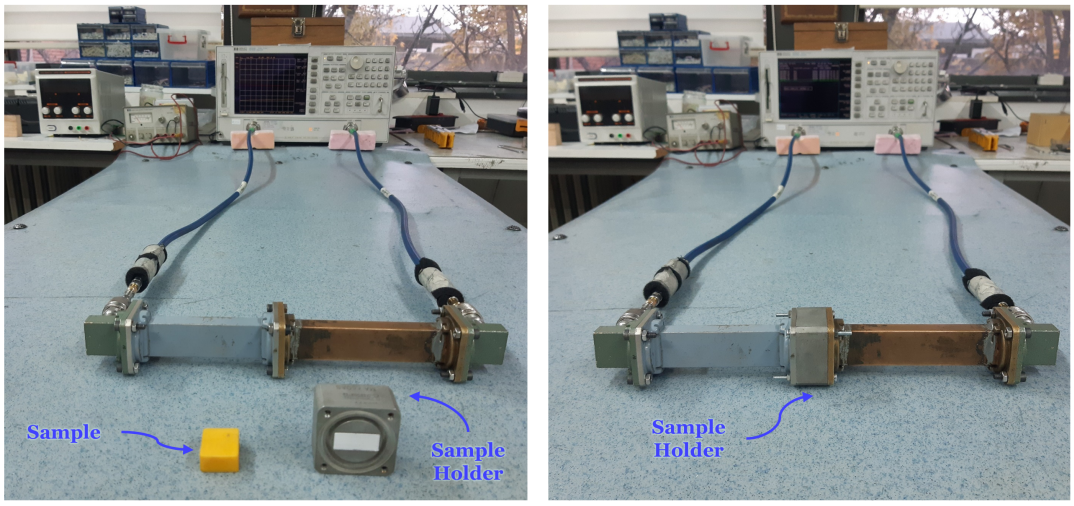

Figure 4.5: Electromagnetic characterization setup when a metallic sample holder waveguide with 20 mm thickness is used.

Figure 4.5 depicts the electromagnetic characterization setup when a metallic rectangular waveguide with 20 mm thickness is used as the sample holder. We use WR-

90 waveguide transmission lines and adapters, which operate in the X-band (8-12 GHz). S-parameters of samples are measured by HP 8720D vector network analyzer. The TRL calibration is made considering the thickness of the sample holder as the line length [101]. A waveguide short is employed as the reflect standard, while two waveguide sections are directly connected to each other to obtain the thru standard in the calibration process.

The transmission factor in a waveguide filled with the material under test can be found as

$$T = e^{-ikL} = e^{-\gamma L} = |T|e^{-i\phi}, \tag{4.1}$$

where γ is the propagation factor, L is the sample thickness inside the waveguide, and ϕ is the phase of the propagation factor. The reflection coefficient at the intersection of filled and empty waveguides can be obtained from the measured reflection and transmission coefficients as

$$\Gamma = K \pm \sqrt{K^2 - 1} \tag{4.2}$$

$$K = \frac{S_{11}^2 - S_{21}^2 + 1}{2S_{11}}, \tag{4.3}$$

where K is an auxiliary parameter. The sign of the square root term in (4.2) can be determined with respect to passivity condition ($|\Gamma| \leqslant 1$). For the transmission factor, we have

$$T = \frac{S_{11} + S_{21} - \Gamma}{1 - (S_{11} + S_{21}\Gamma)}. \tag{4.4}$$

Then, the relative permittivity and permeability of the sample can be computed as

$$\mu_r = \frac{1+\Gamma}{\Lambda(1-\Gamma)\sqrt{1/\lambda_o^2 - 1/\lambda_c^2}} \tag{4.5}$$

$$\epsilon_r = \frac{\lambda_o^2}{\mu_r}\left[\frac{1}{\lambda_c^2} - \left(\frac{\ln(1/|T|) - i\phi + i2\pi n}{2\pi L}\right)^2\right] \tag{4.6}$$

$$\Lambda = \frac{1}{\sqrt{-\left[\frac{1}{2\pi L}(\ln(1/|T|) - i\phi + i2\pi n)\right]^2}}, \tag{4.7}$$

where Λ is an auxiliary parameter, λ_o is the wavelength in vacuum, and λ_c is the cut-off wavelength of the WR-90 waveguides. The accuracy of the obtained ϵ_r and μ_r highly depends on the measured scattering parameter phase data. In addition, (4.5)–(4.7) contain an ambiguity since the propagation factor has 2π periodicity ($n = 0, \pm1, \pm2, ...$). For example, when the material thickness is an integer multiple of the half-wavelength, the phase measurements become ambiguous. In addition, when its thickness is equal to the half of the guided wavelength ($\lambda_g/2$), the NRW method also produces inaccurate results. One way to solve these issues is to use a sufficiently thin sample so that $n = 0$. In particular, the thickness of the sample (hence sample holder) should be less than the half of λ_g considering the maximum operating frequency in order to prevent inaccurate results.

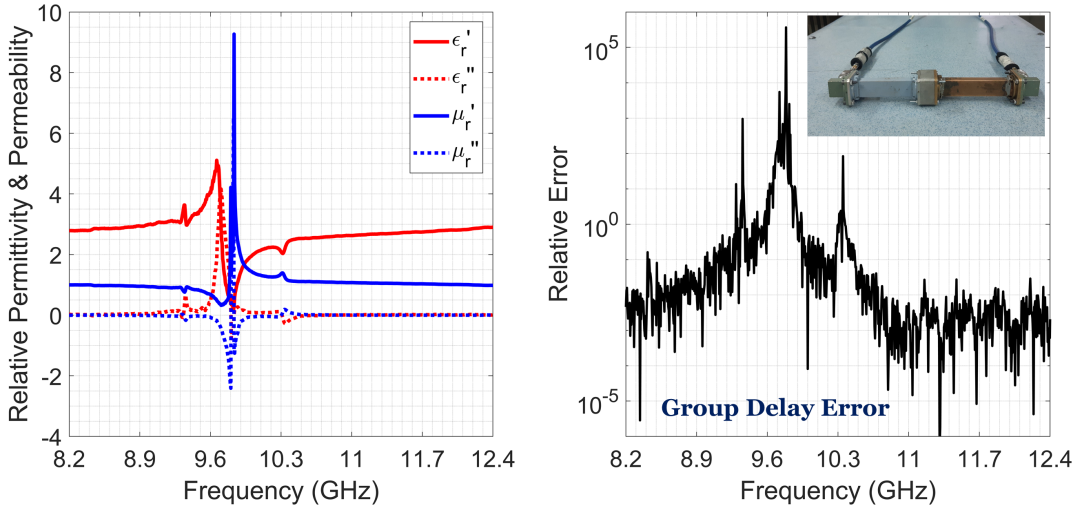

Figure 4.6: Complex relative permittivity and permeability measurement results when a metallic sample holder waveguide with 20 mm thickness is used.

Figure 4.6 illustrates measurement results for complex ϵ_r and μ_r values when a 3D-printed PLA (ColorFabb PLA, 2.85 mm filament thickness) is put under test. Its dimensions are adjusted considering the sample holder's dimensions as 22.86 mm $\times$ 10.16 mm $\times$ 20 mm. 100% infill ratio (filling density) and *lines* infill pattern (the nozzle's movement during the creation of layers) are used as printing settings to obtain an almost homogeneous sample, while a wide frequency range is investigated from 8.2 GHz to 12.4 GHz. We note that 20 mm corresponds to $\lambda_g/2$ when the frequency is nearly 9.67 GHz. Thus, at around this frequency, the measured reflection coefficient becomes almost zero, and erroneous results are obtained for ϵ_r and μ_r. Considering the stable region from 8.2 GHz to 8.9 GHz, we find $\epsilon_r \approx 2.83 + i0.097$, while μ_r is unity with almost zero imaginary part. In order to check the accuracy of the measurements, we calculate the group delay from the measured data. Since we know the thickness of the sample holder (L), the group delay for the sample can be found from the measured ϵ_r and μ_r data as

$$\tau_{gn} = L\frac{d}{df}\left[\left(\frac{\epsilon_r\mu_r}{\lambda_o^2} - \frac{1}{\lambda_c^2}\right)_n^2\right], \tag{4.8}$$

where n is 0 up to $\lambda_g/2$ and 1 after $\lambda_g/2$. Then, the measured group delay is calculated from the slope of the phase of the propagation factor as

$$\tau_g = \frac{1}{2\pi}\frac{d(-\phi)}{df}. \tag{4.9}$$

Accordingly, the relative error between (4.8) and (4.9) can be defined as

$$\text{RE} = \frac{|\tau_{gn} - \tau_g|}{|\tau_g|}. \tag{4.10}$$

On the right-hand side of Figure 4.6, the group delay error obtained by using (4.8)–(4.10) is depicted. The plot confirms the inaccuracy of the measured ϵ_r and μ_r data when the thickness of the sample is approximately $\lambda_g/2$. We also note that the ambiguous measurement region is very close to the design frequency of the NZI shells (10.3 GHz) in this thesis. Thus, in order to overcome the problem, we fabricate thinner sample holders via 3D printing. Figure 4.7 presents the measurement setup with

3D-printed samples and sample holders. A WR-90 waveguide section with 5 mm thickness is 3D-printed using PLA and aluminum tapes are used to cover the inner walls of the structure. Thanks to 3D printing, this kind of a waveguide section with desired dimensions can be fabricated in less than half an hour.

The initial electromagnetic characterization results for PLA are shown in Figure 4.8 when the 3D-printed sample holder is used in the measurements. Dimensions of the sample are 22.86 mm $\times$ 10.16 mm $\times$ 5 mm, while 100% infill ratio and *lines* infill pattern are used. It is remarkable that the $\lambda_g/2$ ambiguity is eliminated in these results. Specifically, nearly smooth (almost horizontal) lines are obtained as frequency-dependent ϵ_r and μ_r values of PLA, as expected. At the same time, the group delay error of the measurement is relatively stable in comparison to the corresponding plot in Figure 4.6, especially considering that the major peak disappears when the thinner sample holder is used. Consequently, we conclude that a highly accurate and efficient electromagnetic characterization setup is constructed. In the following sections, we present ϵ_r and μ_r measurements for various 3D printing filaments. In these experiments, we particularly aim to find a high-contrast dielectric material with relatively low loss values to realize NZI shell structures.

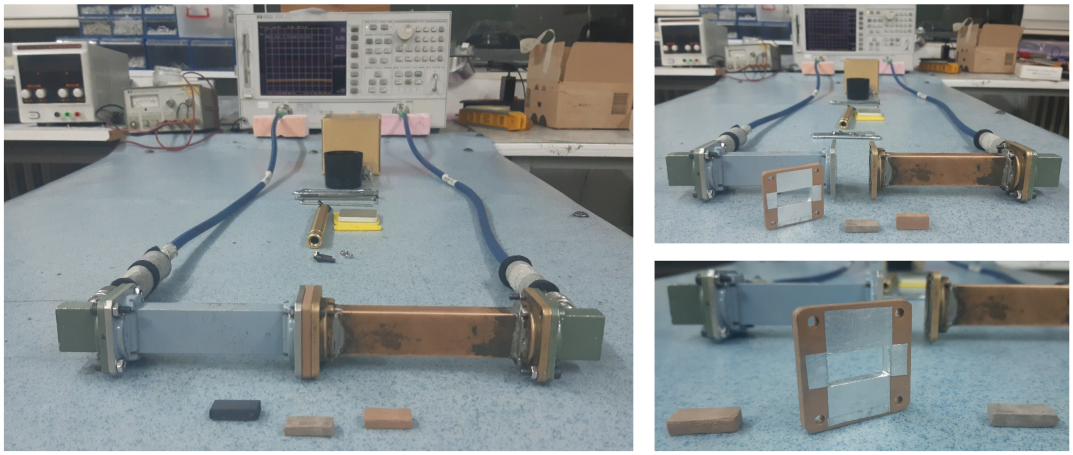

Figure 4.7: Electromagnetic characterization setup when a 3D-printed sample holder with 5 mm thickness is used. An aluminum tape is used to cover inner walls.

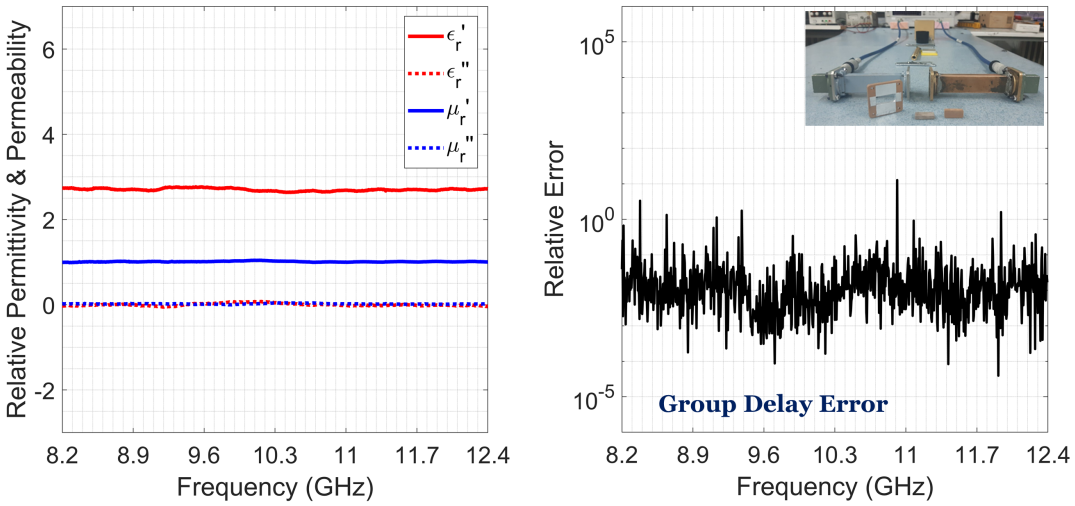

Figure 4.8: Complex relative permittivity and permeability measurement results when a 3D-printed sample holder waveguide with 5 mm thickness is used.

4.2 Material Characterization of 3D Printing Filaments

We examine various 3D printing filaments, which are commercially available in market, in terms of their electromagnetic properties. To avoid porosity and obtain homogeneous structures, 100% infill ratio and *lines* infill pattern are used in all fabrications. Considering the advised printing settings for different materials in their datasheets, 3D printing temperature, bed temperature, and 3D printing speeds are determined. For example, the print speed is generally adjusted to 60 mm/s. After the samples are produced, to remove any leftover blemishes, we sand the samples via an 80 grit sanding sponge. This way, the samples become ready for the measurement process.

Since network analyzers decrease root-mean-square error thru the initial and final frequencies in the calibration process, the frequency band under investigation is decreased to 400 MHz, while the center frequency is adjusted as 10.3 GHz. For each sample, four different measurements are made, and the mean of them is plotted.

4.2.1 Some Plastic Filaments

Thermoplastics generally have low dielectric constants with high loss tangents, as shown in Table 4.2. Their ϵ_{Rr} values are not higher than 3.6 unless some additives

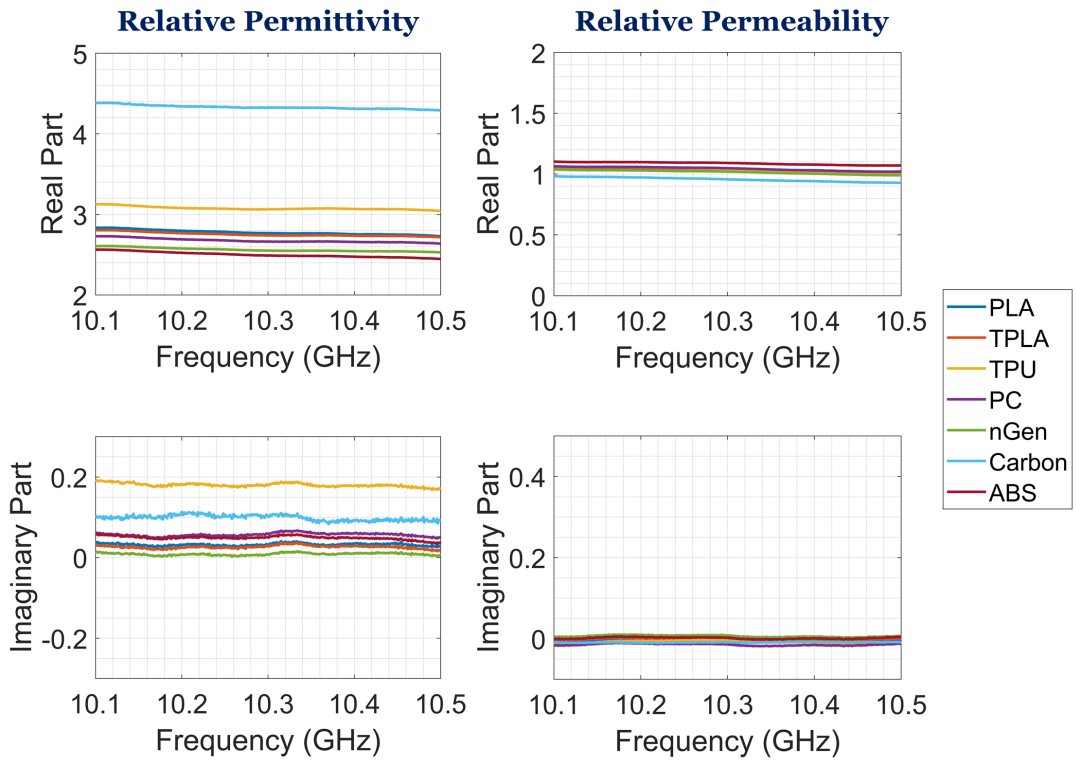

Figure 4.9: Electromagnetic properties of various thermoplastics. The 3D-printed sample holder with 5 mm thickness is used for measurements.

are used, such as metallic powders. In order to measure electromagnetic properties of different thermoplastics in Figure 4.3 and compare the results with those in the literature, we use the measurement setup involving the 3D-printed sample holder, described above. Dimensions of the samples are determined in accordance with the 3D-printed WR-90 waveguide section that has 5 mm thickness. Figure 4.9 depicts measurement results of complex ϵ_r and μ_r values, where seven different thermoplastics are considered. Carbon and TPLA correspond to carbon fiber-filled PLA composite and tough PLA (PLA with toughness similar to ABS), respectively. The real and imaginary parts of ϵ_r and μ_r are presented on the first and second rows in Figure 4.9. We observe that, due to carbon particles' diamagnetic properties, the real part of the relative permeability of the carbon fiber PLA composite is slightly less than unity. In contrast, the others have real relative permeability values slightly higher than unity. In addition, the imaginary parts of the relative permeability values are nearly zero for all materials.

Table 4.3: Measured relative permittivities of various thermoplastics.

Material	ϵ_{Rr}	ϵ_{Ir}	$\tan\delta$
PLA	2.768	0.0311	0.0112
TPLA	2.740	0.0278	0.0101
TPU	3.065	0.1801	0.0588
PC	2.663	0.0581	0.0218
nGen	2.551	0.0071	0.0028
Carbon	4.329	0.1069	0.0247
ABS	2.663	0.0498	0.0187

Examining the relative permittivity results in Figure 4.9, we observe that PLA and TPLA have very close ϵ_r values, while carbon additives clearly increase the relative permittivity of PLA. TPU seems to be the most lossy thermoplastic under test. On the other hand, nGen may be a good candidate for RF applications due to its low-loss values. Table 4.3 further lists dielectric characteristics of thermoplastics at 10.3 GHz (center frequency). PLA and ABS results are similar to those obtained by [44, 45] (in Table 4.2), whereas PC results seem to be different. In particular, our ϵ_{Rr} measurement results for ABS and PC are well-matched to the complex permittivity data in [102], while the obtained loss-tangent values are higher than those in [102]. This difference can be related to the 3D printing fabrication process. Even if the same materials are used, there can be deviations in the uniformity of prints, which highly depends not only on the filament quality but also on the 3D printer's performance.

4.2.2 High-Contrast Dielectric Composite Filaments

In order to realize NZI behavior, we generally need high-contrast dielectric rods with proper dimensions. Up to now, the maximum ϵ_{Rr} value is obtained for 3D-printed Carbon ($\epsilon_r = 4.329 + i0.1069$). On the other hand, as shown in Table 4.2, higher dielectric constants may be obtained with composite filaments involving metallic powders (or ceramics) and thermoplastics. Accordingly, we investigate three different composite filaments with metallic powders and carbon fiber PLA.

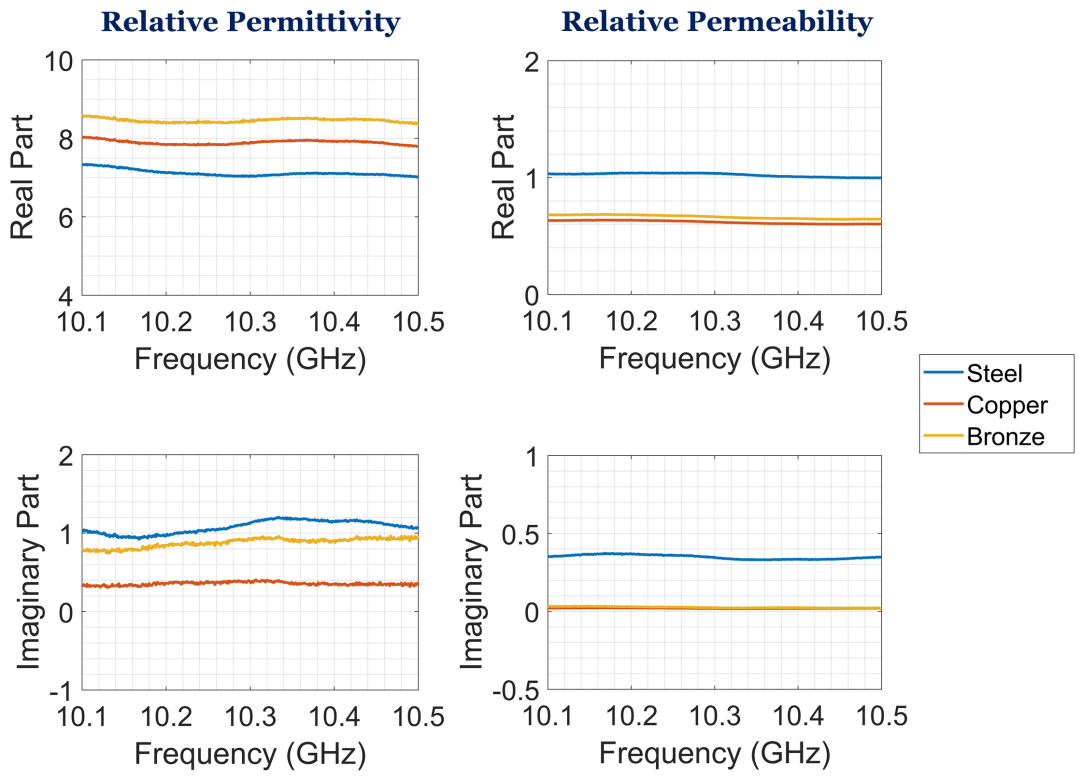

Figure 4.10: Electromagnetic properties of various composite thermoplastics involving metallic powders. A 3D-printed sample holder with 5 mm thickness is used for measurements.

Initially, we examine ColorFabb SteelFill, CopperFill, and BronzeFill filaments with 2.85 mm diameters, while printing settings (such as temperatures and infill ratios) are the same for all samples. These filaments contain approximately 80% metallic powders. They are quite fragile, difficult to print, and highly abrasive (problem for print nozzles). Therefore, we carefully use them with relatively large 0.8 mm brass nozzles. On the other hand, once printing settings are optimized, a sample can be fabricated in less than ten minutes via an Ultimaker 2+ printer. Figure 4.10 illustrates complex ϵ_r and μ_r results, where Steel, Copper, and Bronze correspond to samples made of ColorFabb SteelFill, CopperFill, and BronzeFill filaments, respectively. When we examine μ_r values, we observe that steel-filled PLA has quite high magnetic losses in comparison to others due to iron components. On the other side, although their magnetic losses are small, the copper-filled PLA and the bronze-filled PLA have nearly 0.65 μ_{Rr} values. Actually, since composite filaments contain micro-particles rather

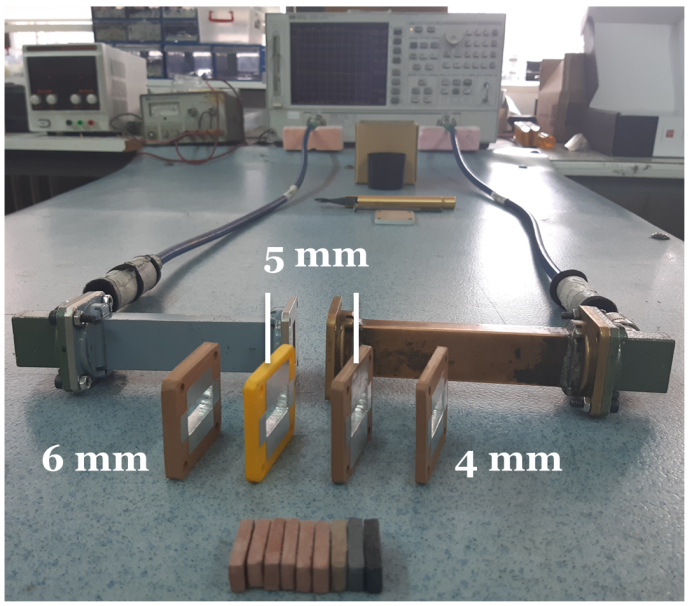

Figure 4.11: 3D-printed waveguides with different thicknesses. Samples are fabricated to perfectly fit into the waveguides.

than fully homogeneous mixtures, the effective μ_{Rr} may be less than unity in the GHz regime, as shown in the literature [103]. If we examine ϵ_r results, we observe that bronze-filled PLA and steel-filled PLA have high loss values, while copper-filled PLA has the best results in terms of loss values together with its relatively high ϵ_{Rr}.

In order to obtain more accurate results, we repeat measurements with several sample thicknesses, as suggested in [96]. Thanks to the 3D printing process, the required sample holder waveguide sections can easily be fabricated, such as depicted in Figure 4.11 where 3D-printed PLA waveguides with 4, 5, or 6 mm thicknesses are shown. Similar to the previous one, their inner walls are covered with aluminum tapes. The samples to be measured are also fabricated with different thicknesses so that they can fit into cavities of the sample holders. We note that a sample holder should be completely filled with the material under investigation to obtain correct results. In addition, considering different thicknesses of the sample holders, we repeat TRL calibration with different line standards.

Figure 4.12 presents relative permittivity and permeability measurement results for the composite filaments. We examine copper-filled PLA, steel-filled PLA, and carbon-fiber-filled PLA. Straight, dashed, and dotted lines correspond to the measurements

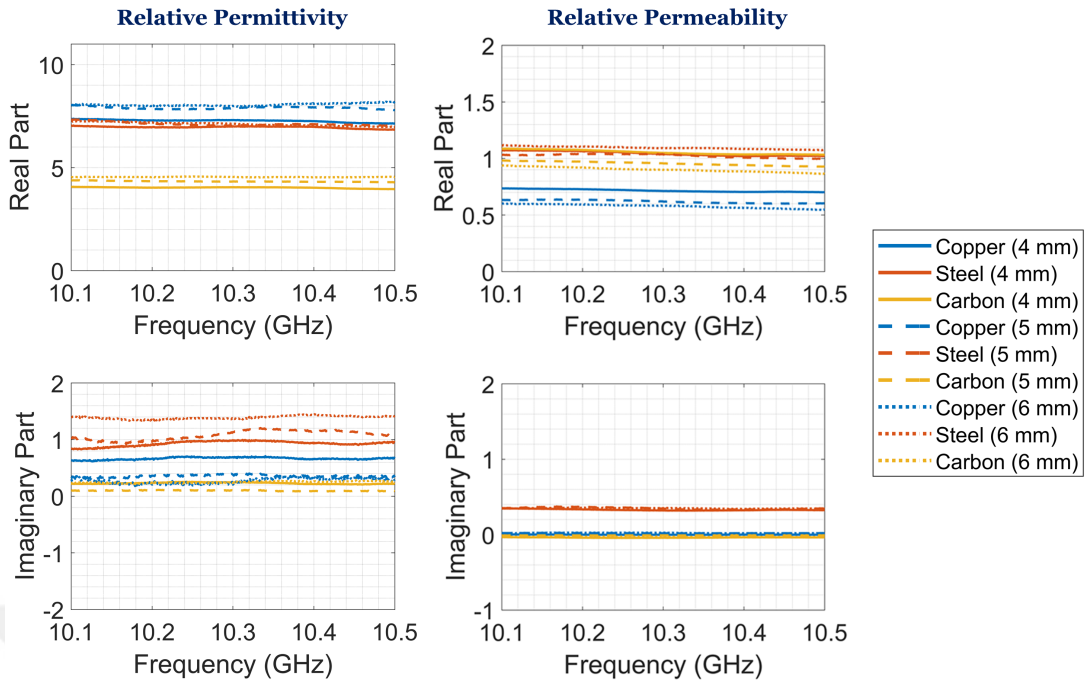

Figure 4.12: Electromagnetic properties of various composite thermoplastics with nanoparticles. 3D-printed sample holders with 4, 5, and 6 mm thicknesses are used for measurements.

with 4, 5, and 6 mm samples, respectively. Both real and imaginary parts of ϵ_r and μ_r values are given in the figure. We have the following conclusions.

- Magnetic losses of the steel-filled PLA are quite high, while the others have nearly zero μ_{Ir} values. Non-unity results of μ_{Rr} should be carefully treated in the simulations since most NZI realization methods assume nonmagnetic properties in their designs.

- While the real parts of permittivities do not change significantly with different sample thicknesses, the deviation in the imaginary parts is relatively high. Actually, the imaginary parts of both ϵ_r and μ_r are highly sensitive to the measured S-parameters. More accurate measurements may be obtained with different methods than NRW, such as cavity techniques.

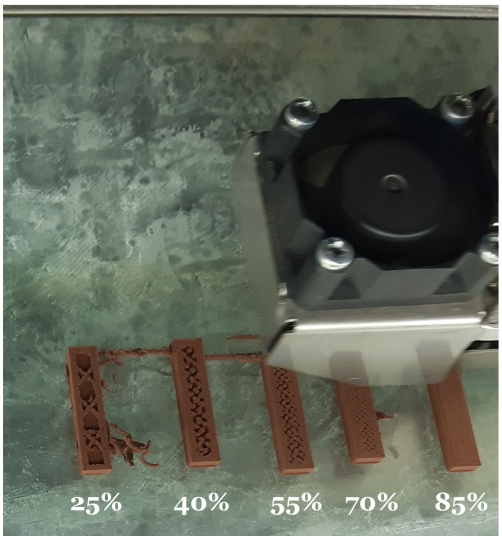

Figure 4.13: Fabrication process for copper-filled PLAs with different infill ratios.

4.2.3 Effects of the Infill Ratio

When the infill ratio is adjusted as 100% with *lines* infill pattern, nearly uniform samples can be obtained. On the other hand, the infill ratio setting can be decreased to have less dense structures. Figure 4.13 depicts five boxes (samples) obtained with different infill ratios using the same 3D printer, where copper-filled PLA is used as the filament. Dimensions of the samples are determined by considering the gap of the 3D-printed WR-90 waveguide section with 5 mm thickness. Figure 4.14 presents complex ϵ_r and μ_r measurement results for these samples. We observe a peculiar behavior of μ_{Rr} with respect to the infill ratio. Since pores (filled with air) increase by decreasing the infill ratio, μ_{Rr} values also increase, while magnetic losses do not alter a lot. On the contrary, ϵ_{Rr} values and dielectric losses decrease when the infill ratio is decreased.

Table 4.4 presents electromagnetic characteristics of some composite filaments at 10.3 GHz. For copper-filled and steel-filled PLAs with 100% infill ratio, means of the results in 4.12 are used, whereas the result for the bronze-filled PLA with 100% infill ratio is directly taken from Figure 4.10 at 10.3 GHz. The other results are obtained from Figure 4.14. The copper-filled PLA with 100% infill ratio seems to be the best option to realize NZI shells owing to its high relative permittivity and low loss values.

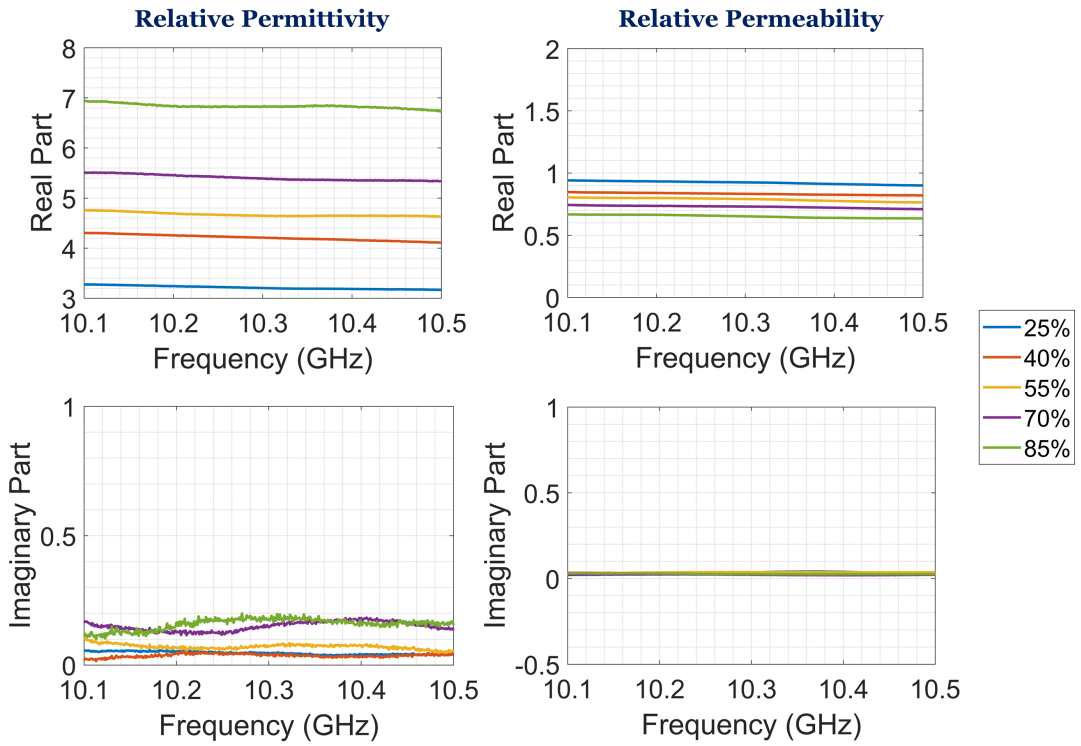

Figure 4.14: Electromagnetic properties of copper-filled PLAs with different infill ratios.

4.3 Fabrications and Measurements of Cylindrical Rods with Predicted Dimensions

After deciding on the copper-filled PLA as the proper material to fabricate high-contrast dielectric rods with 3D printers, we have to adjust the dimensions of the rods, as well as the distances between them. Firstly, the height of the cylindrical rods can be selected as 3λ (≈ 87 mm at 10.3 GHz) since the best beam generator response belongs to rods of this length, as shown in Section 3.4.3. On the other hand, the radius of the rods and the center-to-center distances should be determined carefully to reach an effective NZI.

Figure 4.15 depicts selections of dimensions and material properties to realize NZI behavior. The first two periodic media (black boxes) in Figure 4.15 show effective EMNZ characteristics; their ϵ_r values are different although they have unity μ_r. We note that they are based on the assumption that the rods have nonmagnetic properties

Table 4.4: Measured relative permittivity and permeability values of various composite filaments.

Material	Infill Ratio	ϵ_{Rr}	ϵ_{Ir}	μ_{Rr}	μ_{Ir}
Bronze-filled PLA	100%	8.450	0.920	0.670	0.024
Steel-filled PLA	100%	7.060	1.110	1.050	0.340
Copper-filled PLA	100%	7.800	0.300	0.650	0.018
Copper-filled PLA	85%	6.830	0.179	0.653	0.026
Copper-filled PLA	70%	5.340	0.146	0.730	0.022
Copper-filled PLA	55%	4.650	0.071	0.790	0.038
Copper-filled PLA	40%	4.210	0.038	0.830	0.032
Copper-filled PLA	25%	3.200	0.046	0.920	0.036

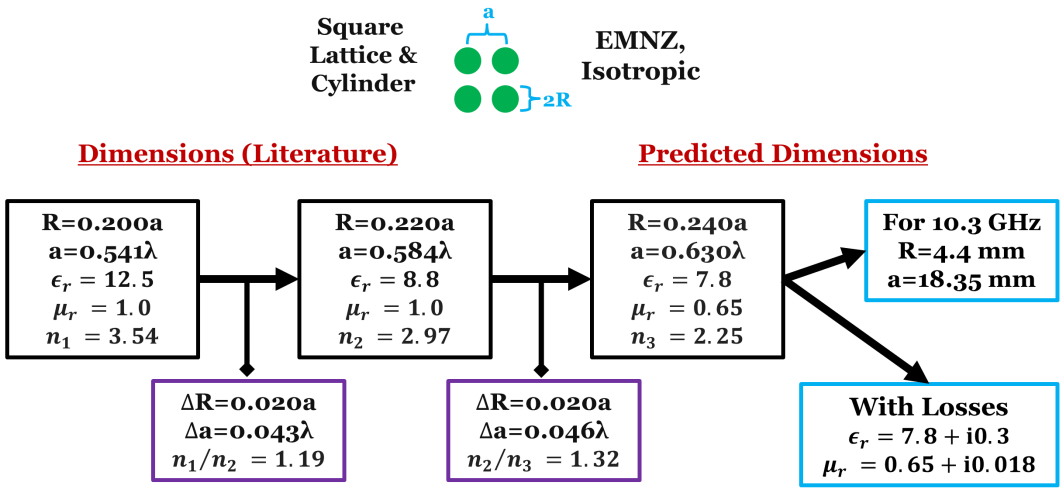

Figure 4.15: The prediction of radiuses and center-to-center distances of rods to be used to realize NZI behavior.

with no loss. For these designs, the refractive indices of the dielectric rods correspond to $n_1 = 3.54$ and $n_2 = 2.97$. In the purple boxes, the differences between radii and center-to-center distances are given, considering that the ratio of the refractive index values is 1.19. We observe that when the refractive index of the rods decreases, as for the second design with alumina, both R and a increase. Similarly, when we use copper-filled PLA instead of alumina, we can readjust the dimensions, considering

the decreased refractive index of the material to be used. As a result, R and a values are determined as 4.4 mm and 18.35 mm, respectively, at 10.3 GHz ($\lambda \approx 29$ mm).

Table 4.5: List of printing settings used to fabricate copper-filled PLA rods.

Parameter	Value
Nozzle temperature	200°C
Build plate temperature	55°C
Layer height	0.1 mm
Printing speed	60 mm/s
Nozzle diameter	0.8 mm
Infill ratio	100%
Infill pattern	Lines
Infill flow	100%
Filament thickness	2.85 mm

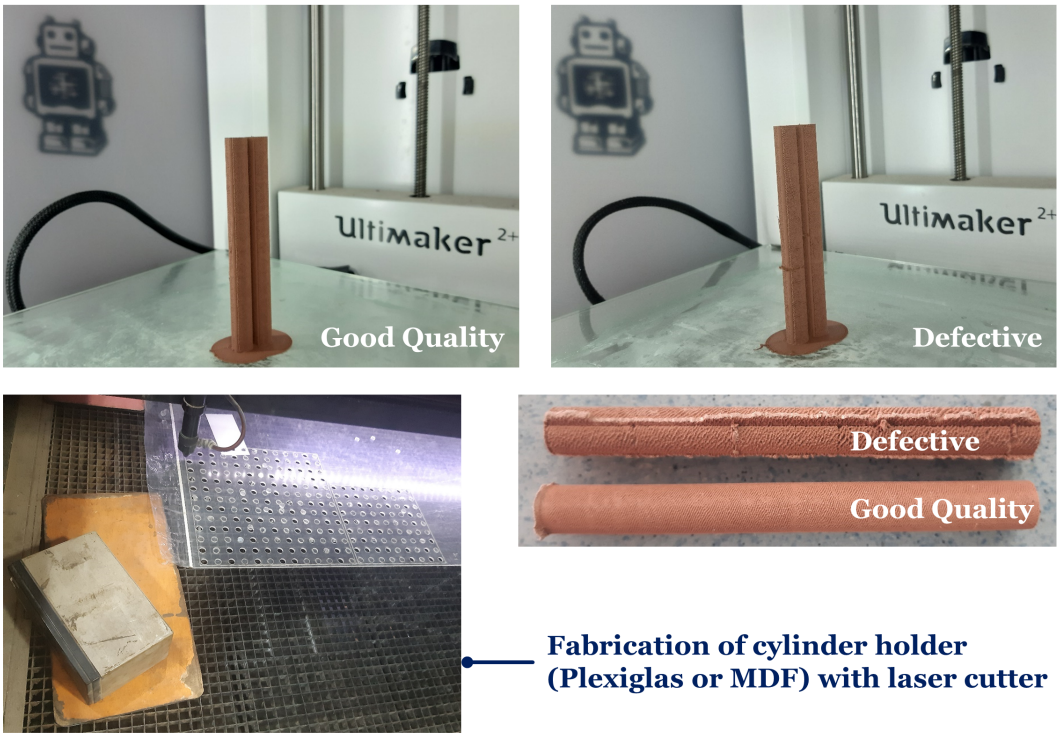

Figure 4.16: Fabrications of copper-filled PLA rods via Ultimaker 2+.

In order to obtain homogeneous rods with high relative permittivity values, the printer parameters are carefully adjusted, as listed in Table 4.5. The proper printing speeds and temperatures are obtained from the advised printing settings of ColorFabb Copperfill PLA. Using these values for the parameters, cylindrical rods are fabricated via Ultimaker 2+ 3D printers, as exemplified in Figure 4.16. While the objects are built on heated plates, we use the build plate adhesion option as brim, which adds a single layer flat area around the base of the objects to prevent warping. Cylindrical rods are fabricated in pairs, and a single pair requires approximately one hour to complete. We note that, as outputs, there are not only good quality rods but also defective ones. Accordingly, to remove leftover blemishes and nonidealities of defective rods, we sand the samples via an 80 grit sanding sponge similar to the samples in the previous measurements. In addition, in order to arrange the rods periodically to construct structures, we use cylindrical holders made of medium-density fibreboard (MDF) or Plexiglas (flat structures with 2 mm thicknesses). The holes whose center-to-center distances and radii are adjusted as 18.35 mm and 4.4 mm, respectively, are opened by a laser cutter.

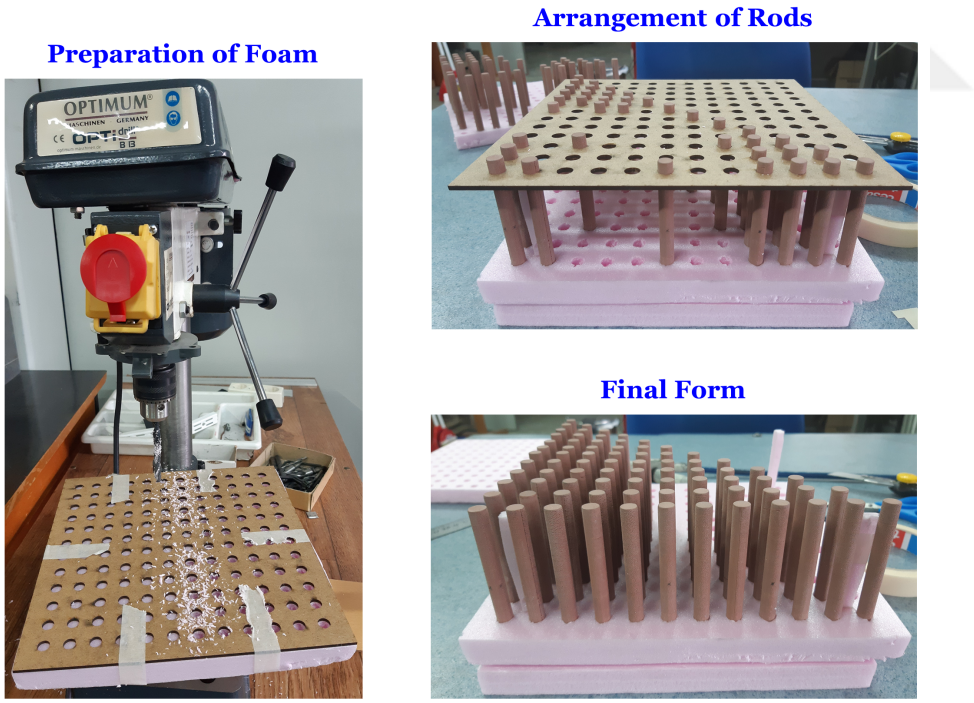

Figure 4.17: The preparation of an effective-refractive-index setup based on arrays of dielectric rods that are arranged to create triangular prisms.

4.3.1 Finding the Effective Refractive Index

We firstly check whether or not the designed periodic arrangement shows NZI characteristics via an effective index measurement setup similar to that given in Section 3.3. It is based on arrays of dielectric rods that are arranged as triangular prisms, while the effective refractive index can be calculated by (3.4). Figure 4.17 depicts the preparation of the setup. We use an MDF cylinder holder as a mask on a foam, on which cylindrical rods are located. We open holes on the foam by using a drilling machine with 7.5 mm drilling bits, which is chosen less than the diameter of the rods (8.8 mm) so that they are tightly inserted into the foam. We use 78 rods in a 12×12 grid such that the overall structure can be used to refract of incoming waves depending on the effective medium parameters that it generates. Figure 4.18 illustrates the effective-refractive-index test for copper-filled PLA rods in the simulation environment when a CSP beam is used to illuminate the structure. In the first row of the figure, $\epsilon_r = 7.80$ and $\mu_r = 0.65$ are used, whereas electromagnetic losses are included in the second row. Based on the Hough line transform, we compute the effective refractive indices as -0.072 and -0.096, respectively, when real and complex parameters are used. We also note that when the complex parameters are used in the simulations, refracted field values decrease due to electromagnetic losses.

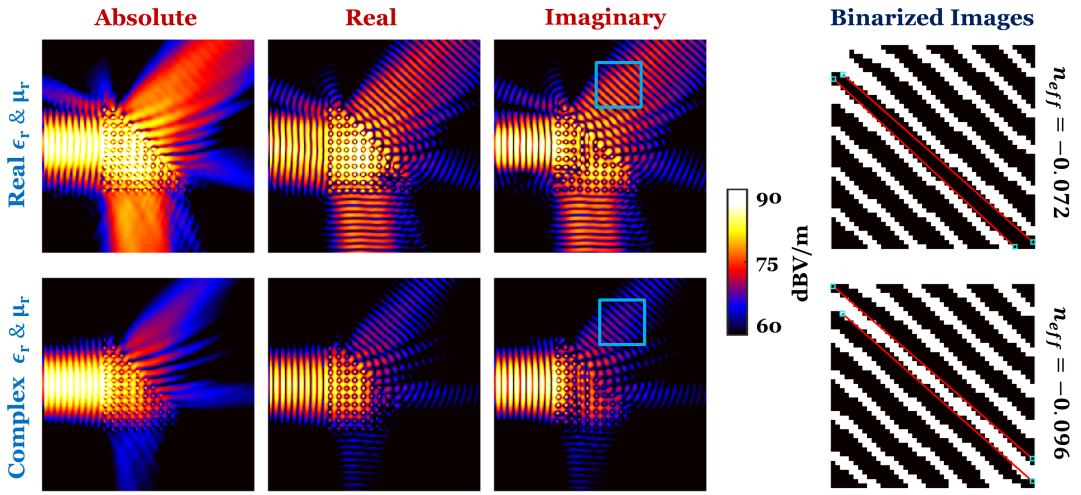

Figure 4.18: Simulated electric field intensities, binary images, and slopes for a triangular prism made of copper-filled PLA rods. A CSP beam illuminates the structure at 10.3 GHz.

Next, we focus on the measurements of the prism structure (12×12 grid), as described in Figure 4.19. The top-left photograph shows the horn antenna and a foam, on which the prism structure in Figure 4.17 can be placed. The photograph on the top-right shows how the prism can be placed in front of the antenna. After electromagnetic waves enter into the prism, they are expected to leave from the hypothetical oblique and bottom surfaces. In particular, we examine refracted beams (RBs) from the hypothetical oblique surface in order to compute the effective refractive index possessed by the structure. In the photographs on the bottom of Figure 4.19, there are two types of settings involving different orientations of the prism. When Setting 1 is employed, RBs should be observed on the right of forward radiation, i.e., fields directly received from the antenna (when the setup is observed from top). On the contrary, when Setting 2 is used, RBs should occur on the left of the forward radiation.

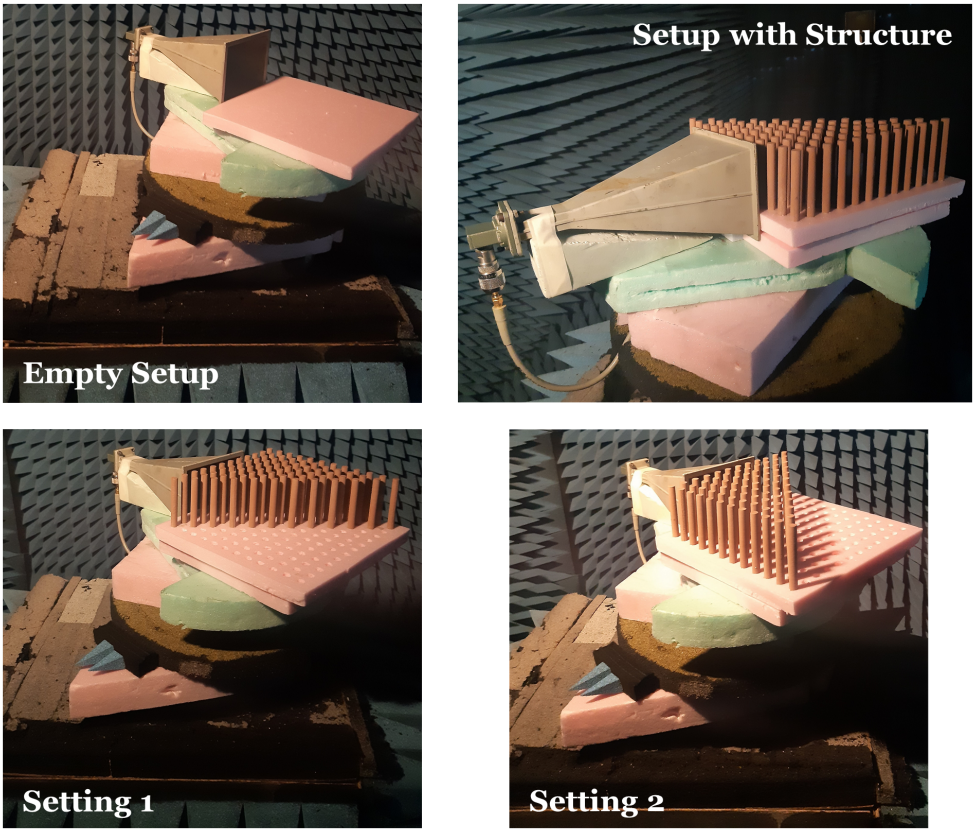

Figure 4.19: The effective-refractive-index-measurement setup in an anechoic chamber. A horn antenna which operates in the X-band is used to illuminate a structure consisting of cylindrical rods.

The radiation characteristics are obtained in an anechoic chamber using HP 8757C scalar network analyzer and HP 83640A synthesized sweeper. Figure 4.20 illustrates far-zone radiation pattern (the mean of four measurements) of the horn antenna without the prism structure. It has a single beam, whereas the back lobe is nearly at -30 dB.

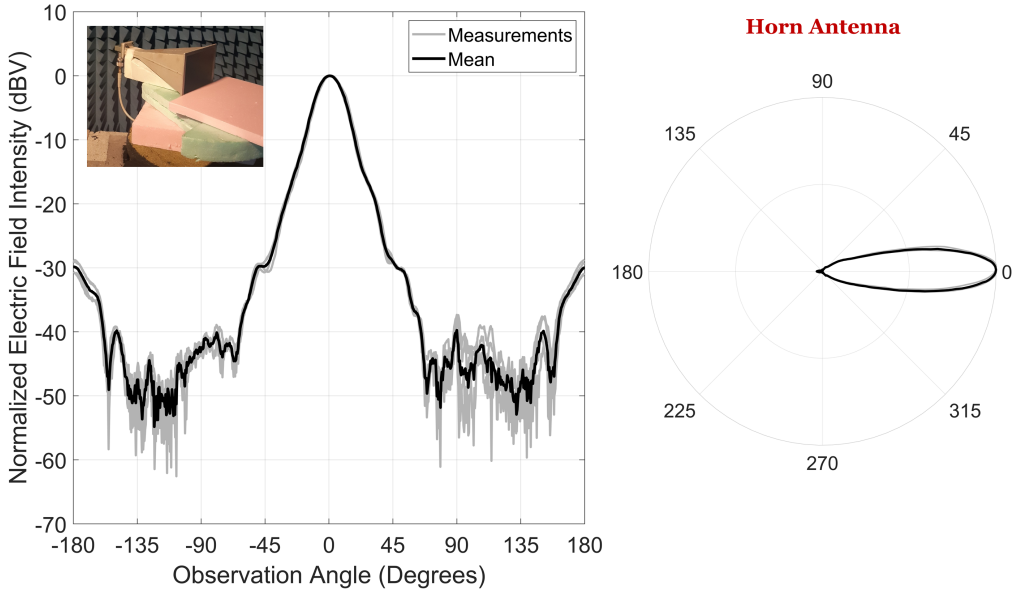

Figure 4.20: The far-zone radiation pattern of an X-band horn antenna, which is used to illuminate cylindrical rods. On the left, a rectangular plot is given in dB scale. On the right, a polar plot is given in linear scale.

Figures 4.21 and 4.22 present the normalized far-zone radiation patterns when the triangular prism is placed according to the setups in Settings 1 and 2, respectively. Simulation and measurement results are given both in rectangular and polar plots, while real ϵ_r and μ_r are used in the simulations (as given in the first row of Figure 4.18). We also note that a CSP beam is used in the simulations to mimic the directive radiation of the horn antenna. RBs from the hypothetical oblique surface of the prism are labeled in both Figure 4.21 and Figure 4.22. In Figure 4.21, RB can be observed at nearly -45°, while the backward and forward radiations occur at -180° and 0°, respectively. On the other hand, in Figure 4.22, RB is directed to nearly 45°, whereas the backward and forward radiations are the same as those in Figure 4.21. We have the following observations.

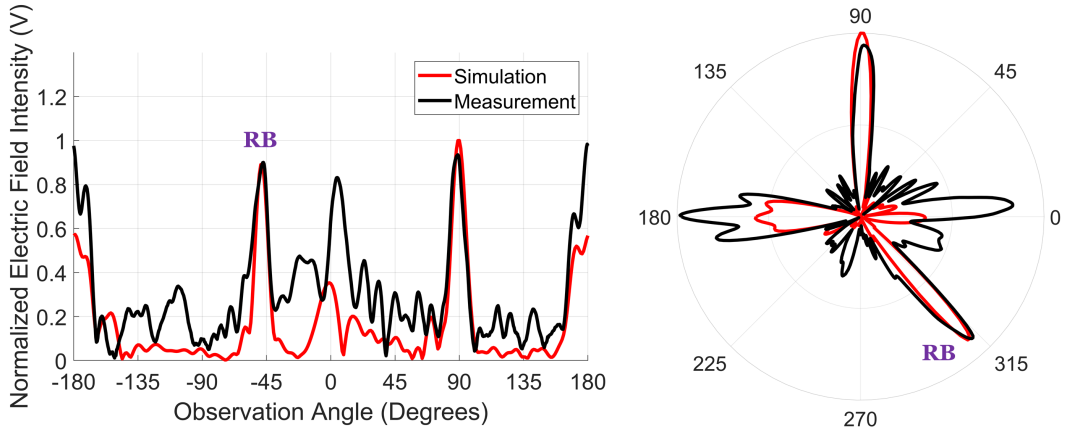

Figure 4.21: The far-zone radiation patterns obtained when the horn antenna is used to illuminate the 12×12 grid of dielectric rods arranged as a triangular prism. The rectangular (left) and polar (right) figures use linear scales. The triangular prism is placed in accordance with Setting 1.

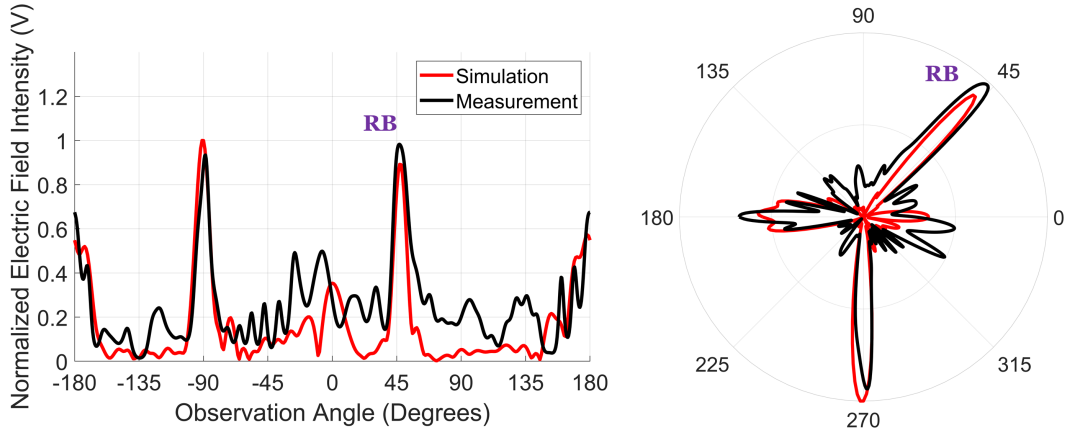

Figure 4.22: The far-zone radiation patterns obtained when the horn antenna is used to illuminate the 12×12 grid of dielectric rods arranged as a triangular prism. The rectangular (left) and polar (right) figures use linear scales. The triangular prism is placed in accordance with Setting 2.

- The effective refractive index values are obtained as 0.013 and 0.0463 using Settings 1 and 2, respectively. Considering far-zone setup in simulations, this value is obtained as 0.0617. Consequently, we clearly demonstrate the NZI characteristics of structures consisting of cylindrical rods made of copper-filled PLA.

- The discrepancy between the simulation and measurement results seems to be related to (1) different excitations in the simulation (CSP beam) and measurement (horn antenna) environment (2) the electromagnetic losses omitted in the simulations.
- The consistency of the backward radiations for Setting 2, even if we employ real ϵ_r and μ_r values in the simulations, is remarkable. Electromagnetic loss values obtained in the characterization measurements may be higher than the actual values.

4.4 Measurements of Beam Generators

In Chapter 3, we show design steps of homogeneous and realized beam generating shells, while alumina rod arrays are used to mimic EMNZ behaviors with realistic shells. On the other side, effective NZI structures can also be realized by periodic arrangements of copper-filled PLA rods instead of alumina rods. Accordingly, in this section, simulations and measurements of NZI shells realized with copper-filled PLA rods are rigorously examined.

4.4.1 Fine-Tuning Periodicity

In order to obtain efficient beam generating structures with copper-filled PLA rods, we heuristically investigate the effects of the periodicity on the far-zone radiation characteristics of realistic structures with square holes. We examine 9×9 grid, while 3×3 of them are removed from the center, leading to an efficient square cavity. The center-to-center distance between the rods varies in a range from 17.00 mm to 19.80 mm. In addition, real ϵ_r and μ_r values are used in the simulations without considering electromagnetic losses, while a Hertzian dipole is used as the primary source, as usual.

Figure 4.23 depicts 3D far-zone radiation results, where the color range is designated to represent values from 1000 V to 20000 V. We observe that the four main beams are clearly visible except for the last two periodicity values. These two cases lead to significant side lobes in various directions. The designs involving center-to-center distances from 18.35 mm to 19.00 mm show relatively strong beam generating characteristics. For more quantitative results, we focus on far-zone electric field intensity

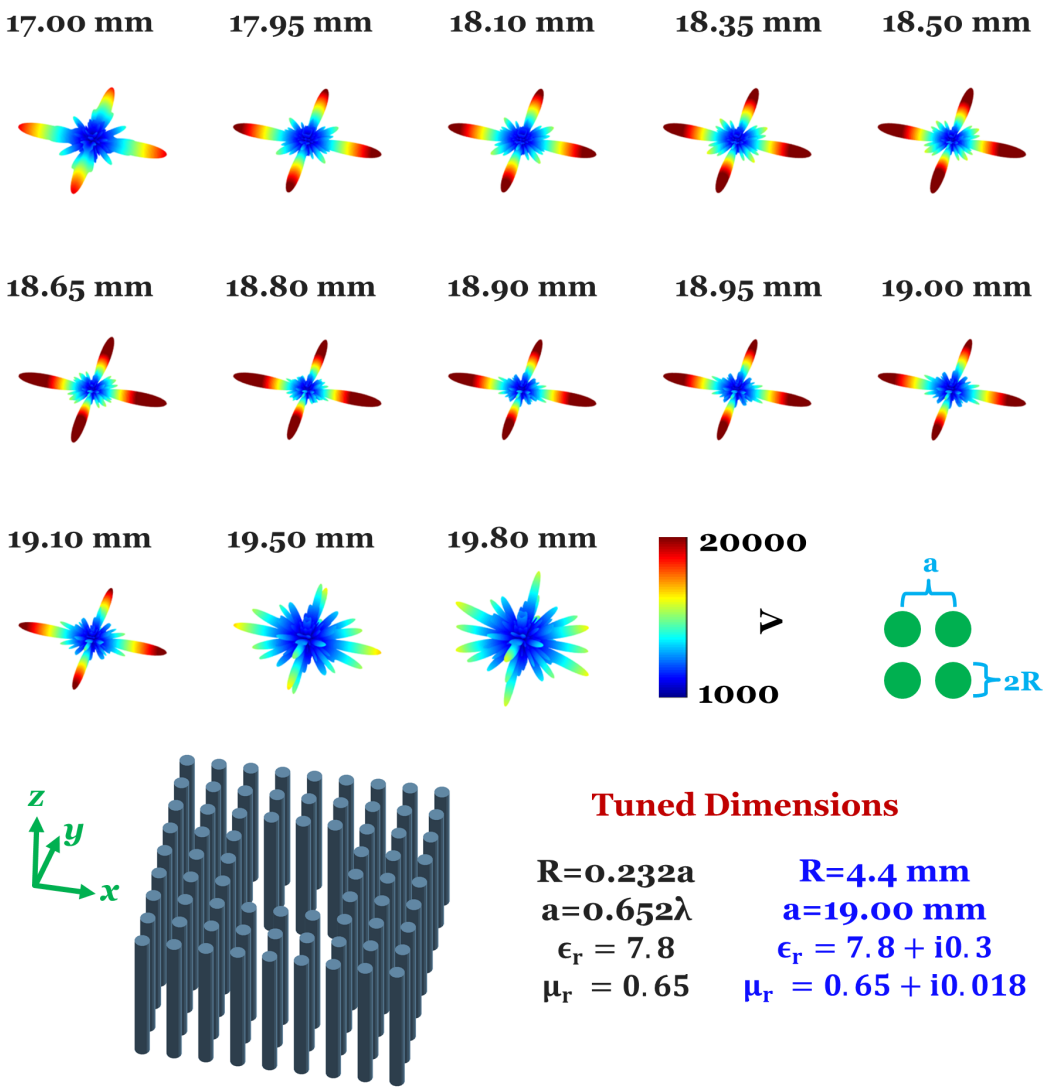

Figure 4.23: 3D far-zone electric field results for realized beam generators with square holes having different periodicities (a). Copper-filled PLA rods with real ϵ_r and μ_r values are used in the simulations.

results in the array plane (x-y plane), as shown in Figure 4.24. From 17.00 mm to 18.65 mm, although the main beam radiation intensities increase, side-lobe levels also increase. On the contrary, the main beams are slightly suppressed slightly decrease when the periodicity is increased to 19.00 mm from 18.80 mm, whereas side-lobe levels decrease as desired. For periodicities above 19.00 mm, the beam characteristics of the shells become worse, i.e., they have weaker main beams and higher side-lobe radiations. When we carefully examine the results, we observe that the best peri-

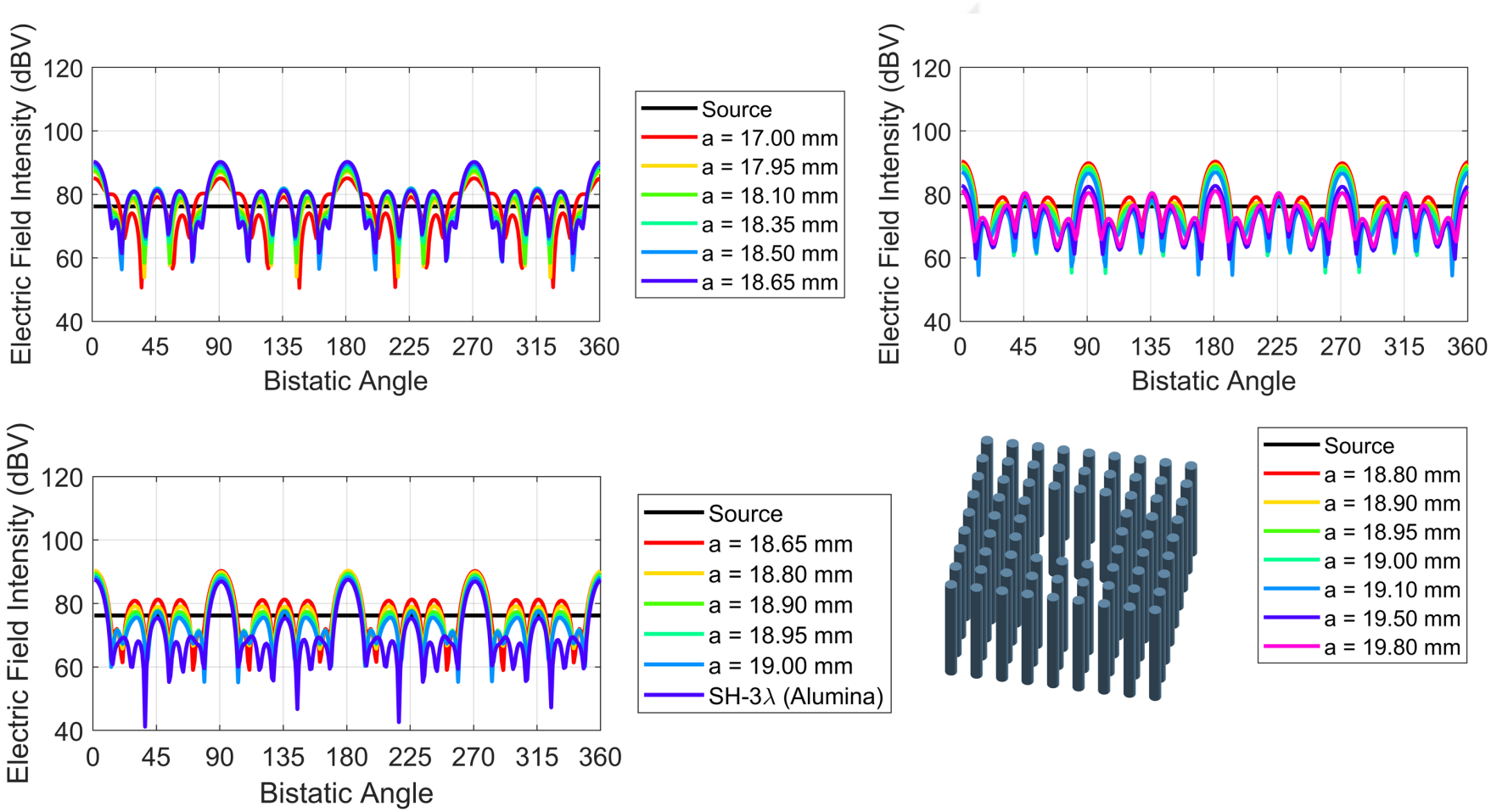

Figure 4.24: Far-zone electric field results for various realized beam generators with respect to the bistatic angle in degrees. Copper-filled PLA rods with real ϵ_r and μ_r values are used in the simulations.

odicity value is 19.00 mm considering both low side-lobe levels and strong (clear) main beams. On the bottom left corner of Figure 4.24 we further compare the shells with copper-filled PLA rods and the one with alumina rods (the SH design with 3λ rods in Figure 3.33). We observe that the main-beam levels of the NZI shell with copper-filled PLA and 19.00 mm periodicity are 1 dB higher than those of the shell with alumina rods, while the side-lobe levels are only 2 dB higher. Consequently, in the following sections, the center-to-center distances between the rods are adjusted as 19.00 mm for both measurements and simulations.

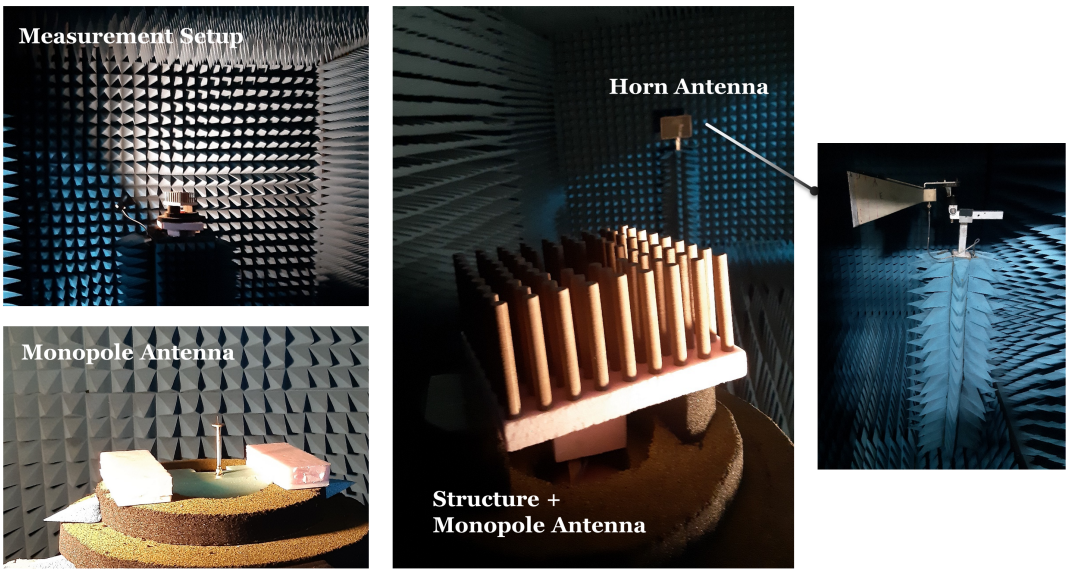

Figure 4.25: The measurement setup for the NZI shells in an anechoic chamber. A monopole antenna is used as the primary source at the centers of the shells, while a horn antenna is used to measure the far-zone radiation patterns.

4.4.2 The Measurement Setup of Beam Generators and the Source Antenna

Now, we examine measurements of the NZI shells acting as efficient beam generators. The beam generators are created by the copper-filled PLA rods used in the effective-index measurements where we arrange them to form triangular prisms. The rod holder foams are prepared as shown in Figure 4.17. Figure 4.25 depicts the measurement setup for the NZI shells in an anechoic chamber. As the primary source to be located at the centers of the shells, we use a monopole antenna having an omnidirectional radiation pattern. The horn antenna is driven by HP 83640A synthesized sweeper,

while the radiation characteristics are obtained by using HP 8757C scalar network analyzer. Figure 4.26 further depicts the fabricated NZI beam generators. Some printing defects can be visible in the figure (bottom-left). We note that these defects are not as much as the deformed rods in Section 3.8.1 (sensitivity analyses); thus, we can expect that they do not significantly affect the radiation characteristics obtained in the measurements.

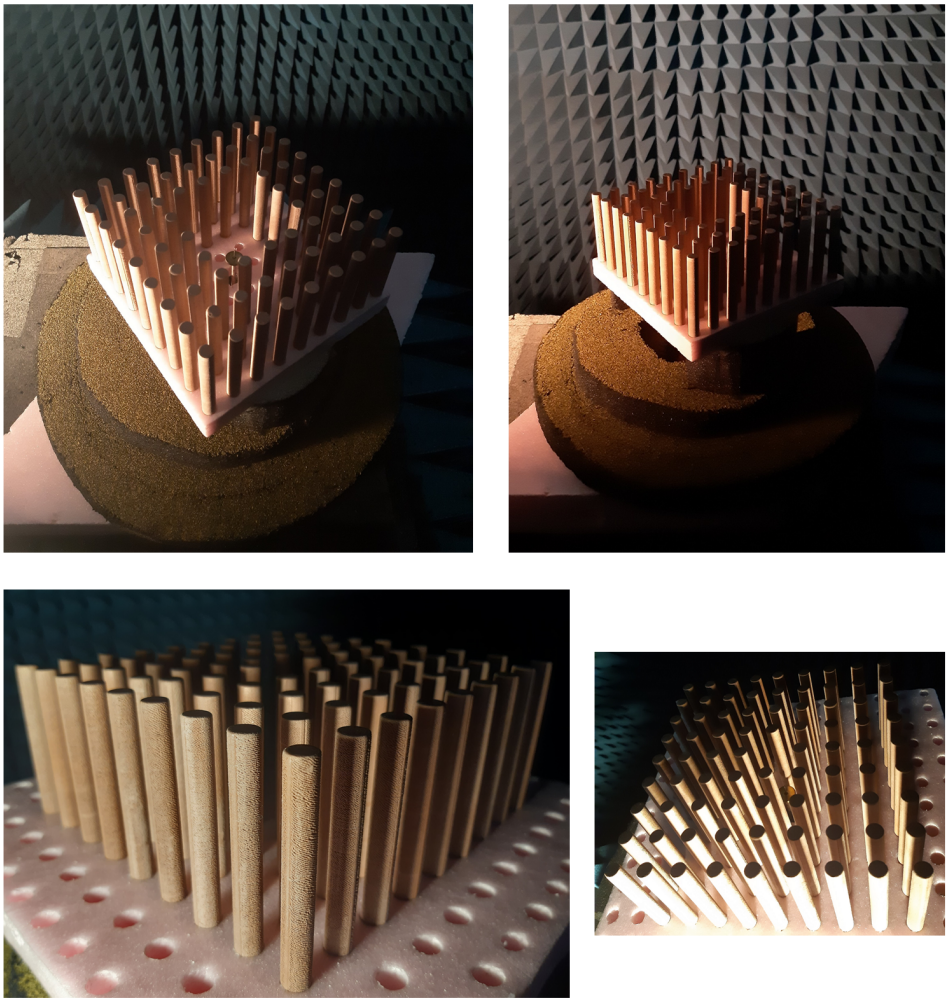

Figure 4.26: Photographs of various NZI shells involving copper-filled PLA rods.

Before measuring the far-zone radiation patterns of the shells, we examine the radiation pattern of the source antenna in Figure 4.27. In these measurements, the operating frequency is 10.3 GHz, while the input power is adjusted as 10 dBm. We only consider the monopole antenna without any interaction. A total of 20 measurements, as well as their means, are shown in a rectangular plot (dB scale) and in a polar plot

(linear scale). Since the H-plane of the monopole is under investigation, we observe a nearly omnidirectional radiation pattern. There are also deviations in the pattern due to (1) vibrations and (2) possible reflections from the rotating setup.

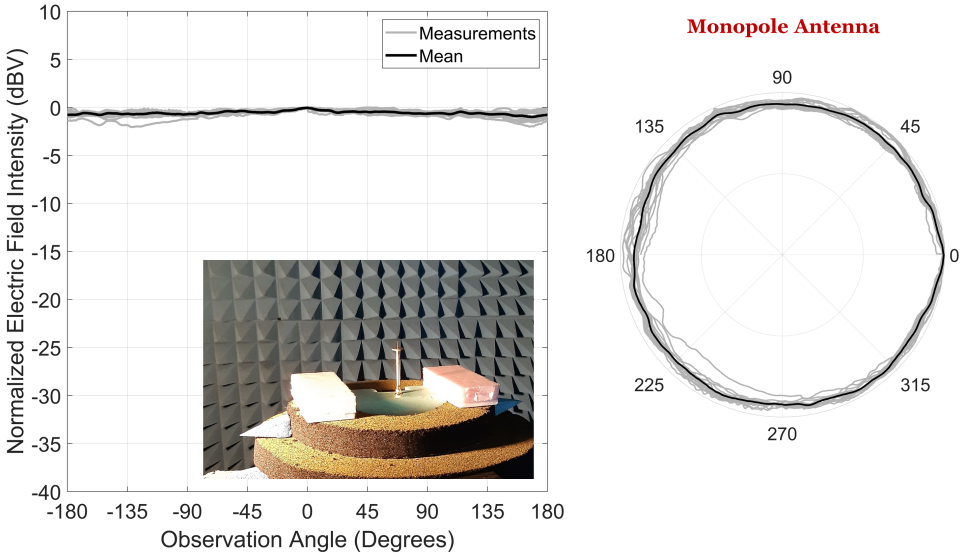

Figure 4.27: The far-zone radiation pattern of the monopole antenna. On the left-hand side, a rectangular plot is given in a dB scale. On the right-hand side, a polar plot is given in a linear scale.

4.4.3 Measurements of Different Cavity Formations

Effective NZI structures can be obtained with copper-filled PLA rods, as shown in the previous sections. With fine-tuned periodicity and radius values, NZI shells with copper-filled PLA rods can show strong beam generating characteristics. Accordingly, relatively simple and compact beam generators with three different cavity formations are investigated in Figure 4.28, when the measured electromagnetic properties of the copper-filled PLA are employed in the simulations. Circular hole (CH), full grid (FG), and square hole (SH) designs are simulated via real (the first three results) or complex (the last three results) electromagnetic parameters. Radii and heights of the rods, and the center-to-center distances between them are set to 4.4 mm, 87 mm, and 19 mm, respectively. With the given dimensions, the 9×9 grid covers 16.08 cm $\times$ 16.08 cm ($\approx 5.5\lambda \times 5.5\lambda$) area. Near-zone power density distributions and far-zone radiation patterns are depicted for the different formations in Figure 4.28. We observe

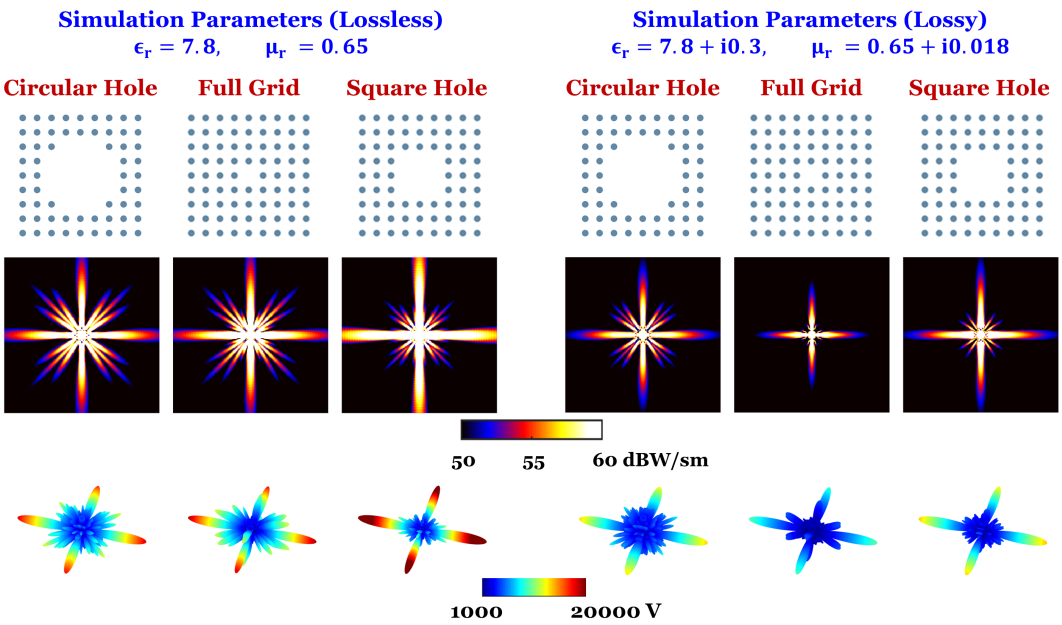

Figure 4.28: Simulation results for NZI shells with copper-filled PLA rods when different cavity formations are investigated.

that the circular hole and the full grid lead to significant side lobes in diagonal directions, as well as four main beams. On the other hand, the square hole leads to strong (clear) main beams together with relatively low side-lobe levels, demonstrating its effectiveness in terms of beam generation. When complex parameters are employed in the simulations, both main-lobe and side-lobe levels decrease; however, the best response still belongs to the square-hole design.

Next, we focus on measurements of the NZI shells with different cavity formations. Figures 4.29–4.31 present simulation and measurement results for the structures with circular hole, full grid, and square hole, respectively. The measurement results are shown without any post-processing on them, i.e., no filtering and averaging. In the simulations, the measured complex ϵ_r and μ_r values of the copper-filled PLA are used. We observe that the structure with circular hole seems to suffer from significant side lobes, while simulation and measurement results have a good agreement in terms of null and main beam directions. Although the far-zone radiation results for the structure with full grid have lower side lobes in diagonal directions, it has shoulder lobes that merge with the major lobes. Considering measurement results, the best results are again obtained with the structure with square hole, which is consistent with

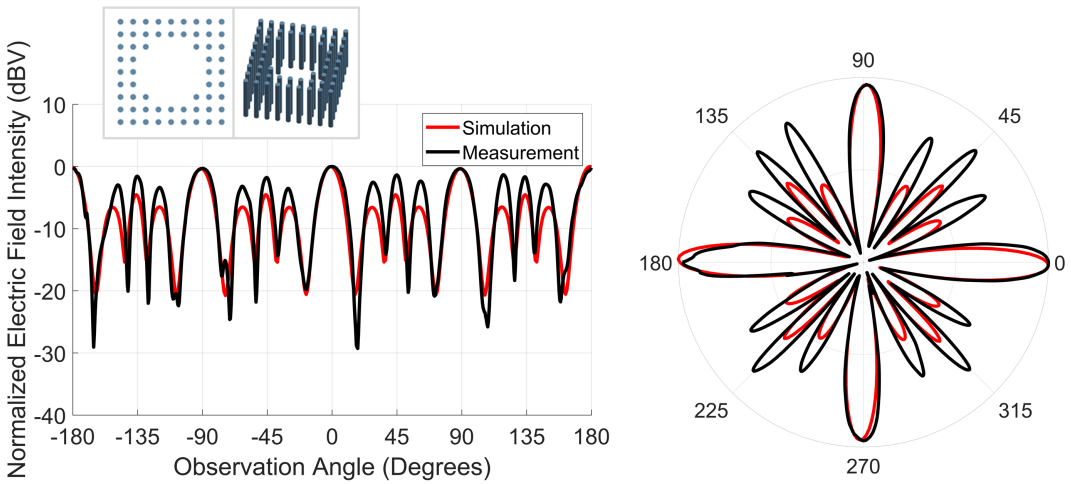

Figure 4.29: Far-zone radiation patterns obtained for the structure with circular hole. On the left-hand side, a rectangular plot is given in a dB scale. On the right-hand side, a polar plot is given in a linear scale.

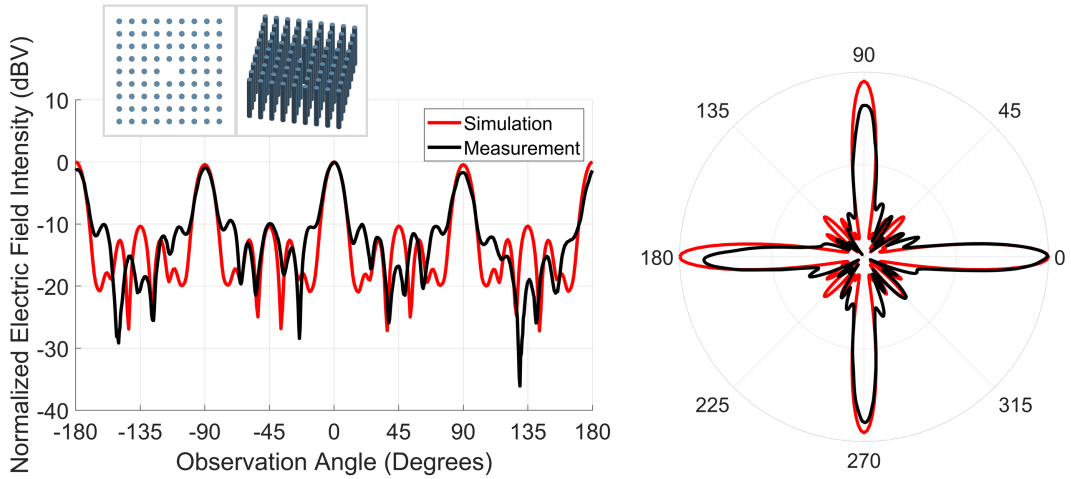

Figure 4.30: Far-zone radiation patterns of obtained for the structure with full grid. On the left-hand side, a rectangular plot is given in a dB scale. On the right-hand side, a polar plot is given in a linear scale.

the simulation results in Figure 4.28. As shown in Figure 4.31, clear main beams and relatively small side lobes can be obtained with this structure (when it is excited by a monopole antenna). It is also remarkable that, for this structure, simulation and measurement results agree very well in terms of the angular distribution of the lobes, as well as both main-beam and side-beam levels. The relatively minor discrepancies

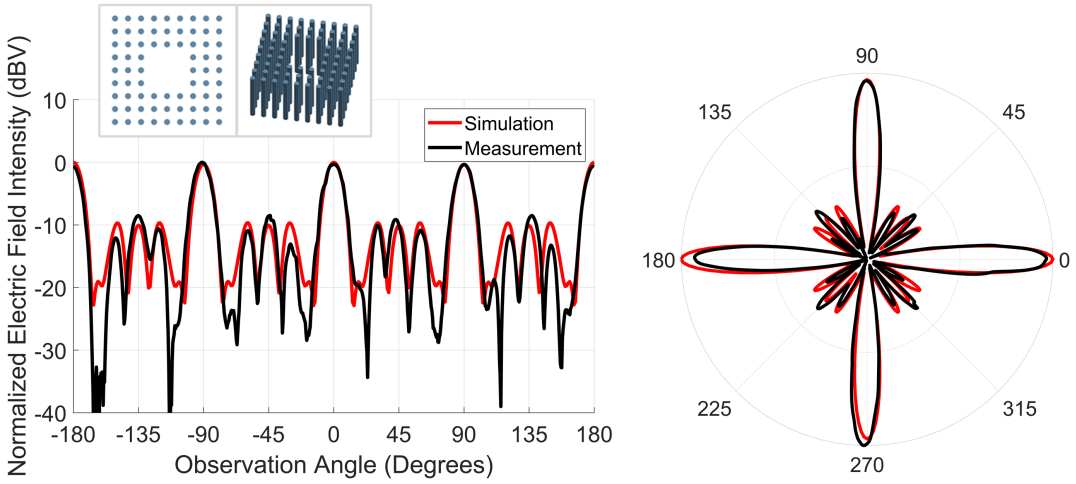

Figure 4.31: Far-zone radiation patterns obtained for the structure with square hole. On the left-hand side, a rectangular plot is given in a dB scale. On the right-hand side, a polar plot is given in a linear scale.

between the simulation and measurement results seem to be related to (1) deformed 3D-printed rods, (2) vibration of the measurement setup, leading to shifted source locations, and (3) slightly inclined and shifted rods in the fabricated arrangement.

4.4.4 Measurements of NZI Lenses and Absorbers

After the measurements of different cavity formations, we focus on the effects of different outer surface designs, as investigated in Section 3.5. We consider square hole as the cavity design, while the rods are extracted from or added to the main structure in order to obtain alternative radiation characteristics. Figure 4.32 depicts simulation results for different configurations and the corresponding (computed) near-zone power density distributions and far-zone radiation patterns. Complex or real electromagnetic parameters are employed in the simulations to analyze lossy and lossless beam generators, respectively. Considering the results, we have the following observations.

- When the rods are extracted from two sides of the structure, as illustrated in the second column (SH Lens), the beams in the corresponding directions are clearly enhanced since the effective apertures of the represented surfaces are increased. Specifically, considering the 2D plot, wider beams are obtained in

the vertical directions, in addition to the increased radiations on these sides.

- The last three shells demonstrate the effects of VGs (NZI absorbers) when we use copper-filled PLA rods. In contrast to alumina VGs in Figure 3.52, the best design is VG-1 in terms of suppression rates when using the copper-filled PLA.
- Loss in materials decreases efficiencies without considerable effects on the beam characteristics.

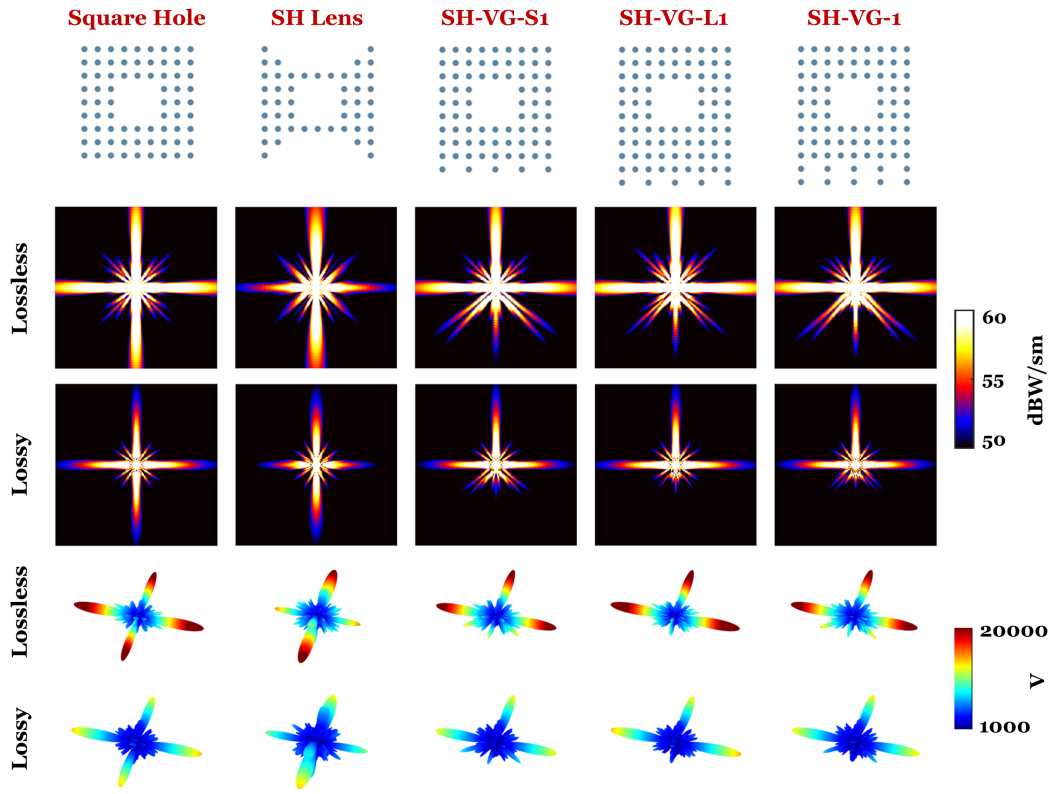

Figure 4.32: Simulation results for NZI shells consisting of copper-filled PLA rods when different outer surface designs (VGs and lenses) are employed.

Figures 4.32–4.35 depict measurement and simulation results for alternative outer surface configurations with square hole as the cavity. Complex ϵ_r and μ_r values are employed in the simulations. Since the fabricated structures are fully reconfigurable, the rods are instantly extracted or added in consecutive measurements. We observe that simulation and measurement results have excellent agreement. The insignificant discrepancies between the results can stem from the reasons emphasized in the previous section.

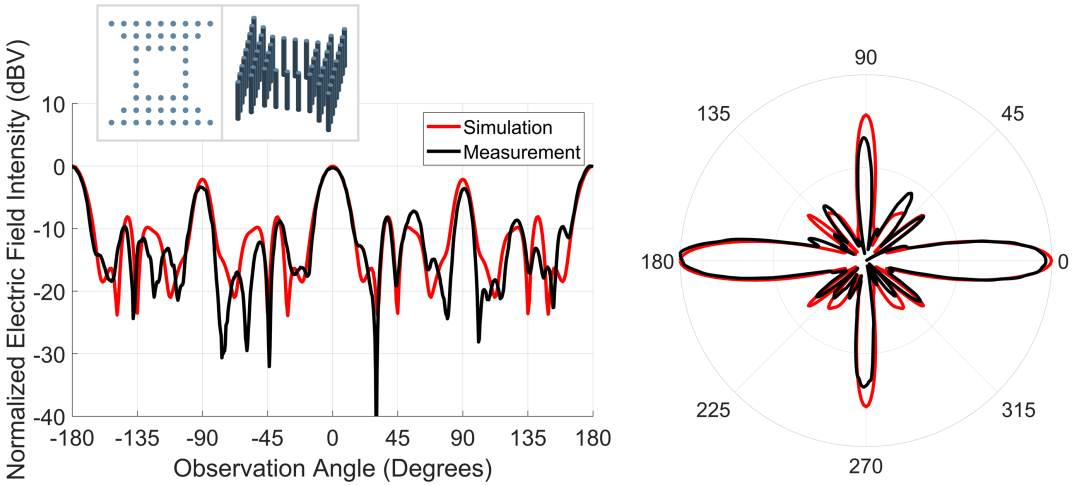

Figure 4.33: Far-zone radiation patterns obtained for SH Lens. On the left-hand side, a rectangular plot is given in a dB scale. On the right-hand side, a polar plot is given in a linear scale.

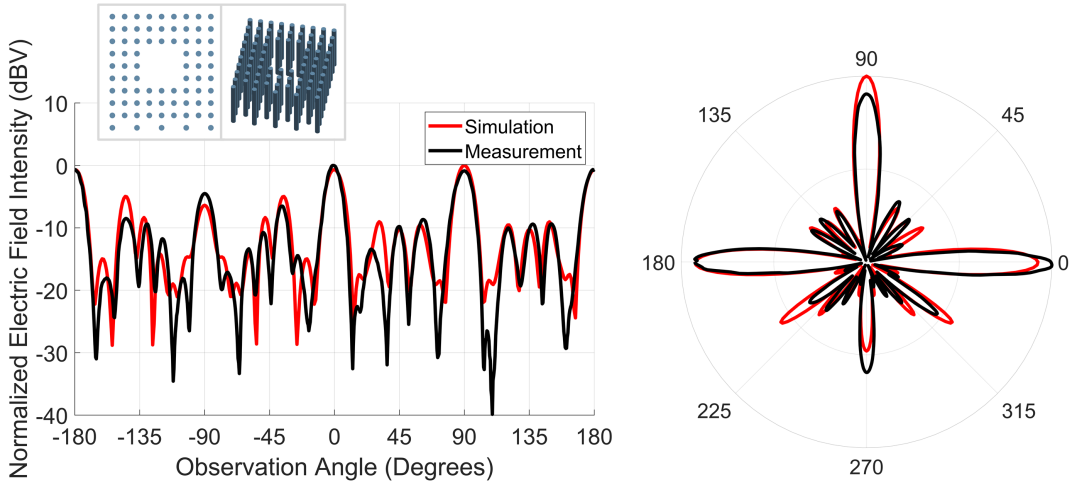

Figure 4.34: Far-zone radiation patterns obtained for SH-VG-S1. On the left-hand side, a rectangular plot is given in a dB scale. On the right-hand side, a polar plot is given in a linear scale.

4.4.5 Measurements of Bidirectional NZI Shells with Vertical Grids

Finally, we place VGs to different sides of the structures with square hole and full grid designs in order to obtain various bidirectional patterns. Figure 4.37 illustrates simulation results when two sides of the NZI shells are modified by VGs. When they

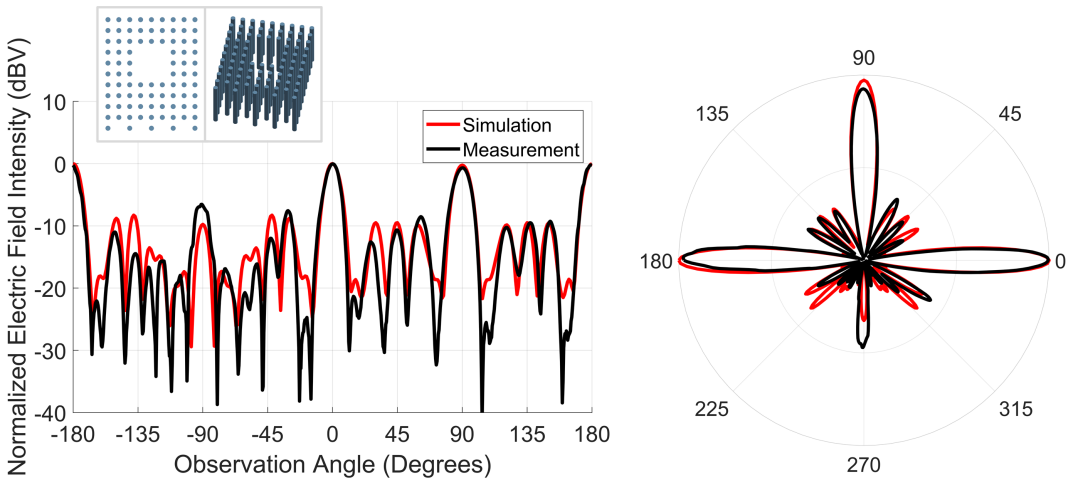

Figure 4.35: Far-zone radiation patterns obtained for SH-VG-L1. On the left-hand side, a rectangular plot is given in a dB scale. On the right-hand side, a polar plot is given in a linear scale.

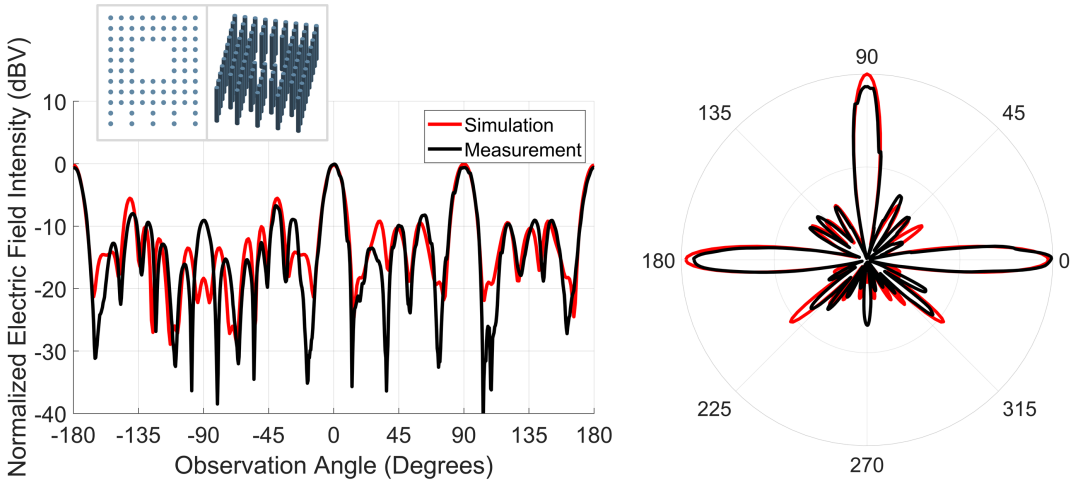

Figure 4.36: Far-zone radiation patterns obtained for SH-VG-1. On the left-hand side, a rectangular plot is given in a dB scale. On the right-hand side, a polar plot is given in a linear scale.

cover two adjacent sides, an asymmetrical radiation pattern is obtained with a $90°$ between the main beams (VG-2A) for the first and third designs in Figure 4.37. On the other side, a symmetrical radiation pattern is provided when two opposite sides of the shells are covered by VGs (VG-2S), as demonstrated by the second and fourth designs in Figure 4.37. We observe that, although the radiation characteristics are

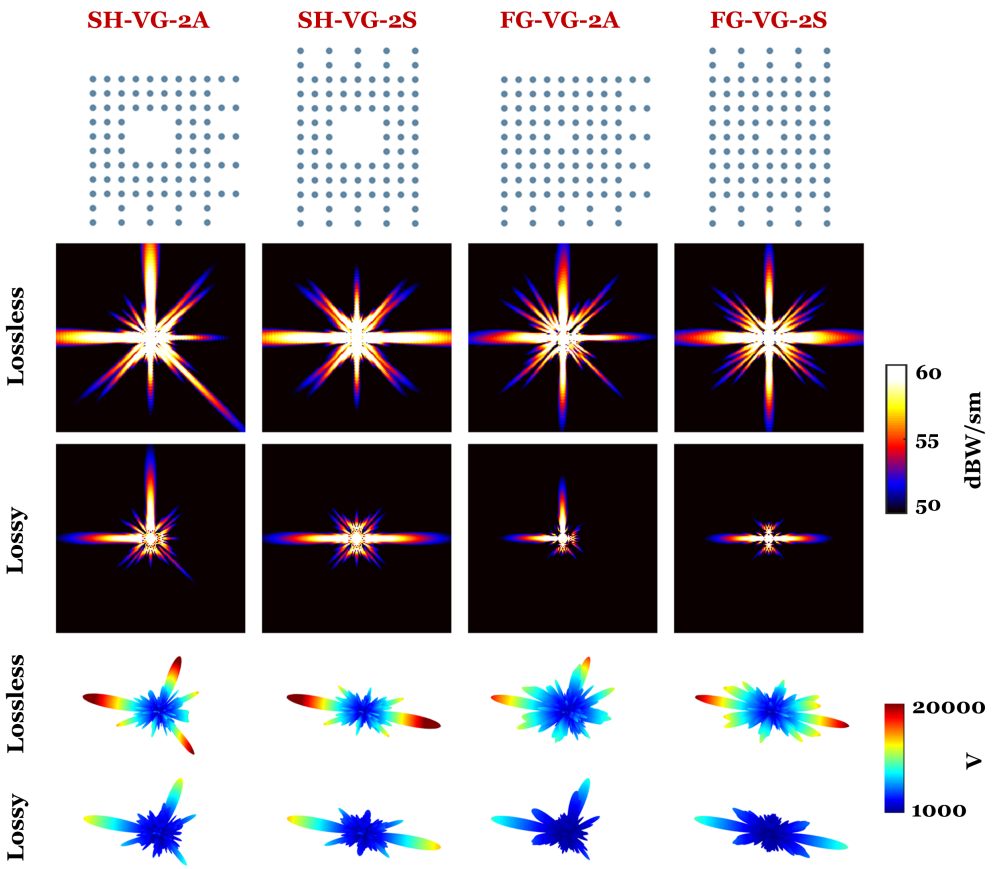

Figure 4.37: Simulation results for NZI shells when different VGs are investigated. Bidirectional radiations are successfully obtained for NZI shells involving copper-filed PLA rods.

similar for the structures with square hole and full grid, stronger main beams are obtained when using the square hole, demonstrating the effect of an efficient NZI cavity. In addition, comparing the results for the lossless and lossy rods, we observe that different double-beam generations are successfully achieved when complex ϵ_r and μ_r are used in the simulations (i.e., despite the introduced loss), especially for the structures with square hole.

Figures 4.38–4.41 show measurement and simulations results for the NZI shells with VGs. In general, the results have good agreement, whereas the desired suppressions are less visible in the measured patterns. Since we insert the measured electromagnetic properties in the simulations, consistent far-zone radiation-pattern measurements of the NZI shells with copper-filled PLA rods show not only the successful

realization of the NZI beam generators but also the accuracy of the electromagnetic characterization of 3D-printed objects.

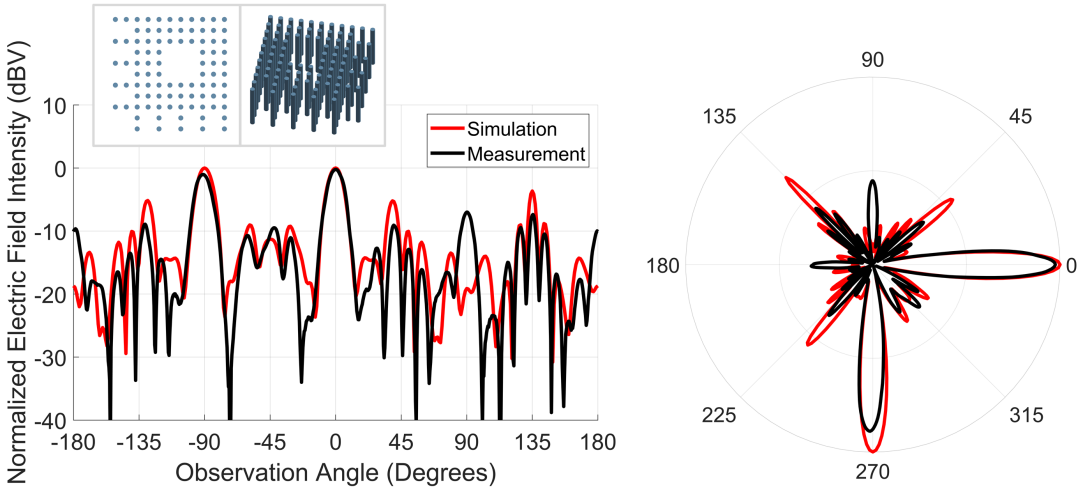

Figure 4.38: Far-zone radiation patterns obtained for SH-VG-2A. On the left-hand side, a rectangular plot is given in a dB scale. On the right-hand side, a polar plot is given in a linear scale.

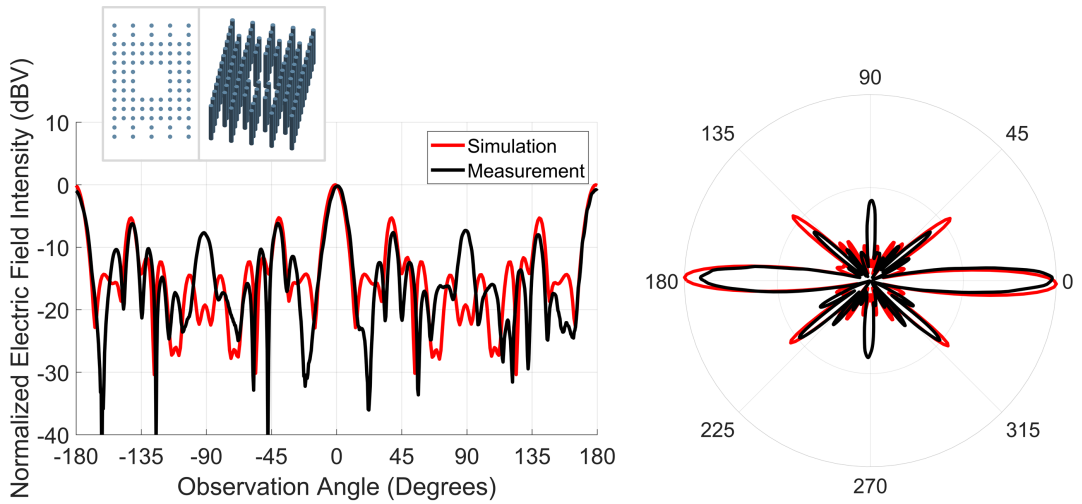

Figure 4.39: Far-zone radiation patterns obtained for SH-VG-2S. On the left-hand side, a rectangular plot is given in a dB scale. On the right-hand side, a polar plot is given in a linear scale.

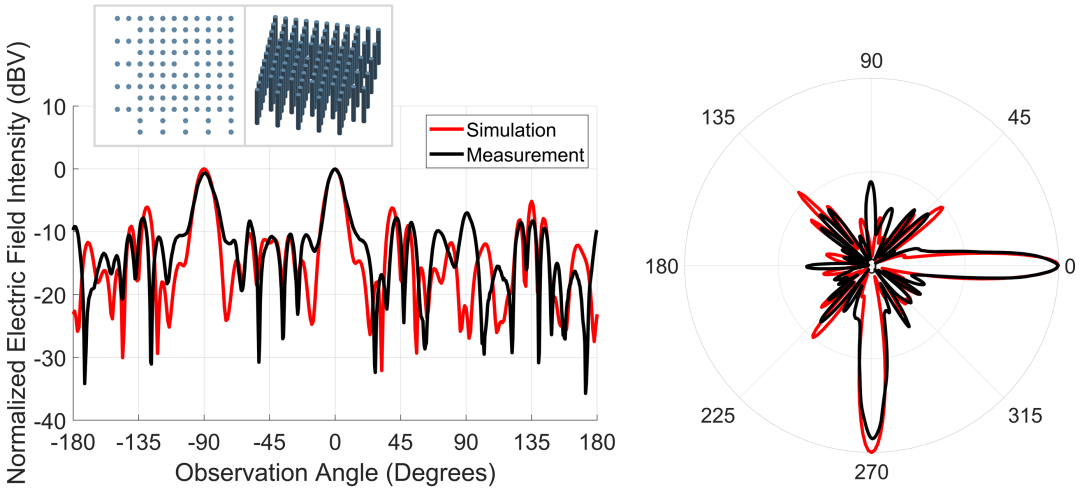

Figure 4.40: Far-zone radiation patterns obtained for FG-VG-2A. On the left-hand side, a rectangular plot is given in a dB scale. On the right-hand side, a polar plot is given in a linear scale.

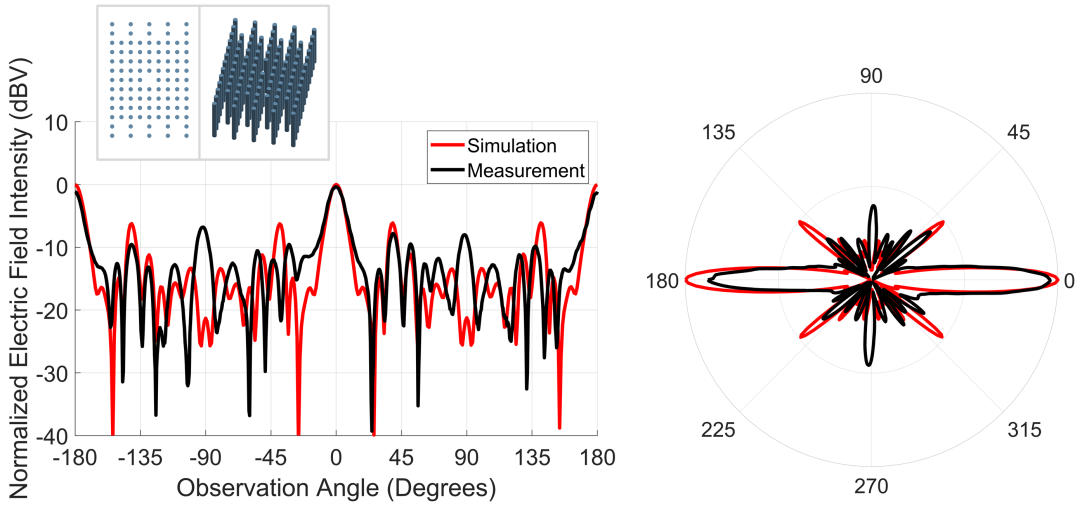

Figure 4.41: Far-zone radiation patterns obtained for FG-VG-2S. On the left-hand side, a rectangular plot is given in a dB scale. On the right-hand side, a polar plot is given in a linear scale.

4.5 Concluding Remarks

NZI structures can be realized by proper arrangements of high-contrast dielectric rods; but, finding such high-contrast materials and using them to fabricate structures of desired sizes can be challenging. Accordingly, we use an electromagnetic charac-

terization setup based on the NRW method to investigate alternative materials to be used for the fabrication of unit cells of realistic NZI structures. Due to accessibility and sophisticated design opportunities, we prefer additive manufacturing to fabricate NZI beam generators, while the ambiguity issue in the NRW method is overcome by employing 3D-printed waveguides. Although commercially available 3D printing materials are not designed particularly for RF applications, copper-filled PLA shows promising features, i.e., high relative permittivity values with relatively low losses. On the other side, in the literature, 3D printing materials are mostly considered as nonmagnetic, which is not true, especially for composite filaments with metallic powders. Thus, the magnetic properties of the materials should also be considered in the designs.

After selecting the material, we predict suitable dimensions of cylindrical rods considering their refractive indices, taking into account relative permeabilities. Based on the effective-index-measurement setup, we demonstrate the NZI characteristics of cylindrical rods made of copper-filled PLA. Before the realization of the beam generators, the periodicity of NZI shells is fine-tuned considering their far-zone radiation patterns. Finally, we test diverse formations of NZI shells in an anechoic chamber thanks to the reconfigurability of the designs. As a result, fabrication and measurement of NZI shells acting as efficient beam generators are successfully achieved.

CHAPTER 5

CONCLUSIONS

In this study, design, simulation, fabrication, and measurement of NZI shell structures with efficient beam generation characteristics are presented. Simulations and measurements of diverse NZI shells involving various cavities, absorbers, and enhancers demonstrate these structures' useful properties in terms of beam generation from isotropic sources.

Simulations of NZI structures are made by using JMCFIE and MF for realistic and homogeneous models, respectively, while using proper solution algorithms. In the simulations of homogeneous structures with extremely small ϵ_r and μ_r values, MF provides stable, accurate, and efficient solutions of NZI shell structures in comparison to other formulations. Iterative solutions of homogenized models are further accelerated by low-frequency-stable AD-MLFMA. On the other side, in order to simulate realistic NZI models involving dielectric rods, JMCFIE and a three-layer preconditioner based on AMLFMA are used, enabling us to analyze high-contrast dielectric rod arrays involving millions of unknowns. Hence, the developed formulations and solution algorithms provide solutions of electromagnetic problems involving complicated and electrically large structures considered in this study.

A summary of the literature on the realization of near-zero relative permittivity and/or permeability in desired frequency regimes is presented. Some homogeneous materials, such as SiC, AZO, and TCOs, behave as ENZ media at their plasma frequencies, while their performances are limited due to losses. Similar to other metamaterials, NZI structures can be built by periodically arranging unit cells, such as dielectric or metallic rods, pillars, and layers. By proper arrangements of dielectric rods, i.e., by carefully designing center-to-center distances, radii, heights, and materials, extraor-

dinary NZI properties can be realized. Rod arrays can show anisotropic or isotropic characteristics, while their NZI behavior depends on both geometric properties and the operating frequency. Although simulations and measurements are performed at 10.3 GHz based on the fabrication and test opportunities, NZI structures can be realized at diverse frequencies, particularly at mmWaves.

In this study, NZI phenomena are rigorously investigated in terms of reflection and refraction properties. An effective-index-analysis setup is developed based on the Hough line transform of binarized near-field images. At the same time, the reflection and transmission coefficients of NZI media are extensively examined considering all NZI properties, i.e., EMNZ, ENZ, and MNZ. Based on these experiences, we develop a process with several steps to design NZI shells. Initially, the number of sides of the outer shell geometry is decided according to the maximum number of beams in the target wave pattern. Then, a source region, where an isotropic source is to be placed, is heuristically optimized to form a cavity that shows strong resonance behaviors for different NZI properties. Thanks to cavities that simply enclose the primary excitation without any physical contact, rotatable, isolated, and replaceable shell structures are obtained. The design process continues with modifying the outer surface of the shell in accordance with the intended beam configuration. VGs and inverted pyramids are designed to suppress selected beams, while NZI lenses are designed to enhance them. The results demonstrate favorable features of these modifications on both homogenized and actual models. It is remarkable that the designed NZI structures are fully reconfigurable, i.e., given a structure, the rods can be extracted and added instantly to obtain alternative radiation scenarios. Accordingly, undesired beams can be suppressed by VGs, while coverage of the structures can be enhanced with NZI lenses in selected directions by arranging and rearranging rods.

In this study, high-contrast dielectric rod arrays are carefully configured in order to induce near-zero relative permittivity and permeability values in their host media, while these dielectric rods are fabricated via low-cost 3D printing. 3D printing has many advantages, particularly being low-cost, highly accessible, and functional by allowing diverse design opportunities. Unfortunately, since most commercially available 3D printing materials are not designed for RF applications, they generally have low dielectric constants and high loss tangents. On the other hand, some composite 3D

printing filaments with metallic powders are known to possess favorable features in terms of permittivity values. Accordingly, a material characterization setup based on the NRW method is used to investigate various available materials. Besides, sample holder waveguides with proper thicknesses are fabricated via 3D printing to overcome the inaccuracy of the NRW method. As a result of rigorous experiments, ColorFabb copper-filled PLA is chosen as the rod material to build NZI shells. In the literature, 3D-printed materials are generally assumed as nonmagnetic; but, this is not correct for composite filaments with metallic powders, as shown via various examples. After selecting the proper material to fabricate high-contrast dielectric rods with 3D printers, the superior performance of the designs is examined by two different measurement setups in an anechoic chamber. The first one is the effective-index-test setup that provides NZI characteristics of cylindrical rods made of copper-filled PLA. In these tests, the refractive index is measured to be approximately 0.013. The second setup enables the measurements of an NZI shell when a monopole antenna is used at its center. Various shell structures are constructed and measured, leading to results that are in very good agreement with simulations. Based on comparisons, we clearly show the feasibility of efficient beam generators that can be designed with the proposed methodology.

Future works may include fabrications using materials with lower loss values in order to reach structures with better efficiencies. For instance, Preperm 3D filaments can be good candidates to realize efficient NZI shells, especially at higher frequencies. Furthermore, only shown for homogeneous models, tapering can be used in realistic NZI shells to decrease side-lobe levels. Finally, reconfigurability of the designed shells (currently manual) can be enhanced by employing opportunities in electronics. For instance, liquid crystals can be used to control the electrical properties of the rods, which may enable alternative radiation characteristics obtained instantly.

REFERENCES

[1] T. S. Rappaport, S. Sun, R. Mayzus, H. Zhao, Y. Azar, K. Wang, G. N. Wong, J. K. Schulz, M. Samimi, and F. Gutierrez, "Millimeter wave mobile communications for 5G cellular: It will work!," *IEEE Access*, vol. 1, pp. 335–349, 2013.

[2] J. G. Andrews, S. Buzzi, W. Choi, S. V. Hanly, A. Lozano, A. C. K. Soong, and J. C. Zhang, "What will 5G be?," *IEEE Journal on Selected Areas in Communications*, vol. 32, no. 6, pp. 1065–1082, 2014.

[3] W. Roh, J. Seol, J. Park, B. Lee, J. Lee, Y. Kim, J. Cho, K. Cheun, and F. Aryanfar, "Millimeter-wave beamforming as an enabling technology for 5G cellular communications: theoretical feasibility and prototype results," *IEEE Communications Magazine*, vol. 52, no. 2, pp. 106–113, 2014.

[4] W. Hong, "Solving the 5G mobile antenna puzzle: Assessing future directions for the 5G mobile antenna paradigm shift," *IEEE Microwave Magazine*, vol. 18, no. 7, pp. 86–102, 2017.

[5] B. Yang, Z. Yu, Y. Dong, J. Zhou, and W. Hong, "Compact tapered slot antenna array for 5G millimeter-wave massive MIMO systems," *IEEE Transactions on Antennas and Propagation*, vol. 65, no. 12, pp. 6721–6727, 2017.

[6] S. X. Ta, H. Choo, and I. Park, "Broadband printed-dipole antenna and its arrays for 5G applications," *IEEE Antennas and Wireless Propagation Letters*, vol. 16, pp. 2183–2186, 2017.

[7] S. Kumar, A. S. Dixit, R. R. Malekar, H. D. Raut, and L. K. Shevada, "Fifth generation antennas: A comprehensive review of design and performance enhancement techniques," *IEEE Access*, vol. 8, pp. 163568–163593, 2020.

[8] M. Imbert, A. Papió, F. De Flaviis, L. Jofre, and J. Romeu, "Design and performance evaluation of a dielectric flat lens antenna for millimeter-wave applica-

tions," *IEEE Antennas and Wireless Propagation Letters*, vol. 14, pp. 342–345, 2015.

[9] M. Imbert, J. Romeu, M. Baquero-Escudero, M. Martinez-Ingles, J. Molina-Garcia-Pardo, and L. Jofre, "Assessment of LTCC-based dielectric flat lens antennas and switched-beam arrays for future 5G millimeter-wave communication systems," *IEEE Transactions on Antennas and Propagation*, vol. 65, no. 12, pp. 6453–6473, 2017.

[10] O. Quevedo-Teruel, M. Ebrahimpouri, and F. Ghasemifard, "Lens antennas for 5G communications systems," *IEEE Communications Magazine*, vol. 56, no. 7, pp. 36–41, 2018.

[11] D. R. Jackson, C. Caloz, and T. Itoh, "Leaky-wave antennas," *Proceedings of the IEEE*, vol. 100, no. 7, pp. 2194–2206, 2012.

[12] N. Engheta and R. W. Ziolkowski, *Metamaterials: Physics and Engineering Explorations*. Wiley, 2006.

[13] R. W. Ziolkowski and N. Engheta, "Metamaterials: two decades past and into their electromagnetics future and beyond," *IEEE Transactions on Antennas and Propagation*, vol. 68, no. 3, pp. 1232–1237, 2019.

[14] V. G. Veselago, "Electrodynamics of substances with simultaneously negative values of ϵ and μ," *Sov. Phys. Usp.*, vol. 10, pp. 509–514, 1968.

[15] J. B. Pendry, A. Holden, W. Stewart, and I. Youngs, "Extremely low frequency plasmons in metallic mesostructures," *Physical Review Letters*, vol. 76, no. 25, p. 4773, 1996.

[16] J. B. Pendry, A. J. Holden, D. J. Robbins, and W. Stewart, "Magnetism from conductors and enhanced nonlinear phenomena," *IEEE Transactions on Microwave Theory and Techniques*, vol. 47, no. 11, pp. 2075–2084, 1999.

[17] R. A. Shelby, D. R. Smith, and S. Schultz, "Experimental verification of a negative index of refraction," *Science*, vol. 292, no. 5514, pp. 77–79, 2001.

[18] A. K. Iyer, A. Alù, and A. Epstein, "Metamaterials and metasurfaces—historical context, recent advances, and future directions," *IEEE Transactions on Antennas and Propagation*, vol. 68, no. 3, pp. 1223–1231, 2020.

[19] J. Hao, W. Yan, and M. Qiu, "Super-reflection and cloaking based on zero index metamaterial," *Applied Physics Letters*, vol. 96, no. 10, p. 101109, 2010.

[20] I. Liberal and N. Engheta, "Near-zero refractive index photonics," *Nature Photonics*, vol. 11, no. 3, pp. 149–158, 2017.

[21] R. Ziolkowski, "Propagation in and scattering from a matched metamaterial having a zero index of refraction," *Physical Review E*, vol. 70, no. 046608, 2004.

[22] X. Huang, Y. Lai, Z. H. Hang, H. Zheng, and C. Chan, "Dirac cones induced by accidental degeneracy in photonic crystals and zero-refractive-index materials," *Nature Materials*, vol. 10, no. 8, pp. 582–586, 2011.

[23] R. Dehbashi, K. S. Bialkowski, and A. M. Abbosh, "Size reduction of electromagnetic devices using double near-zero materials," *IEEE Transactions on Antennas and Propagation*, vol. 65, no. 12, pp. 7102–7109, 2017.

[24] J. P. Turpin, Q. Wu, D. H. Werner, B. Martin, M. Bray, and E. Lier, "Near-zero-index metamaterial lens combined with AMC metasurface for high-directivity low-profile antennas," *IEEE Transactions on Antennas and Propagation*, vol. 62, no. 4, pp. 1928–1936, 2014.

[25] A. Alù, M. G. Silveirinha, A. Salandrino, and N. Engheta, "Epsilon-near-zero metamaterials and electromagnetic sources: Tailoring the radiation phase pattern," *Physical Review B*, vol. 75, no. 155410, 2007.

[26] H. Chu, Q. Li, B. Liu, J. Luo, S. Sun, Z. H. Hang, L. Zhou, and Y. Lai, "A hybrid invisibility cloak based on integration of transparent metasurfaces and zero-index materials," *Light: Science & Applications*, vol. 7, no. 1, pp. 1–8, 2018.

[27] S. Enoch, G. Tayeb, P. Sabouroux, N. Guérin, and P. Vincent, "A metamaterial for directive emission," *Physical Review Letters*, vol. 89, no. 213902, 2002.

[28] H. Zhou, Z. Pei, S. Qu, S. Zhang, J. Wang, Q. Li, and Z. Xu, "A planar zero-index metamaterial for directive emission," *Journal of Electromagnetic Waves and Applications*, vol. 23, no. 7, pp. 953–962, 2009.

[29] B. Wang and K.-M. Huang, "Shaping the radiation pattern with mu and epsilon-near-zero metamaterials," *Progress in Electromagnetics Research*, vol. 106, pp. 107–119, 2010.

[30] J. Brown, "Artificial dielectrics having refractive indices less than unity," *Proceedings of the IEE-Part IV: Institution Monographs*, vol. 100, no. 5, pp. 51–62, 1953.

[31] R. Maas, J. Parsons, N. Engheta, and A. Polman, "Experimental realization of an epsilon-near-zero metamaterial at visible wavelengths," *Nature Photonics*, vol. 7, no. 11, pp. 907–912, 2013.

[32] J. Luo and Y. Lai, "Epsilon-near-zero or mu-near-zero materials composed of dielectric photonic crystals," *Science China Information Sciences*, vol. 56, no. 12, pp. 1–10, 2013.

[33] Y. Wu, J. Li, Z.-Q. Zhang, and C. T. Chan, "Effective medium theory for magnetodielectric composites: Beyond the long-wavelength limit," *Physical Review B*, vol. 74, no. 085111, 2006.

[34] Y. Wu, "A semi-Dirac point and an electromagnetic topological transition in a dielectric photonic crystal," *Optics Express*, vol. 22, no. 2, pp. 1906–1917, 2014.

[35] U. G. Yasa, M. Turduev, I. H. Giden, and H. Kurt, "Full utilization of semi-Dirac cones in photonics," *Physical Review B*, vol. 97, no. 195131, 2018.

[36] Y. Dong and T. Itoh, "Metamaterial-based antennas," *Proceedings of the IEEE*, vol. 100, no. 7, pp. 2271–2285, 2012.

[37] R. W. Ziolkowski, P. Jin, and C.-C. Lin, "Metamaterial-inspired engineering of antennas," *Proceedings of the IEEE*, vol. 99, no. 10, pp. 1720–1731, 2010.

[38] M. M. Bait-Suwailam, M. S. Boybay, and O. M. Ramahi, "Electromagnetic coupling reduction in high-profile monopole antennas using single-negative

magnetic metamaterials for MIMO applications," *IEEE Transactions on Antennas and Propagation*, vol. 58, no. 9, pp. 2894–2902, 2010.

[39] Ö. Eriş, T. Abanuzoğlu, and Ö. Ergül, "Design and simulation of nano-optical beam generators based on zero-index materials," in *International Electromagnetic Compatibility Conference (EMC Türkiye)*, 2019.

[40] Ö. Eriş and Ö. Ergül, "Design and simulation of beam-generating shells with near-zero-index characteristics," in *General Assembly and Scientific Symposium of the International Union of Radio Science (URSI-GASS)*, 2021.

[41] Ö. Eriş and Ö. Ergül, "SOLBOX-21," *URSI Radio Science Bulletin*, no. 374, 2020.

[42] Ö. Eriş and Ö. Ergül, "SOLBOX-20," *URSI Radio Science Bulletin*, no. 373, 2020.

[43] B. Behzadnezhad, B. D. Collick, N. Behdad, and A. B. McMillan, "Dielectric properties of 3D-printed materials for anatomy specific 3D-printed MRI coils," *Journal of Magnetic Resonance*, vol. 289, pp. 113–121, 2018.

[44] J. C. Booth, M. Whitley, C. Rudd, and M. Kranz, "Material database for additive manufacturing techniques," tech. rep., AMRDEC Redstone Arsenal United States, 2017.

[45] H. García-Martínez, E. Ávila-Navarro, G. Torregrosa-Penalva, A. Rodríguez-Martínez, C. Blanco-Angulo, and M. de la Casa-Lillo, "Low-cost additive manufacturing techniques applied to the design of planar microwave circuits by fused deposition modeling," *Polymers*, vol. 12, no. 9, p. 1946, 2020.

[46] A. Goulas, S. Zhang, J. R. McGhee, D. A. Cadman, W. G. Whittow, J. C. Vardaxoglou, and D. S. Engstrøm, "Fused filament fabrication of functionally graded polymer composites with variable relative permittivity for microwave devices," *Materials & Design*, vol. 193, p. 108871, 2020.

[47] E. Huber, M. Mirzaee, J. Bjorgaard, M. Hoyack, S. Noghanian, and I. Chang, "Dielectric property measurement of PLA," in *IEEE International Conference on Electro Information Technology (EIT)*, pp. 0788–0792, 2016.

[48] A. E. H. Love, "The integration of the equations of propagation of electric waves," *Philosophical Transactions of the Royal Society A*, vol. 197, no. 287-299, pp. 1–45, 1901.

[49] S. Rao, D. Wilton, and A. Glisson, "Electromagnetic scattering by surfaces of arbitrary shape," *IEEE Transactions on Antennas and Propagation*, vol. 30, no. 3, pp. 409–418, 1982.

[50] Ö. Ergül and L. Gürel, *The Multilevel Fast Multipole Algorithm (MLFMA) for Solving Large-Scale Computational Electromagnetics Problems*. Wiley-IEEE, 2014.

[51] C. Önol, A. Üçüncü, and Ö. Ergül, "Efficient multilayer iterative solutions of electromagnetic problems using approximate forms of the multilevel fast multipole algorithm," *IEEE Antennas and Wireless Propagation Letters*, vol. 16, pp. 3253–3256, 2017.

[52] J. Volakis and K. Sertel, *Integral Equation Methods for Electromagnetics*. SciTech Publishing, 2012.

[53] R. F. Harrington, *Field Computation by Moment Methods*. Macmillan, 1968.

[54] J. Mautz and R. Harrington, "H-field, E-field, and combined field solutions for conducting body of revolution," *AEÜ*, vol. 32, pp. 157–164, 1978.

[55] X. Sheng, J.-M. Jin, J. Song, W. Chew, and C.-C. Lu, "Solution of combined-field integral equation using multilevel fast multipole algorithm for scattering by homogeneous bodies," *IEEE Transactions on Antennas and Propagation*, vol. 46, no. 11, pp. 1718–1726, 1998.

[56] Ö. Ergül and L. Gürel, "Comparison of integral-equation formulations for the fast and accurate solution of scattering problems involving dielectric objects with the multilevel fast multipole algorithm," *IEEE Transactions on Antennas and Propagation*, vol. 57, no. 1, pp. 176–187, 2009.

[57] P. Ylä-Oijala and M. Taskinen, "Application of combined field integral equation for electromagnetic scattering by dielectric and composite objects," *IEEE Transactions on Antennas and Propagation*, vol. 53, no. 3, pp. 1168–1173, 2005.

[58] C. Müller, *Foundations of the Mathematical Theory of Electromagnetic Waves*. Springer, 1969.

[59] P. Ylä-Oijala and M. Taskinen, "Well-conditioned Müller formulation for electromagnetic scattering by dielectric objects," *IEEE Transactions on Antennas and Propagation*, vol. 53, no. 10, pp. 3316–3323, 2005.

[60] A. J. Poggio and E. K. Miller, "Integral equation solutions of three-dimensional scattering problems," in *Computer Techniques for Electromagnetics* (R. Mittra, ed.), ch. 4, pp. 159–264, Pergamon Press, 1973.

[61] Y. Chang and R. Harrington, "A surface formulation for characteristic modes of material bodies," *IEEE Transactions on Antennas and Propagation*, vol. 25, no. 6, pp. 789–795, 1977.

[62] T. K. Wu and L. L. Tsai, "Scattering from arbitrarily-shaped lossy dielectric bodies of revolution," *Radio Science*, vol. 12, no. 5, pp. 709–718, 1977.

[63] P. Ylä-Oijala, M. Taskinen, and S. Järvenpää, "Surface integral equation formulations for solving electromagnetic scattering problems with iterative methods," *Radio Science*, vol. 40, no. 6, 2005.

[64] B. Karaosmanoğlu, A. Yılmaz, and Ö. Ergül, "A comparative study of surface integral equations for accurate and efficient analysis of plasmonic structures," *IEEE Transactions on Antennas and Propagation*, vol. 65, no. 6, pp. 3049–3057, 2017.

[65] B. Karaosmanoğlu, U. Özmü, and Ö. Ergül, "Novel SIE formulations for accurate and stable analysis of near-zero-index materials," in *IEEE International Symposium on Antennas and Propagation (APS)*, pp. 1453–1454, 2019.

[66] B. Karaosmanoğlu, Y. Koyaz, H. İbili, and Ö. Ergül, "Fast and accurate analysis of three-dimensional structures involving near-zero-index materials," in *International Conference on Electromagnetics in Advanced Applications (ICEAA)*, pp. 1019–1024, 2019.

[67] H. İbili, Y. Koyaz, U. Özmü, B. Karaosmanoğlu, and Ö. Ergül, "Novel SIE implementations for efficient and accurate electromagnetic simulations of

zero-index materials," in *Photonics & Electromagnetics Research Symposium (PIERS)*, pp. 3772–3780, 2019.

[68] Ö. Ergül, "Fast and accurate analysis of homogenized metamaterials with the surface integral equations and the multilevel fast multipole algorithm," *IEEE Antennas and Wireless Propagation Letters*, vol. 10, pp. 1286–1289, 2011.

[69] P. Ylä-Oijala, J. Markkanen, S. Jarvenpaa, and S. P. Kiminki, "Surface and volume integral equation methods for time-harmonic solutions of Maxwell's equations," *Progress in Electromagnetics Research*, vol. 149, pp. 15–44, 2014.

[70] H. İbili, "Computational simulation and realization of three-dimensional metamaterials with various exotic properties," Master's thesis, Middle East Technical University, 2019.

[71] Ö. Eriş, G. Karaova, and Ö. Ergül, "Accurate and stable solutions of densely discretized conductors with a novel combined potential-field formulation," in *General Assembly and Scientific Symposium of the International Union of Radio Science (URSI-GASS)*, 2021.

[72] Ö. Eriş, G. Karaova, and Ö. Ergül, "Combined potential-field surface formulations for resonance-free and low-frequency-stable analyses of three-dimensional closed conductors," in *European Conference on Antennas and Propagation (EuCAP)*, 2021.

[73] N. Engheta, W. D. Murphy, V. Rokhlin, and M. S. Vassiliou, "The fast multipole method (FMM) for electromagnetic scattering problems," *IEEE Transactions on Antennas and Propagation*, vol. 40, no. 6, pp. 634–641, 1992.

[74] R. Coifman, V. Rokhlin, and S. Wandzura, "The fast multipole method for the wave equation: A pedestrian prescription," *IEEE Antennas and Propagation magazine*, vol. 35, no. 3, pp. 7–12, 1993.

[75] J. Song, C.-C. Lu, and W. C. Chew, "Multilevel fast multipole algorithm for electromagnetic scattering by large complex objects," *IEEE Transactions on Antennas and Propagation*, vol. 45, no. 10, pp. 1488–1493, 1997.

[76] W. C. Chew, E. Michielssen, J. Song, and J.-M. Jin, *Fast and Efficient Algorithms in Computational Electromagnetics*. Artech House, 2001.

[77] Ö. Ergül, ed., *New Trends in Computational Electromagnetics*. SciTech Publishing, 2020.

[78] Y. P. Chen, J. L. Xiong, and W. C. Chew, "A mixed-form thin-stratified medium fast-multipole algorithm for both low and mid-frequency problems," *IEEE Transactions on Antennas and Propagation*, vol. 59, no. 6, pp. 2341–2349, 2011.

[79] T. Xia, L. L. Meng, Q. S. Liu, H. H. Gan, and W. C. Chew, "A low-frequency stable broadband multilevel fast multipole algorithm using plane wave multipole hybridization," *IEEE Transactions on Antennas and Propagation*, vol. 66, no. 11, pp. 6137–6145, 2018.

[80] I. Bogaert, J. Peeters, and F. Olyslager, "A nondirective plane wave MLFMA stable at low frequencies," *IEEE Transactions on Antennas and Propagation*, vol. 56, no. 12, pp. 3752–3767, 2008.

[81] Ö. Ergül and B. Karaosmanoğlu, "Broadband multilevel fast multipole algorithm based on an approximate diagonalization of the Green's function," *IEEE Transactions on Antennas and Propagation*, vol. 63, no. 7, pp. 3035–3041, 2015.

[82] Ö. Ergül and B. Karaosmanoğlu, "Approximate stable diagonalization of the Green's function for low frequencies," *IEEE Antennas and Wireless Propagation Letters*, vol. 13, pp. 1054–1056, 2014.

[83] Ö. Eriş, H. İbili, and Ö. Ergül, "SOLBOX-15," *URSI Radio Science Bulletin*, no. 368, 2019.

[84] Ö. Ergül, T. Malas, and L. Gürel, "Solutions of large-scale electromagnetics problems using an iterative inner-outer scheme with ordinary and approximate multilevel fast multipole algorithms," *Progress in Electromagnetics Research*, vol. 106, pp. 203–223, 2010.

[85] K. Tap, *Complex source point beam expansions for some electromagnetic radiation and scattering problems*. PhD thesis, The Ohio State University, 2007.

[86] C.-T. Chan, X. Huang, F. Liu, and Z. H. Hang, "Dirac dispersion and zero-index in two dimensional and three dimensional photonic and phononic systems," *Progress in Electromagnetics Research*, vol. 44, pp. 163–190, 2012.

[87] S. Kita, Y. Li, P. Camayd-Munoz, O. Reshef, D. I. Vulis, R. W. Day, E. Mazur, and M. Loncar, "On-chip all-dielectric fabrication-tolerant zero-index metamaterials," *Optics Express*, vol. 25, pp. 8326–8334, Apr 2017.

[88] C. R. Simovski, P. A. Belov, A. V. Atrashchenko, and Y. S. Kivshar, "Wire metamaterials: physics and applications," *Advanced Materials*, vol. 24, no. 31, pp. 4229–4248, 2012.

[89] P. Moitra, Y. Yang, Z. Anderson, I. I. Kravchenko, D. P. Briggs, and J. Valentine, "Realization of an all-dielectric zero-index optical metamaterial," *Nature Photonics*, vol. 7, no. 10, pp. 791–795, 2013.

[90] M. Dubois, C. Shi, X. Zhu, Y. Wang, and X. Zhang, "Observation of acoustic Dirac-like cone and double zero refractive index," *Nature Communications*, vol. 8, no. 1, pp. 1–6, 2017.

[91] Y. Fu, Y. Xu, and H. Chen, "Inhomogeneous field in cavities of zero index metamaterials," *Scientific Reports*, vol. 5, no. 1, pp. 1–10, 2015.

[92] S. J. Orfanidis, "Electromagnetic Waves and Antennas." `https://www.ece.rutgers.edu/~orfanidi/ewa/`, 2016. Accessed: 2021-03-01.

[93] A. Mavrokefalos, S. E. Han, S. Yerci, M. S. Branham, and G. Chen, "Efficient light trapping in inverted nanopyramid thin crystalline silicon membranes for solar cell applications," *Nano Letters*, vol. 12, no. 6, pp. 2792–2796, 2012.

[94] C. A. Balanis, *Antenna Theory: Analysis and Design*. Wiley, 2016.

[95] W. B. Weir, "Automatic measurement of complex dielectric constant and permeability at microwave frequencies," *Proceedings of the IEEE*, vol. 62, no. 1, pp. 33–36, 1974.

[96] T. L. Blakney and W. Weir, "Comments on "Automatic measurement of complex dielectric constant and permeability at microwave frequencies"," *Proceedings of the IEEE*, vol. 63, no. 1, pp. 203–205, 1975.

[97] F. Costa, M. Borgese, M. Degiorgi, and A. Monorchio, "Electromagnetic characterisation of materials by using transmission/reflection (T/R) devices," *Electronics*, vol. 6, no. 4, p. 95, 2017.

[98] D. M. Pozar, *Microwave Engineering*. Wiley, 2011.

[99] Y. Wu, D. Isakov, and P. S. Grant, "Fabrication of composite filaments with high dielectric permittivity for fused deposition 3D printing," *Materials*, vol. 10, no. 10, p. 1218, 2017.

[100] A. Nicolson and G. Ross, "Measurement of the intrinsic properties of materials by time-domain techniques," *IEEE Transactions on Instrumentation and Measurement*, vol. 19, no. 4, pp. 377–382, 1970.

[101] A. Technologies, *User's Guide HP 8719D/20D/22D Network Analyzers*. Agilent Technologies, 1999.

[102] B. Riddle, J. Baker-Jarvis, and J. Krupka, "Complex permittivity measurements of common plastics over variable temperatures," *IEEE Transactions on Microwave Theory and Techniques*, vol. 51, no. 3, pp. 727–733, 2003.

[103] T. Galek, K. Porath, E. Burkel, and U. Van Rienen, "Extraction of effective permittivity and permeability of metallic powders in the microwave range," *Modelling and Simulation in Materials Science and Engineering*, vol. 18, no. 2, p. 025015, 2010.

APPENDIX A

DERIVATION OF INCIDENT POTENTIALS AND FIELDS

When a Hertzian dipole is used for excitation, incoming fields and potentials can be written as

$$\boldsymbol{A}^{\text{inc}}(\boldsymbol{r}) = \mu \boldsymbol{I}_d g_0(\boldsymbol{r}, \boldsymbol{r}_d) \tag{A.1}$$

$$\Phi^{\text{inc}}(\boldsymbol{r}) = \frac{1}{i\omega\epsilon\mu}\nabla \cdot \boldsymbol{A}^{\text{inc}}(\boldsymbol{r}) = \frac{1}{i\omega\epsilon}\nabla \cdot \boldsymbol{I}_d g_0(\boldsymbol{r}, \boldsymbol{r}_d) = \frac{1}{i\omega\epsilon}\boldsymbol{I}_d \cdot \nabla g_0(\boldsymbol{r}, \boldsymbol{r}_d) \tag{A.2}$$

$$= \frac{1}{i\omega\epsilon}\boldsymbol{I}_d \cdot (\boldsymbol{r} - \boldsymbol{r}_d)\frac{\exp(ik|\boldsymbol{r} - \boldsymbol{r}_d|)}{4\pi|\boldsymbol{r} - \boldsymbol{r}_d|^2}\left(ik - \frac{1}{|\boldsymbol{r} - \boldsymbol{r}_d|}\right), \tag{A.3}$$

where $\boldsymbol{I}_d$ is the dipole moment and $\boldsymbol{r}_d$ is the location of the dipole. To calculate incident electric field, we need to consider both magnetic vector and scalar electric potentials, which are related via the Lorentz gauge. Accordingly, the incident electric field intensity can be derived as

$$\boldsymbol{E}^{\text{inc}}(\boldsymbol{r}) = i\omega\boldsymbol{A}^{\text{inc}}(\boldsymbol{r}) - \nabla\Phi^{\text{inc}}(\boldsymbol{r}) = i\omega\boldsymbol{A}^{\text{inc}}(\boldsymbol{r}) - \frac{1}{i\omega\epsilon\mu}\nabla\nabla \cdot \boldsymbol{A}^{\text{inc}}(\boldsymbol{r}) \tag{A.4}$$

$$= i\omega\mu\boldsymbol{I}_d g_0(\boldsymbol{r}, \boldsymbol{r}_d) - \frac{1}{i\omega\epsilon}\nabla\left[\boldsymbol{I}_d \cdot \nabla g_0(\boldsymbol{r}, \boldsymbol{r}_d)\right] \tag{A.5}$$

$$\begin{aligned} &= i\omega\mu\boldsymbol{I}_d\frac{\exp(ik|\boldsymbol{r} - \boldsymbol{r}_d|)}{4\pi|\boldsymbol{r} - \boldsymbol{r}_d|} \\ &- \frac{1}{i\omega\epsilon}\nabla\left[\boldsymbol{I}_d \cdot (\boldsymbol{r} - \boldsymbol{r}_d)\frac{\exp(ik|\boldsymbol{r} - \boldsymbol{r}_d|)}{4\pi|\boldsymbol{r} - \boldsymbol{r}_d|^2}\left(ik - \frac{1}{|\boldsymbol{r} - \boldsymbol{r}_d|}\right)\right] \end{aligned} \tag{A.6}$$

$$\begin{aligned} &= i\omega\mu\boldsymbol{I}_d\frac{\exp(ik|\boldsymbol{r} - \boldsymbol{r}_d|)}{4\pi|\boldsymbol{r} - \boldsymbol{r}_d|} \\ &- \frac{1}{i\omega\epsilon}\nabla\left[\boldsymbol{I}_d \cdot (\boldsymbol{r} - \boldsymbol{r}_d)\right]\left[\frac{\exp(ik|\boldsymbol{r} - \boldsymbol{r}_d|)}{4\pi|\boldsymbol{r} - \boldsymbol{r}_d|^2}\left(ik - \frac{1}{|\boldsymbol{r} - \boldsymbol{r}_d|}\right)\right] \\ &- \frac{1}{i\omega\epsilon}\left[\boldsymbol{I}_d \cdot (\boldsymbol{r} - \boldsymbol{r}_d)\right]\nabla\left[\frac{\exp(ik|\boldsymbol{r} - \boldsymbol{r}_d|)}{4\pi|\boldsymbol{r} - \boldsymbol{r}_d|^2}\left(ik - \frac{1}{|\boldsymbol{r} - \boldsymbol{r}_d|}\right)\right]. \end{aligned} \tag{A.7}$$

At this stage, the required identities can be written as

$$\nabla \left[\boldsymbol{I}_d \cdot (\boldsymbol{r} - \boldsymbol{r}_d) \right] = \boldsymbol{I}_d \tag{A.8}$$

$$\nabla \left[\frac{\exp(ik|\boldsymbol{r} - \boldsymbol{r}_d|)}{4\pi|\boldsymbol{r} - \boldsymbol{r}_d|^2} \left(ik - \frac{1}{|\boldsymbol{r} - \boldsymbol{r}_d|} \right) \right] = -(\boldsymbol{r} - \boldsymbol{r}_d) \frac{\exp(ik|\boldsymbol{r} - \boldsymbol{r}_d|)}{4\pi|\boldsymbol{r} - \boldsymbol{r}_d|^3} \left(k^2 + \frac{i3k}{|\boldsymbol{r} - \boldsymbol{r}_d|} - \frac{3}{|\boldsymbol{r} - \boldsymbol{r}_d|^2} \right), \tag{A.9}$$

leading to

$$\boldsymbol{E}^{\text{inc}}(\boldsymbol{r}) = i\omega\mu \boldsymbol{I}_d \frac{\exp(ik|\boldsymbol{r} - \boldsymbol{r}_d|)}{4\pi|\boldsymbol{r} - \boldsymbol{r}_d|} - \frac{\boldsymbol{I}_d}{i\omega\epsilon} \left[\frac{\exp(ik|\boldsymbol{r} - \boldsymbol{r}_d|)}{4\pi|\boldsymbol{r} - \boldsymbol{r}_d|^2} \left(ik - \frac{1}{|\boldsymbol{r} - \boldsymbol{r}_d|} \right) \right] + \frac{(\boldsymbol{r} - \boldsymbol{r}_d)}{i\omega\epsilon} \left[\boldsymbol{I}_d \cdot (\boldsymbol{r} - \boldsymbol{r}_d) \right] \frac{\exp(ik|\boldsymbol{r} - \boldsymbol{r}_d|)}{4\pi|\boldsymbol{r} - \boldsymbol{r}_d|^3} \left(k^2 + \frac{i3k}{|\boldsymbol{r} - \boldsymbol{r}_d|} - \frac{3}{|\boldsymbol{r} - \boldsymbol{r}_d|^2} \right) \tag{A.10}$$

$$= i\omega\mu \frac{\exp(ik|\boldsymbol{r} - \boldsymbol{r}_d|)}{4\pi|\boldsymbol{r} - \boldsymbol{r}_d|} \left[\boldsymbol{I}_d \left(1 + \frac{i}{k|\boldsymbol{r} - \boldsymbol{r}_d|} - \frac{1}{k^2|\boldsymbol{r} - \boldsymbol{r}_d|^2} \right) - (\boldsymbol{r} - \boldsymbol{r}_d) \frac{\boldsymbol{I}_d \cdot (\boldsymbol{r} - \boldsymbol{r}_d)}{|\boldsymbol{r} - \boldsymbol{r}_d|^2} \left(1 + \frac{3i}{k|\boldsymbol{r} - \boldsymbol{r}_d|} - \frac{3}{k^2|\boldsymbol{r} - \boldsymbol{r}_d|^2} \right) \right]. \tag{A.11}$$

Then, the incident magnetic field intensity can be found as

$$\boldsymbol{H}^{\text{inc}}(\boldsymbol{r}) = \frac{1}{\mu} \nabla \times \boldsymbol{A}^{\text{inc}}(\boldsymbol{r}) = \nabla \times \boldsymbol{I}_d g_0(\boldsymbol{r}, \boldsymbol{r}_d) = -\boldsymbol{I}_d \times \nabla g_0(\boldsymbol{r}, \boldsymbol{r}_d) \tag{A.12}$$

$$= \boldsymbol{I}_d \times (\boldsymbol{r} - \boldsymbol{r}_d) \frac{\exp(ik|\boldsymbol{r} - \boldsymbol{r}_d|)}{4\pi|\boldsymbol{r} - \boldsymbol{r}_d|^2} \left(\frac{1}{|\boldsymbol{r} - \boldsymbol{r}_d|} - ik \right). \tag{A.13}$$

As two examples, the real part of the electric field intensity radiated by a Hertzian dipole and a CSP at 10.3 GHz can be seen in Figure A.1. Although, the Hertzian dipole has an omnidirectional radiation, the CSP has a directive radiation towards the x axis. We note that, if the complex location was changed as $x = i10\lambda$, the radiation direction would change as $-x$.

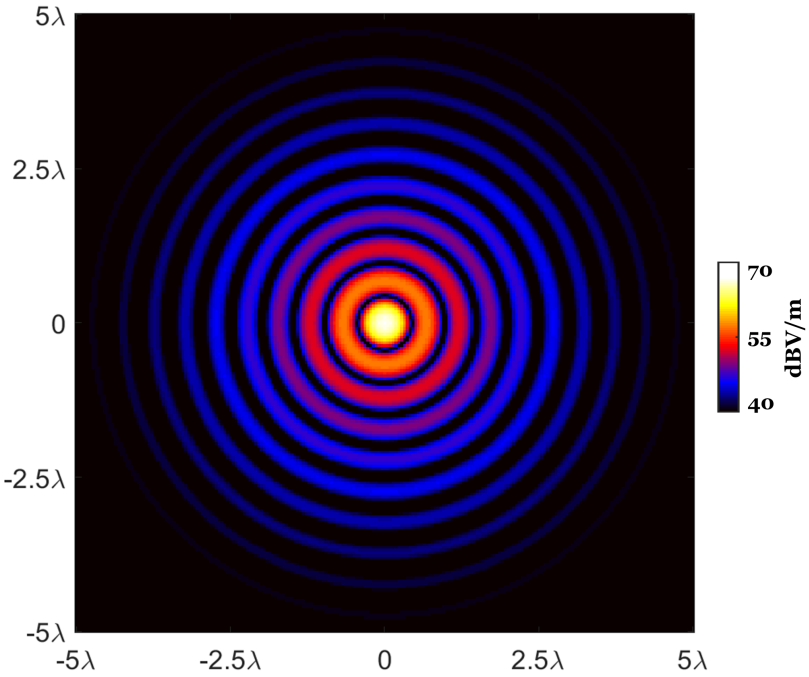

(a) Hertzian dipole at $\{x, y, z\} = \{0, 0, 0\}$.

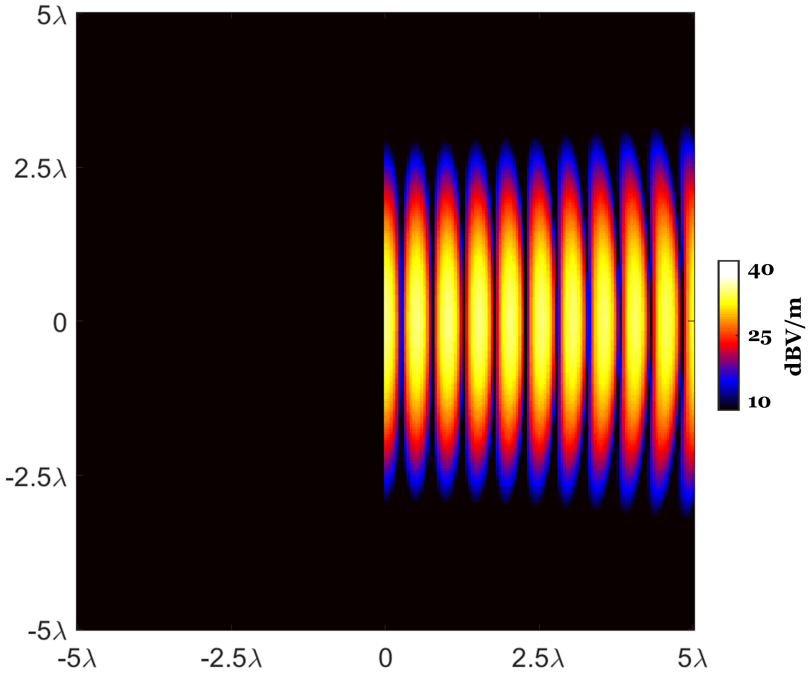

(b) Hertzian dipole at $\{x, y, z\} = \{-i10\lambda, 0, 0\}$.

Figure A.1: Real part of the electric field intensity in the x-y plane when a Hertzian dipole with $\boldsymbol{I}_d = \hat{\boldsymbol{z}}$ is located (a) at the origin and (b) at a position on the imaginary x axis.

APPENDIX B

MATRIX FORMS OF JMCFIE AND MF FOR NZI SIMULATIONS

Matrix systems constructed for penetrable objects can be written as

$$\begin{bmatrix} \bar{\boldsymbol{Z}}_{11} & \bar{\boldsymbol{Z}}_{12} \\ \bar{\boldsymbol{Z}}_{21} & \bar{\boldsymbol{Z}}_{22} \end{bmatrix} \cdot \begin{bmatrix} \boldsymbol{a}_J \\ \boldsymbol{a}_M \end{bmatrix} = \begin{bmatrix} \boldsymbol{v}_1 \\ \boldsymbol{v}_2 \end{bmatrix}. \tag{B.1}$$

Considering the coefficients given in Section 2.1.3, matrix elements for JMCFIE can be written as

$$\bar{\boldsymbol{Z}}_{11}^{\text{JMCFIE}} = \bar{\boldsymbol{Z}}_{22}^{\text{JMCFIE}} = \bar{\boldsymbol{T}}_o^T + \bar{\boldsymbol{T}}_i^T + \bar{\boldsymbol{K}}_o^N - \bar{\boldsymbol{K}}_i^N - \bar{\boldsymbol{I}}^T \tag{B.2}$$

$$\bar{\boldsymbol{Z}}_{12}^{\text{JMCFIE}} = -\eta_o^{-1}\bar{\boldsymbol{K}}_o^T - \eta_i^{-1}\bar{\boldsymbol{K}}_i^T - \frac{1}{2}(\eta_o^{-1} - \eta_i^{-1})\bar{\boldsymbol{I}}^N + \eta_o^{-1}\bar{\boldsymbol{T}}_o^N - \eta_i^{-1}\bar{\boldsymbol{T}}_i^N \tag{B.3}$$

$$\bar{\boldsymbol{Z}}_{21}^{\text{JMCFIE}} = \eta_o\bar{\boldsymbol{K}}_o^T + \eta_i\bar{\boldsymbol{K}}_i^T + \frac{1}{2}(\eta_o - \eta_i)\bar{\boldsymbol{I}}^N - \eta_o\bar{\boldsymbol{T}}_o^N + \eta_i\bar{\boldsymbol{T}}_i^N. \tag{B.4}$$

On the other hand, matrix elements for MF can be written as

$$\bar{\boldsymbol{Z}}_{11}^{\text{MF}} = \bar{\boldsymbol{T}}_o^T + \epsilon_i\epsilon_o^{-1}\eta_i\eta_o^{-1}\bar{\boldsymbol{T}}_i^T + \bar{\boldsymbol{K}}_o^N - \mu_i\mu_o^{-1}\bar{\boldsymbol{K}}_i^N - \frac{1}{2}(1 + \mu_i\mu_o^{-1})\bar{\boldsymbol{I}}^T \tag{B.5}$$

$$\begin{aligned}\bar{\boldsymbol{Z}}_{12}^{\text{MF}} = {} & -\eta_o^{-1}\bar{\boldsymbol{K}}_o^T - \epsilon_i\epsilon_o^{-1}\eta_o^{-1}\bar{\boldsymbol{K}}_i^T - \frac{1}{2}\eta_o^{-1}(1 - \epsilon_i\epsilon_o^{-1})\bar{\boldsymbol{I}}^N \\ & + \eta_o^{-1}\bar{\boldsymbol{T}}_o^N - \mu_i\mu_o^{-1}\eta_i^{-1}\bar{\boldsymbol{T}}_i^N\end{aligned} \tag{B.6}$$

$$\begin{aligned}\bar{\boldsymbol{Z}}_{21}^{\text{MF}} = {} & \eta_o\bar{\boldsymbol{K}}_o^T + \mu_i\mu_o^{-1}\eta_o\bar{\boldsymbol{K}}_i^T + \frac{1}{2}\eta_o(1 - \mu_i\mu_o^{-1})\bar{\boldsymbol{I}}^N \\ & - \eta_o\bar{\boldsymbol{T}}_o^N + \epsilon_i\epsilon_o^{-1}\eta_i\bar{\boldsymbol{T}}_i^N\end{aligned} \tag{B.7}$$

$$\bar{\boldsymbol{Z}}_{22}^{\text{MF}} = \bar{\boldsymbol{T}}_o^T + \mu_i\mu_o^{-1}\eta_o\eta_i^{-1}\bar{\boldsymbol{T}}_i^T + \bar{\boldsymbol{K}}_o^N - \epsilon_i\epsilon_o^{-1}\bar{\boldsymbol{K}}_i^N - \frac{1}{2}(1 + \epsilon_i\epsilon_o^{-1})\bar{\boldsymbol{I}}^T. \tag{B.8}$$

Considering NZI cases, i.e., EMNZ case when $\{\epsilon_r, \mu_r\} \to \{0, 0\}$, ENZ case when $\{\epsilon_r, \mu_r\} \to \{0, \mu_o\}$, and MNZ case when $\{\epsilon_r, \mu_r\} \to \{\epsilon_o, 0\}$, discretized matrix elements for JMCFIE have the following limit forms:

EMNZ

$$\bar{\boldsymbol{Z}}_{11}^{\text{JMCFIE}} = \bar{\boldsymbol{Z}}_{22}^{\text{JMCFIE}} \to \bar{\boldsymbol{T}}_i^T \tag{B.9}$$

$$\bar{\boldsymbol{Z}}_{12}^{\text{JMCFIE}} \to -\eta_i^{-1}\bar{\boldsymbol{T}}_i^N \tag{B.10}$$

$$\bar{\boldsymbol{Z}}_{21}^{\text{JMCFIE}} \to \eta_i\bar{\boldsymbol{T}}_i^N . \tag{B.11}$$

ENZ

$$\bar{\boldsymbol{Z}}_{11}^{\text{JMCFIE}} = \bar{\boldsymbol{Z}}_{22}^{\text{JMCFIE}} \to \bar{\boldsymbol{T}}_i^T \tag{B.12}$$

$$\bar{\boldsymbol{Z}}_{12}^{\text{JMCFIE}} \to -\eta_o^{-1}\bar{\boldsymbol{K}}_o^T - \frac{1}{2}\eta_o^{-1}\bar{\boldsymbol{I}}^N + \eta_o^{-1}\bar{\boldsymbol{T}}_o^N - \eta_i^{-1}\bar{\boldsymbol{T}}_i^N \tag{B.13}$$

$$\bar{\boldsymbol{Z}}_{21}^{\text{JMCFIE}} \to \eta_i\bar{\boldsymbol{T}}_i^N . \tag{B.14}$$

MNZ

$$\bar{\boldsymbol{Z}}_{11}^{\text{JMCFIE}} = \bar{\boldsymbol{Z}}_{22}^{\text{JMCFIE}} \to \bar{\boldsymbol{T}}_i^T \tag{B.15}$$

$$\bar{\boldsymbol{Z}}_{12}^{\text{JMCFIE}} \to -\eta_i^{-1}\bar{\boldsymbol{T}}_i^N \tag{B.16}$$

$$\bar{\boldsymbol{Z}}_{21}^{\text{JMCFIE}} \to \eta_o\bar{\boldsymbol{K}}_o^T + \frac{1}{2}\eta_o\bar{\boldsymbol{I}}^N - \eta_o\bar{\boldsymbol{T}}_o^N + \eta_i\bar{\boldsymbol{T}}_i^N . \tag{B.17}$$

The inner $\bar{\boldsymbol{T}}$ operator involving the scalar potential generally dominates the other operators. For ENZ and MNZ cases, due to the intrinsic impedance or inverse of it, one of the diagonal blocks dominates the matrix equation. Therefore, we cannot obtain a well-posed system with JMCFIE for NZI cases. On the other hand, when we investigate MF, we obtain the following limit forms:

EMNZ

$$\bar{\boldsymbol{Z}}_{11}^{\text{MF}} \to \bar{\boldsymbol{T}}_o^T + k_i k_o^{-1}\bar{\boldsymbol{T}}_i^T + \bar{\boldsymbol{K}}_o^N - \frac{1}{2}\bar{\boldsymbol{I}}^T \tag{B.18}$$

$$\bar{\boldsymbol{Z}}_{12}^{\text{MF}} \to -\eta_o^{-1}\bar{\boldsymbol{K}}_o^T - \frac{1}{2}\eta_o^{-1}\bar{\boldsymbol{I}}^N + \eta_o^{-1}\bar{\boldsymbol{T}}_o^N - \omega^{-1}\mu_o^{-1}k_i\bar{\boldsymbol{T}}_i^N \tag{B.19}$$

$$\bar{\boldsymbol{Z}}_{21}^{\text{MF}} \to \eta_o\bar{\boldsymbol{K}}_o^T + \frac{1}{2}\eta_o\bar{\boldsymbol{I}}^N - \eta_o\bar{\boldsymbol{T}}_o^N + \omega^{-1}\epsilon_o^{-1}k_i\bar{\boldsymbol{T}}_i^N \tag{B.20}$$

$$\bar{\boldsymbol{Z}}_{22}^{\text{MF}} \to \bar{\boldsymbol{T}}_o^T + k_i k_o^{-1}\bar{\boldsymbol{T}}_i^T + \bar{\boldsymbol{K}}_o^N - \frac{1}{2}\bar{\boldsymbol{I}}^T . \tag{B.21}$$

ENZ

$$\bar{\boldsymbol{Z}}_{11}^{\mathrm{MF}} \to \bar{\boldsymbol{T}}_o^T + k_i k_o^{-1} \bar{\boldsymbol{T}}_i^T + \bar{\boldsymbol{K}}_o^N - \mu_i \mu_o^{-1} \bar{\boldsymbol{K}}_i^N - \frac{1}{2}(1 + \mu_i \mu_o^{-1}) \bar{\boldsymbol{I}}^T \tag{B.22}$$

$$\bar{\boldsymbol{Z}}_{12}^{\mathrm{MF}} \to -\eta_o^{-1} \bar{\boldsymbol{K}}_o^T - \frac{1}{2}\eta_o^{-1} \bar{\boldsymbol{I}}^N + \eta_o^{-1} \bar{\boldsymbol{T}}_o^N - \omega^{-1} \mu_o^{-1} k_i \bar{\boldsymbol{T}}_i^N \tag{B.23}$$

$$\bar{\boldsymbol{Z}}_{21}^{\mathrm{MF}} \to \eta_o \bar{\boldsymbol{K}}_o^T + \mu_i \mu_o^{-1} \eta_o \bar{\boldsymbol{K}}_i^T + \frac{1}{2}\eta_o (1 - \mu_i \mu_o^{-1}) \bar{\boldsymbol{I}}^N - \eta_o \bar{\boldsymbol{T}}_o^N + \omega^{-1} \epsilon_o^{-1} k_i \bar{\boldsymbol{T}}_i^N \tag{B.24}$$

$$\bar{\boldsymbol{Z}}_{22}^{\mathrm{MF}} \to \bar{\boldsymbol{T}}_o^T + k_i k_o^{-1} \bar{\boldsymbol{T}}_i^T + \bar{\boldsymbol{K}}_o^N - \frac{1}{2} \bar{\boldsymbol{I}}^T. \tag{B.25}$$

MNZ

$$\bar{\boldsymbol{Z}}_{11}^{\mathrm{MF}} \to \bar{\boldsymbol{T}}_o^T + k_i k_o^{-1} \bar{\boldsymbol{T}}_i^T + \bar{\boldsymbol{K}}_o^N - \frac{1}{2} \bar{\boldsymbol{I}}^T \tag{B.26}$$

$$\bar{\boldsymbol{Z}}_{12}^{\mathrm{MF}} \to -\eta_o^{-1} \bar{\boldsymbol{K}}_o^T - \epsilon_i \epsilon_o^{-1} \eta_o^{-1} \bar{\boldsymbol{K}}_i^T - \frac{1}{2}\eta_o^{-1} (1 - \epsilon_i \epsilon_o^{-1}) \bar{\boldsymbol{I}}^N + \eta_o^{-1} \bar{\boldsymbol{T}}_o^N - \omega^{-1} \mu_o^{-1} k_i \bar{\boldsymbol{T}}_i^N \tag{B.27}$$

$$\bar{\boldsymbol{Z}}_{21}^{\mathrm{MF}} \to \eta_o \bar{\boldsymbol{K}}_o^T + \frac{1}{2}\eta_o \bar{\boldsymbol{I}}^N - \eta_o \bar{\boldsymbol{T}}_o^N + \omega^{-1} \epsilon_o^{-1} k_i \bar{\boldsymbol{T}}_i^N \tag{B.28}$$

$$\bar{\boldsymbol{Z}}_{22}^{\mathrm{MF}} \to \bar{\boldsymbol{T}}_o^T + k_i k_o^{-1} \bar{\boldsymbol{T}}_i^T + \bar{\boldsymbol{K}}_o^N - \epsilon_i \epsilon_o^{-1} \bar{\boldsymbol{K}}_i^N - \frac{1}{2}(1 + \epsilon_i \epsilon_o^{-1}) \bar{\boldsymbol{I}}^T. \tag{B.29}$$

It should be noted that, using MF, all operators are well-balanced with each other in all NZI cases. In addition, identity operators remain in the diagonal blocks, making MF produce well-conditioned matrix equations.